Evaluating new Oxygen Transfer Materials for Air Separation, Oxy-Fuel Combustion and other Processes

Richard Hinrich Görke

Department of Engineering

University of Cambridge

This dissertation is submitted for the degree of

Doctor of Philosophy

Homerton College

September 2018

To my parents

DECLARATION

This dissertation is the result of my own work and includes nothing which is the outcome of work done in collaboration except where specifically indicated in the text. It has not been previously submitted, in part or whole, to any university or institution for any degree, diploma, or other qualification.

In accordance with the Department of Engineering guidelines, this thesis does not exceed the prescribed word limit.

This Dissertation contains approximately 53,400 words, 35 tables and 68 figures.

Richard Hinrich Görke

Department of Engineering
University of Cambridge

September 2018

ABSTRACT

Chemical looping air separation was the pre-dominant commercial process to produce oxygen until it was superseded by the Hampson–Linde cycle in the early 20th century. A chemical air separation loop is characterised by the cyclic reduction and oxidation of solid material serving as an oxygen carrier, which has the capacity to release gas phase oxygen. At the time, the so-called Brin process suffered from the deactivation of the oxygen carrier material due to carbonation if the air was not pre-treated. In the past decade, however, the process has gained considerable attention due to advances in material science. The objective of this Dissertation is to suggest novel materials suitable for this air separation process.

In this Dissertation, the entire process from the identification of, in theory, suitable oxygen transfer materials *via* the synthesis and evaluation (regarding thermochemical properties) of these materials through to the investigation of the kinetic parameters and stability over many redox cycles is carried out. Although oxygen is an important industrial gas used for many applications, here, chemical looping air separation is investigated as a method of avoiding the emission of CO_2 from a power plant *via* oxy-fuel combustion and subsequent CO_2 capture.

First, a fully heat integrated model of a power station, linked to a model of chemical looping air separation system is developed to back calculate the thermochemical properties, *i.e.* enthalpy ($\Delta H^o_{r,298\,K}$) and entropy ($\Delta S^o_{r,298\,K}$) of reaction, of the oxygen carrier required for efficient operation. It is demonstrated that an oxy-fuel steam power plant fed with oxygen from chemical looping air separation can be operated with an energy penalty of as low as 1.5 percentage points. However, this is only possible for materials possessing a narrow range of $\Delta H^o_{r,298\,K}$ and $\Delta S^o_{r,298\,K}$. From a list of oxygen carriers possessing favourable thermodynamic properties, the perovskite $SrFeO_{3-\delta}$ is selected for further investigation.

In a tubular micro-reactor, developed and optimised for minimum noise and response time, oxygen transfer capacities and reaction kinetics of the pure, Mn-doped and Co-doped $SrFeO_{3-\delta}$ are investigated. The rate constants of the reduction reaction have been

successfully extracted, however, this was not possible for the oxidation which proceeded too rapidly. The apparent activation energy, $E_{a,app}$, and the pre-exponential factor, A', for $SrFeO_{3-\delta}$, $SrMn_{0.1}Fe_{0.9}O_{3-\delta}$, $SrCo_{0.4}Fe_{0.6}O_{3-\delta}$ are 128.9, 45.3 and 271.3 kJ/mol, and $3.9 \cdot 10^5$, 6.29 and $35.5 \cdot 10^{12}$ mol/s/Pa/m^3, respectively.

$SrMn_{0.1}Fe_{0.9}O_{3-\delta}$ showed both the highest oxygen transfer capacity and rate of reduction and $SrCo_{0.4}Fe_{0.6}O_{3-\delta}$ the lowest; around 325 and 117 µmol of O_2 per gram of oxygen carrier material at 898 K, respectively. When subjecting $SrFeO_{3-\delta}$ and $SrMn_{0.1}Fe_{0.9}O_{3-\delta}$ to 1000 redox cycles, both showed an increase in the maximum observed rate of reduction and the oxygen transfer capacity.

ACKNOWLEDGEMENTS

First and foremost, I would like to thank my supervisor, Dr Stuart Scott. As much as his support and guidance have been immeasurable to the success of my PhD project, discussions with him and his impetuousness to try out new ideas (blow-up Friday) have filled it with joy. I am grateful to my advisor, Prof. John Dennis, for his advice along the way.

This PhD project had many contributors, a list too long to fit in a document of equal size to this work; without those who lent a helping hand here and there or contributed equipment, such as a Gilibrator to validate gas flows, high-precision flow controllers or simply a peculiar Swagelok fitting, I would be lost in the lab to this day.

I would like to extend special thanks to Dr Ewa Marek for discussions, feedback and help with the preparation of oxygen carrier materials, TGA experiments and XRD analyses. My thanks go to Dr Kieran Hegarty, Dr Paul Dickinson and Prof. Nick Collings who provided me with an oxygen sensor system without which the experiments described in this work would be preposterous.

I thank everyone from my research group, namely, Drs Martin Chan, Felix Donat, Hermenegildo Garcia, Paul Hodgson, Ross Hubble, Mauro Malizia and Matthias Schnellmann; Zachariah Bond, Samuel Gabra, Clayton Rabideau, Mohammad Saghafifar, Michael Sargent and Yaoyao Zheng. Further, I am thankful to the supporting staff at Division A of the Department of Engineering, Robert Leroy, Mark Vining, John Harvey, Roy Slater, Ken Griggs and Peter Benie, who provided simple solutions for complex questions.

I am truly grateful for the friends who made my time at Cambridge unforgettable and the Homerton College Boat Club for providing the opportunity to experience countless sunrises, despite not having asked for it. Keval Patel, Max Hawkins, Jack Hugo and Hugo Venthan, thanks for being there in tough times. Nguyen Anh Khoa Doan, Felix Donat, Christian Höcker, Nicholas Jamieson, Robert Nishida, Mohammad Saghafifar and Philip Sitte for lunch or pub escapes or the odd spontaneous trip to the countryside or Berlin. I thank my house mates Oliver Melvill, Stephanie Payne and Kevin Kay for a great time full of BBQs and board games.

Finally, I extend gratitude to my family for their support and to my wife, Bentje, for believing in me and enduring years and years of long-distance relationship.

CONTENTS

LIST OF TABLES

LIST OF FIGURES

1 Introduction

1.1 Background

Coal currently accounts for roughly 38 % of the global electricity generation and the demand for coal is forecasted to increase by ~34 % by 2040 when assuming the Current Policies Scenario which considers only measures and policies already implemented as outlined in the IEA (International Energy Agency) World Energy Outlook 2017 (IEA, 2017). In light of an increasing public awareness of the anthropogenic climate change and likely changes in policies by major industrial nations – for example, at the time of publication of the World Energy Outlook 2017 five European nations were discussing the phase out of coal of which Germany has since announced it – one of the two other outlined scenarios, the New Policies Scenario and the Sustainable Development Scenario, seem more probable. The New Policies Scenario, the main scenario in the World Energy Outlook 2017, takes into account assumptions about the future developments in the coal price relative to other fuels and macroeconomics as well as announced policies (IEA, 2017). In this scenario, a stabilisation for the demand for coal of ~5.5 Gt coal equivalent (Gtce) by 2040, up from ~5.37 Gtce in 2016, is predicted. Further, the report forecasts a significant shift in the demand for coal from the US, Europe and China to Southeast Asia and, above all, India. In contrast to the Current Policy and New Policy scenarios, the Sustainable Development Scenario achieves the goals set out by the Paris Agreement. Here, the share of electricity generated from coal decreases to 6 % by 2040, with 60 % of the installed power com-

ing from coal power plants fitted with carbon capture and storage (CCS) technologies. While there are several advantages to the utilisation of coal, *i.e.* its abundance by providing 64 % of fossil fuel reserves, its low cost and security of supply, it is the leading carbon-dioxide emitting fossil fuel (IEA, 2012). Hence, under the Sustainable Development Scenario, there will be a shift from coal to gas for mid-load and baseload power generation, and to provide flexible balancing capacity to accommodate the variable power from renewables. Still, at least 10 % of the gas-fired power plants must be fitted with CCS to achieve the carbon emissions goals set in the Paris Agreement (IEA, 2017). As per the Sustainable Development Scenario, it is not just the power sector that must adopt technologies for decarbonisation but also the industry sector which will be responsible for ~60 % of the increase in the global demand for natural gas by 2040. In the industry sector, large amounts of carbon dioxide emissions do not originate from the combustion of fuel but the respective industrial process itself; for example, in 2014, the production of cement was responsible for approximately 8 % of the global anthropogenic CO_2 emissions of which more than half could be attributed to the decarbonation of limestone ($CaCO_3 \rightarrow CaO + CO_2$) (Olivier *et al.*, 2015). For both the industry and energy sector, large-scale CCS facilities exist already, such as the Petra Nova CCS facility in Houston, USA, which is the largest operational CCS facility in the power generation sector and captures some 1.4 Mt CO_2 from an adjacent power plant, or the Abu Dhabi CCS facility, the first fully commercial facility in the steel industry[1]. In both cases however, only a fraction of the carbon dioxide that is produced by the adjacent plants is captured. Further research of carbon capture technologies is therefore necessary.

In the energy sector, in principle, three strategies for capturing CO_2 exist: pre-, post- and oxy-fuel combustion. The concepts of these strategies are outlined in Figure 1-1 for solid fuels. In the pre-combustion capture process, in a first step, oxygen is separated from air to be used for the gasification of a solid fuel or partial oxidation of a gaseous or liquid fuel following (Jansen *et al.*, 2015)

$$C_xH_y + \frac{x}{2}O_2 \rightleftarrows xCO + \frac{y}{2}H_2 \qquad (1\text{-}1)$$

[1] A list of current and planned CCS projects is compiled by the Global CCS Institute on https://co2e.co

Another route to produce the syngas does not require air separation and, instead, the first step in the pre-combustion capture process consists of steam reforming, where steam is added to the fuel (Romano *et al.*, 2010; Jansen *et al.*, 2015):

$$C_xH_y + xH_2O \rightleftarrows xCO + \frac{x+y}{2}H_2 \qquad (1\text{-}2)$$

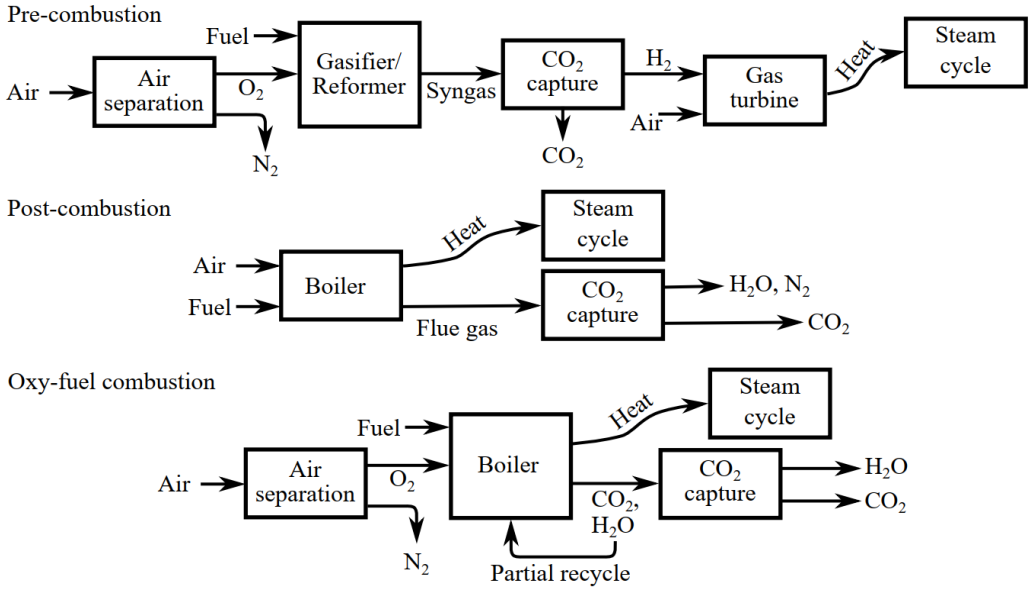

Figure 1-1: Concepts of carbon capture and storage technologies for the generation of electricity

It should be noted that the gasification or partial oxidation is exothermic, and the steam reforming process is endothermic. Therefore, by adding oxygen to the steam reforming process it is possible to cancel its endothermicity and achieve what is called autothermal reforming or autothermal gasification.

Using the water gas shift reaction (reaction (1-3)), the produced carbon monoxide is shifted to hydrogen and carbon dioxide ready for separation (Romano *et al.*, 2010; Jansen *et al.*, 2015). As shown in Figure 1-1, the hydrogen is then used to drive a combined cycle power plant.

$$CO + H_2O \rightleftarrows CO_2 + H_2 \qquad (1\text{-}3)$$

The post-combustion capture process would be the easiest of the three CCS technologies to implement from a process engineering point of view as only a CO_2 capture unit is required to treat the flue gas. However, the capture of the carbon dioxide is more

difficult due to a much lower partial pressure of CO_2 in the flue gas and impurities such as SO_x and NO_x as well as dust when a solid fuel is used (Kanniche *et al.*, 2010).

Alongside these, the oxy-fuel combustion with CO_2 capture offers the lowest development risk for existing coal-fired power plants as it is retrofittable and allows for both in-situ CO_2 capture and near-zero emissions of NO_x, particulate matter, SO_2, mercury and other air pollutants (McCauley, Moorman and McDonald, 2011; Shah *et al.*, 2013). In the oxy-fuel process the air used for combustion is replaced by oxygen diluted in recycled flue gas leading to a product stream primarily consisting of CO_2 and H_2O. Condensation of the water vapour yields a stream of CO_2 sufficiently pure for sequestration in geological formations (Shah *et al.*, 2013).

However, similar to pre-combustion CO_2 capture, this technology is accompanied by a major drawback: the requirement for pure oxygen to first be separated from the air. Current technologies for producing oxygen by separating air comprise cryogenic distillation, adsorption, *i.e.* pressure swing adsorption (PSA) and vacuum-PSA, and advanced technologies such as membrane separation or ceramic autothermal recovery (Krishnamurthy, Acharya and Fitch, 2008; Shah *et al.*, 2013). Cryogenic air separation, despite being a mature technology, imposes an energy penalty of approximately 8 percentage points on the power plant's gross power output (Davison, 2007). Pfaff and Kather (2009) conducted a thermodynamic analysis of a high temperature membrane separation process on basis of a power plant of 600 MW gross electricity output. The reduction in the efficiency of the plant was estimated to be between 9.1 and 10.8 percentage points.

The application of the oxy-fuel combustion technology to coal power plants is currently at technology readiness level (TRL) 7, a scale from 1 to 9 where 7 and 9 mark the demonstration and commercial scale, respectively, and significant investments and commercial interest are now needed to advance on the TRL scale (Bui *et al.*, 2018). However, ways must be found to reduce the energy penalty associated with this technology to raise the interest of the industry. One promising process to produce oxygen efficiently is chemical looping (Shah *et al.*, 2013).

1.2 Chemical Looping

Chemical looping processes make use of a solid to transport oxygen between two reactors. One of the earliest examples of its use was in the Brin Process (Jensen, 2009), used to produce pure oxygen from air, or the Lane (1913) and Messerschmitt (1910) processes for hydrogen production in the early 1900s (Lane, 1909, 1913; Messerschmitt, 1910). At this time, there was little interest in the potential for carbon capture, since global warming is a relatively modern concern. When using metal oxides, the basic process consists of an oxidation and reduction carried out in two different reactors, or the same reactor but at different times, *i.e.*

$$\text{Reduction:} \quad MeO + reducing\ agent \rightarrow Me + oxidised\ species$$

$$\text{Oxidation:} \quad Me + air\ or\ oxidising\ agent \rightarrow MeO$$

The Lane and Messerschmitt processes used fixed beds of Fe_2O_3, which was first reduced to Fe_3O_4, then to iron by a fuel, and then oxidised not with air, but with steam, to produce hydrogen and Fe_3O_4. Reed and Berg (1953) proposed using interlinked, fluidised beds instead of fixed beds. This hydrogen producing process also became known as the steam-iron process or the cyclic water gas shift. A more recent development had been to use iron oxide-based solids in a moving bed with coal as fuel *i.e.* the Coal Direct Chemical Looping (CDCL) process (Tong *et al.*, 2014).

In the combustion system, the reducing species is fuel, and the oxidised gaseous product consists of only water and carbon dioxide. The water can be removed by condensation, leaving CO_2 which has been captured, but without the energy penalty usually associated with carbon capture. The first suggestion of this as a carbon avoidance technology was in 1954 (Lewis and Gilliland, 1954), not as a way of mitigating global warming, but rather as a way of producing purified CO_2 for sale.

In 1983, chemical looping combustion was suggested as a way to avoid the irreversible direct combustion of fuel in power stations, the purpose being to increase efficiency, not carbon capture (Richter and Knoche, 1983). The combustion reaction itself is one of the major thermodynamic losses associated with power generation technologies. Ishida and Jin (1994) first suggested chemical looping combustion as a low energy

penalty carbon avoidance technology for power systems. Initial work focussed on gaseous fuels *e.g.* syngas or methane (Jin and Ishida, 2002, 2004; Mattisson *et al.*, 2007). Gaseous fuels are simpler and there are no complications with solid ash contaminating the system. In chemical looping combustion, solid fuels are more difficult to convert since the solid oxygen carrier will not interact directly with the fuel; the fuel must first be converted to a gas, *viz.* pyrolysis, followed by gasification of the char. Whilst it is relatively easy to convert the fuel volatile matter, the char that remains will only gasify slowly. This has been overcome using solid oxygen carriers which can produce gas phase oxygen in the CLOU (chemical looping with oxygen uncoupling) process (Mattisson, Lyngfelt and Leion, 2009).

1.2.1 Chemical Looping Air Separation

A conceivable solution to achieve air separation at a lower energy penalty than conventional methods uses a technique commonly referred to as chemical looping air separation. A chemical air separation loop is characterised by the cyclic reduction and oxidation of solid material serving as an oxygen carrier, which has the capacity to release gas phase oxygen. Figure 1-2 illustrates the concept of this process.

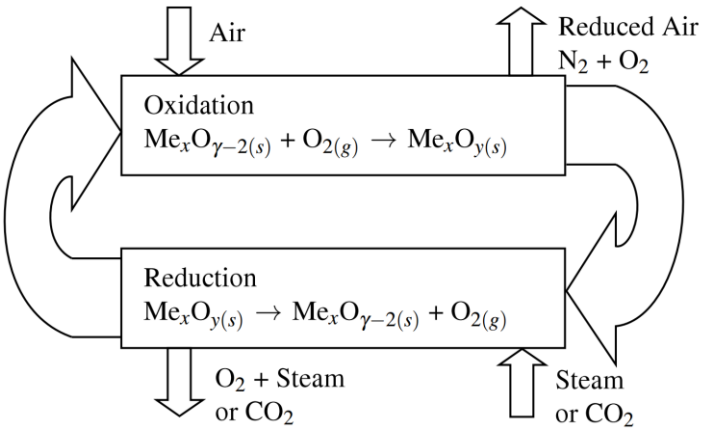

Figure 1-2: Concept of chemical looping air separation [reproduced from (Shah *et al.*, 2013)][2]

[2] Published under copyright license number 4726390207289

During the oxidation phase, the oxygen carrier stores oxygen from air which is released in a low-oxygen atmosphere during the reduction cycle, exploiting equilibrium thermodynamics. Departure from equilibrium causes the oxygen carrier system to oxidise when the actual partial pressure of oxygen is above its equilibrium partial pressure $pO_{2,eq}$, defined in equation (1-4).

$$\frac{pO_{2,eq}}{p_{tot}} = exp\left(-\frac{\Delta G_r^o}{RT}\right) \tag{1-4}$$

ΔG_r^o is the Gibbs free energy of reaction for the unmixed reactants at atmospheric pressure and temperature T, *i.e.*

$$MeO_2 \rightleftarrows Me + O_2 \tag{1-5}$$

where Me is the reduced form of the oxygen carrier. The ΔG_r^o is itself a function of temperature. Hence, the concentration, and amount of oxygen which can be obtained is linked to the temperature and the properties of the oxygen carrier material via ΔG_r^o, and the stoichiometry of the decomposition reaction.

The earliest reports of chemical air separation processes date back to the second half of the 18th century (Du Motay and Maréchal, 1867; Mallet, 1868). Roughly a decade later, *viz.* in 1880, the concept of chemical looping air separation was successfully realised for the commercial production of oxygen by Arthur and León Brin (Jensen, 2009). Both the process of Du Motay and the process of the Brin brothers were put out of business by the cryogenic air separation process in the early 19th century. One of the drawbacks of the Brin process, which looped between BaO in and the peroxide BaO_2, was the need to first remove the carbon dioxide present in the air input, which will irreversibly form $BaCO_3$ with the oxygen carrier. In the late 2000s, the idea of exploiting a chemical loop for the separation of air was reintroduced (Yin, Kniep and Lin, 2008; Moghtaderi, 2010), in this case using copper, manganese and cobalt based materials as the oxygen carrier. At high temperatures, copper and other transition metal oxides do not react with the CO_2 in air to form carbonates.

A preliminary cost analysis conducted by Moghtaderi (2010) proved the process of chemical looping air separation to be feasible with a specific power consumption of around 11 % of that for cryogenic air separation (CAS). This estimate was based on

0.4 kWh/Nm³ of O_2 for the cryogenic distillation process and presumes that the majority of the heat required by CLAS is recovered. Still, assuming that energy cost of O_2 from CAS will improve, *e.g.* 0.20 kWh/Nm³ O_2 in 2015 and 0.17 kWh/Nm³ O_2 in 2020 as predicted by Perrin *et al.* (2014), the specific power consumption of producing oxygen *via* chemical looping amounts to approximately 22.5 and 26.5 % of CAS, respectively. In a follow-up study, the specific power consumption for manganese, cobalt and copper oxides was re-evaluated. As shown in Figure 1-3, a specific power consumption of below 100 kWh/t O_2, *i.e.* around 0.143 kWh/Nm³ O_2, may be achieved (Song, 2014). Figure 1-3 further illustrates the distinct optimal temperature intervals at which different oxygen carrier systems should be operated. Further, Figure 1-3 indicates that the most energy efficient oxygen carrier material might not be practical as the operating temperature of the CLAS reactor might be dictated by external processes, as described in the following section 1.2.2.

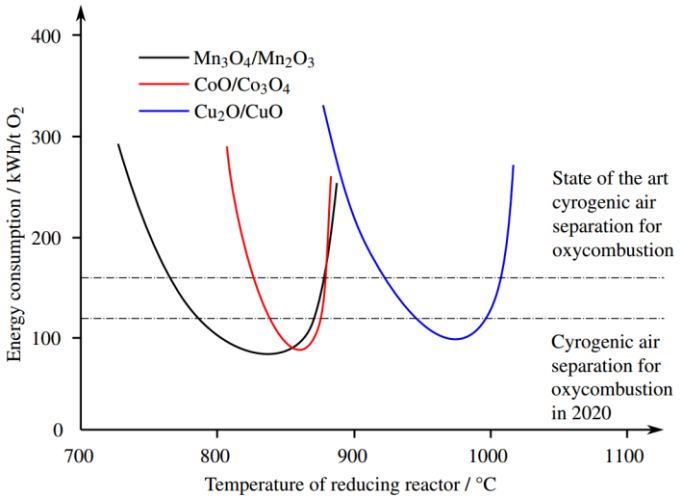

Figure 1-3: Comparison between cryogenic air separation (CAS) and CLAS using different oxygen carrier systems [adapted from Song (2014)]

1.2.2 Power Plant Integration

The predominant issue with the integration of CLAS into the power station flowsheet is that the reduction, *i.e.* oxygen release, is endothermic. The problem is compounded by the need to bring the incoming gases up to the reactor temperature. Given that these cycles operate above the turbine inlet temperature, the heat must come from the furnace or be provided by an external source (*e.g.* Shah *et al.* (2013)).

To understand how the CLAS process might integrate with a steam power plant or why an external heat source might be required, a heat integration analysis can be conducted. Figure 1-4 shows the flowsheet of a steam power plant located near Frankfurt, Germany, and commissioned in 1992. The plant produces around 510 $MW_{el,net}$ at a net efficiency, η, of roughly 43 %; around 1,183 MW of coal are combusted in the boiler or furnace at an efficiency of 95 %, *i.e.* ~1,124 MW of heat energy are transferred the steam cycle, as shown in Figure 1-4. The plant consists of three steam turbine stages, a high-pressure, an intermediate-pressure and a low-pressure stage with one reheating step taking place after the high-pressure turbine, to drive the generator.

A graphical representation of the heating utility available from the boiler and the cooling utility provided by the steam cycle is shown in Figure 1-5a; the "shifted temperature" is based on a minimum allowable temperature difference, here 20 K, which enforces a technically and economically viable process integration *via* a heat exchanger network (Zoughaib, 2017). The actual temperature of the heat source, the combustion of fuel inside the boiler, and the heat sink, the steam generation from water, are shifted by half of the minimum temperature difference downwards and upwards, respectively. The composite curves of the hot and cold streams are calculated *via* (Zoughaib, 2017)

$$\Delta\dot{H}_{hot} = \sum m_i \, c_{p,i} \, \Delta T_i \tag{1-6}$$

$$\Delta\dot{H}_{cold} = \sum m_i \, c_{p,i} \, \Delta T_i \tag{1-7}$$

where *i* denotes any fluid stream, *e.g.* constituents of the exhaust gas from the oxy-fuel combustor in the case of $\Delta\dot{H}_{hot}$ or the stream of water from the feedwater tank and the steam from the outlet of the high-pressure turbine passing through the boiler

(B in Figure 1-4) for $\Delta\dot{H}_{cold}$ and $m,\ c_p$ and ΔT are the mass, specific heat capacity and change in temperature.

In the example shown in Figure 1-5a, the heat energy supplied by the combustion of the coal matches the demand for heat of the steam cycle. It can be noted that any heat that is available at temperatures below the boiler inlet temperature of 275.7 °C (548.85 K) remains unused. This is highlighted when composing the Grand Composite curve of the steam power plant by subtracting the temperature *vs.* heat (T-Q) curves of the boiler and the steam cycle (Figure 1-5a), as shown in Figure 1-5b. The red and blue arrows in the Grand Composite curve of Figure 1-5b depict the heat release and heat demand of the integrated process which is perfectly heat integrated as the heat demand of the steam cycle is exactly matched by the heat release of the boiler.

If the steam cycle were to be driven by oxy-fuel combustion, any process to produce the oxygen would be required to either heat integrate with the combustion taking place in the furnace and the steam generation or use electricity to cover the energy demand, effectively reducing the net electricity output of the power plant. It is therefore desirable to find a way to heat integrate the oxygen production process instead of using electricity which will unavoidably lead to a decrease in the net efficiency of the power plant.

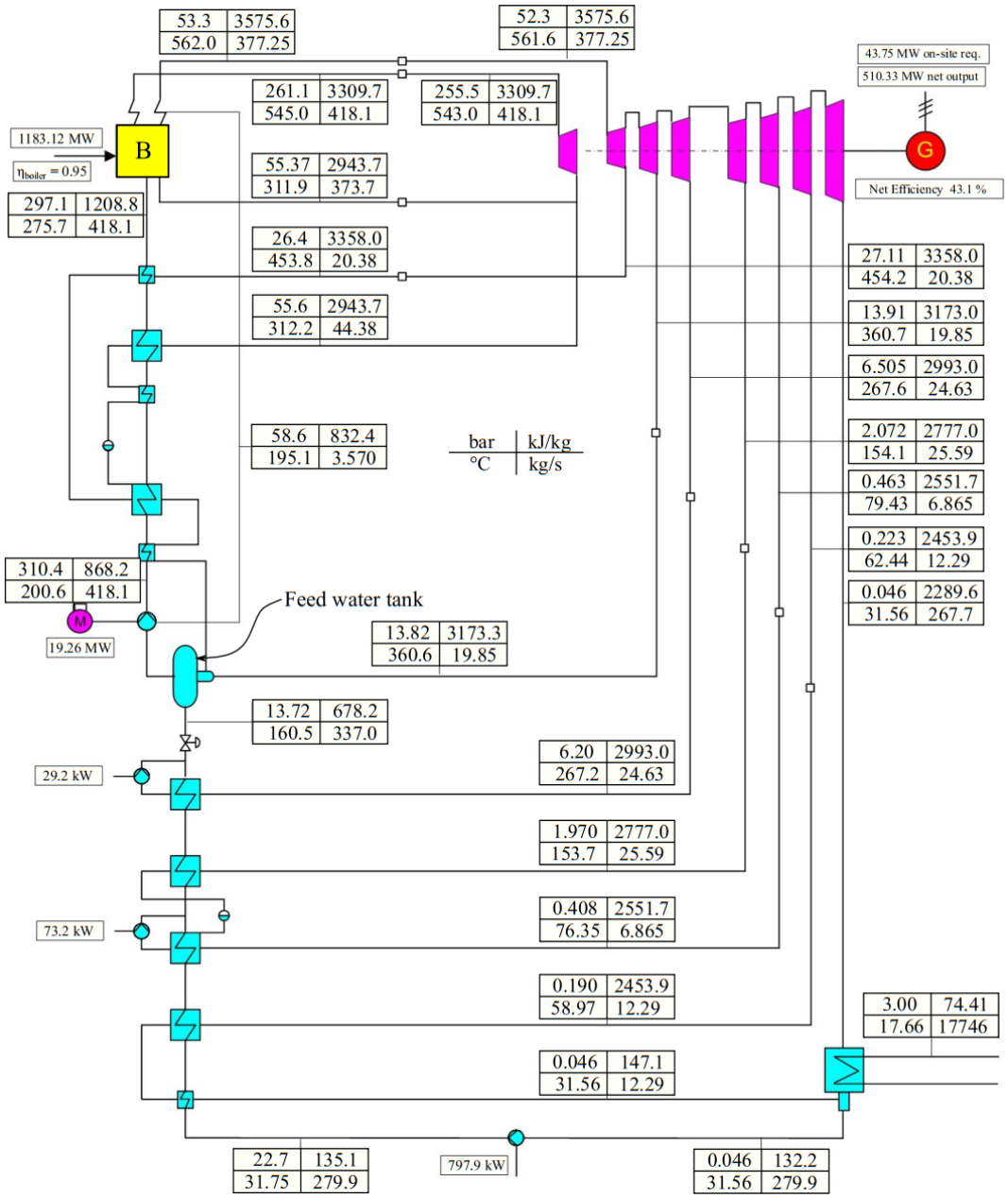

Figure 1-4: Flow sheet of unit 5 of the coal power plant Staudinger, Germany (Sperlich, 2002)[3]

[3] Published under the CC BY-SA 2.0 license: https://creativecommons.org/licenses/by-sa/2.0/

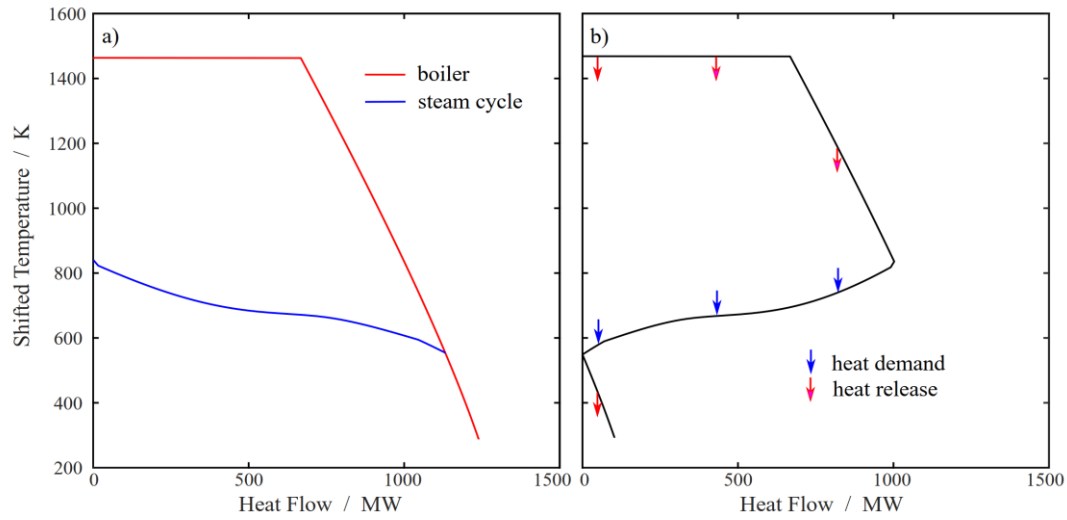

Figure 1-5: a) T-Q and b) Grand Composite curves of the steam power plant depicted in Figure 1-4.

In order to investigate the possible heat integration of the oxygen production process, its heat demand or release must be considered. One way to achieve a continuous chemical loop, for example to produce oxygen, is *via* a dual circulating fluidised bed reactor (Adanez *et al.*, 2012; Lyngfelt and Linderholm, 2017). In a dual circulating fluidised bed, the oxidation and reduction of the solid oxygen carrier are spatially separated, as shown in Figure 1-6. When operated at similar pressures, the endothermic reduction reaction, *i.e.* the reaction at which oxygen is released from the oxygen carrier material, must occur at a higher temperature than the operating temperature of the oxidizer if oxygen partial pressures similar or higher than the pO_2 at the inlet to the oxidizer are to be achieved, as described in section 1.2.3. The low pO_2 fluid passed into the reducer depends on the subsequent, oxygen utilising process, but is likely to consist mainly of carbon dioxide and water vapour for oxy-fuel combustion, as shown in Figure 1-1. The inflows to the reactors require heating up and the outflows might be cooled down, again depending on the process following the oxygen release in the reducer. An example of the T-Q curves of the oxidiser and reducer of a dual circulating fluidised reactor used to produce one mole of oxygen at a partial pressure of oxygen of 0.34 bar is provided with Figure 1-7a. Here, the CuO/Cu_2O oxygen carrier system is chosen and the operating temperatures of the two reactors are set at 40 K away from the temperature at which equilibrium at pO_2 of 0.34 bar is reached, *i.e.* the operating temperatures of the oxidizer and reducer are 1283 and 1363 K, respectively.

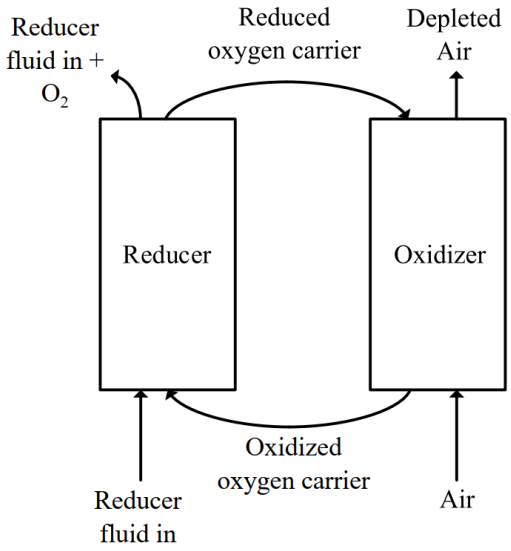

Figure 1-6: Schematic of a dual circulating fluidised bed (DCFB) reactor in which a continuous flow of oxygen is produced via chemical looping air separation.

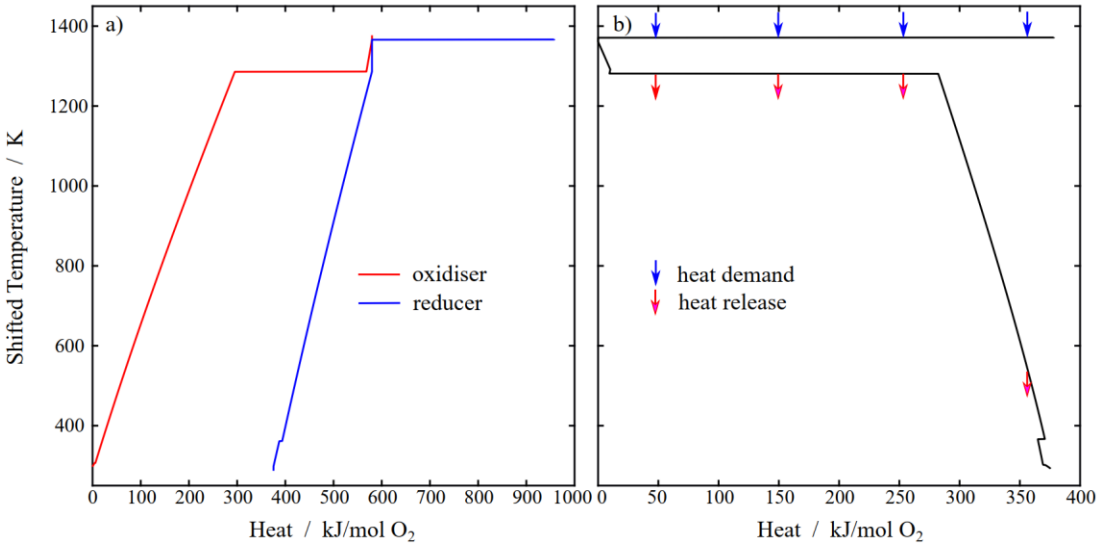

Figure 1-7: a) T-Q and b) Grand Composite curves of a CLAS dual circulating fluidised bed (DCFB) reactor producing one mole of oxygen from $4CuO \rightleftarrows 2Cu_2O + O_2$ at pO_2 of 0.34 bar

The Grand Composite curve of the dual circulating fluidised bed, as shown in Figure 1-7b, highlights the challenge in the heat integration of a chemical loop: heat is required at temperatures above the temperature at which heat is released. Shah *et al.* (2013) investigated several schemes to integrate chemical looping oxygen production into a steam cycle. Figure 1-8 and Figure 1-9 show the most promising of seven ex-

amined schemes. They considered the reactors to be continuously stirred tank reactors with perfect mixing. For the energy balance, thermodynamic equilibrium is assumed.

In the temperature swing method, the reactors are operated with a temperature difference of 100 to 300 K, while other approaches are run isothermally. The advantage of the temperature swing approach is the exploitation of the temperature dependence of the equilibrium thermodynamics. As described in the following section 1.2.3, it is favourable to operate the oxidation reactor at lower temperatures while the reduction benefits from higher temperatures. Due to the higher equilibrium partial pressure of oxygen at elevated temperatures, the demand for steam and/or CO_2 can be reduced. In conclusion, the energy required by the temperature swing method is therefore lower compared to isothermal methods (Shah *et al.*, 2013).

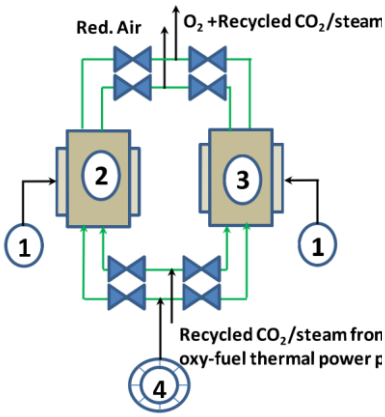

Figure 1-8: Temperature swing CLAS

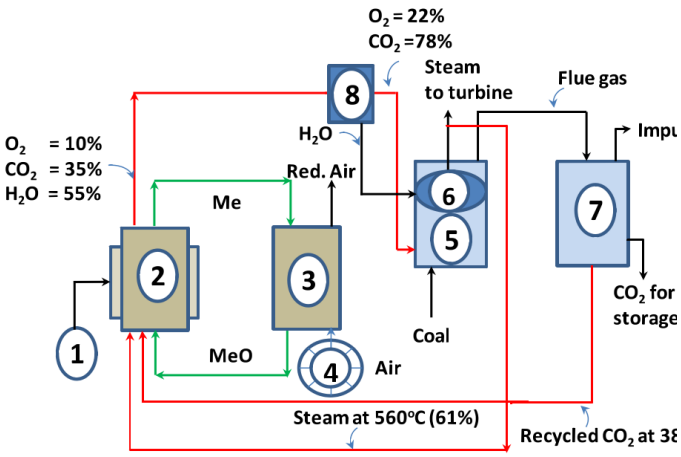

Figure 1-9: CLAS hybrid steam/recycled CO2 system [reproduced from (Shah *et al.*, 2013)][2]

1: Heater, 2: Reduction reactor, 3: Oxidation reactor, 4: Air blower, 5: Oxy-combustor, 6: Steam drum, 7: Flue gas cleaning and CO_2 processing unit, 8: Condenser

Furthermore Shah *et al.* (2013) found that, depending on the heat source covering the reactors' heat requirement, compared to a cryogenic ASU operating costs may decrease by up to 50 % and 80 % for the isothermal and temperature swing system, respectively. Simulations with four different oxygen carrier systems, MnO_2/Mn_2O_3, Mn_2O_3/Mn_3O_4, CuO/Cu_2O and CoO/Co_3O_4, showed that isothermal methods must be supplied with at least 61 % steam in order to produce an oxygen content of 22 wt.% in the product stream, which is the minimal requirement of an retrofitted oxy-fuel combustor (Wall *et al.*, 2009). The addition of steam and recycled CO_2, as shown in Figure 1-9, arises from the marginal difference between the actual and the equilibrium partial pressure of oxygen. Dilution of the product stream by introducing an enhanced amount of steam and/or CO_2 leads to an increase in the driving force [$f(pO_2)$ in equation 1.17]. Hence, the yield of oxygen is raised. In contrast, the temperature swing approach is capable of achieving oxygen contents of around 90 wt.% when CoO/Co_3O_4 is used (Shah *et al.*, 2013).

While each method suggested by Shah *et al.* (2013) is based on two circulating fluidised bed reactors, running several packed bed reactors in parallel may also be possible. The advantage of a packed bed over a circulating fluidised bed reactor is that a higher conversion of the solids can be achieved for the same volume. Additionally, attrition of the particles is less of a problem compared to fluidised beds. In such packed bed reactors, the oxygen carrier is stationary while the air and inert gas feeds are alternated to force oxygen uptake and release by the oxygen carrier. This concept has already been studied successfully for chemical looping (Zaabout *et al.*, 2014).

1.2.3 Oxygen carriers

There are certain characteristics that oxygen carriers are required to display (Adánez *et al.*, 2004; Imtiaz, Hosseini and Rüdiger, 2013):

- High reaction rates for reduction and oxidation
- Sufficient chemical stability over many reaction cycles
- High mechanical strength to avoid attrition
- Resistance to sintering and agglomeration
- Low cost
- Environmentally friendly
- Suitable thermodynamics

Due to more mature techniques utilising oxygen carriers with similar requirements, in particular chemical looping combustion, over 700 combinations of different materials have been proposed and tested, most of which can be found in the appendix of the review paper of Adanez *et al.* (2012). Chemical looping combustion (CLC) is a combustion process where the oxygen carrier is circled between an air reactor and a fuel reactor. In the latter the oxygen carrier is reduced while oxidising the fuel. Importantly, the oxygen carrier in chemical looping combustion does not have to give up gas phase oxygen directly, with oxygen being removed from the oxygen carrier by reaction with the fuel.

Despite a hiatus in interest in the chemical looping oxygen production process, research conducted on oxygen carriers for chemical looping combustion may be used as a starting point. In the CLAS process, lower operating temperatures are favourable in order to maximise energy efficiency by optimising low temperature heat integration. Low operating temperatures lead to a decrease in the rate of reaction of the oxygen carrier. Ideally, oxygen carriers should therefore exhibit high reaction rates at low to medium temperatures, *i.e.* 373 to 1273 K (Shah, Moghtaderi and Wall, 2012).

Investigations conducted explicitly for oxygen carriers for the process of chemical looping air separation evaluated suitable oxygen carriers on basis of the equilibrium

partial pressure of oxygen ($pO_{2,eq}$) in the desired temperature interval. The equilibrium partial pressure of oxygen is calculated from the Gibbs free energy of reaction, ΔG_r

$$\Delta G_r = -RT \ln K_p \tag{1-8}$$

where ΔG_r can be computed from:

$$\Delta G_r^o = \Delta H_r^o - T\Delta S_r^o \tag{1-9}$$

where ν_i is the stoichiometric coefficient of species i in the reaction. Both the molar enthalpy (H_i^o) and the entropy (S_i^o) of the species involved in the oxidation reaction may be obtained from data tables. K_p denotes the equilibrium constant which is equal to the equilibrium partial pressure of oxygen assuming reaction (1-5) and providing that the activities of the solid reactants are unity following

$$MeO_2 \rightleftarrows Me + O_2$$

$$K_{eq} = \frac{\alpha_{Me}\,\alpha_{O_2}}{\alpha_{MeO_2}} \tag{1-10}$$

where K_{eq} is the equilibrium constant in terms of activities and α_{Me}, α_{O_2} and α_{MeO_2} are the activities of some metal, gaseous oxygen and some corresponding metal oxide compound, respectively. The activity of substance *i* is defined by (Mortimer, 2008)

$$\alpha_i = e^{\frac{\mu_i - \mu_i^o}{RT}} \tag{1-11}$$

where μ_i is the chemical potential of substance *i* and μ_i^o is the chemical potential of substance *i* at standard state. Assuming that the molecular volume of substance *i*, $V_{m,i}$, in solid state is constant and O_2 behaves like an ideal gas, which are good approximations for pressures discussed in this thesis, it follows

$$\alpha_{Me} = e^{\frac{V_{m,i}(p-p^o)}{RT}} \approx 1 \tag{1-12}$$

$$\alpha_{MeO_2} = e^{\frac{V_{m,i}(p-p^o)}{RT}} \approx 1 \tag{1-13}$$

$$\alpha_{O_2} = \frac{pO_{2,eq}}{p_{tot}} \tag{1-14}$$

Therefore, K_{eq} is equal to $pO_{2,eq}/p_{tot}$ and equations (1-4) and (1-8) are equivalent under these assumptions.

From the equilibrium partial pressure of oxygen, the operating temperatures in the oxidation and reduction process are derived. In the oxidation process, *i.e.* when air is present, the $pO_{2,eq}$ must be lower than the oxygen partial pressure of air and vice versa during reduction when an inert gas or steam is introduced. In Figure 1-10 the equilibrium partial pressure of oxygen is plotted for both Mn_2O_3 and CuO. The Gibbs free energy was computed using thermodynamic data from Barin and Knacke (1974) and NASA data tables (McBride, Zehe and Gordon, 2002) for Mn_2O_3/Mn_3O_4 and CuO/Cu_2O, respectively. From the graph it is obvious that oxidation is not possible at temperatures above approximately 1150 and 1300 K for Mn_3O_4 and Cu_2O, respectively, when air is used.

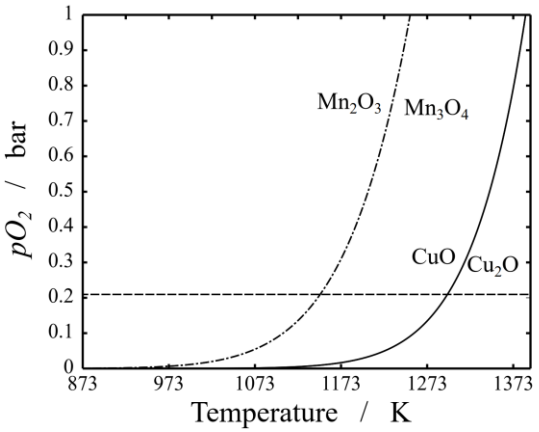

Figure 1-10: Equilibrium partial pressure of oxygen of Mn_2O_3 and CuO as a function of temperature

To date 44 metal oxide systems have been reviewed, the majority of which are listed in Table 1-1 (Mullhaupt and Stern, 1969; Shah, Moghtaderi and Wall, 2012; Wang, Yu and Qin, 2013).As mentioned before, these systems were assessed solely on the Gibbs' free energy already available from various databases, and on theoretical capacity (from the stoichiometry of reaction). This approach to screening has a major drawback: Most metal oxide systems that seem promising in terms of oxygen transport capacity and equilibrium, fail due to costs, toxicity, stability of the states or impractical material properties such as high density or low melting point.

Table 1-1: Analysis of different metal oxide systems for the suitability as oxygen carriers in CLAS [reproduced from (Song 2014)]

Metal oxide system	Oxygen transport capacity	Molecular weight (g/mol)	Density (kg/m^3)	Melting point (°C)	Safety risk[a]	Cost[a]	Temp.[b] (°C)	Remarks
Al/AlO	0.372	26.98/42.98	2700/N/A	660/N/A	L	H	597-857	Unstable state of AlO
V_3O_5/V_5O_9	0.027	232.82/398.7	N/A/N/A	1827/N/A	M	M	481-504	Toxic and unstable states
Cr_2O_3/CrO_2	0.095	151.99/83.99	5220/4890	2330/N/A	M	M	24-94	Toxic and slower kinetics
Cr_2O_3/Cr_5O_{12}	0.159	151.99/451.97	5220/N/A	2330/N/A	M	M	68-107	Toxic and slower kinetics
CrO_2/Cr_5O_{12}	0.071	83.99//451.97	4890/N/A	N/A/N/A	M	M	36-136	Toxic and slower kinetics
Mn_3O_4/Mn_2O_3	0.034	228.81/157.87	4840/4500	1562/1347	M	M	744-1000	Potential carrier candidate
MnO/MnO_2	0.184	70.94/86.94	5370/5080	1842/N/A	M	M	804-1000	Hard oxidation to MnO_2
Mn_3O_4/MnO_2	0.123	228.81/86.94	4840/5080	1562/N/A	M	M	476-622	Hard oxidation to MnO_2
Mn_2O_3/MnO_2	0.092	157.87/86.94	4500/5080	1347/N/A	M	M	405-529	Hard oxidation to MnO_2
CoO/Co_3O_4	0.066	74.93/240.80	6450/6110	1830/N/A	M	M	811-933	Potential carrier candidate
Cu_2O/CuO	0.101	143.09/79.55	6000/6310	1235/1446	M	M	882-1119	Potential carrier candidate
MoO_2/Mo_9O_{26}	0.100	127.94/1279.4	6470/N/A	1927/N/A	M	M	908-935	Unstable state of Mo_9O_{26}
Rh_2O/RhO	0.067	221.81/118.90	N/A/N/A	1127/N/A	L	H	416-548	Very expensive
Rh_2O/Rh_2O_3	0.126	221.81/253.81	N/A/8200	1127/N/A	L	H	775-974	Very expensive
RhO/Rh_2O_3	0.063	118.90/253.81	N/A/8200	N/A/N/A	L	H	1104-1200	Very expensive
Pd/PdO	0.131	106.40/122.40	12020/8300	1555/750	L	H	648-816	Very expensive and high density
Sb_2O_3/SbO_2	0.052	291.50/153.75	5580/N/A	570/N/A	L	M	1043-1173	Low melting point
PbO/Pb_3O_4	0.023	223.20/685.60	9530/8920	887/830	M	L	292-417	Toxic and high density
PbO/Pb_2O_3	0.035	223.20/462.40	9530/10050	887/N/A	M	L	252-381	Toxic and high density
Pb_3O_4/PbO_2	0.045	685.60/239.20	8920/9640	830/N/A	M	L	287-397	Toxic and high density
Re/Re_2O_3	0.114	186.21/420.41	21000/N/A	3185/N/A	L	H	1102-1200	Very expensive and high density
Os/OsO_2	0.144	190.20/222.20	22590/11370	3033/650	M	H	1094-1200	Very expensive and high density
OsO_2/OsO_4	0.126	222.20/254.20	11370/5100	650/41	H	H	1108-1200	Highly toxic (OsO_4) and expensive
Pt/PtO	0.076	195.09/211.09	21450/14100	1768/N/A	L	H	404-567	Very expensive and high density
PtO/PtO_2	0.070	211.09/227.09	14100/11800	N/A/450	L	H	301-423	Very expensive
Tl_2O/Tl_2O_3	0.070	424.74/456.74	9520/10200	579/834	H	M	678-845	Highly toxic
Hg/HgO	0.074	200.59/216.59	13534/11140	-39/476	H	M	448-584	Highly toxic
Hg_2O/HgO	0.037	417/216.59	9800/11140	-646/476	H	M	769-1200	Highly toxic
Ir/Ir_2O_3	0.111	192.22/432.44	22500/N/A	2446/N/A	L	H	689-846	Very expensive and high density
Ir/IrO_2	0.143	192.22/224.22	22500/11665	2446/N/A	L	H	849-1098	Very expensive and high density
Pr_2O_3/PrO_2	0.046	329.81/172.91	6900/6820	2300/427	M	H	1119-1200	Expensive
Pr_2O_3/Pr_6O_{11}	0.031	329.81/1021.4	6900/N/A	2300/N/A	M	H	585-732	Expensive
Tb_2O_3/TbO_2	0.042	365.85/190.92	7910/N/A	2410/N/A	M	H	395-524	Expensive
Tb_2O_3/Tb_6O_{11}	0.028	365.85/1129.6	7910/N/A	2410/2410	M	H	237-327	Expensive

[a] L, Low; M, Medium; H, High. [b] Operating temperatures are obtained as the equilibrium temperatures corresponding to oxygen equilibrium partial pressure in the range of 0.01 to 1.

The oxygen transport capacity *OTC* in Table 1-1 is defined as the ratio of the difference in mass of the oxygen carrier in the oxidised and reduced state over the mass when oxidised, as expressed in equation (1-15) (Wang, Yu and Qin, 2013).

$$OTC = \frac{m_{ox} - m_{red}}{m_{ox}} \qquad (1\text{-}15)$$

Some identified Mn_3O_4/Mn_2O_3, CoO/Co_3O_4 and Cu_2O/CuO as the most promising metal oxide systems (Hu Song *et al.*, 2014).

1.2.3.1 Reaction kinetics

The thermodynamic analysis, however, disregards reaction kinetics, which are in fact crucial to the material's application as an oxygen carrier. In a fluidised bed, the economy and practicality of the oxygen carrier is dictated by rates of oxidation and reduction and the oxygen transfer capacity but also the rates of attrition or agglomeration, *i.e.* the required rate of replenishment of the solid inventory (Adanez *et al.*, 2012).

For example, the composite curves for the DCFB reactor plotted in Figure 1-7 assumed that only fully reduced or oxidised phases were cycled between the oxidiser and the reducer and did not take into account any temporal requirements such as the time needed to fully convert the oxygen carrier or the residence time of the solids in the reactors. Any unreacted portion of the oxygen carrier would show up in the energy and mass balance of the system but would not contribute to the production of oxygen, just like any non-catalytic or inert support material. Schnellmann *et al.* (2018) have investigated the mean conversion of particles leaving the oxidiser or reducer as a function the reactors' mean residence times, $\bar{t}$, and the time it takes for a particle to fully oxidise or reduce, t_{ox} and t_{red}, respectively. The experimental data underlying their calculations is taken from a small-scale dual connected fluidised bed, described by Donat *et al.* (2016). $\bar{t}_{ox}$ and $\bar{t}_{red}$ of the ~400g of solids were found to be 22.2 and 36.0 s, respectively.

To relate the residence times of the reactors and the reaction rate of the oxygen carrier to the conversion, Schnellmann *et al.* (2018) defined a dimensionless time, θ, as

$$\theta = \begin{cases} \bar{t}_{ox}^{-1}\, t_{ox}, & oxidiser \\ \bar{t}_{red}^{-1}\, t_{red}, & reducer \end{cases} \qquad (1\text{-}16)$$

The conversion of the particles leaving the oxidiser and the reducer is plotted over θ in Figure 1-11; in the figure, the air reactor denotes the oxidizer and the fuel reactor is the reactor in which the oxygen carrier is reduced. The mean residence times affect the mean conversion of the solids only for $\theta > 0.2$, as shown in Figure 1-11. Therefore, approximately full conversion is only achieved when the mean residence time is 5 times the time it takes for the oxygen carrier to fully oxidise or reduce. The natural conclusion of this is that, holding the mean conversion at the reactor outlets constant, faster reaction kinetics would allow for a higher solid circulation rate, leading to an

increased oxygen production; but at the expense of a higher heat demand as discussed in section 1.2.2.

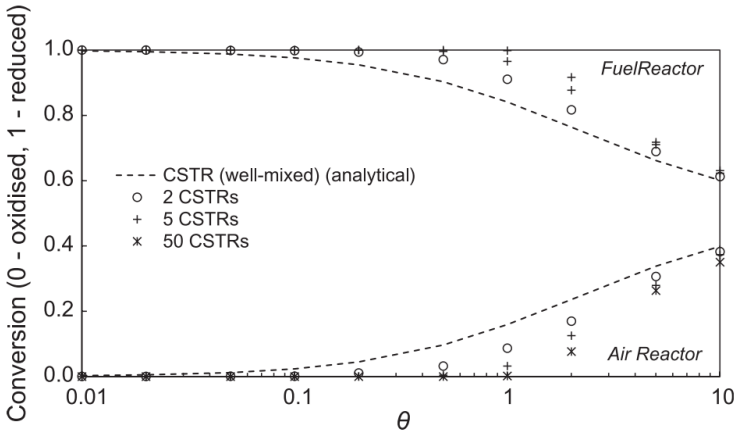

Figure 1-11: Mean conversion of the oxygen carrier particles leaving the oxidiser (air reactor) and the reducer (fuel reactor) for different residence time distributions (RTDs, 1, 2, 5 and 50 CSTRs) [reproduced from (Schnellmann *et al.*, 2018)]

In chemical looping air separation, a general equation to obtain the change in the conversion, X, of an oxygen carrier particle is

$$\frac{dX}{dt} = f(T)f(pO_2)f(X) \tag{1-17}$$

where the factors denote functions of the temperature, the oxygen partial pressure and the conversion of the solid, respectively, and the conversion, X, is defined by

$$X(t) = \frac{m(t) - m_{red}}{m_{ox} - m_{red}} \tag{1-18}$$

$f(T)$ is typically represented by a rate constant, k, and is given by the Arrhenius equation

$$f(T) = k = A\ exp\left(-\frac{E_a}{RT}\right) \tag{1-19}$$

where A denotes the pre-exponential factor and E_a is the activation energy. The Arrhenius-type equation for f(T) indicates that an increase in the temperature results in an increase in the rate at which the oxygen carrier is oxidised or reduced. At the same time, however, it highlights a trade-off between increasing the temperature to achieve a higher rate of reaction for a given oxygen carrier and the decrease in heat available

from combusting fuel with the produced oxygen at a higher temperature (section 1.2.2).

Further, the characteristics of the oxygen carrier particle, *i.e.* the particle shape and size as well as the number of pores and their size distribution, play an important role in chemical reaction engineering. The general mechanism for the oxygen release or uptake occurs in several steps, as shown in Figure 1-12, each of which could limit the overall rate at which the lattice oxygen of the oxygen carrier and the bulk gas interact. The external mass transfer coefficient, k_{eg}, is a function of the Sherwood number, Sh, that links the convective mass transfer to the molecular diffusion, *i.e.*

$$Sh = \frac{convective\ mass\ transfer\ rate}{molecular\ diffusion\ rate} = \frac{k_{eg} d_{p,0}}{D_{O_2}} \tag{1-20}$$

where $d_{p,0}$ is the initial diameter of the particle which may change as the reaction progresses and D_{O_2} is the gas molecular diffusivity of oxygen in the surrounding gas. For a single, spherical particle in flowing fluid, the Sherwood number can be expressing as

$$Sh = Sh_0 + K\ Re^m Sc^{1/3} \tag{1-21}$$

where Sh_0 is the Sherwood number in stagnant flow and K and m are constants which are typically assumed to be 0.69 and 0.5, respectively, when $Re < 10^5$ (Hayhurst, 2000). Sh_0 is equal to 2 under the equimolar counterdiffusion assumption in stagnant flow (Hayhurst, 2000), *i.e.* $Re = 0$, which states that at any moment in time and point in the gas film, the total number of moles do not change as oxygen diffuses into the bulk gas but other constituents of the bulk gas diffuse into the gas film. The external mass transfer coefficient, k_{eg}, is then

$$k_{eg} = \left(2 + 0.69\ Re^{1/2} Sc^{1/3}\right) \frac{D_{O_2}}{d_{p,0}} \tag{1-22}$$

and the conditions at the surface of the particle in steady state are

$$k_{eg}(C_s - C_\infty)\ =\ k\ f(C)\ f(X)\ = -D_e \frac{\partial C}{\partial r}\bigg|_{r=r_p} \tag{1-23}$$

where C_∞ and C_s are the concentration of oxygen in the bulk gas and the surface of the particle, respectively, the middle term is the driving force as a function of the concentration of oxygen, C, r_p is the radius of the particle and D_e is the effective gas diffusivity inside the porous particle (Wang, Li and Cai, 2019).

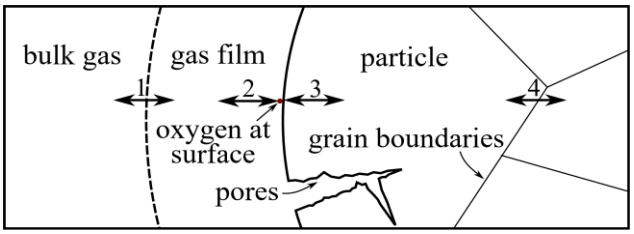

Figure 1-12: Transport processes involved in the oxygen uptake and release of an oxygen carrier: 1. Molecular diffusion, 2. Surface reaction, 3. Chemical diffusion, 4. Transfer across grain boundaries. [modified from Merkle and Maier (2008)]

The overall effective reaction rate may be limited by any of k_{eg}, k or D_e; *e.g.* if k_{eg} is small but k and D_e are large, then the effective reaction rate is controlled by the external mass transfer through the gas film. The effect of each of these three limiting cases, *i.e.* chemical reaction control, external gas film control and product layer diffusion control, on the mean conversion of the particles are plotted Figure 1-13; here, the shrinking core model (SCM) was chosen which assumes that the particle size is constant but the unreacted core of the particle shrinks as the outer layers of the particle form an inwardly growing product layer (Levenspiel, 1999). Figure 1-13 shows that the process is relatively insensitive towards the speed at which the chemical reaction or the diffusion though the product layer occurs, as long as the mean residence time was smaller than the time taken for the oxygen carrier to react fully, *i.e.* $\theta < 1$ (Schnellmann *et al.*, 2016). In the case of external mass transfer control, a mean conversion of over 0.95 is only achieved for $\theta < 0.1$.

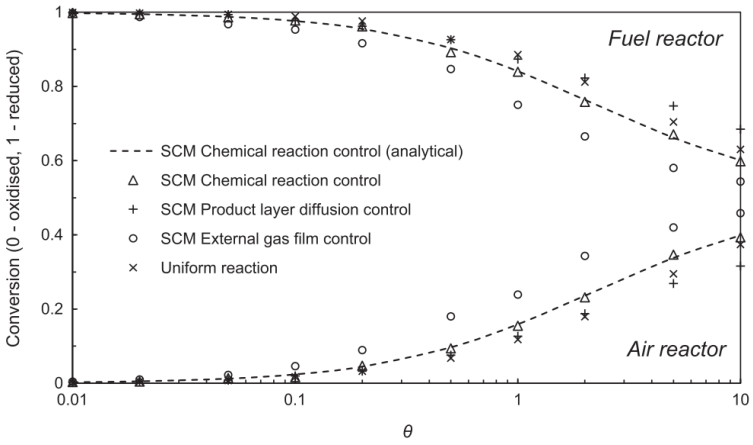

Figure 1-13: Mean particle conversion for different reaction models; θ is defined in equation (1-16) and the fuel reactor and the air reactor are the reducing and oxidising reactor, respectively. SCM denotes the shrinking core model [reproduced from Schnellmann *et al.* (2016)]

Song (2014) studied reaction kinetics, for five consecutive cycles of oxidation and decomposition, in a thermogravimetric analyser (TGA) for the three aforementioned metal oxide systems dry impregnated onto SiO_2 and Al_2O_3, respectively, as well as spray dried $CuO/MgAl_2O_4$. The TGA tests ran at temperatures of 1073, 1123, 1173 and 1223 K. Addition of a support such as SiO_2 or Al_2O_3 is required due to *e.g.* agglomeration, low mechanical strength or slow reaction kinetics of the unsupported metal oxide. It was found that for both Mn- and Co-oxide, impregnation onto aluminium oxide or silicon dioxide did not yield improvements in the thermodynamic limitations: At temperature above 1173 K the equilibrium partial pressure of oxygen is required to be higher than air. Oxygen uptake from air is therefore not possible at those temperatures. This disadvantage of Mn- and Co-oxide is accompanied by instabilities due to the formation of aluminates when supported with Al_2O_3 (Song, 2014).

In contrast, CuO with SiO_2 displayed stability throughout the temperatures examined over the five redox cycles. It is assumed that this system may have fewer issues with agglomeration than CuO/Al_2O_3 and does not show much interaction between the support and CuO; CuO supported with Al_2O_3 is known to form $CuAl_2O_4$ (Hu *et al.*, 2016). The best results, however, were achieved using CuO in combination with $MgAl_2O_4$ (Song, 2014). In a second experiment, CuO/SiO_2 and $CuO/MgAl_2O_4$ were tested over 41 continuous cycles in a TGA in the range of 1073 to 1248 K. $CuO/MgAl_2O_4$ was found to be superior in terms of stability, oxygen transport capacity and the rate of

oxygen transport. However, the material would be unsuitable for the chemical looping air separation due its low mechanical strength. They therefore conclude that the most suitable oxygen carrier was CuO/SiO_2 which is not only cheaper than Co_3O_4 and Mn_2O_3 but also more stable with regard to the loss of oxygen transport capacity (Song, 2014).

An investigation into Co_3O_4 impregnated onto ZrO_2 revealed that after 23 redox cycles the oxygen transport capacity and reaction rate did decrease and changes in pore size or grain growth were not observed. Agglomeration did not occur at temperatures up to 1273 K (Wang *et al.*, 2014). While for reduction, conversion times drastically decrease as the temperature increases, 99 % conversion is achieved after 20, 3.5 and 2.5 minutes at 1123, 1173 and 1198 K, respectively, for oxidation, the conversion time starts to increase at above 1073 K. Wang *et al.* (2014) have attributed this to a faster decrease in the driving force term of $f(pO_2)$ in equation 1.17 than the increase of $f(T)$, here $exp(-E_a/RT)$.

From this, it is obvious that evaluations of potential oxygen carriers based on thermodynamics only are not sufficient. The suitability of an oxygen carrier system is in fact heavily dependent on its reaction kinetics.

1.2.3.2 Non-stoichiometric Materials

It is expected that certain types of crystal lattices are more suitable for oxygen storage. Hence, screening would benefit notably if a certain crystalline structure proves particularly promising. A promising lattice configuration is expected to be found in perovskite-type mixed metal oxides. The crystal structure of perovskites is characterised by ABO_3, where A may be an alkali, rare-earth or alkaline earth metal ion and B a transitional metal ion.

Perovskites have received attention in the research for oxygen conducting membranes, as used in *e.g.* solid oxide fuel cells (SOFC), as well as chemical looping, more specifically chemical looping with oxygen uncoupling (CLOU) (Richter *et al.* 2009; Leion *et al.* 2009; Jing *et al.* 2013). CLOU is a process similar to chemical looping combustion but in contrast is characterised by the release of gas-phase oxygen in the fuel reactor. The advantage of the perovskite structure is its variability: By introducing different cations to yield more complex structures, *e.g.* $A'_xA''_{1-x}B'_yB''_{1-y}O_{3-\delta}$, it is pos-

sible to optimise for the desired material properties such as oxygen transport capacity and equilibrium partial pressure of oxygen (Schaak & Mallouk 2002; Richter et al. 2009).

1.3 Objectives

Here, chemical looping air separation is investigated as a method of avoiding the emission CO_2 from a power plant *via* oxy-fuel combustion and subsequent capture of CO_2. It is apparent from the previous discussion any evaluation of the merits of CLAS as a carbon avoidance technology must integrate knowledge of the materials with how they will be used at the process scale. The efficiency (or efficiency penalty) is a result of the material properties and the effect this has on the heat integration. Previous studies have attempted to evaluate CLAS by looking at materials in isolation or modelling the power station for select few promising materials. Therefore, the objectives in this thesis are to

1. Properly evaluate the material space available for chemical looping air separation (CLAS) integrated with carbon capture, taking into account optimal heat integration, from theoretically determined thermochemical data.
2. To suggest materials based on the materials space as candidates for CLAS
3. To prepare the suggested materials and evaluate their actual thermochemical properties (compared to the theoretical properties).
4. To evaluate the kinetics of oxygen uptake and release from these materials.

Chapter 2 uses a fully heat integrated model of a power station, linked to a model of CLAS system to perform “inverse-design”, *i.e.* to back calculate the thermochemical properties of materials required for efficient operation. This is combined with a screening of available DFT calculations and other data sources to suggest real materials which have potential for CLAS.

Chapter 3 describes the experimental methods used in later chapters. This includes the development of a small micro-reactor system to measure the kinetics of oxygen uptake and release, as well as more standard methods (*e.g.* Thermogravimetric analysis). This

chapter also describes the theory used to evaluate the reaction kinetics in later chapters.

Chapter 4 presents the measured equilibrium properties of Sr-Fe-O based materials. The perovskite $SrFeO_3$ is identified as a potential candidate material in Chapter 2. This material is a non-stoichiometric oxide, the properties of which can be altered by doping. Hence, here the effect of doping manganese into the structure is also evaluated.

Chapters 5 and 6 present the analysis for measuring the kinetics of oxygen uptake and release, and the results obtained for the strontium ferrite and doped strontium ferrite materials.

Chapter 7 elucidates on the behaviour of $SrFeO_{3-\delta}$ and $SrMn_{0.1}Fe_{0.9}O_{3-\delta}$ over 1000 redox cycles.

Chapter 2 was published as Görke, R.H. *et al.*, 2018. Exploration of the material property space for chemical looping air separation applied to carbon capture and storage. *Applied Energy*, 212, pp.478–488. A preliminary version of the model developed for chapter 2 which is not presented here, contributed to a life cycle assessment comparing the environmental impact of electricity produced *via* a coal-fired power plant linked to a chemical looping air separation unit to other energy sources. This study was published as Tagliaferri *et al*., 2018. Life cycle assessment of optimised chemical looping air separation systems for electricity production. *Chemical Engineering Research and Design*, 131, pp.686–698.

Chapter 4 and 5 formed the basis for conference paper submitted for the 5th International Conference on Chemical Looping in Utah, USA. The conference paper is titled "Reduction and Oxidation Behavior of Strontium Perovskites for Chemical Looping Air Separation" (by Görke, R.H., Marek, E., Scott, S.A., 2018). The conference paper, extended by parts of chapter 7 was subsequently invited to apply and, on October 29th, 2019, accepted for publication in the *International Journal of Greenhouse Gas Control* as Görke, R.H., Marek, E., Donat, F. and Scott, S.A, 2020. Reduction and Oxidation Behavior of Strontium Perovskites for Chemical Looping Air Separation.

2 Exploration of the Material Property Space for CLAS applied to CCS

In this chapter, the main objective is to identify oxygen carrier materials that are suited for the process of chemical looping air separation and heat integrate well with a steam cycle. This is achieved by modelling a dual circulating fluidised bed reactor integrated with a steam power plant at steady-state. The screening for oxygen carrier materials is performed by first identifying material properties critical for CLAS and then conducting a parameter sweep to map combinations of these material properties to the net efficiency of the CLAS oxy-fuel power plant. Based on the highest net efficiencies, a material database is scanned for material systems, *i.e.* reduced and oxidised phase, that possess these favourable material properties and are worth investigating experimentally.

2.1 Introduction

After the Brin process ($2BaO_2 \rightleftarrows 2BaO + O_2$) was superseded by the cryogenic separation of air in the early 20th century, the idea of exploiting a chemical loop for the separation of air was reintroduced, in this case using a complex perovskite (here, $La_xSr_{1-x}Co_yFe_{1-y}O_{3-\delta}$, LSCF) as the oxygen carrier (Lin, MacLean and Zeng, 2000; Yang, Lin and Zeng, 2002). Later, simpler compounds, such as CuO/Cu_2O, Mn_2O_3/Mn_3O_4 and CoO/Co_3O_4, were considered as oxygen carriers (Li, Zhang and Cai, 2008; Moghtaderi, 2010). At high temperatures, copper oxide and other transition metal oxides do not react with the CO_2 in air to form stable carbonates under process conditions. In these cases, the idea was to integrate the chemical looping air separation into the power production flow sheet. It is this integration that potentially leads to the

lower energy penalty for oxy-fuel combustion. The chemical looping cycle operates at a high temperature and so the heat used to drive the equilibrium reaction can in principle be recuperated back into the power cycle to generate steam. Such an approach can lead to potentially low energy penalties. This contrasts with low energy temperature cycles, in which heat recovery is not possible, and the power used to drive the gas separation is, in effect, wasted. For a more detailed discussion see, for example, chapter 5 in Bui *et al.* (2018). This means it is impossible to assess how good or bad a potential chemical looping agent is, without considering how the resulting chemical looping cycle will be heat integrated with the power station.

A putative process flow diagram for a CLAS-oxy-fuel power plant is shown in Figure 2-1. The power plant can be subdivided into three parts: (i) the chemical looping air separation (CLAS) unit, (ii) combustion of the fuel including carbon sequestration, and (iii) a steam cycle for power generation. The flue gas leaving the oxy-fuel combustor will require cleaning to remove particulate matter and sulphurous gases, derived from the fuel. The CLAS unit would consist of two interconnected fluidised beds, *viz.* the oxidizer and reducer (Moghtaderi, 2010). By cycling the oxygen carrier between the oxidizer and reducer, continuous oxygen production can be achieved in the latter. If an existing power plant were to be retrofitted for oxy-fuel combustion, the composition of the incoming oxidizing gas would have to allow the combustor to operate within its envelope of design parameters (*e.g.* to ensure a correct heat transfer coefficient, stability of combustion, NO_x emissions, *etc.*) (Buhre *et al.*, 2005; Wall, 2005; Wall *et al.*, 2009). Accordingly, an oxy-fuel combustor would typically require a mole fraction of oxygen of around 0.3 to 0.35, with the balance being CO_2 when a dry recycle is used (oxy-dry combustion) (Wall, 2005; Wall *et al.*, 2009). The condenser in Figure 2-1 allows the mass fraction of oxygen entering the combustor to be altered, by allowing for the removal of water, which may have been injected into the reducer as steam.

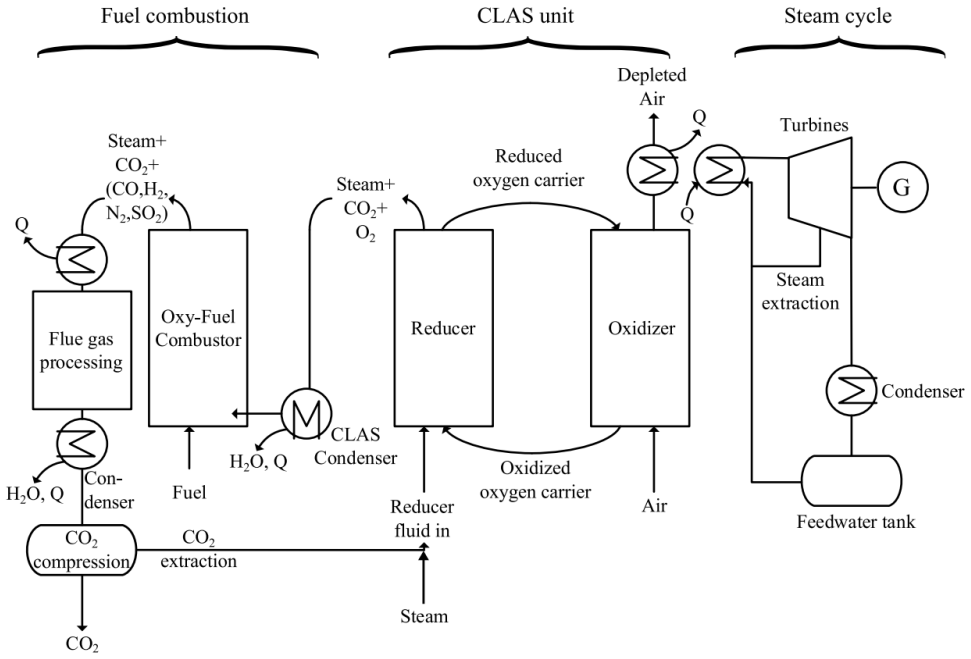

Figure 2-1: Flow diagram of the proposed CLAS-oxy-fuel power plant underlying the steady-state model. Q denotes a heat source or sink as indicated by the arrows

The selection and identification of suitable oxygen carrier materials is crucial to the feasibility of a CLAS process. Oxygen carriers must operate at intermediate to high temperatures for a long period of time to give economic production of oxygen. Three different types of oxygen carriers have been identified for use in more general chemical looping processes, *e.g.* chemical looping combustion: single metal oxides (Adanez *et al.*, 2004, 2012; Chuang *et al.*, 2008; Imtiaz, Hosseini and Rüdiger, 2013); composite metal oxides (Adanez *et al.*, 2012; Imtiaz, Hosseini and Rüdiger, 2013; Siriwardane *et al.*, 2015; Zhang *et al.*, 2017); and perovskite-type oxides (Adanez *et al.*, 2012; Imtiaz, Hosseini and Rüdiger, 2013; Galinsky *et al.*, 2015; Ikeda, Tsuchida, *et al.*, 2016; Taylor *et al.*, 2016). In the listed order, the oxygen transfer capacity per unit mass of the carrier generally decreases and the mechanical strength and cost of material generally increases. In chemical looping systems, a material combining both a high oxygen transfer capacity and rapid rates of reaction for both oxidation and reduction is desirable because this gives the lowest rate of circulation between the reactors. The work here is focused on the thermodynamic properties of the oxygen carrier. Whilst other criteria, such as mechanical strength or high reaction rates, are important, the thermodynamics of the oxygen release reaction,

$$MO_2 \rightleftarrows M + O_2$$

determine, to a large extent, the feasibility of the CLAS process. In particular, the equilibrium partial pressure ($pO_{2,\mathrm{eq}}$) for this reaction as a function of temperature determines possible operating regimes, and is related to the Gibbs free energy of reaction, ΔG_r^o by equation 1.17.

In previous studies, materials that are thought to perform well as oxygen carriers were selected first and only subsequently assessed. The work undertaken in this chapter takes a different approach. The desired material properties required by the process first, followed by the identification of materials possessing such properties using first-principles computations, such as calculations using density functional theory (DFT).

2.2 Methodology

The inverse design approach is a method that identifies the desired material properties required by the process first, followed by the identification of materials possessing such properties using first-principles computations, such as calculations using density functional theory (DFT). This approach has been successfully executed for the identification of unreported and thermodynamically-stable ternary materials (Zhang *et al.*, 2012; Zakutayev *et al.*, 2013; Dunstan *et al.*, 2016). Here, the inverse design approach has been applied to identify functional oxygen carrier materials for CLAS. The strategy involves constructing a full (steady state) model of a CLAS system integrated with an oxy-fuel power station. This model assumes the availability of a generic oxygen carrier material with an arbitrary set of characteristic thermodynamic properties. Searching the space of thermodynamic properties of the generic material then allows desirable characteristics to be identified and compared with known or computed oxide materials.

2.2.1 CLAS Integration with a Steam Power Plant

In the model, the energy penalty imposed by flue gas processing and carbon dioxide compression was neglected, because these processes present an equal decrease in efficiency for all oxy-fuel power plants. The reducing reactor has to be fluidised by a gas with a low partial pressure of oxygen. Here, this can be either recycled CO_2 with or without injected steam. The steam needed could either be provided by the steam cycle, *e.g.* from the low-pressure turbine, or by using other sources of heat to evaporate water.

Here, the oxy-fuel combustor requires a fluidising gas containing a mole fraction of oxygen of roughly 0.35 at ambient pressure when operating with a dry recycle, *i.e.* when almost no steam is present in the gas. This should then give a rate of heat transfer between the gases leaving the combustor and boiler tubes comparable to that when combusting with air (Wall, 2005). The CLAS condenser shown Figure 2-1 allows the partial pressure of oxygen to be increased to the desired level by condensing injected steam. Assuming that steam can be bled from, or introduced into, the low-pressure turbine, and water can be withdrawn from, or introduced into, the feedwater tank, then evaporation of the water condensed in the CLAS condenser and its reintroduction into the low-pressure turbine would theoretically close the steam cycle. Further, the partial pressure of oxygen required by the combustor, $pO_{2,req}$, and the operating partial pressure of oxygen of the reducing reactor, $pO_{2,red}$, dictate the amount of steam required in the reducer:

$$pO_{2,red} = \frac{\dot{n}_{O_2,red}}{\dot{n}_{steam} + \dot{n}_{CO_2} + \dot{n}_{O_2,red}} \times p_{tot} \tag{2-1}$$

$$pO_{2,req} \equiv 0.35 \times p_{tot} = \frac{\dot{n}_{O_2,red}}{\dot{n}_{steam} + \dot{n}_{CO_2} + \dot{n}_{O_2,red} - \dot{n}_{H_2O}} \times p_{tot} \tag{2-2}$$

where p_{tot} is the operating pressure of the reducer, $\dot{n}_{O_2,red}$, $\dot{n}_{steam}$ and $\dot{n}_{CO_2}$ are the molar flow of oxygen, steam and carbon dioxide at the reducer outlet. $\dot{n}_{H_2O}$ is the molar flow of water separated out in the CLAS condenser, which can be determined by performing a dew point calculation given by

$$T_{dew} = \frac{243.12a_1}{17.62 - a_1} - 273.15K \tag{2-3}$$

$$a_1 = \frac{ln\,RH + 17.62(T - 273.15)}{T - 30.03} \tag{2-4}$$

where RH is the relative humidity and T the temperature in Kelvin (Sonntag, 1990).

2.2.2 Thermodynamics and modelling the CLAS system

Each reactor in Figure 2-1, *viz.* the oxidizing and reducing reactors of the CLAS dual fluidised bed and the oxy-fuel combustor, was modelled as being well mixed with respect to both gas and solid phases, and assuming thermodynamic equilibrium between the exit streams, as discussed in this section.

Assuming equilibrium, the oxygen released by the oxygen carrier in the reducing reactor of the CLAS unit depends solely on the equilibrium partial pressure of oxygen of the material's oxygen release reaction, which in turn depends on ΔG_r^o. It follows from equation (1-9) that the Gibbs free energy of reaction is a function of the enthalpy of reaction, ΔH_r^o, the temperature, T, and the entropy of reaction, ΔS_r^o. Using the van't Hoff equation

$$\frac{\partial}{\partial T}\left(\frac{\Delta G_r^o}{T}\right) = -\frac{\Delta H_r^o}{T^2} \tag{2-5}$$

the Gibbs free energy of reaction can be rewritten as a function of the enthalpy of reaction, ΔH_r^o, and temperature only, where

$$\Delta H_r^o(T_2) = \Delta H_r^o(T_1) + \int_{T_1}^{T_2} \Delta C_{p,r}\, dT \tag{2-6}$$

In subsequent calculations, it was assumed that the solids obey the Dulong-Petit law which states that for a solid made up of n atoms

$$C_p \cong 3Rn \tag{2-7}$$

where C_p is the molar heat capacity. In other words, every atom in the chemical formula of the solid adds $3R$ to its molar heat capacity. Considering that

$$\Delta H_r = \sum_i H_i \, \nu_\mathrm{i} \tag{2-8}$$

where H_i and ν_i denote the enthalpy of formation and the signed stoichiometric coefficient of the reactants and the products, respectively, and

$$C_{p,i} = \left(\frac{\partial H_i}{\partial T}\right)_p \tag{2-9}$$

it follows that

$$\left(\frac{\partial \Delta H_r}{\partial T}\right)_p = \left(\frac{\partial \sum H_i \nu_\mathrm{i}}{\partial T}\right)_p = \Delta C_{p,r} \tag{2-10}$$

In a reaction typical for CLAS, two oxygen atoms, each contributing $3R$ to the C_p of the oxidised oxygen carrier, decouple from the solid oxygen carrier and, therefore, the molar heat capacity of reaction, $\Delta C_{p,r}$, is linked to the molar heat capacity of the oxygen released, $C_{p,O_2}(T)$, by

$$\Delta C_{p,r}(T) = \nu_{O_2}\left(C_{p,O_2}(T) - 6R\right) \tag{2-11}$$

where ν_{O_2} denotes the stoichiometric coefficient of oxygen in the reduction reaction; here, the stoichiometric coefficient of oxygen is set to 1.

The Gibbs free energy of reaction at temperature T_1 and T_2 are then related by

$$\begin{aligned} \frac{\Delta G_r^o(T_2)}{T_2} - \frac{\Delta G_r^o(T_1)}{T_1} &= -\int_{T_1}^{T_2} \frac{\Delta H_r^o(T)}{T^2}\, dT \\ &= \Delta H_r^o(T_1)\left(\frac{1}{T_2} - \frac{1}{T_1}\right) - \int_{T_1}^{T_2} \frac{\int_{T_1}^{T} \Delta C_{p,r}(T'\ )dT'}{T^2}\, dT \end{aligned} \tag{2-12}$$

The enthalpy of reaction, $\Delta H_r^o(T_{eq})$ at the temperature of the reducing reacting reactor (T_{eq}) can then be linked to the equilibrium partial pressure of oxygen in the reducing reactor and the temperature of oxidising reactor (which is constrained to operate with a partial pressure below 0.21 bar, if air is used as an oxidising agent) by

$$R ln\left(\frac{pO_{2,red}}{pO_{2,ox}}\right) = \Delta H_r^o(T_{eq})\left(\frac{1}{T_{ox}} - \frac{1}{T_{eq}}\right) + F(T_{ox}, T_{eq}) \quad (2\text{-}13)$$

using equation (1-4) to link ΔG_r^o and pO_2 *via*

$$-\frac{\Delta G_r^o(T_{eq})}{T_{eq}} = R\ ln(pO_{2,\mathrm{eq}}) \quad (2\text{-}14)$$

so that

$$\frac{\Delta G_r^o(T_2)}{T_2} - \frac{\Delta G_r^o(T_1)}{T_1} = R\ \left(ln(pO_{2,1}) - ln(pO_{2,2})\right) = R ln\left(\frac{pO_{2,1}}{pO_{2,2}}\right) \quad (2\text{-}15)$$

where (1) and (2) denote the reducer and the oxidizer, respectively. In the following calculations, the difference in the operating temperatures of the reducer and the oxidizer is set to 80 K; this was chosen as a trade-off between an increase in the heat demand in the reducer for heating up the incoming oxidised oxygen carrier and an increase in the air flow to the oxidizer as more oxygen is required to oxidize the oxygen carrier at smaller temperature differences, as described in section 2.3.3. Shah *et al.* (2013) use temperature differences of the two reactors between 70 and 140 K for modelling a CLAS-oxy-fuel power plant using different oxygen carriers.

If the temperature difference between the oxidizer and the reducer in equation (2-13) is fixed (here to 80 K), the effect of the material on the system is therefore determined by three parameters, $\Delta H_r^o(T_{eq})$, T_{eq}, and the reaction stoichiometry, given a desired value of $pO_{2,red}$. There is a minor contribution from the term $F(T_{ox}, T_{eq})$, which arises from the change in heat capacity for the reaction, *i.e.* the inner integral of equation (2-12), and can largely be ignored. Here, $F(T_{ox}, T_{eq})$ is retained simply to ensure consistency in the calculations. Whilst the heat capacities of the solids have little effect on the equilibrium partial pressure, they do have a large effect on the heat balance, since they determine how much heat is circulated between the reducer and the oxidizer.

The mass and energy balances for the CLAS oxy-fuel system were computed in MATLAB. For the fictitious materials and those derived from density functional theory (DFT), since only the differences in enthalpy and entropy between reduced and oxidised states are important, the values for the reduced phase were set arbitrarily and the oxidised phases set relative to that. In addition, for the entropy, it was assumed that the production of gaseous oxygen dominates the entropy of reaction at 298 K, *i.e.* $\Delta S_r^o(298\ K) \equiv S_{O_2}^o(298\ K)$ (Dunstan *et al.*, 2016). The values of the molar heat capacity, C_p, for the oxidized and reduced phases were set using the Dulong-Petit law.

Subject to constraints to ensure conservation of atoms, the equilibrium was found by minimizing the total Gibbs energy, $G_T = \sum \mu(i) N_i$, using the optimization toolbox of MATLAB. For solids, the chemical potential is equal to the standard molar Gibbs free energy of formation, *i.e.*

$$\mu_{solid}(i) = G_i^o \tag{2-16}$$

where

$$G_i^o = H_i^o - TS_i^o \tag{2-17}$$

For gases, which are assumed to be ideal in this case, a term taking into account mixing effects must be included, leading to

$$\mu_{gas}(i) = G_i^o + (RT)\left(ln\frac{p_{tot}}{p^o} + ln\, y_i\right) \tag{2-18}$$

where T is the temperature, p_{tot} is the total pressure, y_i is the mole fraction of species i in the gas phase. The outlet of the oxy-fuel combustor was constrained to contain 1 % of the initial carbon as unburned coal (Kimura *et al.*, 1995; Tan *et al.*, 2006).

2.2.3 Modelling the steam system and heat integration

From the heat released, composite curves were generated for heat integration analysis. The CLAS dual fluidised bed reactor was fully heat integrated with the oxy-fuel combustor and then both were scaled to match the heat demand of a steam cycle for a specific gross power output; in this case 500 MW_{el}. The reference steam cycle was based on unit 5 of the Großkrotzenburg Power Station, Germany, and is characterised by gross electricity generated at 1.31 MW/kg of steam and a specific heat demand of the steam as shown in Figure 2-2 (Sperlich, 2002; Grote and Feldhusen, 2007).

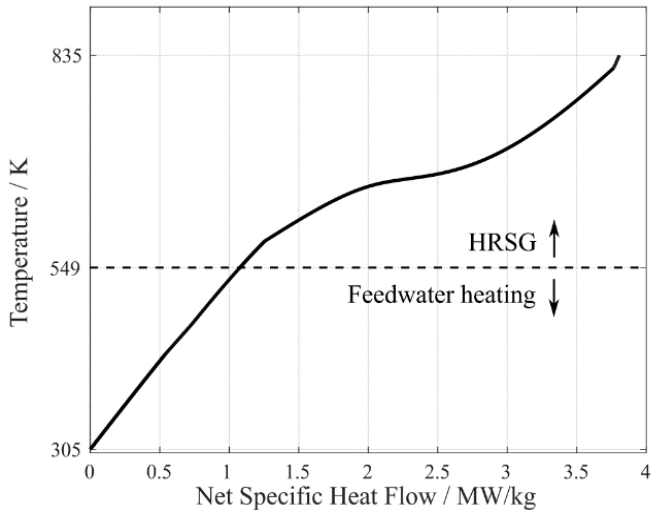

Figure 2-2: Specific heat demand of the underlying steam cycle; HRSG: Heat recovery steam generator

It should be noted that the specific electricity generation involves only the heat demand of the heat recovery steam generator (HRSG). The maximum steam cycle temperature, which is an important parameter for the heat integration and overall process efficiency, is 835 K, as shown in the reference flowsheet in Figure 1-4. In this model, the properties of the steam around the steam cycle were calculated using the IAPWS IF-97 method (XSteam) (Cooper *et al.*, 2012). The net efficiency of the base steam cycle was calculated to be 42.1 %. Deviations from 42.1 % are possible when the operating temperature of the oxidizer falls below the maximum steam cycle temperature,

i.e. the highest turbine inlet temperature; in this case, heat integration is not possible without modifying the turbines in the steam cycle.

When the CLAS unit operates below the top turbine temperature of the reference steam plant flowsheet, the turbine train must be modified to allow heat integration. The properties of the streams leaving the turbines are recalculated to account for the lower boiler exit temperature by fixing the polytropic efficiencies of the high-pressure (HP), intermediate-pressure (IP), and low-pressure (LP) turbines to those of the reference steam cycle, *i.e.* 0.889, 0.9045 and 0.8205, respectively. As the inlet temperature is reduced, it is possible to maintain the overall pressure ratio (and the inlet pressures of the IP and LP turbine), until a point at which the outlet from the HP turbine enters the two-phase region. In this case, to avoid the two-phase flow in the HP and IP turbines, the outlet pressure of the turbine is instead set by following the polytropic expansion line to saturated conditions. The outlet of the IP turbine is also constrained in a similar manner. If the inlet pressure of the HP turbine is within 5 bar of the inlet pressure of the intermediate-pressure turbine from the reference steam cycle, the HP turbine is dropped altogether; *i.e.* the pressure in the boiler is set to the inlet pressure of the IP turbine in the reference plant. Neglecting the high-pressure turbine and, thus, converting the three-stage expansion process into a two-stage process (IP and LP turbines) leads to a significant decrease in the overall efficiency, as shown in Figure 2-3; Figure 2-3 shows the steam cycle efficiency as a function of the operating temperature of the reducer. A smoother net efficiency curve might be achieved if the HP turbine were to be replaced by another IP turbine, *i.e.* the three stages and the reheating are maintained, but this would also necessitate likely difficult repressurisation. The outlet of the LP turbine is constrained to a vapour fraction of at least 88 % (Sarkar, 2015) in a similar manner. If the pressure leaving the LP turbine differs from the reference cycle, the steam is assumed to condense isobarically to saturation at this new pressure, and the conditions at feed water tank altered accordingly.

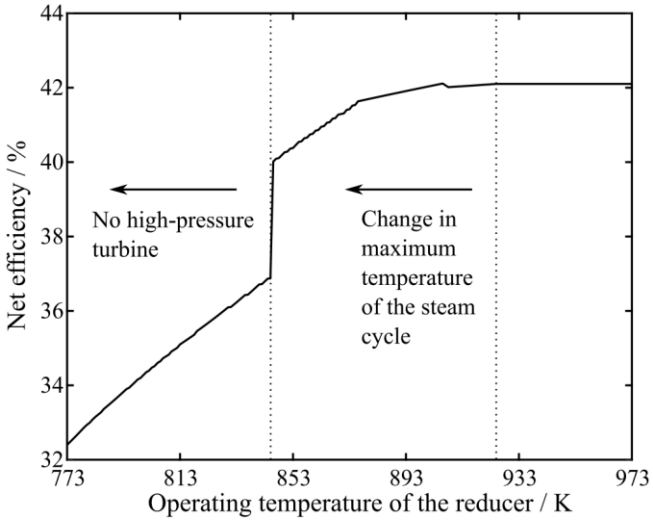

Figure 2-3: Net efficiency of the steam cycle as a function of operating temperature of the reducer, assuming a difference in the operating temperatures of the CLAS reactors of 80 K and a temperature difference of heat transfer between the oxidizer and the steam cycle of 10 K

2.2.4 Oxygen Carrier Materials

The redox reaction for the oxygen carrier systems was assumed to follow

$$4MO \rightleftarrows 2M_2O + O_2$$

where M may resemble any combination of elements, as long as the reaction stoichiometry is maintained, *e.g.* $4CuO \rightleftarrows 2Cu_2O + O_2$. The main effect of altering the number of atoms in M is to alter the rate at which heat is transferred by between the reducer and oxidizer (*via* changes in the heat capacity). For the fictitious materials, in the base case, the stoichiometry for copper oxide decomposition is assumed for the purposes of setting the solid heat capacities.

Fictitious oxygen carriers were assessed on the basis of a parameter sweep. The sweep was performed for the enthalpy of reaction, $\Delta H_r^o(T_{eq})$, and the equilibrium temperature, T_{eq}, at a fixed $pO_{2,red}$. With the desired $pO_{2,red}$ set, the rate of flue gas re-circulation (and solid oxide circulation) are then determined to give full conversion of the oxygen carrier in the reducer. From equation (2-13), it becomes apparent that specify-

ing ΔH_r^o, T_{eq}, $pO_{2,red}$, and the temperature difference between the oxidizer determines the entropy of reaction, ΔS_r^o. Therefore, in the parameter sweep

$$100\frac{kJ}{mol} \leq \Delta H_r^o(T_{eq}) \leq 400\,\frac{kJ}{mol}$$

$$773\ K \leq T_{eq} \leq 1173\ K$$

the entropy of reaction, ΔS_r^o, is a function of $\{\Delta H_r^o, T_{eq}\}$. Hence, for the parameter sweep, the lower and upper limit of ΔS_r^o are 94.2 J/mol/K and 526.4 J/mol/K, respectively.

$pO_{2,red}$ is limited by the requirement of the oxy-fuel combustor to have an inlet partial pressure of oxygen, $pO_{2,req}$, of roughly 0.35 bar. In the base case, $pO_{2,red}$ was set to 0.34 bar so that the typical oxygen concentration entering the combustor was ~0.35 bar once a fraction of water in the stream was removed by the CLAS condenser; *i.e.* the actual pO_2 entering the combustor varied slightly between cases. The outlet temperature of the CLAS condenser was assumed to be 298 K. This base case has no additional steam input into the CLAS reducer, other than that carried around with the wet flue gas.

Except for the fictitious oxygen carrier materials, the underlying thermodynamic data were taken from the NASA Glenn database (McBride, Zehe and Gordon, 2002), NIST-JANAF (Chase, 1998) and Barin and Knacke's (Barin and Knacke, 1974) tables, if such data existed (here, CuO/Cu_2O, Mn_2O_3/Mn_3O_4 and CoO/Co_3O_4). Otherwise the enthalpies of reaction at standard state for various materials were computed based on density functional theory calculations from the Materials Project (Ong *et al.*, 2008; Jain *et al.*, 2013). Additional corrections to account for temperature effects and optimal Hubbard U values for transition elements were employed as described in previous studies (Wang, Maxisch and Ceder, 2006; Ong *et al.*, 2010). The assumptions made for materials taken from the Materials Project regarding the entropy of reaction and the temperature dependence of the thermodynamic properties were the same as for the fictitious materials.

2.2.5 Fuels

Three different solid fuels, a lignite (Hambach lignite) and two bituminous coals (Illinois No. 5 and Taldinskaya), were considered as well as methane (Dennis *et al.*, 2010). The composition of the exhaust gas of the oxy-fuel combustor as well as the rate of circulation of the oxygen carrier in the CLAS unit are dependent on the fuel used. The amount of oxygen supplied is 5 % above that required stoichiometrically to achieve complete combustion (Buhre *et al.*, 2005). Table 2-1 shows the ultimate analysis of the solid fuels. The higher heating values of the dried fuels were calculated using the following formula given by Boie (Mason and Gandhi, 1983)

$$HHV(\mathrm{MJ/kg}) = 0.352\,(\mathrm{C}) + 1.162\,(\mathrm{H}) + 0.105\,(\mathrm{S}) - 0.111\,(\mathrm{O}) + 0.063\,(\mathrm{N})$$

where the elements are in weight percent. The lower heating value for the fuel as received is calculated from the HHV from

$$LHV = \left[HHV - \Delta h_{vap}\left(\frac{M_{H_2}}{M_{H_2O}}(H) + (M)\right)/100\right]\left(1 - \frac{(M)}{100}\right)$$

to account for the enthalpy of vaporization, Δh_{vap}, required to evaporate combustion water and moisture (M) as received. For low-rank coal, such as the Hambach lignite the moisture content lowers the LHV significantly.

Table 2-1: Ultimate analysis of different fuels on dry basis in wt.%.(Dennis *et al.*, 2010) The moisture content is also included here as received

Fuel type	C wt.%	O wt.%	H wt.%	S wt.%	N wt.%	Ash wt.%	Moisture wt.%	LHV MJ/kg
Hambach Lignite	66.6	22.4	5.2	0.3	0.9	4.6	54.0	11.3
Illinois No. 5	70.2	11.8	4.3	2.6	1.7	9.4	7.1	25.7
Taldinskaya	66.1	6.6	4.9	0.42	2.0	19.98	9.2	24.6

The lower heating value per mole of oxygen required by the fuel, Θ, can then be calculated by first including the moisture content in the results from the ultimate analysis as any moisture is not in the fuel as received is not combustible. Then, the number of moles of each of the elements (now including H_2O as moisture) per unit weight, *e.g.* 1 g, of fuel is obtained by dividing the mass fraction by their molar masses, as shown

in Table 2-2. For the Hambach lignite, combustion with such a high moisture content would not take place but drying would be required (Karthikeyan *et al.* 2009). However, drying is not assumed in this work. The requirement for oxygen in moles, $n_{O_2,fuel}$, to fully combust the, *e.g.*, 1 g of fuel is

$$n_{O_2,fuel} = n_C - n_{O_2} + \frac{1}{2} n_{H_2} + n_S \tag{2-19}$$

The lower heating value per mole of oxygen required by the fuel, Θ, is then obtained by dividing the LHV as presented in Table 2-1 by $n_{O_2,fuel}$. The result for the three coals investigated in this work is listed in Table 2-2. It should be noted that Θ of the three coals is very similar despite the large difference in the LHV of the lignite and the two bituminous coals.

Table 2-2: Molar amount (mmol) of the constituents of different fuels per one gram of fuel. $n_{O_2,fuel}$ is the molar requirement to combust 1 g of fuel and θ is the molar lower heating value. The Hambach lignite is assumed to be dried to a moisture content of 12.5 wt.%.

Fuel type	C	O_2	H_2	S	N_2	H_2O	$n_{O_2,fuel}$	Θ
			mmol/g				mmol O_2/g	kJ/mol O_2
Hambach Lignite	25.53	3.22	11.96	0.04	0.15	30.00	28.33	398.8
Illinois No. 5	54.35	3.43	19.97	0.76	0.56	3.94	61.66	416.8
Taldinskaya	50.01	1.87	22.25	0.12	0.65	5.11	59.38	414.3

Using the same method and applying it to methane (CH_4), which is used in section 2.3.7, the mass fractions of which are 0.75 and 0.25 for carbon and hydrogen, respectively, Θ of methane turns out to be 400 kJ/mol O_2 assuming a LHV of 50 MJ/kg.

2.2.6 Determination of Optimal Steam Flow to Reducer

In many cases the steam cycle is poorly matched to the characteristics of the oxygen carrier. Often heat remains unused at temperatures below the entrance temperature of the HRSG, *viz.* 549 K. This surplus heat was assumed to generate extra steam which was introduced into the low-pressure turbine to produce additional electricity. Similarly, additional steam is bled from the low-pressure turbine if the requirement for steam exceeds the amount of steam that could be produced efficiently. This means that the steam required by the reducer is met partially by evaporation of water from available heat and partially by extracting extra steam from the steam turbine. This leads to a modification of the underlying flow sheet and changes the amount of electricity generated per kg of steam. Three different cases were identified:

- Case 1: insufficient heat supplied to the reducer, *viz.* the heat demand of the oxygen production is higher than the heat supplied by the combustion of fuel,
- Case 2A: autothermal operation,
- Case 2B: autothermal operation with significantly decreased efficiencies (*i.e.* higher energy penalties).

2.2.6.1 Case 1: Insufficient Heat supplied to the Reducer

In this case, the oxy-fuel combustor does not provide sufficient heat to drive the reducer. This can be seen in Figure 2-4, which shows the grand composite curve of a CLAS-oxy-fuel power plant producing 500 MW_{el}; in both cases shown in the figure, the combined CLAS unit + the oxy-fuel combustor are scaled to match the heat demand of the steam cycle. In Figure 2-4a, the CLAS unit is sized to produce enough oxygen to combust the fuel (with 5 % excess). The grand composite curve in Figure 2-4a shows that, with this particular material, producing all the oxygen by CLAS is not feasible; the heat provided by the oxy-fuel combustor is insufficient to match the

demands of the reducer. In the case shown, using an oxygen carrier with $T_{eq}(pO_{2,red} = 0.34$ bar) of 973 K and ΔH_r^o of 250 kJ/mol with Illinois No. 5 coal results in a deficit in heat of 10.3 %. Therefore, either heat or additional oxygen must come from elsewhere.

Figure 2-4b shows the same plant with a scaled-up oxy-fuel combustor to cover the unmatched heat demand (but keeping the CLAS heat demands constant). Of course, this requires extra oxygen to be provided from elsewhere, with an accompanying energy penalty, such as a cryogenic air separation unit. For modern cryogenic air separation units (CASU), this penalty is as low as 0.16 kWh per kg of O_2, assuming a CASU plant size of 5,000 t per day and a purity of 95 % O_2 (Trainer, Perrin and Darde, 2008). In the case of a CLAS-oxy-fuel power plant, it should be noted that the energy penalty might be larger owing the demand for oxygen being much lower than 5000 t per day (*i.e.* ~600 t per day). In practice, because of economies of scale, cryogenic air separation would not complement CLAS and is more likely to substitute it.

Figure 2-4a also illustrates that at low temperatures, heat is rejected (Q_2) which could be used to raise steam. Here, this additional heat is utilised by generating additional steam at 427 K, which is then introduced into the low-pressure turbine to generate additional electricity; thus, optimizing the efficiency of the plant. This additional heat sink has been included Figure 2-4b, and is included in all subsequent calculations. In this case, this raises the overall efficiency to 40.3 % from 38.5 % because of the additional production of 64.2 kg/s of steam. A flowsheet listing the example shown in Figure 2-4a is presented in the Appendix 12.1.

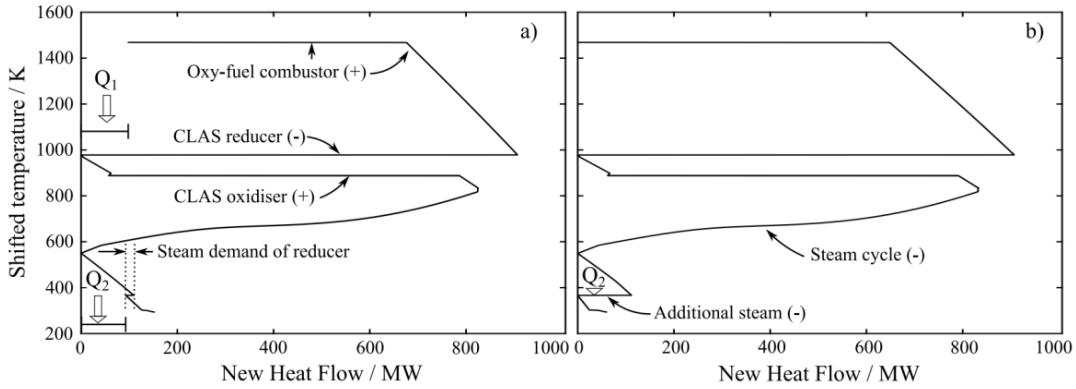

Figure 2-4: Grand composite curve of the a) non-optimized and b) optimized power plant producing 500 $MW_{el,net}$ running at a heat deficit (Q_1, the part of the heat demand of the CLAS reducer that cannot be satisfied by the oxy-fuel combustor) and using an oxygen carrier system with $T_{eq}(pO_{2,red}$=0.34 bar) = 973 K and ΔH_r^o = 250 kJ/mol; here, the maximum temperature of the unmodified steam cycle is 835 K. Q_1 in b) is assumed to be overcome by supplying additional oxygen. Q_2 is heat available at temperatures below the steam generator (HRSG) inlet temperature of 549 K. (-) and (+) denote heat sinks and heat sources, respectively

2.2.6.2 Case 2: Autothermal Operation

For some CLAS materials, it is possible to produce all the oxygen required for combusting fuel, and supply all of the heat required from the system, which is referred to as autothermal operation in this work. Broadly speaking, two cases arise: (A) operation with the steam cycle able to operate with an unmodified high-pressure and intermediate-pressure turbine; (B) operation with reduced efficiencies owing to modifications to the high-pressure and intermediate-pressure section of the steam cycle.

Case 2A: In terms of the grand composite curve, case 2A is similar to the optimised case 1, but with all the heat demands of the CLAS system being met by the heat release from combustion. All the heat from CLAS system can be utilised by the steam cycle. CLAS oxygen carrier materials which give composite curves of this kind are desirable.

Case 2B: Case 2B only occurs for oxygen carrier systems with an equilibrium temperature, $T_{eq}(pO_{2,ox})$, below the maximum temperature of the base steam cycle, 835 K, as described in section 2.2.3. In this case, the composite curve of the steam cycle would influence the pinch point at the operating temperature of the CLAS unit.

To continue to generate 500 MW electricity, more steam must be produced to make up for the removal of the high temperature turbine segments. In this model, the operating temperature of the steam cycle is kept below that of the oxidizing reactor. In theory, a small amount of heat is still available above the base-case maximum turbine temperature, but to harness it, the steam cycle would have to be reconfigured to utilise the small steam flow which could be produced (heat available between the operating temperatures of the reducer and oxidizer, as shown in Figure 2-4); *i.e.* effectively there would have to be either an additional high-pressure turbine or turbine section to process this flow, which is likely to be expensive.

From these considerations it follows that a comparison of the heat released per mole of oxygen from the fuel, H_{comb}, and the enthalpy of reaction of the oxygen releasing reaction, *i.e.*

$$H_{comb}(T_{red}) \geq \Delta H_r^o(T_{red}) \tag{2-20}$$

is a sensible rough estimate of whether autothermal operation is achievable with a certain oxygen carrier. This case is shown in Figure 2-5a and it can be noted that both, CuO and Mn_2O_3, are expected to operate autothermally. However, this criterion describes the ideal case, which is not realisable in practice. For example, when oxygen is produced by swinging the temperature to cross the equilibrium partial pressure curve, then the heat demand of the reducing reactor, H_{red}, is increased by the need to heat up the oxidised oxygen carrier which enters the reducing reactor at roughly the operating temperature of the oxidising reactor. This is calculated by

$$H_{red}(T_{red}) = \Delta H_r^o(T_{red}) + n_{ox} \int_{T_{ox}}^{T_{red}} C_{p,ox}\, dT \tag{2-21}$$

where n_{ox} is the molar amount of oxidised oxygen carrier material entering the reducing reactor and $C_{p,ox}$ is the molar heat capacity of the oxidised phase. The dash-dotted black line in Figure 2-5b shows the increase in the head demand for $4CuO \rightleftarrows 2Cu_2O + O_2$. Here, the four moles of cupric oxide enter the reducing reactor, which operates at $\mathrm{T_{red}} = 1290\ K$, at a temperature of $\mathrm{T}_{ox} = 1170\ K$; temperatures typical for temperature swinging CuO/Cu_2O (Shah *et al.*, 2013).

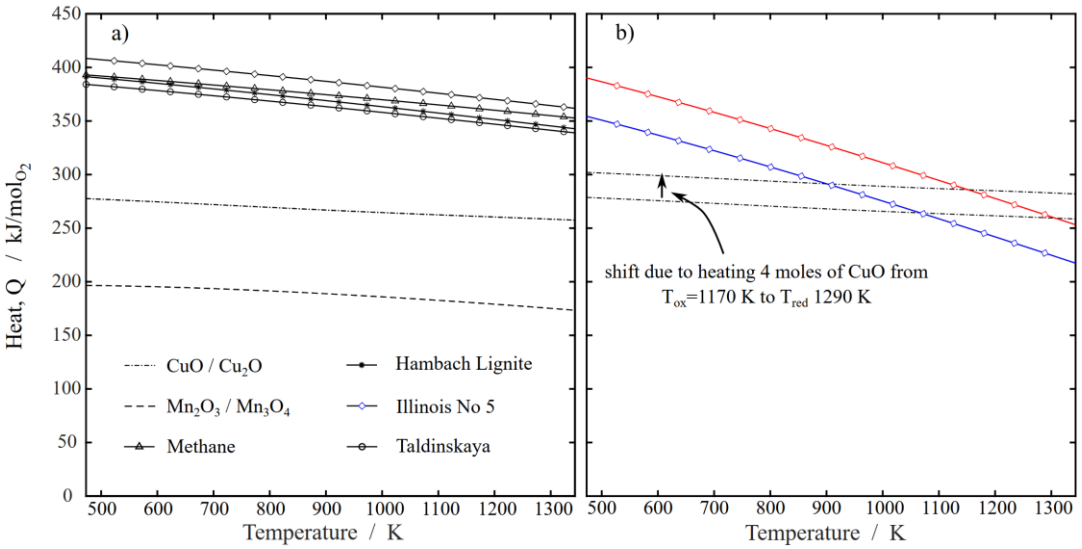

Figure 2-5: a) Heat demand of the oxygen release reactions $4CuO \rightleftarrows 2Cu_2O + O_2$ and $6Mn_2O_3 \rightleftarrows 4Mn_3O_4 + O_2$ and heat of combustion with one mol of oxygen of different fuels. b) Heat demand of $4CuO \rightleftarrows 2Cu_2O + O_2$ including heat required to bring CuO from $T_{ox} = 1170\ K$ to $T_{red} = 1290\ K$ (equation (2-21)) and heat available from combusting Illinois No5 coal with one mol of O_2 in 2.86 mol of CO_2, *i.e.* pO_2 of 0.35 bar, without pre-heating the gases (blue line) and with preheating to 623 K.

The heat that is available from the oxy-fuel combustor depends on the level to which the incoming fuel and gas are pre-heated. The combustion air for fuels, including pulverised coals, can be pre-heated to very high temperatures using high-temperature air combustion (HiTAC) but requires the combustion to proceed at low oxygen concentrations to reduce NO_x formation and maintain stable combustion (Saffari and Weihong, 2014; Zhu *et al.*, 2018). The red solid line in Figure 2-5b shows the heat available from combusting Illinois No5 coal under the assumption that it is possible to optimise the oxy-fuel pulverised coal burner in such a way that a stable flame with pO_2 of 0.35 bar and pre-heating the gaseous inflow to the burner to 623 K, the combustion air temperature usually found in pulverised coal burners (Suda *et al.*, 2002), can be achieved. The blue line shows the case where no pre-heating of the gaseous inflow to the burner takes place and the gases enter at 298 K. It can be noted that the change in available heat from the oxy-fuel combustor due to pre-heating the inflowing gases is significant.

In summary, the question of whether an oxygen carrier can be operated autothermally or not depends on the fuel, *i.e.* its composition and its lower heating value per mole of oxygen, the degree of pre-heating inflows to the oxy-fuel combustor and the CLAS unit, the stoichiometry of the reaction, the heat capacity and the enthalpy of reaction of the oxygen carrier and the desired pO_2 in the reducer outlet, which dictates the gaseous inflow to the reducer as well as the temperature difference between the CLAS reactors. The partial pressure of oxygen depends on the enthalpy and entropy of reaction of the oxygen carrier, as shown in equations 1-4 and 1-9.

2.3 Results and Discussion

2.3.1 Variable Entropy of Reaction

The parameter sweep $\{\Delta H_r^o, T_{eq}\}$ described above allows for a variable entropy of reaction. The result of the parameter sweep is plotted in Figure 2-6, when operating the reducing reactor of the CLAS unit at an equilibrium partial pressure of oxygen of 0.34 bar and using Illinois No. 5 coal. The area for "potential oxygen carriers" shows combinations of ΔH_r^o and T_{eq} likely to be accessible by existing materials; this region is computed by considering the base case (*i.e.* using the thermodynamic assumptions made previously, and the law of Dulong-Petit with $\Delta S_{r,298K}^o \equiv S_{O_2,298K}^o = 205.2$ J/mol/K) as shown, with the limits set by potential differences in the value of $\Delta S_{r,298K}^o$. Here it is assumed that $\Delta S_{r,298K}^o$ can differ from the base case by $\pm$ 25% (although as noted below, some materials could fall outside this bound). The solid iso-lines, showing contours of constant efficiency, indicate that the overall net efficiency of the power plant reaches a plateau at around 40.6 % for case 2A. For this case, there is little energy penalty and the overall efficiency is dominated by that of the underlying steam cycle. A vertical boundary separates case 2B and case 2A at 925 K, the temperature at which the operating temperature of the oxidizer forces the maximum temperature of the steam cycle to decrease.

In Figure 2-6, the region labelled case 1 corresponds to the situation where the CLAS system cannot be driven by the oxy-fuel combustor as described previously. To operate with these materials would require either heat to be supplied from elsewhere, or extra oxygen to be provided to allow the oxy-fuel combustor to be scaled up to supply the heat demand of the CLAS unit.

From Figure 2-6, it is obvious that whether or not the oxy-fuel combustor delivers enough heat is a function of the enthalpy of reaction and the operating temperature of the reducer. With an increase in the temperature at which the oxygen carrier releases oxygen at a specified partial pressure, here 0.34 bar, the maximum feasible enthalpy of reaction, ΔH_r^o, decreases. The gradient of this transition line and its location are a function of the lower heating value of the fuel per mole of oxygen required to combust the fuel. Hence, oxygen carrier systems close to the transition from case 1 to cases 2A and 2B might be feasible when using a fuel with a higher heat of combustion per mole of oxygen required.

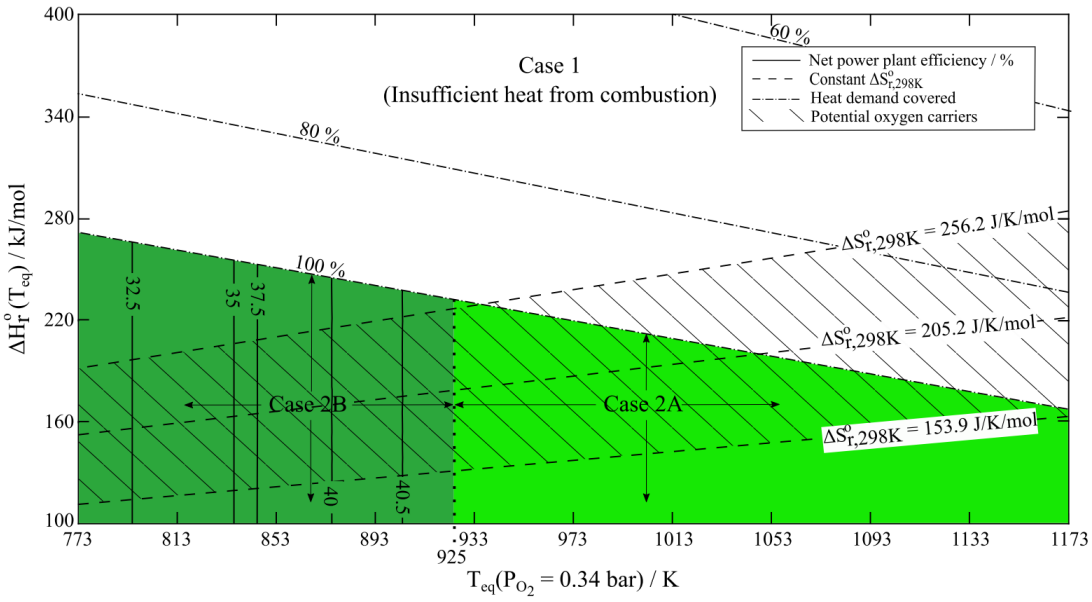

Figure 2-6: Efficiency of the CLAS-oxy-fuel power plant (using Illinois No. 5 as fuel) depending on thermodynamic properties of the oxygen carrier at an equilibrium partial pressure of oxygen of 0.34 bar in the reducer for the reaction stoichiometry $4MO \rightleftarrows 2M_2O + O_2$. The dash-dotted lines show the proportion of the heat demand of the CLAS unit which could be met by a hypothetical oxy-fuel combustor using only the oxygen from the CLAS unit. The temperature difference between the oxidizer and reducer is 80 K. The green region denotes the case where enough heat is supplied from the combustion of fuel.

The effect of using different fuels in the combustion process can be viewed in Figure 2-7 and Figure 2-8, which map the efficiency of the Hambach lignite and the Taldinskaya coal, respectively. Between these two fuels, a slight shift in the transition from Case 1 and Case 2 can be observed. Furthermore, net efficiencies of over 40 % were not achieved using the lignite, in contrast to the Taldinskaya coal and the Illinois No. 5 coal shown in Figure 2-6. In terms of the fuels, for the envelope of thermodynamic properties with which auto-thermal operation can be achieved, it is Illinois No. 5 > Taldinskaya coal > Hambach lignite.

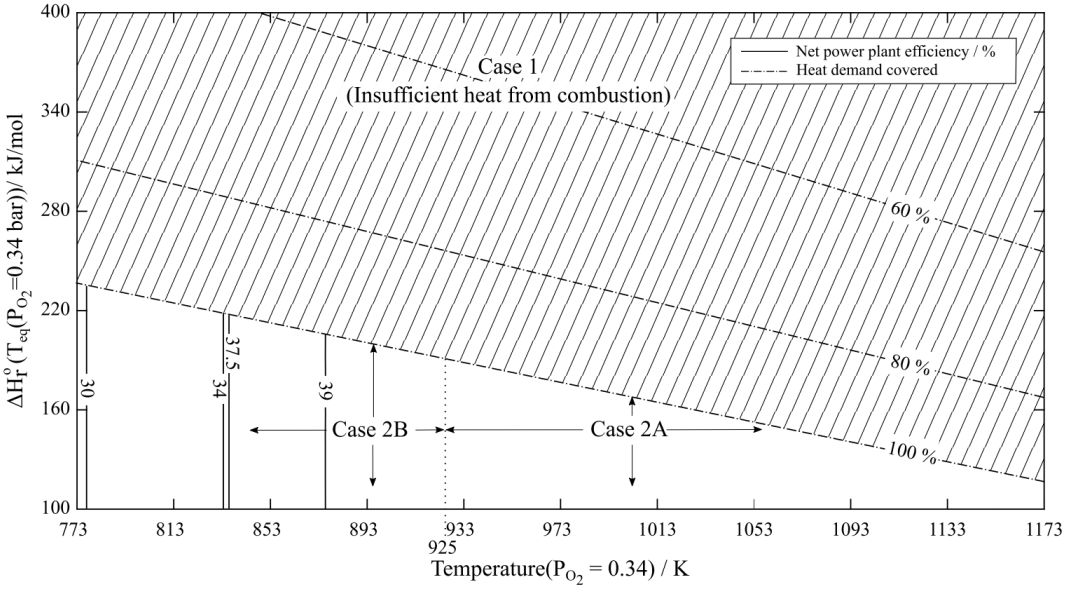

Figure 2-7: Efficiency of the CLAS-oxy-fuel power plant depending on thermodynamic properties of the oxygen carrier at an equilibrium partial pressure of oxygen of 0.34 bar in the reducer for the reaction stoichiometry $4M_{ox}O \rightleftarrows 2M_{red}O + O_2$ and using Hambach lignite

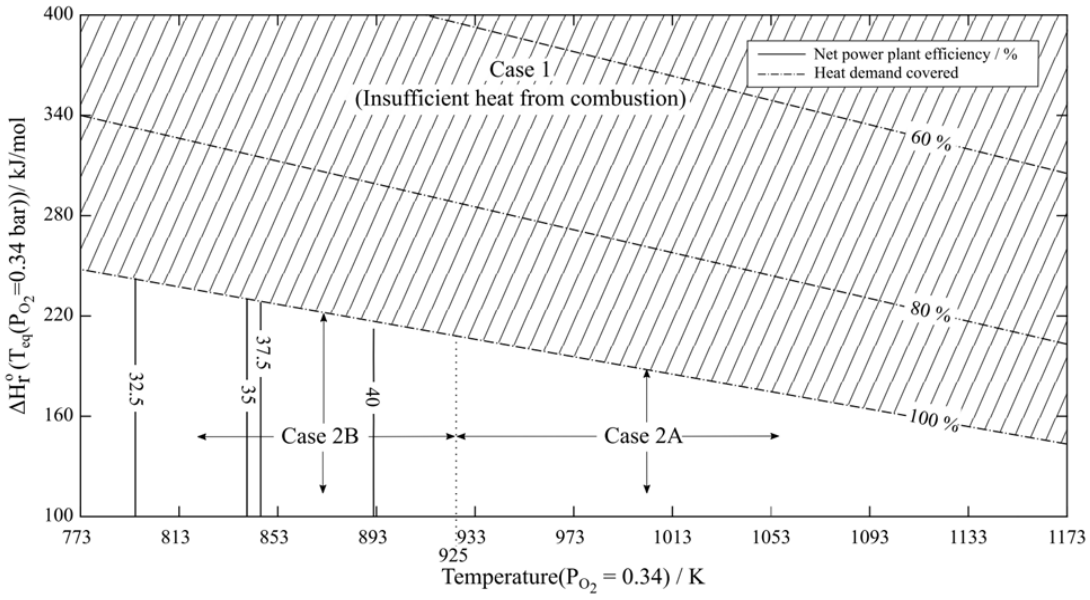

Figure 2-8: Efficiency of the CLAS-oxy-fuel power plant depending on thermodynamic properties of the oxygen carrier at an equilibrium partial pressure of oxygen of 0.2 bar in the reducer for the reaction stoichiometry $4M_{ox}O \rightleftarrows 2M_{red}O + O_2$ and using Taldinskaya coal

2.3.2 Fixed Entropy of Reaction

Lines of constant entropy of reaction are shown on Figure 2-6 (*e.g.* the base case as illustrated), for a constant temperature difference between the reactors. If, instead, the entropy of reaction is fixed (and the temperature difference is allowed to vary), the operating space can be replotted. Figure 2-9 shows such a plot, with the entropy of reaction fixed to $\Delta S^{o}_{r,298K} = 205.2$ J/mol/K.

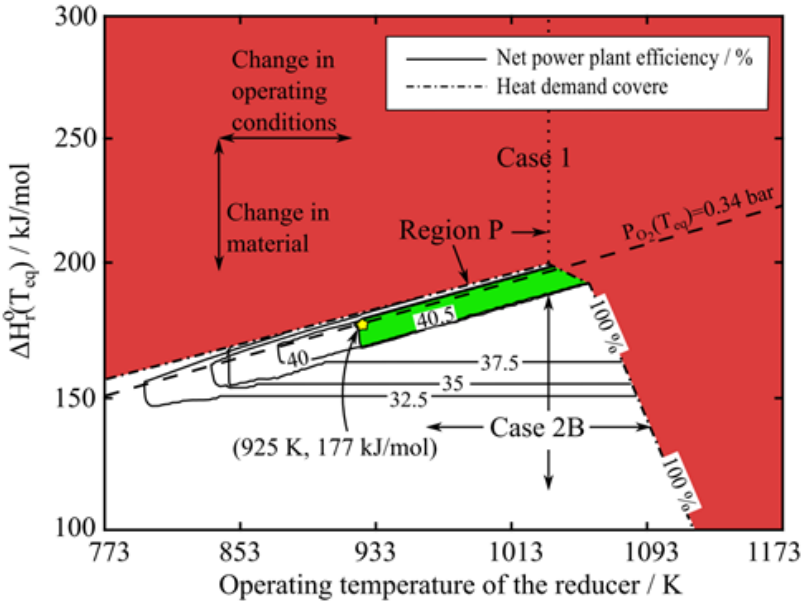

Figure 2-9: Efficiency of the CLAS-oxy-fuel power plant depending on thermodynamic properties of the oxygen carrier at a fixed entropy of reaction, $\Delta S_r^o(298\ \mathrm{K}) = 205.2$ J/mol/K. Along the dashed line (which indicates an equilibrium partial pressure of oxygen of 0.34 bar in the reducer), the star marks the transition from case 2B to case 2A, where the efficiency of the plant plateaus at 40.5 %. In region P the reducer operates at very low oxygen partial pressures. The red region represents case 1. The green region represents case 2A

Region P in Figure 2-9 shows cases where the reducer is operated at very low oxygen partial pressure and, therefore, requires substantial amounts of steam (which is separated out in the CLAS condenser), to meet the requirement of $pO_{2,req} \cong 0.35$ bar. The steam does not participate in any reactions but has inert thermal mass that needs to be heated up to T_{red} and separated out again in the condenser. Therefore, this high demand for additional steam leads to a significant decrease in the overall net efficiency of the power plant. The dash-dotted line indicates the point at which the oxy-fuel combustor cannot satisfy the heat demand of the CLAS unit, *viz.* transition to case 1 occurs.

Moving horizontally along a line in Figure 2-9, the temperature difference between the oxidizer and the reducer can initially be maintained at 80 K to allow $pO_{2,ox} < 0.21$ bar. However, if the reducing reactor is operated above a critical temperature, the difference in temperature between the oxidizer and reducer must be increased to allow the oxidizer to operate with $T_{ox} \rightarrow T_{eq}(pO_2 = 0.21\ \mathrm{bar})$.

The transition between case 2A (*i.e.* minimal energy penalty, shaded green) and case 2B in Figure 2-9 now occurs for two reasons: (1) vertically at an enthalpy of reaction of around 177 kJ/mol and $T_{eq}\left(pO_{2,red} = 0.34 \text{ bar}\right)$ of 925 K, where the oxidizer operates at a temperature of which impacts the steam cycle; (2) along a line parallel to the dashed line, where, as the temperature of the reducer increases, the air flow to the oxidizer rises as $T_{ox} \rightarrow T_{eq}(pO_2 = 0.21 \text{ bar})$, leading to a higher demand in heat to heat up the air that can only be partially recovered into the generation of steam, leading to more heat energy rejected unused and reducing the overall efficiency.

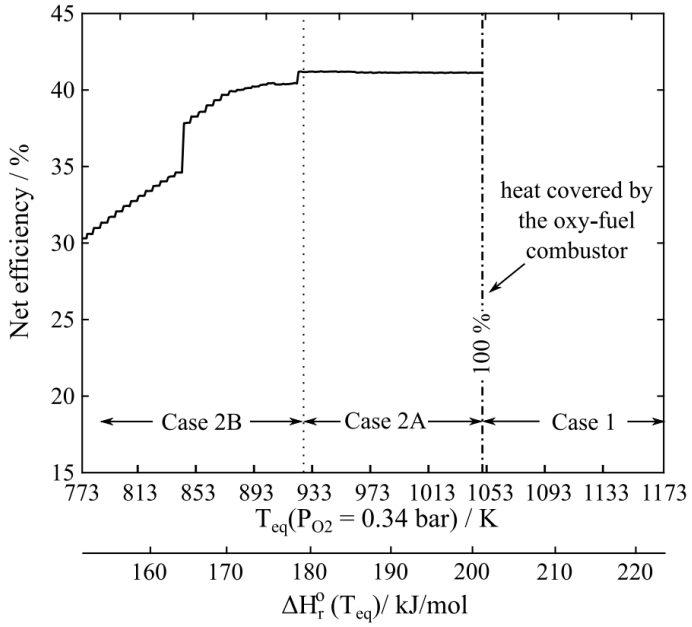

Figure 2-10: Net efficiency of the power plant vs oxygen carrier materials with an entropy of reaction of 205.2 J/mol/K, an equilibrium partial pressure of oxygen of 0.34 bar in the reducer a reaction. a stoichiometry of $4MO \rightleftarrows 2M_2O + O_2$ and difference in the operating temperatures of the CLAS reactors of 80 K

Figure 2-10 shows the net efficiency of the base case, *i.e.* $\Delta S^o_{r,298K} = 205.2$ J/mol/K. Here, the CLAS reactors were operated with a difference in temperature of 80 K, where $T_{eq}\left(pO_{2,red} = 0.34 \text{ bar}\right)$ is the operating temperature of the reducer. When evaluating oxygen carrier materials for which the assumption of $\Delta S^o_{r,298K} = S^o_{O_2,298K}$ holds, the efficiency of the power plant is maximized when $177 \text{ kJ/mol} < \Delta H^o_r(T_{eq}) < 201 \text{ kJ/mol}$.

2.3.3 Sensitivity to Temperature Difference of the CLAS Reactors

The difference between the temperature of the oxidizer and the equilibrium temperature for a partial pressure of oxygen of 0.21 bar plays a significant role in the heat integration. The closer the temperature of the oxidizer to $T_{eq}\left(pO_2 = pO_{2,air} = 0.21 \text{ bar}\right)$, the more air must be supplied to oxidize the reduced oxygen carrier. In the model, the air flow is set to the limiting minimum air flow that allows the oxygen carrier to be fully oxidized, *i.e.* when the depleted air flow has a partial pressure of oxygen, $pO_{2,ox}$, equal to the equilibrium partial pressure of oxygen of the material at the oxidizer temperature, *i.e.* $pO_{2,ox} = pO_2(T_{ox})$. The molar flow of oxygen entering the oxidizer is given by

$$\dot{n}_{O_2,ox,in} = \frac{\dot{n}_{O_2,red}\left(1 - pO_{2,ox}\right)}{1 - \frac{pO_{2,ox}}{pO_{2,air}}} \tag{2-22}$$

where $\dot{n}_{O_2,red}$ is the molar flow of oxygen leaving the reducer, *i.e.* the amount of oxygen required to combust one mole of fuel, and $pO_{2,ox}$ the equilibrium partial pressure of oxygen at the operating temperature of the oxidizer. When $pO_{2,ox}$ approaches $pO_{2,air}$, *i.e.* when $T_{ox} \rightarrow T_{eq}(pO_2 = 0.21 \text{ bar})$, the air flow must increase, and in the limiting case of $T_{ox} = T_{eq}(pO_2 = 0.21 \text{ bar})$ is infinite. Figure 2-11 shows both the net efficiency of the power plant and the air flow as a function of the operating temperature of the oxidizer for three materials with the same $T_{eq}(pO_{2,red} = 0.34 \text{ bar})$, different enthalpies of reaction, and, hence, varying entropies of reaction. For a given $T_{eq}(pO_{2,red} = 0.34 \text{ bar})$ the gradient of the equilibrium curve increases for materials with higher enthalpies of reaction and the oxidizer can be operated at a temperature closer to that of the reducer.

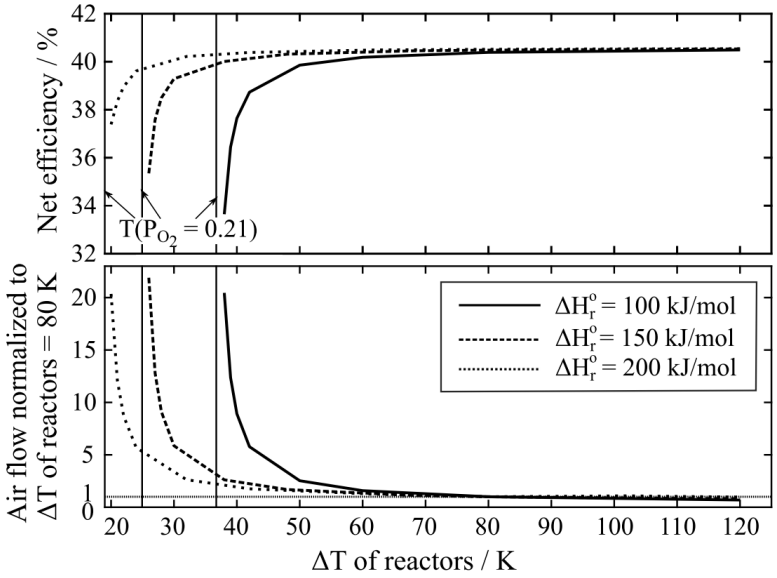

Figure 2-11: Sensitivity of the net efficiency of the CLAS oxy-fuel power plant and the normalized air flow to the oxidizer with respect to the temperature difference between oxidizer and reducer and three oxygen carriers. Here, the reducer is operated at 973 K

2.3.4 Support material and partial conversion

If either a support material is used or there is only partial conversion of the oxygen carrier, solid material is circulated that does not participate in the redox reaction. This inert material circulates heat between the colder oxidizer and the hotter reducer. Hence, the addition of inert support material, here α-Al_2O_3 or β-SiO_2, decreases the combinations of ΔH_r^o and T_{eq} at which autothermal operation is possible. In Figure 2-12 these combinations are plotted for molar fractions of inert material of 0 %, 50 % and 75 % and autothermal operation can be achieved below the respective lines. Similar to the addition of inert material, the heat load of the reactors changes if partial conversion is assumed or the flue gas recirculation rate is increased, *i.e.* lowering the operating partial pressure of oxygen in the reducer; results for the latter are plotted Figure 2-13.

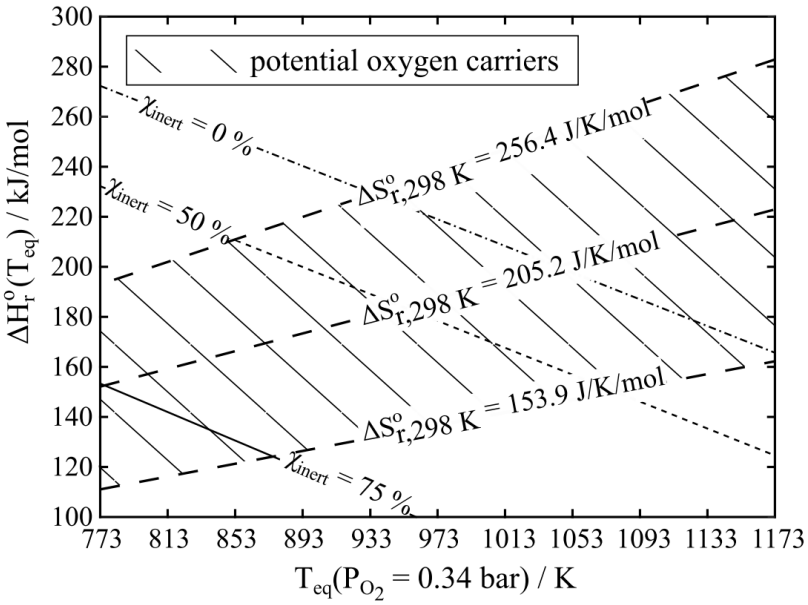

Figure 2-12: Suitable regions for autothermal operation using 0 mol-%, 50 mol-% or 75 mol-% of α-Al_2O_3 below the respective lines using fictitious oxygen carriers following the reaction $4MO \rightleftarrows 2M_2\ O + O_2$ and Illinois No. 5 coal

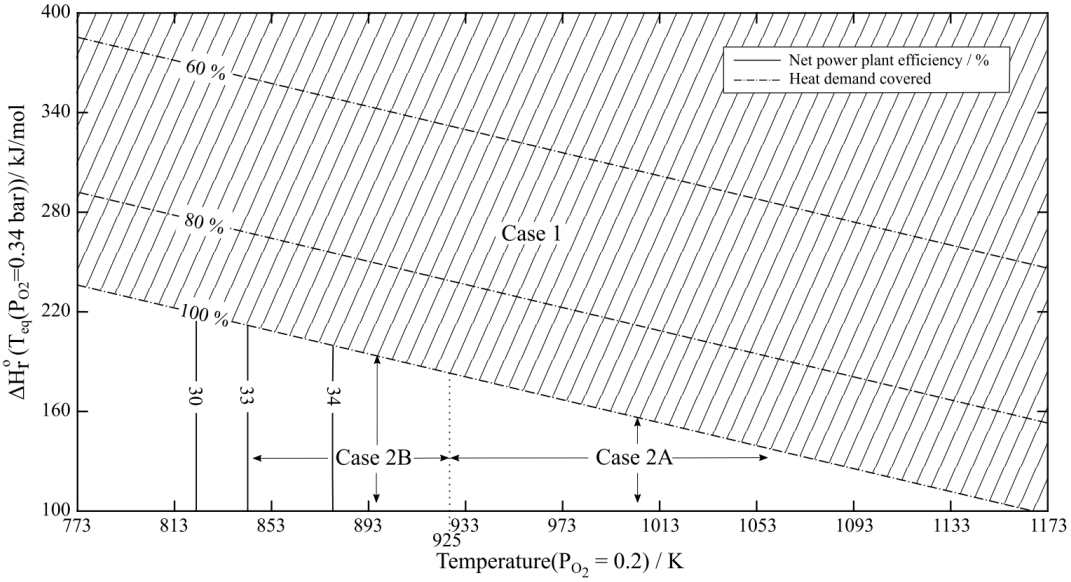

Figure 2-13: Efficiency of the CLAS-oxy-fuel power plant depending on thermodynamic properties of the oxygen carrier at an equilibrium partial pressure of oxygen of 0.2 bar in the reducer for the reaction stoichiometry $4M_{ox}O \rightleftarrows 2M_{red}O + O_2$ and using Illinois No 5 coal

2.3.5 Effect of the Specific Heat Capacity of the Solids

Previously, it was assumed that the law of Dulong-Petit holds to obtain the molar heat capacity, C_p, for the solids. This is likely to lead to little error in terms of the equilib-

rium calculation, because only the difference in molar heat capacity of reaction, $\Delta C_{p,r}$, is important. However, from the point of view of heat integration, the absolute value of C_p is important, because the solids transport sensible heat between the colder oxidizer and the hotter reducer. All the previous calculations have assumed absolute values for the molar heat capacity of the reduced, $C_{p,red}$, and oxidized phase, $C_{p,ox}$, derived from the atoms and stoichiometry, which gives a $\Delta C_{p,r}$ that is only a function of the stoichiometric coefficient of oxygen. Figure 2-14 shows the efficiency of the CLAS-oxy-fuel power plant with a different reaction stoichiometry ($6M_{4/3}O \rightleftarrows 4M_2O + O_2$) than the previously assumed, *i.e.* $4MO \rightleftarrows 2M_2O + O_2$. The range of $\{\Delta H_r^o, T_{eq}\}$ decreases due to higher molar heat capacities of the solids transferring heat between the CLAS reactors. Hence, the sensitivity of the previous calculations has the same as that described above, *i.e.* any increase in absolute C_p has the same effect as adding inert material or partially converting the solid.

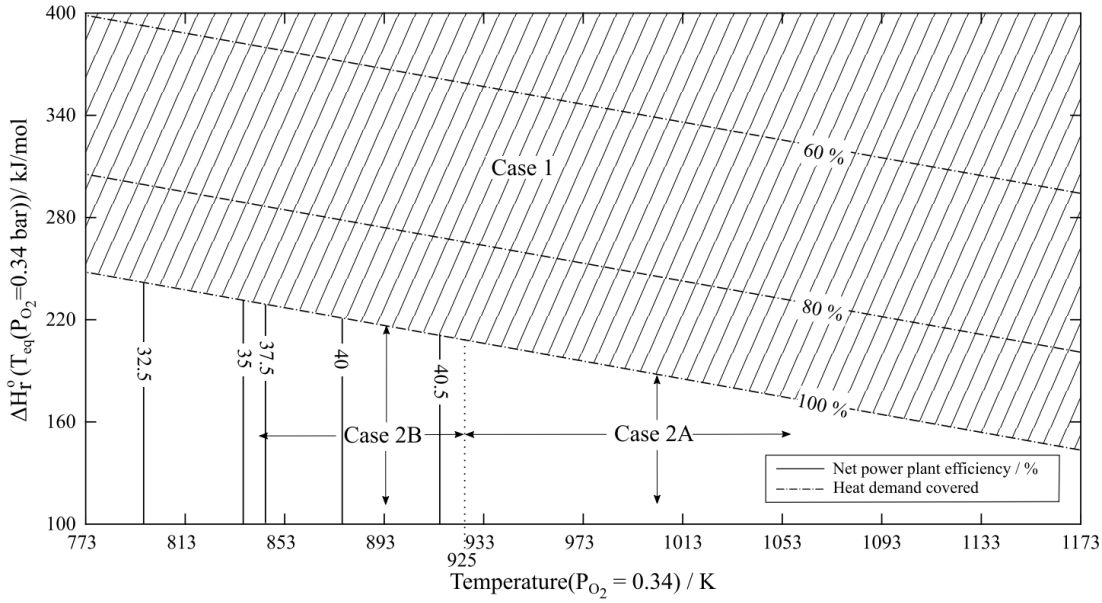

Figure 2-14: Efficiency of the CLAS-oxy-fuel power plant depending on thermodynamic properties of the oxygen carrier at an equilibrium partial pressure of oxygen of 0.34 bar in the reducer for the reaction stoichiometry $6M_{ox}O \rightleftarrows 4M_{red}O + O_2$ and using Illinois No 5 coal

2.3.6 Screening Materials based on DFT

A full list of the 2857 candidates screened from the Materials Project data base is too extensive to be given here, but can be found in the supplementary information of (Görke *et al.*, 2018). Of these, only 79 had equilibrium operating temperatures,

$T_{eq}(pO_{2,red} = 0.34\ \text{bar})$, in the range of 673 K to 1323 K (a slightly wider temperature range than that used previously to allow for errors in the DFT) and a bimolecular oxidation reaction only. These candidate materials, the thermodynamic data of which were derived from density functional theory (DFT), are shown on the plot of $\Delta H_r^o(T_{eq})$ *vs.* $T_{eq}(pO_{2,red} = 0.34\ \text{bar})$ in Figure 2-15 (the complete list of the 79 oxygen carriers is provided in Table 12-3 in Appendix 12.4). The figure shows the boundary between cases 1 and 2 for the case where Illinois No. 5 coal is used, and the molar heat capacities are set in accordance with the law of Dulong-Petit. The position of this line therefore can vary slightly depending on fuel and stoichiometry of the oxygen release reaction as discussed previously. Of the candidate materials, 34 were found to achieve autothermal operation, but, since there are both errors in the DFT and the boundary for autothermal operation can move, oxygen carrier materials might work, too.

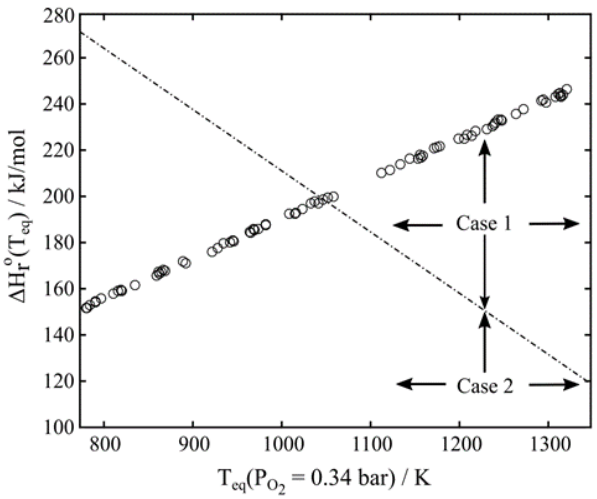

Figure 2-15: Enthalpy of reaction and equilibrium temperature of 79 shortlisted oxygen carrier systems for 673 K $\leq T_{eq} \leq$ 1323 K based on dft calculations; the dash-dotted line denotes the transition between autothermal (case 2) and endothermic operation (case 1) when using Illinois No. 5 coal, *i.e.* 100 % heat energy provided (as in Figure 2-6)

Table 12-3 in Appendix 12.4 contains materials that are unsuitable due to, *e.g.* a melting point lower than the desired equilibrium temperature, toxicity, radioactivity, or a very high price. Most of the 15 materials predicted to allow autothermal operation without significant energy penalty, *i.e.* case 2A, are unsuitable due to their low melting points; the melting points are ~773 K for CsO_2 (Touzain, 1976), 437 K for Cs_3O (Tsai,

Harris and Lassettre, 1956), 894 K for CsI (Sigma Aldrich, 2016), 532 K for HgI_2 (IFA, 2016), 387 K for Iodine (IFA, 2016), 959 K for KI (Lyday and Kaiho, 2015), 309 K for $NaMnO_4$ (Reidies, 2000), and 563 K for PbO_2 (Larrañaga, Lewis and Lewis, 2007). Anhydrous $KBiO_3$ is reported to decompose to Bi_2O_3 and K_2O at temperatures above 773 K (Nguyen *et al.*, 1993), compared to the desired operating temperature for this material is approximately 944.7 K, based on an enthalpy of reaction of 193 kJ/mol as stated by the MaterialsProject (Jain *et al.*, 2011). $Tl(IO_3)_3$ is reported to start losing iodine and oxygen at around 753 K (Yeon, Kim and Halasyamani, 2009), making the oxygen carrier system of $Tl(IO_3)_3/TlI_3$ infeasible for the desired operating temperature of 1037 K. Likewise, KAgO is not suitable as it is said to decompose upon contact with air (Sabrowsky and Hoppe, 1958).

However, for the Cobalt(II) Selenate, $CoSeO_4$, and Cobalt(II) Selenite, $CoSeO_3$ system, both have been synthesized at temperatures above 473 K and 587 K respectively (Vlaev, Genieva and Georgieva, 2006; Melot *et al.*, 2010). While thermal stability has not been further investigated for $CoSeO_3$, anhydrous $CoSeO_4$ was reported to form from $CoSeO_3 \cdot 2\ H_2O$ for mass fractions of SeO_2 below 0.4 at temperatures as low as 473 K, and remain thermally stable up to 573 K, though the higher temperatures required here were not explored (Vlaev, Genieva and Georgieva, 2006). The applicability of Co-Se compounds is questionable as both materials are accompanied by health and safety concerns (Alfa Aesar, 2015). The equivalent manganese system, $MnSeO_4/MnSeO_3$ is perhaps less of concern from the point of view of safety. Manganese selenate can be synthesized by dehydration of $MnSeO_4 \cdot 5\ H_2O$ at temperatures of above 533 (Koleva, 1999). The Selenite, $MnSeO_3$, however, could not be synthesized by hydrothermal treatment of $MnSeO_3.H_2O$ at temperatures up to 573 K (Vlaev and Tavlieva, 2007), but was found to form in acidic environments at ambient temperature (Elrashidi *et al.*, 1987; Vuori *et al.*, 1994) or at high pressures of above 20 kbar (Kohn *et al.*, 1975). Despite these difficulties, it is available for purchase under the CAS number 15702-34-8 at high purities (2N to 5N) from American Elements (American Elements, 2016). The remaining two oxygen carriers to fall into case 2A are $NaMnO_4$ and $NaBiO_3$. The former is likely to disqualify due to a boiling point of only 337 K (IFA, 2016). For $NaBiO_3$ and $NaBiO_2$ synthesis was achieved at temperatures above

473 K (Kumada, Kinomura and Sleight, 2000; Keller and Röhr, 2008), but further information on the thermal stability was not found.

Table 2-3, which shows only those materials that could theoretically give an autothermal system, toxicity and cost have been neglected. The main criterion was that only one crystallographic phase transition occurs at the temperatures of interest. It should be noted that Table 2-3 has to be treated with caution; for some materials, their suitability as an oxygen carrier has been questioned. For example, BaO_2, the material used in the Brin process, is vulnerable to carbonation (Jensen, 2009). For BaO_2, at a partial pressure of oxygen of 0.34 bar, the predicted equilibrium temperature of around 784 K is in reasonable agreement with an equilibrium temperature of around 865 K observed experimentally (Till, 1971). However, using the DFT calculated equilibrium temperature of 784 K would lead to an efficiency as low as 31.5 %, according to the model underlying this study. If instead, the experimentally-determined value of $T_{eq}\left(pO_{2,red} = 0.34\text{ bar}\right) = 865$ K were used, from Figure 2-6, the efficiency would be ~39 %. This again highlights that materials operating in non-desirable regions, *viz.* case 2B, might still be worth investigating.

Finally, considering melting points, thermodynamic stability and health hazards, the suggested list of potentially suitable oxygen carriers in Table 2-3 reduces to $BaFeO_3$ / $Ba_2Fe_2O_5$, $LiBiO_3$ / $LiBiO_2$, $MnPO_4$ / $Mn_2P_2O_7$, $SrFeO_3$ / $Sr_2Fe_2O_5$, and $Sr_2Cu_2O_5$ / $SrCuO_2$. The perovskite $BaFeO_{2.93}$ was found to decompose into the brownmillerite phase $Ba_2Fe_2O_5$ giving off oxygen equal to 2.9 % of its mass at around 1073 K (Parras *et al.*, 1993). Here, the error in the DFT-derived equilibrium temperature becomes apparent; under the assumptions used in the model, decomposition to $Ba_2Fe_2O_5$ was expected at 901 K at an oxygen partial pressure of 0.21 bar. While the reduction of the perovskite phase is possible, it was found that oxidation of $Ba_2Fe_2O_5$, *i.e.* cooling in air, did not proceed (Parras *et al.*, 1993). For $LiBiO_3$, the release of oxygen was reported at temperatures above 573 K (Kumada, 1996). Full reduction to $LiBiO_2$ was achieved at around 773 K (Kumada, 1996; Sathiyamoorthi *et al.*, 2005), re-oxidation, however, was not evaluated. $SrFeO_3$ was found to cycle between the perovskite phase and the brownmillerite phase, Sr_2Fe_2O5, reversibly for at least two cycles at 973 K (Taylor *et al.*, 2016), and for at least 20 cycles at 823 K without showing susceptibility towards carbonation when reduced in CO_2 (Lau *et al.*, 2017). $Sr_2Cu_2O_5$ was synthe-

sized at 1123 K and 100 kbar using $SrCuO_2$ as a precursor (Chen *et al.*, 1996), conditions beyond those expected in chemical looping systems. However, $SrCuO_2$ was used as an oxygen carrier in chemical looping combustion, releasing oxygen equal to around 8 % of its mass at 873 K to form $SrCuO_{1.075}$ (Ksepko, 2015). This oxygen carrier system exhibited further stability over 20 redox cycles at 1223 K.

Table 2-3: Promising oxygen carrier systems deduced from DFT calculations. The short list of highlighted oxygen carriers (OC) remain after considering melting points, thermodynamic stability and health hazards.

Oxidized OC	Reduced OC	$T_{eq}\left(P_{O_2,red} = 0.34\right)$ / K	$\Delta H_r^o(T_{eq})$ / kJ mol^{-1}	Net efficiency	Case
$CoSeO_4$	$CoSeO_3$	928	178	40.6%	2A
CsO_2	$Cs_{11}O_3$	1041	197	40.6%	2A
CsO_2	Cs_3O	942	180	40.6%	2A
$CsIO_4$	CsI	946	181	40.6%	2A
$Hg(IO_3)_2$	HgI_2	1015	193	40.6%	2A
$KAgO_2$	KAgO	965	184	40.6%	2A
$KBiO_3$	$KBiO_2$	945	181	40.6%	2A
$MnSeO_4$	$MnSeO_3$	970	185	40.6%	2A
$NaMnO_4$	$Na_2Mn_2O_3$	982	188	40.6%	2A
$NaBiO_3$	$NaBiO_2$	1009	192	40.6%	2A
PbO_2	PbO	935	180	40.6%	2A
$Sm_2Mn_2O_7$	$SmMnO_3$	979	188	40.6%	2A
$Tl(IO_3)_3$	TlI_3	1037	198	40.6%	2A
$V_2Hg_2O_7$	$VHgO_3$	1030	197	40.6%	2A
Ag_2SeO_4	Ag_2SeO_3	892	171	40.4%	2B
$BaFeO_3$	$Ba_2Fe_2O_5$	922	176	40.6%	2B
BaO_2	BaO	781	152	31.5%	2B
$CdSeO_4$	$CdSeO_3$	780	152	31.4%	2B
Eu_3ReO_8	Eu_3ReO_7	860	166	39.3%	2B
Hg_2SeO_5	Hg_2SeO_3	862	166	39.4%	2B
$Ho_2(SeO_4)_3$	$Ho2(SeO_3)_3$	835	162	35.0%	2B
$LiBiO_3$	$LiBiO_2$	784	153	31.7%	2B
$MnPO_4$	$Mn_2P_2O_7$	820	159	34.1%	2B
MnO_2	Mn_3O_4	869	168	39.8%	2B
$Mn(SeO_3)_2$	$MnSe_2O_5$	791	154	32.2%	2B
$NaAgO_2$	NaAgO	865	167	39.6%	2B
$Na_2Cr_2O_7$	$NaCrO_2$	811	158	33.6%	2B
RbO_3	Rb_2O_3	819	159	34.0%	2B
$SbOF_3$	SbF_3	889	172	40.4%	2B
$SrFeO_3$	$Sr_2Fe_2O_5$	816	159	33.9%	2B
$SrCr_2O_7$	$SrCr_2O_4$	791	155	32.2%	2B
$Sr_2Cu_2O_5$	$SrCuO_2$	797	156	32.6%	2B
Ti_2O_7	Ti_3O_5	867	168	39.7%	2B
V_2O_5	V_3O_7	861	167	39.4%	2B

2.3.7 Commonly-cited Materials for CLAS

When looking at established oxygen carrier systems, *i.e.* CuO/Cu_2O, Mn_2O_3/Mn_3O_4 and CoO/Co_3O_4, the respective combinations of thermodynamic properties fall well within case 1, *viz.* endothermic operation. However, the previous results did not allow for any heat recovery in the form of preheating of the recycled flue gas to the reducer or gaseous inflow to the oxy-fuel combustor. Both these can alter the boundary for autothermal operation, though it should be noted that the compressor and fans used in recycle systems would limit the degree of possible preheating.

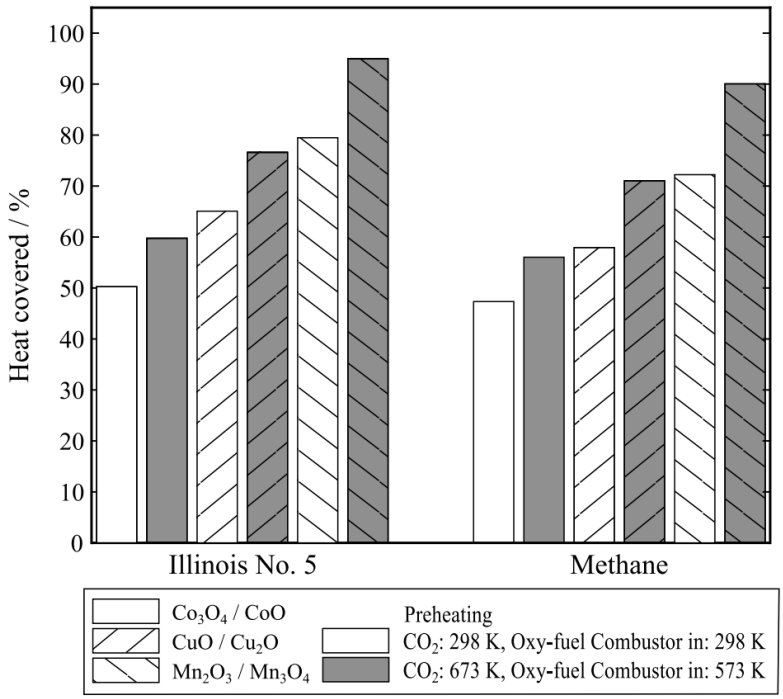

Figure 2-16: Amount of heat demand of the reducer covered by the combustion of Illinios No. 5 coal or methane for CuO/Cu_2O, Mn_2O_3/Mn_3O_4 and CoO/ Co_3O_4 and different preheating temperatures for CO_2 to the reducer and gas flow to the oxy-fuel combustor

Figure 2-16 shows that for CuO/Cu_2O, Mn_2O_3/Mn_3O_4 and CoO/Co_3O_4, the requirement for additional oxygen to combust more fuel to meet the heat demand or direct heat is significant, particularly if there is no preheating of the recycled flue gas or the incoming air. Among the fuels discussed here, the Illinois No. 5 coal achieves the least deficit in heat (Q_1 in Figure 2-4); using Illinois No. 5 coal with Mn_2O_3/Mn_3O_4 and preheating the CO_2 stream to the reducing reactor and gaseous inflow to the oxy-fuel combustor to 673 K and 573 K, respectively, allows for 95.6 % of the heat demand of

the reducing reactor to be met by the heat released in the oxy-fuel combustor. These temperatures were chosen in accordance with the maximum operation temperature of radial fans of 723 K for the scales required, and favourable temperatures for gas entering the oxy-fuel combustor of 473 to 673 K, respectively (Kather and Scheffknecht, 2009). The LHV per mole of oxygen of both Taldinskaya coal and Hambach lignite are lower than that of Illinois No. 5 coal and therefore neglected here.

Furthermore, the results provided in Figure 2-16 assume no doping with support material. In practice, however, these materials require the addition of support material owing to either their inability to reoxidise without support material, such as Mn_2O_3/Mn_3O_4 (Shulman *et al.*, 2009), or the desired mechanical strength and resistance against sintering (Chuang *et al.*, 2008; Gayán *et al.*, 2012; Shah, Moghtaderi and Wall, 2012; Arjmand *et al.*, 2013).

It should be noted that the combination of the equilibrium temperature, $T_{eq}\left(pO_{2,red} = 0.34\right)$, and enthalpy of reaction, $\Delta H^o_{r,298K}$, of the Cobalt oxide, as shown in Table 2-4, is outside of the region of potential oxygen carriers of Figure 2-6. The reason is the significant deviation in the entropy of reaction from the assumed entropy of reaction, $\Delta S^o_{r,298K}$, of 205.2 J/mol/K, *i.e.* outside the ± 25 % shown in Figure 2-6.

Table 2-4: Model input, T_{eq} and ΔH_r, and output for CuO/Cu_2O, Mn_2O_3/Mn_3O_4 and CoO/ Co_3O_4.

Oxygen carrier	$T_{eq}(pO_{2,red} = 0.34$ bar) K	$\Delta H^o_{r,298K}$ kJ/mol	$\Delta S^o_{r,298K}$ J/mol/K
CuO/Cu_2O(McBride, Zehe and Gordon, 2002)	1324	281.1	219.4
Mn_2O_3/Mn_3O_4(Barin and Knacke, 1974)	1179	195.0	158.3
Co_3O_4/CoO (Chase, 1998)	1185	393.6	293.4

2.3.8 Limitations of this Approach

There are a number of limitations to the methods used in this study. The assessment of oxygen carriers of which only the enthalpy of reaction is known, as is the case with oxygen carrier systems deduced from the Materials Project (Jain *et al.*, 2013), might give inaccurate results due to a significant deviation of the entropy of reaction from the assumed value, as described above.

Secondly, the integration of heat with the steam cycle takes a fairly basic approach, leading to case 2B when the operating temperature of the oxidizer falls below 845 K (assuming a ΔT_{min} of heat exchange of 10 K). For example, instead of lowering the maximum temperature of the steam cycle, an additional high-pressure turbine could be employed to operate at temperatures above the reducer if the oxygen carrier were able to release oxygen at low enough temperatures, as mentioned previously. Entirely different designs of the oxy-fuel power plant are conceivable as well, such as a combined cycle, provided the enthalpy of reaction of the oxygen carrier is small compared to the lower heating value per mole of oxygen of the fuel. Here, a gas turbine could generate electricity at temperatures above the operating temperature of the reducer and supply heat to the reducer. The oxidizer would then be the major source of heat for the steam cycle.

Another major limitation to the approach taken here to identify suitable oxygen carriers of CLAS is the neglect of the reaction kinetics. Candidate materials that seem suitable for CLAS might in fact react slowly, a typical example being the oxidation of Mn_3O_4 to Mn_2O_3 which was reported to be unachievable at 1173 K (Zafar *et al.*, 2007; Shulman *et al.*, 2009; Francis, Perkins and Weimer, 2010), even though it is thermodynamically feasible.

The study of heat integration performed in this paper suggests that employing a temperature swing between the reducer and oxidizer to separate air is not ideal. If, instead, pressure swing could be used, the temperature at which the transition between cases 2A and 2B occurs would decrease. Therefore, oxygen carriers releasing oxygen at temperatures above the maximum temperature of the steam cycle would fall into case 2A, *i.e.* autothermal operation with very little energy penalty.

2.4 Conclusion

A model was constructed which links the thermodynamic properties of an oxygen carrier to the steady state operation of an oxy-fuel power plant to estimate the viability of oxygen carriers for chemical looping air separation. This methodology allows the impact on the process of material properties, *i.e.* enthalpy ($\Delta H^o_{r,298\,K}$) and entropy ($\Delta S^o_{r,298\,K}$) of reaction, to be rationally assessed. The CLAS-oxy-fuel process can be characterised fully by a 2D map in which performance is a function of either $\Delta H^o_{r,298\,K}$ and $\Delta S^o_{r,298\,K}$ or, as presented here, as a function of the temperature at which the material is in equilibrium with 0.34 mol.% O_2 (T_{eq}), and the heat of reaction at T_{eq}, $\Delta H^o_r(T_{eq})$.

Superimposing (1) measured data from known materials, (2) prospective materials with properties drawn from the Materials Project database of theoretical DFT calculations, and (3) hypothetical materials allows the following conclusions to be drawn:

1. Lower values of T_{eq} of the oxygen carrier material widen the range of acceptable values of $\Delta H^o_r(T_{eq})$ for autothermal operation, *i.e.* when there is sufficient heat from the oxy-fuel combustion to support the metal oxide reduction.
2. The range of $\Delta H^o_r(T_{eq})$ and T_{eq} which allow for autothermal operation (as opposed to requiring additional heat from external sources) increases with the molar lower heating value per mole of oxygen required by the fuel, Θ, and the degree of preheating. More heat being available from the combustion of fuel allows for more endothermic reactions in the reducer, *i.e.* higher ΔH^o_r.
3. Using the investigated fuels, *viz.* Hambach lignite ($\Theta = 399$ kJ/mol O_2), Illinois No. 5 coal ($\theta = 417$ kJ/mol O_2) and Taldinskaya coal ($\Theta = 414$ kJ/mol O_2), commonly-cited oxygen carriers CuO/Cu_2O, CoO/Co_3O_4 and Mn_2O_3/Mn_3O_4 do not allow for autothermal operation; even without the addition of support materials α-Al_2O_3 or β-SiO_2. Here, both the gaseous inflow to the oxy-fuel combustor and the carbon dioxide stream to the reducer were preheated to 573 K and 673 K, respectively.
4. Operating the oxidizing reactor at temperatures below the maximum steam temperature of the unmodified steam cycle (here 835 K) leads to reduced net

efficiencies, and requires the steam cycle to be operated with a lower turbine inlet temperature.

5. Having identified suitable combinations of ΔH_r^o and T_{eq}, 34 oxygen carrier systems allowing for an autothermal operation of the CLAS-oxy-fuel power plant have been suggested, based on DFT calculations. Of these, five systems seem particularly promising, namely $BaFeO_3/Ba_2Fe_2O_5$, $LiBiO_3/LiBiO_2$, $MnPO_4/Mn_2P_2O_7$, $SrFeO_3/Sr_2Fe_2O_5$, and $Sr_2Cu_2O_5/SrCuO_2$.

These results show that a parameter sweep of thermodynamic properties using a macro-model of a power plant is an efficient approach to identify novel oxygen carrier candidates, when tied to density functional theory.

3 Experimental Methods

In this chapter, the method of synthesis and characterisation of the investigated oxygen carriers are described. Further, a description of the tubular micro-reactor is provided, which is used to investigate the kinetic parameters of the oxygen carrier materials and their stability over many redox cycles. A summary of the experiments carried out in this work is given in Table 3-1.

Table 3-1: Summary of experiments

Apparatus	Purpose	Procedure	Conditions	
			pO_2 bar	Temperatures K
TGA	Determining (pO_2, δ, T) at equilibrium conditions	Temperature treatment with isothermal steps every 25 K	10^{-5}, 0.015, 0.075 0.15, 0.21	823-1323
Packed bed	Evaluating kinetics	Redox cycling in air and N_2, each step for 90 s	10^{-5}, 0.21	773-898
Packed bed	Stability over 1000 cycles	Redox cycling in air and N_2, each step for 60 s	10^{-5}, 0.21	873 ($SrFeO_{3-\delta}$) 898 ($SrMn_{0.1}Fe_{0.9}O_{3-\delta}$)

3.1 Preparation and Source of Oxygen Carrier Materials

The $SrFeO_{3-\delta}$ and $SrMn_{0.1}Fe_{0.9}O_{3-\delta}$ oxygen carriers were prepared following the same procedure: In a planetary ball mill (MTI, model MSK-SFM-1), Fe_2O_3 and $SrCO_3$ powders were mixed in a molar ratio of 1:2 to produce $SrFeO_{3-\delta}$ and, for $SrMn_{0.1}Fe_{0.9}O_{3-\delta}$, Fe_2O_3 powder was mixed with $SrCO_3$ and Mn_2O_3 in molar ratios of 0.45:1:0.05 for 3 h at 25 Hz (all powders were obtained from Sigma Aldrich at purities of at least 98 wt%). Ethanol (99.8 %, Fischer Scientific) was added to the powders to enhance the mixing in the ball mill. In a second step, the mixtures were dried for 24 h at 323 K in an electric oven. The sieve fraction consisting of particles with a diameter of 180-355

μm were then calcined in 4 stages to remove the carbon as CO_2; each stage consisted of calcination at 1273 K for 3 h in a muffle furnace and a subsequent cooling to room temperature. Both the drying and the calcination took place in static air.

The $SrCo_{0.4}Fe_{0.6}O_{3-\delta}$ used in this study was prepared by mixing 1 molal solutions of cobalt (II) nitrate, iron (III) nitrate and strontium nitrate. The mixture was then dried overnight and, subsequently, calcined at 773 K for three hours (using a heating ramp rate of 2 K min^{-1}) and at 1473 K for 6 hours (using a heating ramp rate of 5 K min^{-1}). All nitrates were purchased from Sigma Aldrich.

3.2 Characterisation of the Solids

3.2.1 X-ray powder diffraction

The purity of the phases of the different oxygen carriers was confirmed using X-ray powder diffraction (XRD) and Rietveld refinement. The XRD analysis of the manganese-doped and pure $SrFeO_{3-\delta}$ was carried out at the University of Cambridge. $SrCo_{0.4}Fe_{0.6}O_{3-\delta}$ was investigated *via* XRD at ETH Zurich by Felix Donat. The composition of the materials was found to be dominated by the cubic perovskite phase, as shown in Table 3-2. The starting structures of phases considered were Starting structures of phases used were $Sr_3Fe_2O_7$ (ICSD 74422), $SrFe_{12}O_{19}$ (ICSD 69022), $SrFeO_3$ (ICSD 91062), $SrFeO_{2.5}$ (ICSD 91065), CoO_2 (ICSD 88721), Co_3O_4 (ICSD 36256), Mn_2O_3 (ICSD 9091) and Mn_3O_4 (ICSD 68174). It should be noted that the freshly prepared manganese-doped $SrFeO_{3-\delta}$ contained Mn_3O_4 which indicates that the manganese was not entirely incorporated into the perovskite structure.

Table 3-2: Results from Rietveld refinement of the collected XRD spectra. The precision in the last digit is given in the parentheses, and corresponds to the estimated standard deviations determined by the regression.

Oxygen carrier	$Sr_3Fe_2O_7$	$SrFeO_3$	Mn_3O_4
$SrFeO_{3-\delta}$	3.0 (5)	96.9 (5)	-
$SrMn_{0.1}Fe_{0.9}O_{3-\delta}$	2.8 (2)	93.0 (4)	4.1 (3)
$SrCo_{0.4}Fe_{0.6}O_{3-\delta}$	16.7 (3)	83.3 (4)	-

3.2.2 Thermogravimetric analysis

The oxygen non-stoichiometry, δ, was determined *via* thermogravimetric analysis. The system used to conduct tests in the thermogravimetric analyser (TGA, Mettler Toledo TGA/DSC 1 STARe system) is shown in Figure 3-1. The two mass flow controllers (Bronkhorst EL-FLOW series) allow for mixing air with nitrogen to achieve different oxygen partial pressures. The mass flows to the three inlets to the TGA were controlled *via* rotameters to supply 50 ml/min (293 K, 1 bar) to the purge, protective and reaction gas lines. An insignificant excess flow was set at MFC2 to ensure all rotameters can operate at their desired set point. This excess flow (<20 ml/min) was vented. Inside the TGA, the sample material is placed in a crucible which rests on a microbalance accurate to 1 µg, allowing for precise measurements of any loss or gain in mass of the sample. The reactive gas is injected *via* a capillary at distance of 9 mm upstream of the centre of the crucible. The purpose of the purge gas and the protective gas is to protect the walls of the furnace chamber when highly reactive gases are used. Here, to eliminate issues with mixing in the TGA, the TGA experiments were run with identical purge, protective and reaction gases, *i.e.* all gas inlets of the TGA device were connected to the same gas mixture, as shown in Figure 3-1.

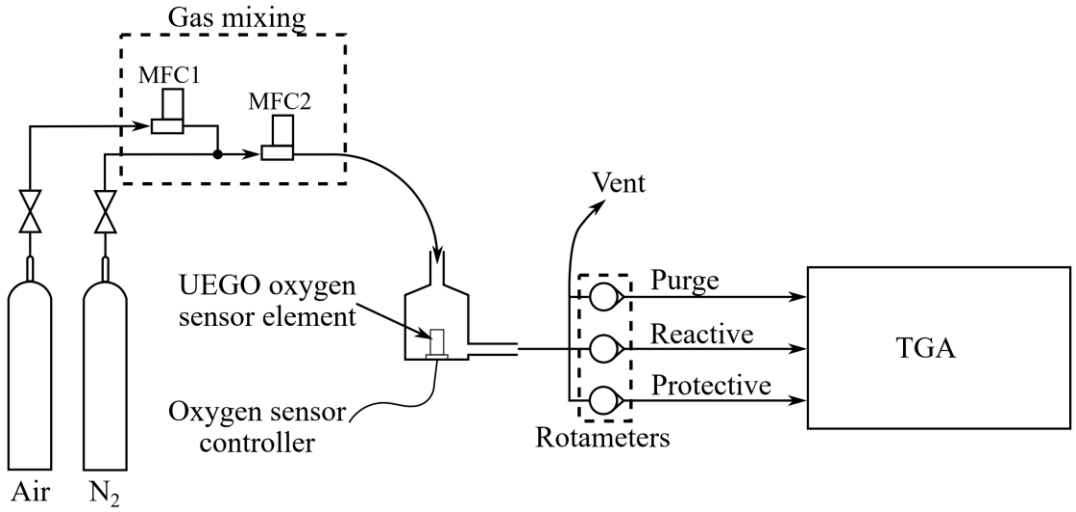

Figure 3-1: Schematic of the TGA set up

The oxygen sensor is used to verify that the desired partial pressure of oxygen in the gaseous flow is reached. The oxygen sensor used in the experiments is the Bosch 4.9 LSU wideband UEGO, which is connected to a control unit made by Cambustion Limited. The wideband UEGO sensor indirectly measures the oxygen partial pressure of the sample gas *via* the current needed to maintain a constant partial pressure of oxygen in a measurement cavity, $pO_{2,cav}$, that is separated from the sample gas by a diffusion barrier built from layers of yttria-stabilised zirconia (YSZ) (Harris and Collings, 2015). As oxygen in the form of O^{2-} ions diffuse from the sample gas to the measurement cavity, $pO_{2,cav}$ changes and with it the Nernst potential, E_N, to a reference cavity filled with air according to

$$E_N = \frac{RT}{4\,F} ln\left(\frac{pO_{2,ref}}{pO_{2,cav}}\right) \tag{3-1}$$

where F is Faraday's constant. If the Nernst potential is lower than the desired reference voltage, *i.e.* $pO_{2,ref} < pO_{2,cav}$, then a feedback control system increases the current to a pump cell to increase the rate at which O^{2-} ions are pumped out of the measurement cavity (Harris and Collings, 2015). Since the gas diffusion across the diffusion barrier is proportional to the gradient in the oxygen concentration between the sample gas and measurement cavity (Fick's first law) and the applied current to the pump cell is proportional to the measured voltage (Ohm's law), the measured voltage is also proportional to the partial pressure of oxygen in the sample gas. Further, the sensor output, *i.e.* measured voltage, is linear for $pO_2 < 0.21$ bar so that a one-point calibration can be performed as the entire response curve is known as long as one point on it is identified. The output signal of the oxygen sensor is converted to the mole fraction of oxygen in the outflow of the bed, $x_{O_2,out}$, using the following formula which was provided by Cambustion Limited

$$x_{O_2,out} = 1 - \left(1 - x_{O_2,amb}\right)^{\frac{V_s - V_0}{V_{amb} - V_0}} \tag{3-2}$$

where $x_{O_2,amb}$ is the mol fraction of oxygen of the ambient air, V_s, V_0 and V_{amb} the voltages measured for the sample, for nitrogen and ambient air, respectively. It is therefore necessary to take a measurement in air and nitrogen to convert the measured voltage to the mole fraction of oxygen. It should be noted, that in this case ambient air

is defined as dry air provided by BOC. The sensor voltage was calibrated with air before each run.

Figure 3-2 shows the change in mass of $SrFeO_{3-\delta}$ and $SrMn_{0.1}Fe_{0.9}O_{3-\delta}$ at a heating rate of 10 K min^{-1} over time, from which the initial oxygen stoichiometry, $3-\delta_0$, of the perovskites was determined; subject to a temperature-controlled program in the thermogravimetric analyser, the samples were heated in 5 % H_2 in nitrogen, supplied by BOC in purity of > 99.999 % (5N), and the change in mass was recorded. A mostly gradual release of oxygen is observed as long as the cubic phase of the perovskite is present. At the point at which the gradient of the change in mass changes abruptly it is assumed that the reduction to the brownmillerite phase, *i.e.* δ of 0.5, has been completed. Noting the loss of mass until the material has fully reduced to the brownmillerite phase, δ_0 can be calculated as the material is expected to only lose mass due to the release of oxygen (Marek *et al.*, 2018). One way to find points of abrupt changes in the gradient is to use MATLAB's "findchangepts" function. Here, the number of expected change points was set to two, one for the start of the thermal decomposition and one for the point at which the brownmillerite phase is reached. δ_0 is then calculated from

$$\delta_0 = 2.5 + 2\frac{m_0 - m_{bm}}{m_{bm}}\frac{M_{bm}}{M_{O_2}} \tag{3-3}$$

where δ_0 and m_0 are the oxygen non-stoichiometry and the mass of the initial sample at the last temperature before the material starts the release of oxygen. This was done to minimise the effect of buoyancy where the recorded mass in a TGA increases as the temperature rises. For $SrFeO_{3-\delta}$ and $SrMn_{0.1}Fe_{0.9}O_{3-\delta}$ this temperature was 623 K and 603 K, respectively. m_{bm} denotes the mass of the sample when the brownmillerite phase has formed, *i.e.* at the inflection point. M_{bm} and M_{O_2} are the molecular masses of the brownmillerite and oxygen, respectively. Considering that the number of moles of oxygen released, n_{O_2}, can be expressed as $(m_0 - m_{bm})\, M_{O_2}^{-1}$ and the number of moles of brownmillerite is given by $n_{bm} = m_{bm}M_{bm}^{-1}$, then equation (3-3) can be written as

$$\delta_0 = 2.5 + 2\frac{n_{O_2}}{n_{bm}} \tag{3-4}$$

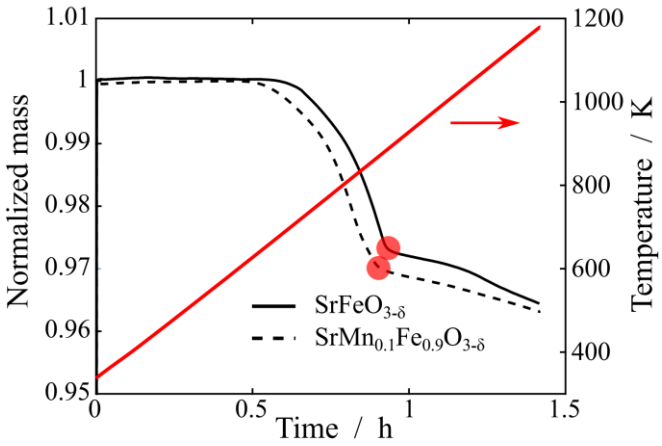

Figure 3-2: Change in mass of $SrFeO_{3-\delta}$ and $SrMn_{0.1}Fe_{0.9}O_{3-\delta}$ when heated in a mixture of 5 % hydrogen in nitrogen at a heating rate of 10 K min^{-1} as recorded *via* thermogravimetric analysis. The red dots indicate the inflection points, i.e. $\delta = 0.5$.

Once the initial oxygen non-stoichiometry, δ_0, of the fresh sample was determined, further TGA experiments were performed to characterise the equilibrium partial pressure of oxygen curves of the materials. For this, the mass of the oxygen carriers was measured under different atmospheres, specifically nitrogen, air ($pO_2 \approx 0.21$ bar) and mixtures thereof ($pO_2 \approx 0.015$, 0.075 and 0.15 bar). In each experiment, the temperature was increased from 823 K to 1323 K, at intervals of at least 50 K and the measured mass allowed to settle for up to an hour at each temperature; at these temperatures, a nearly constant mass was achieved within minutes for all materials.

The mass at the end of each temperature step was assumed to be equilibrium mass of the oxygen carrier with the partial pressure of oxygen the material was exposed to. Using

$$\delta(pO_2, T) = 2.5 + 2\frac{m(pO_2, T) - m_{bm}}{m_{bm}}\frac{M_{bm}}{M_{O_2}} \tag{3-5}$$

the oxygen non-stoichiometry, δ, is calculated for every temperature interval and at the different oxygen partial pressures. The models used to then fit an isothermal equilibrium partial pressure curve to $pO_2(\delta)$ are described in chapter 4. From these isotherms, equilibrium partial pressure curves $pO_2(T)$ can be constructed.

It should be noted, that defining an end point in time does not necessarily ensure that equilibrium is reached. In particular, the change in mass achieved under the nitrogen

atmosphere should be treated with caution for several reasons: 1. from a thermodynamic point of view, perovskites would release oxygen until their most reduced, stable phase is reached if pO_2 = 0 bar is assumed, *e.g.* $SrFeO_{3-\delta}$ reduces to $SrFeO_{2.47}$ under $pO_2 \approx 3 \cdot 10^{-7}$ bar at 1173 K and above (Yoo *et al.*, 2017); 2. the actual pO_2 at the sample might deviate from the assumed value when a second gas is used as purge gas, or there may be marginal leakages of air into the system or some contamination.

Measures were taken to ensure nitrogen is treated correctly: 1. The molar fraction of oxygen in the supplied nitrogen has been determined by calibrating it using CuO, for which the author thanks Wenting Hu (of Newcastle University). For this, Cu_2O was heated in nitrogen in the TGA. The crucible containing the Cu_2O was covered with a lid that is punctured at its centre to limit the reaction by mass transfer. The oxygen concentration in the nitrogen gas can then be calculated from the Stefan-Maxwell diffusion as described in Hu *et al.* (2014). The oxygen concentration in the compressed nitrogen supplied by BOC was found to be 10 ppm of oxygen in N_2, as specified by BOC; no significant leakage of air into the nitrogen line was found and, therefore, in the following calculations it is assumed that the nitrogen contains 10 ppm of oxygen. 2. The reactive, purge and protective gas inlets are supplied with the same gas mixture to ensure a homogeneous pO_2 at the sample, as described above.

There are several factors that influence the TGA measurements which can lead to errors:

1. The gas mixtures of nitrogen and dry air are calibrated using the UEGO sensor which measures the partial pressure of oxygen. On the dates the experiments reported in this work were conducted, the daily variation in the atmospheric pressures was insignificant, as shown in Table 3-3.
2. The sensors of the TGA introduce errors owed to their accuracy; the accuracy of the scale is given as 1 µg, as mentioned earlier, and the thermocouple is accurate to within 1 K. In the TGA experiments, at least 20 mg of material were used making these errors insignificant considering the mass loss of roughly 4.2 % when reducing $SrFeO_{3-\delta}$ to $SrFeO_{2.5}$.

3. Potential humidity in the compressed air, supplied by BOC at a purity of 99.99 %, introduces oxygen which may oxidise some metals at high temperatures. In this work, however, when air is used the partial pressure of oxygen is at least 0.015 bar so that any oxygen introduced by the humidity in the air has only insignificant effects on the measurements.

Table 3-3: Daily variation in the atmospheric pressure on test dates, including the 95 % confidence interval (Hopper, 2019)

Date	Pressure mbar
20171130	1010.3±0.3
20171212	1004.7±1.0
20180117	1000.0±1.4
20180119	1006.3±0.3
20180531	1016.6±0.2
20180601	1018.7±0.2

3.3 Kinetic measurements

For the experimental part of this study, a tubular micro reactor was used to (1) determine the reaction kinetics of the potential oxygen carriers and (2) analyse the stability over many redox cycles.

3.3.1 Apparatus

Typically, flow reactors are the reactor type of choice when investigating reaction kinetics of heterogeneous reactions (Davis and Davis, 2003; Froment, Bischoff and De Wilde, 2011). In the reactor, it is desirable to achieve isothermicity and avoid radial temperature and concentration gradients, which limits the diameter of the reactor. Simultaneously, the velocity should be high relative to the kinematic viscosity of the fluid and the ratio of the diameters of the particles and the reactor should exceed ten (to avoid near-wall flow velocity maxima due to increased voidage) to approach a uniform velocity profile, *i.e.* plug flow (Froment, Bischoff and De Wilde, 2011). The two types of plug flow reactors (PFRs) are the integral bed reactor and the differential bed reactor (Levenspiel, 1999; Davis and Davis, 2003; Froment, Bischoff and De Wilde, 2011). A discussion about whether the assumption of a differential bed reactor holds or not is presented in section 0.

The reactor system is shown in Figure 3-3 and the inflow to the micro reactor is switched between air and nitrogen using two low internal volume solenoid flipper valves (Bürkert Type 6124 – 2/2 way) to produce a rapid step change. All the components of the reactor system are designed such that they minimise the volume of the system. The mass flow is controlled by an orifice (0.008” ID) that is inserted into the outlet of the valve manifold which was calibrated using a bubble meter (model: Gilian Gilibrator 2). A pressure sensor (Honeywell ABPMANN004BGAA5) is glued into a bore hole drilled into the Swagelok® adapter, which connects the valve manifold and the ⅛” tube leading to the reactor, downstream of the valve system. The section of the reactor that contains the solids is made of a 48 mm long, stainless steel tube with an outer diameter of ¼”. The dimensions of the different sections of the system from the orifice to the oxygen sensor cavity are presented in Table 3-4. The reactor tube is heated with an ultra-high temperature heating tape (Omegalux STH series) able to

resist temperatures of 973 K reversibly. The temperature is measured about 5 mm downstream of the solid bed. The oxygen sensor used was the Bosch 4.9 LSU wide-band UEGO, as described in section 3.2.2.

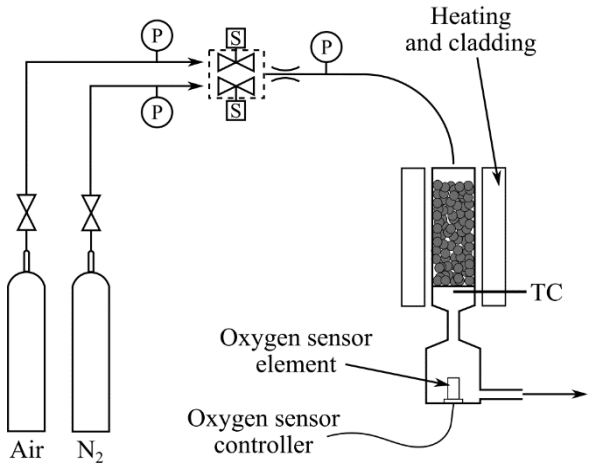

Figure 3-3: Schematic of the micro reactor system. The oxygen sensor element is an UEGO sensor. P and S denote pressure transducers and solenoid flipper valves, respectively. TC is the thermocouple.

Table 3-4: Dimensions of the differential bed reactor system from the orifice to the oxygen sensor.

Description	Length mm	Inner Diameter mm	Volume ml
¼" to ⅛" adapter	15.2	4.760	0.270
⅛" tube section to reactor	60.0	1.588	0.119
¼" reactor tube to mesh/distributor	48.0	4.760	0.854
⅛" tube section to the sensor	70.0	1.588	0.139
sum	193.2	12.695	1.382

By using ⅛" tubing except for the section containing the solids, as described previously, and minimising the volume of the cavity in which the oxygen sensor is inserted, the response time of the system (10 % to 90 % of the signal), $\tau_{10\rightarrow90}$, was reduced to 231 ms and 238 ms for nitrogen to air and air to nitrogen, respectively, when a mass flow of roughly 750 sccm is applied. Here, nitrogen is assumed to contain 10 ppm of oxygen, as stated by the supplier, BOC. The output of the oxygen sensor and the pressure transducer, which records the pressure upstream of the bed, is plotted in Figure 3-9 for a typical test for reaction kinetics. Here, the oxygen carrier was $SrFeO_{3-\delta}$ and the conditions are ambient leading to sharp steps in the signal of the oxygen sensor as any chemical reaction or sorption process is negligible.

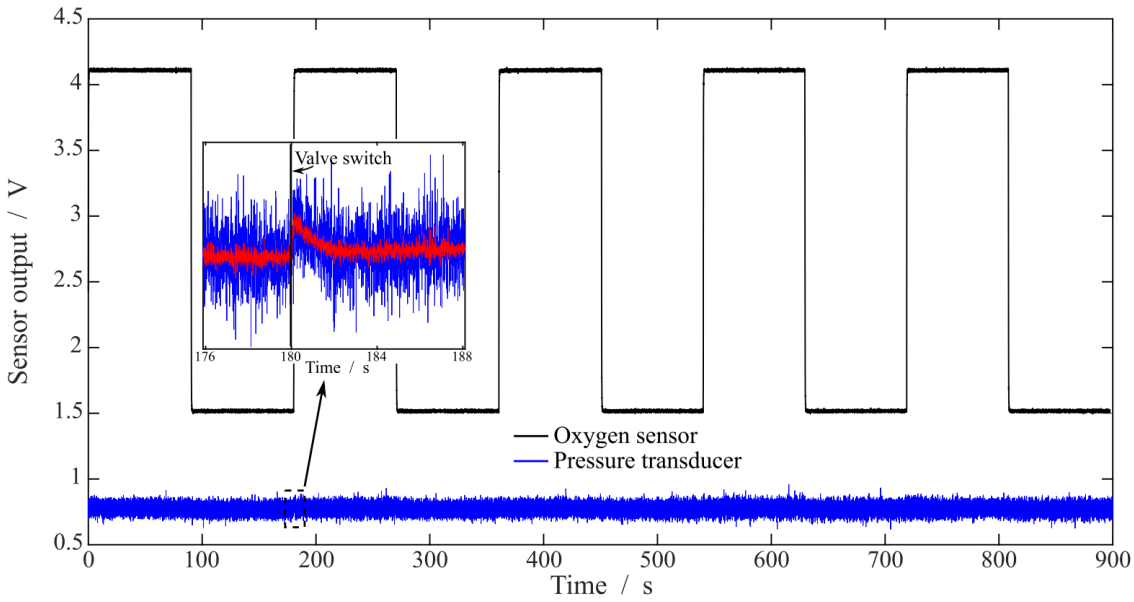

Figure 3-4: Data recorded by the Bosch UEGO oxygen sensor and the pressure transducer for $SrFeO_{3-\delta}$ at 293 K over 900 s with gas switches every 90 s. The red line in the magnified section of the signal of the pressure transducer represents the filtered signal.

The time delay of the reactor system, *i.e.* the components downstream of the valve system and the oxygen sensor, was determined experimentally by evaluating the time between the valve switch and the change in the output signal of the oxygen sensor, as shown in Figure 3-5. Upon switching the valves, a marginal, temporary disturbance in the pressure signal is observed, as depicted in the magnified section in Figure 3-4. The MATLAB function "findchangepts" (which is based on the work of Lavielle (2005) and Killick et al. (2012)) is employed to identify the exact position of these marginal changes in the pressure signal. The time at which the breakthrough at the oxygen sensor is observed following the valve switch is determined *via* the same function. Table 3-5 lists the time delays of the system using 1.1 g Al_2O_3 as bed material and a flow rate of 750 sccm at different temperatures. The valve is switched approximately 20 ms after being triggered by the gas switching electronics every 90 s. The time it then takes to observe a change in the signal of the oxygen sensor, *i.e.* the breakthrough, is dependent on temperature as the flow passes through the heated section of the reactor and the volumetric flow rate increases.

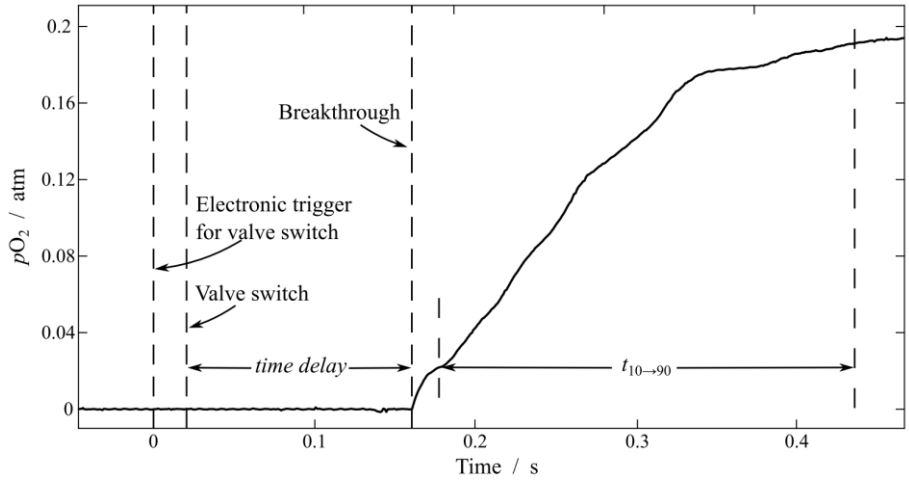

Figure 3-5: Raw data of the oxygen partial pressure after a gas switch from nitrogen to air is triggered at t = 0 s for a bed of 1 g of solids with a particle size between 255 and 350 µm at 293 K. The time delay describes the time it takes until the breakthrough occurs at the oxygen sensor after the valve switch has been measured. $t_{10\rightarrow90}$ denotes the duration for the signal to reach 90 % of its maximum value from 10 %.

Table 3-5: Average delay from triggering a gas switch every 90 s until the valve switch and the breakthrough are recorded at the pressure transducer and the oxygen sensor, respectively, for 1.1g Al_2O_3 at different temperatures. The time delay is the mean difference in the individual valve switch and breakthrough time of the nine gas switches and σ is the standard deviation of the time delay.

Temperature K	Average valve switch ms	Average breakthrough ms	Time delay ms	σ
298	22.1	141.7	119.6	8.16
373	21.9	130.3	108.4	8.02
523	18.6	119.0	100.4	7.07
723	21.0	110.0	89.0	9.12
898	22.2	106.3	84.1	9.62

The first five seconds of the pO_2 signal of the oxygen sensor are plotted for a bed of Al_2O_3 for a gas switch from air to nitrogen and vice versa in Figure 3-6a and b, respectively. The results suggest that the influence of temperature on the response time was insignificant; all measured response times, $\tau_{10\rightarrow90}$, were within 25 ms and the fastest average response time was measured at 373 K, not at 898 K, the highest temperature tested.

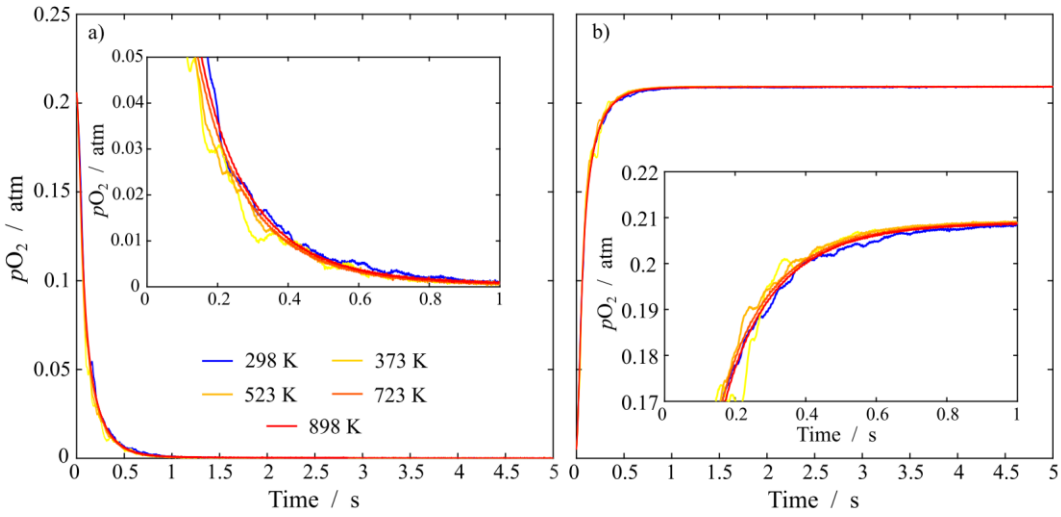

Figure 3-6: Oxygen partial pressure over time for a gas switch from a) air to nitrogen and b) nitrogen to air through a bed of 1.1 g of Al_2O_3 with a particle size between 255 and 350 µm at different temperatures.

As the signal is volatile at low temperatures, it was decided to construct a mean curve for the data recorded at room temperature. For this, the time delay and breakthrough time are used to align the curves of the reduction and oxidation intervals as will be described later on when dealing with non-inert materials; at this point, however, inert Al_2O_3 is discussed, and therefore the curves are aligned only with respect to the breakthrough. Once aligned, a mean (or typical) reduction and oxidation curve is constructed by averaging over each of the reduction and oxidation intervals. Such a mean curve is shown in Figure 3-7 including the minimum and maximum values for every gas switch from air to nitrogen in the 900 s long test using Al_2O_3 at 298 K. Once the mean curves are computed for both oxidation and reduction, the molar fraction of oxygen in the outflow of the bed, $x_{O_2,out}$, is calculated using equation (3-2) and converted to the partial pressure of oxygen, pO_2, by multiplication with 1 bar, the approximate pressure inside the sensor chamber.

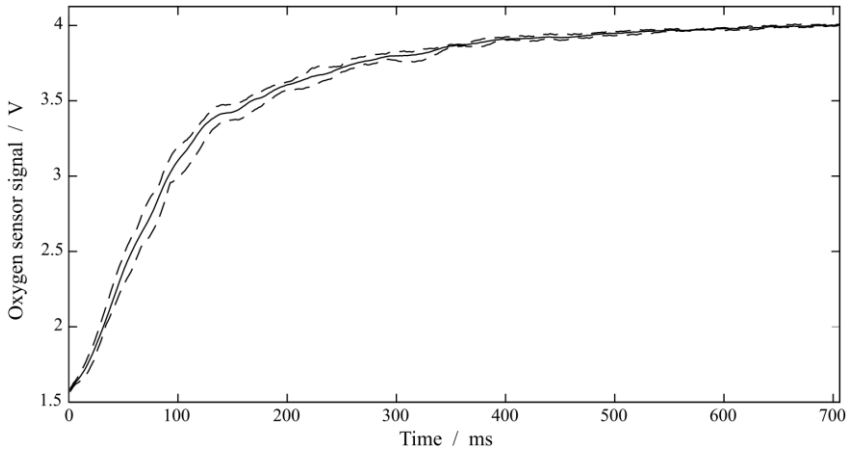

Figure 3-7: Mean oxidation curve, *i.e.* gas switch from nitrogen to air, for Al_2O_3 at 298 K. The dashed lines indicate the minimum and maximum values when overlaying the curves of each gas switch nitrogen to air; t = 0 corresponds to the measured breakthrough.

After the mean pO_2 curves are obtained, a constrained, cubic spline was fitted through 10 points to enforce monotonicity of the curves as the calculated means may not be strictly monotonic, a property that would be expected when subjecting oxygen carriers to partial pressure swings. The spline was then shifted by linear interpolation to ensure that the starting points of the curves for different cycles are identical; here, the interpolation between two data points that are merely 1 ms apart was seen as a valid approximation. At elevated temperatures, the raw sensor signal is also shifted using linear interpolation to align the starting points of the different cycles at high temperature and the starting point of the mean blank curve, as sketched in Figure 3-8. In this work, the blank experiment, carrier out at room temperature, was not conducted with inert Al_2O_3 but with the active bed material which is assumed to be inert at room temperature, since it is difficult to pack an inert bed with exactly the same flow properties as the active bed.

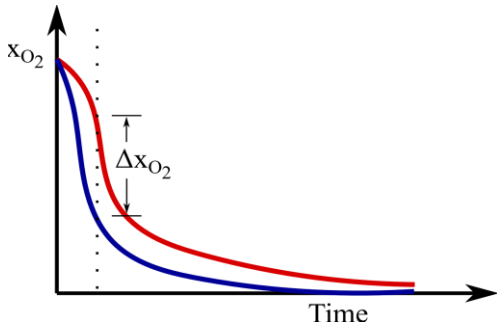

Figure 3-8: Sketch of curves of mol fraction of oxygen at the oxygen sensor; blue at ambient conditions, red at elevated temperature.

To obtain rates of reaction the ideal experiment would involve a sudden step change in input concentration to the bed. If the bed is purely differential and the time taken to switch the input gases is much shorter than the time of experimental interest, then rates can be found by simply taking the difference between the input and measured concentration. In practice, a blank experiment which characterises the change in concentration expected when there is no reaction, must be subtracted from the experimental results to obtain rates of oxygen consumption or production. In addition, the experimentally measured curves during the reaction must be aligned correctly with respect to the blank; if there is a breakthrough time, the appearance or disappearance of oxygen cannot be used to align the curves.

When considering the reduction reaction, upon switching the inlet gas from air to N_2, there is a brief period during which the concentration front moves through the bed, replacing the air with N_2; the gas residence time of the bed is ~5 ms at 750 sccm. From this time onwards the material reacts to produce oxygen and the rate of oxygen production, *i.e.* that leaving the bed, is equal to

$$\dot{n}_{O_2} = \left(y - y^{blank}\right) \dot{n}_{N_2} \tag{3-6}$$

where $\dot{n}_{N_2}$ is the molar flow rate of nitrogen and

$$y = \frac{x_{O_2,out}(t)}{1 - x_{O_2,out}(t)} \tag{3-7}$$

The rate at which oxygen is released from the material at time *t*, $r_{O_2,prod}$, is then given by

$$r_{O_2,prod} = \frac{\Delta x_{O_2,out}}{\left(1 - x_{O_2,out}\right)\left(1 - x_{O_2,out}^{blank}\right)} \quad \dot{n}_{N_2} \tag{3-8}$$

3.3.2 Differential vs. Integral Analysis

In a fixed bed of one of the synthesized perovskites, *e.g.* $SrFeO_{3-\delta}$, the oxygen carrier takes up and releases oxygen according the equilibrium reaction

$$ABO_{3-\delta} + \frac{\delta}{2} O_{2(g)} \rightleftarrows ABO_3 \tag{3-9}$$

where A and B denote the A-sites and B-sites, which are typically occupied by alkali, alkaline-earth, or rare-earth ions and transition metals, respectively; here, A is strontium and B is iron. The rate at which oxygenis released from perovskite-type materials, r_{O_2}, should depend on the reaction kinetic parameters, the driving force and the stoichiometry, as discussed in section 1.2.3.1. Thus, here, the rate is assumed to be of the form:

$$r_{O_2} = k\left(pO_2 - pO_{2,eq}(T,\delta)\right) f(\delta) \tag{3-10}$$

where $pO_2 - pO_{2,eq}$, is the driving force, $f(\delta)$ is a function representing the dependence of the rate on the oxygen non-stoichiometry, δ, being a proxy for conversion and the rate constant k is assumed to follow $k = Ae^{-\frac{E}{RT}}$. In the analysis that follows, rates are expressed per unit volume of packed bed, giving A units of $mol\ s^{-1}Pa^{-1}m^{-3}$.

The bed, as shown in Figure 3-9, is described by

$$C\frac{\partial x_{O_2}}{\partial t}\epsilon = -C\left(\frac{\partial v x_{O_2}}{\partial z}\right) + CD_{ax}\left(\frac{\partial^2 x_{O2}}{\partial z^2}\right) - k\left(pO_2 - pO_{2,eq}(\delta)\right) \tag{3-11}$$

$$\rho_{OC}(1-\epsilon)\frac{\partial(3-\delta)}{\partial t} = 2k\left(pO_2 - pO_{2,eq}(\delta)\right) \tag{3-12}$$

where z is the distance along the bed, t is time, ϵ is the voidage, ρ_{OC} is the apparent molar density of the oxygen carrier, D_{ax} is the axial dispersion coefficient, v is the superficial velocity (mole average), C is the total molar gas concentration. Here, the rate constant k incorporates $f(\delta)$.

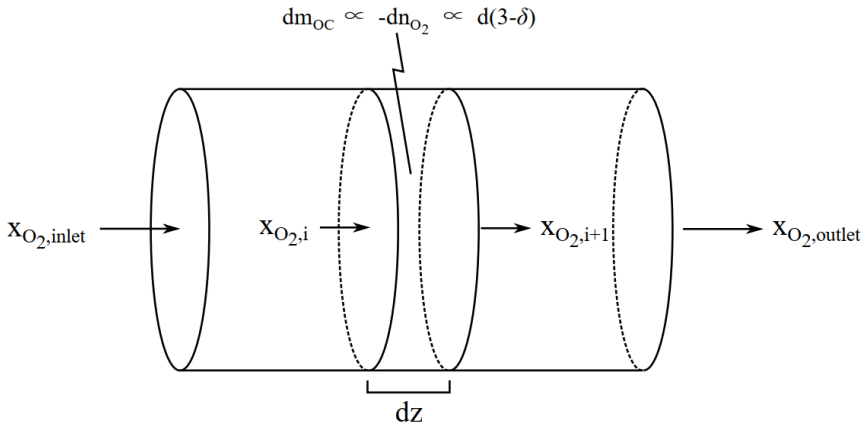

Figure 3-9: Element of a tubular packed bed reactor. x_{O_2} is the molar fraction of oxygen in the gas phase, dm_{OC} is the change in the mass of the oxygen carrier, dn_{O_2} denotes the molar amount of oxygen released into the gas phase and dz is a finite element along the bed.

Equations (3-11) and (3-12) can be expressed in dimensionless terms to examine the criteria to operate the reactor with an differential bed. Introducing

$$z' = \frac{z}{L} \tag{3-13}$$

$$v' = \frac{v}{v_{in}} \tag{3-14}$$

$$t' = \frac{t}{\tau_c} \tag{3-15}$$

$$\tau_g = \frac{L\epsilon}{v_{in}} \tag{3-16}$$

where L is the length of the solid bed, v_{in} is the superficial velocity at the inlet to the bed, τ_g is the gas residence time, and τ_c is the time constant for the conversion of the oxygen carrier, defined by

$$\tau_c = \frac{\rho_{OC}(1-\epsilon)}{2kCRT} \tag{3-17}$$

equations (3-11) and (3-12), in dimensionless terms, become

$$\frac{\tau_g}{\tau_c}\frac{\partial x_{O_2}}{\partial t'} = -\left(\frac{\partial v' x_{O_2}}{\partial z'}\right) + \frac{1}{Pe_r}\left(\frac{\partial^2 x_{O2}}{\partial z^2}\right) - \frac{kRTL}{v_{in}}\left(x_{O_2} - x_{O_2,eq}(\delta)\right) \tag{3-18}$$

$$\frac{\partial(3-\delta)}{\partial t'} = \left(x_{O_2} - x_{O_2,eq}(\delta)\right) \tag{3-19}$$

The reactor Péclet number, ,also known as Bodenstein number (Fogler, 2011), is defined as

$$Pe_r = \frac{v\,L}{D_{ax}} = Pe_f\,\frac{L}{d_p} \tag{3-20}$$

where Pe_f is the Péclet number which, for gaseous flows through packed beds, can be approximated by (Gunn, 1987)

$$\frac{1}{Pe_f} = \frac{1}{\tau_p}\frac{\epsilon}{Sc\,Re} + \frac{1}{2} \tag{3-21}$$

Assuming a tortuosity factor for spherical particles, τ_p, of $\sqrt{2}$, a bed voidage, ϵ, of 0.4 and Schmidt number for gases of ~1 (Levenspiel, 1999), Pe_r is equal to 239 and 236 for temperatures 723 and 898 K, respectively. At such high reactor Péclet numbers, it is valid to neglect axial dispersion (Fogler, 2016).

At a gas inflow of 750 sccm and temperatures between 798 K and 898 K, τ_g is around 5 ms and the time constant for the full conversion of the oxygen carrier, τ_c, approximately 10 s, as shown in chapter 5. Therefore, the transient term in equation (3-18) is now small and the gas mass balance equation can be solved as if it is pseudo steady-state, *i.e.*

$$\frac{\partial v'\,x_{O_2}}{\partial z'} \sim -\frac{kRTL}{v_{in}}\left(x_{O_2} - x_{O_2,eq}(\delta)\right) \tag{3-22}$$

From equation (3-22), the following three cases arise:

1. $\frac{kRTL}{v_{in}} \ll 1$: From this, it follows that x_{O_2} is approximately constant across the bed, *i.e.* $\frac{\partial v'\;x_{O_2}}{\partial z'} \ll 1$, and, therefore, δ of the oxygen carrier is approximately constant across the bed, too.
2. $\frac{kRTL}{v_{in}} \sim 1$: In this case, changes of x_{O_2} across the bed are not negligible, but not to the effect that the oxygen carrier is at equilibrium at $z = L$.

3. $\frac{kRTL}{v_{in}} \gg 1$: The convective mass transport is low compared to $kRTL$ and a distinctive profile of δ forms across the bed; in other words, a front w.r.t. δ. The length scale of this front is $\frac{v_{in}}{kRT}$.

3.3.2.1 Equilibrium limit

For case 3, two subcases exist: First, in the limiting case that $\frac{kRTL}{v_{in}} \to \infty$, *i.e.* $kRTL$ is so large compared to the longitudinal convection that the gradient of δ not only across the solid bed but across each infinitesimally small element shown in Figure 3-9 would approach infinity if the driving force, $x_{O_2} - x_{O_2,eq}(\delta)$, is significant. To keep $\frac{\partial v' \; x_{O_2}}{\partial z'}$ finite, $x_{O_2} \to x_{O_2,eq}(\delta)$ at each point along the bed as $\frac{kRTL}{v_{in}} \to \infty$. The reaction is therefore equilibrium limited and x_{O_2} can be linked to the oxygen stoichiometry of the oxygen material *via* the equilibrium partial pressure of oxygen curve of the material. In this equilibrium limited case, for each element *i* shown in Figure 3-9, equations (3-11) and (3-12) can be written as

$$\frac{\partial\left(C\epsilon x_{O_2,eq}\right)}{\partial t} = -\frac{\partial}{\partial z}\left(Cvx_{O_2,eq} - CD_{ax}\frac{\partial x_{O_2,eq}}{\partial z}\right) - \frac{\rho_{OC}(1-\epsilon)}{2}\frac{\partial(3-\delta)}{\partial t} \quad (3\text{-}23)$$

when accounting for changes in the molar flow rate due to oxygen production. Neglecting axial diffusion and rearranging the terms, equation (3-23) becomes

$$\frac{\partial\left(C\epsilon x_{O_2,eq}\right)}{\partial t} + \frac{\partial\left(Cvx_{O_2,eq}\right)}{\partial z} = -\frac{\rho_{OC}(1-\epsilon)}{2}\frac{\partial(3-\delta)}{\partial t} \quad (3\text{-}24)$$

Applying the chain rule then gives

$$C\epsilon\frac{\partial x_{O_2,eq}}{\partial t} + x_{O_2,eq}\frac{\partial(C\epsilon)}{\partial t} + Cv\frac{\partial x_{O_2,eq}}{\partial z} + x_{O_2,eq}\frac{\partial(Cv)}{\partial z} = -\frac{\rho_{OC}(1-\epsilon)}{2}\frac{\partial(3-\delta}{\partial t} \quad (3\text{-}25)$$

and factorising leads to

$$C\epsilon\frac{\partial x_{O_2,eq}}{\partial t} + Cv\frac{\partial x_{O_2,eq}}{\partial z} + x_{O_2,eq}\left[\frac{\partial(C\epsilon)}{\partial t} + \frac{\partial(Cv)}{\partial z}\right] = -\frac{\rho_{OC}(1-\epsilon)}{2}\frac{\partial(3-\delta)}{\partial t} \quad (3\text{-}26)$$

Here, the term in the square brackets is a source term as a change in the superficial velocity with respect to the position in the bed, and a change in the total molar concentration and bed voidage over time can only come from the bed material itself. In

this work, it is assumed that the only reaction that takes place is the uptake or release of oxygen, *e.g.* reaction (3-9). This source term must therefore be equal to the source term on the right-hand side of equation (3-26), leading to

$$C\epsilon\frac{\partial x_{O_2,eq}}{\partial t}+Cv\frac{\partial x_{O_2,eq}}{\partial z}=-\frac{\rho_{OC}(1-\epsilon)}{2}\frac{\partial(3-\delta)}{\partial t}\left(1-x_{O_2,eq}\right) \tag{3-27}$$

Noting that the constant molar flux of nitrogen, $j_{N_2}^m$, is

$$j_{N_2}^m=vC_{N_2}=vC\left(1-x_{O_2}\right) \tag{3-28}$$

so that equation (3-27) becomes

$$C\epsilon\frac{\partial x_{O_2,eq}}{\partial t}+\frac{j_{N_2}^m}{\left(1-x_{O_2,eq}\right)}\frac{\partial x_{O_2,eq}}{\partial z}=-\frac{\rho_{OC}(1-\epsilon)}{2}\frac{\partial(3-\delta)}{\partial t}\left(1-x_{O_2,eq}\right) \tag{3-29}$$

At approximately constant mass in element *i* it is valid to write

$$\frac{\partial(3-\delta)}{\partial t}=\frac{\partial x_{O_2,eq}}{\partial t}\frac{\partial(3-\delta)}{\partial x_{O_2,eq}} \tag{3-30}$$

Therefore

$$C\epsilon\frac{\partial x_{O_2,eq}}{\partial t}+\frac{\rho_{OC}(1-\epsilon)}{2}\left(1-x_{O_2,eq}\right)\frac{\partial x_{O_2,eq}}{\partial t}\frac{\partial(3-\delta)}{\partial x_{O_2,eq}}+\frac{j_{N_2}^m}{\left(1-x_{O_2,eq}\right)}\frac{\partial x_{O_2,eq}}{\partial z}= \tag{3-31}$$

Factorising with respect to $\frac{\partial x_{O_2,eq}}{\partial t}$ and rearranging the terms lead to

$$\frac{\partial x_{O_2,eq}}{\partial t}+\frac{j_{N_2}^m}{C\epsilon\left(1-x_{O_2,eq}\right)\left(1+\frac{(1-\epsilon)\left(1-x_{O_2,eq}\right)\rho_{oc}}{2\epsilon C}\frac{d(3-\delta)}{dx_{O_2,eq}}\right)}\frac{\partial x_{O_2,eq}}{\partial z}=0 \tag{3-32}$$

The velocity at which the concentrations fronts, or fronts of δ, convect through the solid bed is

$$v_{front}=\frac{j_{N_2}^m}{C\epsilon\left(1-x_{O_2,eq}\right)\left(1+\frac{(1-\epsilon)\left(1-x_{O_2,eq}\right)\rho_{oc}}{2\epsilon C}\frac{d(3-\delta)}{dx_{O_2,eq}}\right)} \tag{3-33}$$

From equation (3-33) it can be noted that v_{front} will increase with an increase in $x_{O_2,eq}$, provided all else is approximately constant. Therefore, by calculating v_{front} for each of the possible molar fractions, *i.e.* $0.0 \leq x_{O_2} \leq 0.21$, the breakthrough curves for the

equilibrium limited case can be computed. Whether the reaction is equilibrium limited or not can then be determined by comparing the expected breakthrough curve from the equilibrium limited case to the experimentally measured curve.

3.3.2.2 Mass transfer limit

The second subcase of case 3, *i.e.* $\frac{kRTL}{v_{in}} \gg 1$, assumes that the reaction is limited by the external mass transfer, as described in section 1.2.3.1. . The rate of oxygen uptake or release in terms of the volume of the bed, $r_{O_2}^V$, is in this approximately

$$r_{O_2}^V = k_{eg}(1-\epsilon)\frac{A_p}{V_p RT}\left(pO_2 - pO_{2,eq}(\delta)\right) = \frac{6\,k_{eg}(1-\epsilon)}{d_p\,RT}\left(pO_2 - pO_{2,eq}(\delta)\right) \quad (3\text{-}34)$$

where k_{eg} is the external mass transfer coefficient, A_p, V_p and d_p are the surface area, volume and diameter of a single particle, respectively. The apparent reaction rate constant in the external mass transfer limit, k^m, is then

$$k^m = \frac{6\,k_{eg}(1-\epsilon)}{d_p\,RT} = \frac{6\,D_{O_2}\,Sh\,(1-\epsilon)}{d_p^2\,RT} \quad (3\text{-}35)$$

where Sh is the Sherwood number as defined in equation (1-20) and D_{O_2} is the gas diffusivity of oxygen. The experimentally determined apparent reaction rate constant can be compared to k^m to determine whether the observed rate is limited by external mass transfer.

3.3.2.3 $\frac{kRTL}{v_{in}} \ll 1$ and $\frac{kRTL}{v_{in}} \sim 1$

For cases 1 and 2, at time, t, equal to zero, no profile of δ across the length of the bed had time for form, *i.e.* $\delta = \delta_o$, and, hence, in pseudo steady-state equation (3-11) becomes

$$\frac{\partial v x_{O_2}}{\partial z} = -kRT\left(x_{O_2} - x_{O_2,eq}(\delta_0)\right) \quad (3\text{-}36)$$

Using equation (3-28), it follows that

$$\frac{\partial\left(\frac{x_{O_2}}{1-x_{O_2}}\right)}{\partial z} = -\frac{CkRT}{j_{N_2}^m}\left(x_{O_2} - x_{O_2,eq}(\delta_0)\right) \quad (3\text{-}37)$$

Rearranging and taking the integral gives

$$\int_{x_{O_2,in}}^{x_{O_2,out}} \frac{1}{\left(x_{O_2} - x_{O_2,eq}(\delta_0)\right)\left(1 - x_{O_2}\right)^2} dx_{O_2} = -\frac{CkRT}{j_{N_2}^m} \int_0^L dz \tag{3-38}$$

The analytical solution to this integral, which accounts for a change in the flow rate, is given in the appendix 12.2. If the velocity is assumed to be constant, then equation (3-36) becomes

$$\int_{x_{O_2,in}}^{x_{O_2,out}} \frac{1}{\left(x_{O_2} - x_{O_2,eq}(\delta_0)\right)} dx_{O_2} = -\frac{kRT}{v_{in}} \int_0^L dz \tag{3-39}$$

and integration yields

$$\frac{kRTL}{v_{in}} = ln\left(\frac{x_{O_2,in} - x_{O_2,eq}(\delta_0)}{x_{O_2,out} - x_{O_2,eq}(\delta_0)}\right) \tag{3-40}$$

Under the assumption that the entire solid bed is exposed to the inlet concentration of oxygen, *i.e.* in the limit of a differential reactor (case 1 of equation (3-22)), using Taylor expansion, equation (3-40) becomes

$$\frac{kRTL}{v_{in}} = \frac{x_{O_2,in} - x_{O_2,out}}{x_{O_2,in} - x_{O_2,eq}(\delta_0)} \tag{3-41}$$

Further, for case 2, *i.e.* $\frac{kRTL}{v_{in}} \sim 1$, where there is a non-negligible change in the molar flow rate, the apparent (or measured) reaction rate constant for the oxygen release, k_{app}, is

$$k_{app} = \frac{r_{O_2,prod}}{\left(x_{O_2,in} - x_{O_2,eq}(\delta_0)\right)\, p\, V_{bed}} \tag{3-42}$$

where $r_{O_2,prod}$ is the measured rate of oxygen production, as defined in equation (3-8), p is the pressure (here, 1 bar) and V_{bed} denotes the volume of the bed.

3.3.3 Non-isothermality

In the previous derivation, it was assumed that the bed is isothermal. However, for fast reaction rates and large enthalphies of reaction, this might not be a valid assumption. Using equations (1-4) and (1-8) the enthalpy of reaction, ΔH_r^o, can be linked to the equilbrium partial pressure of oxygen by

$$pO_2 = e^{-\frac{\Delta G_r^o}{RT}} = e^{-\frac{\Delta H_r^o}{RT}} e^{\frac{\Delta S_r^o}{R}} \tag{3-43}$$

It should be noted that for perovskites, the equilibrium partial pressure of oxygen is a function of the oxygen stoichiometry of the material, *i.e.* $pO_2(\delta)$. Therefore, the enthalpy of reaction and entropy of reaction change not only due to temperature but also the oxygen stoichiometry of the material. As described in section 2.2.2, in this work, it is assumed that the uncoupling of oxygen from the solid is the dominant effect in the entropy of reaction for chemical looping air separation materials (Dunstan *et al.*, 2016; Lau *et al.*, 2017). As described previously, ΔS_r^o is set to 205.2 J mol^{-1} K^{-1}. From equation (3-43) , it follows that the instantaneous enthalpy of reaction per mole of oxygen released from the oxygen carrier is given by

$$\Delta H_r^o = T\,\Delta S_r^o - ln(pO_2) \tag{3-44}$$

Here, two ways of estimating the change in temperature in the bed due to the oxygen uptake or release reaction are presented. One order of magnitude estimate for the upper bound of the change in temperature from the set point, ΔT_{ub}^1, can be determined by assuming radial heat conduction inside the reactor only, *i.e.*

$$r_{O_2}^V \Delta H_r^o = \frac{\lambda}{r_r}\frac{d}{dr_r}\left(r_r \frac{dT}{dr_r}\right) \tag{3-45}$$

where $r_{O_2}^V \cdot \Delta H_r^o$ is the heat generated per mole of oxygen taken up or heat required per mole of oxygen released per volume of the bed and λ is the radial thermal conductivity. Therefore

$$\Delta T_{ub}^1 = \frac{r_{O_2} \Delta H_r^o\, r_r^2}{4\,\lambda} \tag{3-46}$$

ΔT_{ub}^1 is overestimated because the change in temperature assumes radial conductive heat transfer only and any effects that would decrease the change in temperature, such

as longitudinal convective heat transfer and the heat capacity of the solids which would prevent the bed from developing this temperature gradient before the gas is switched and the reverse reaction takes place, are disregarded.

The second approach to calculate the maximum deviation in temperature, ΔT_{ub}^2, assumes that the reactor is adiabatic. Therefore, all the heat produced by the reaction is taken up by the solids up until the time the reaction rate is evaluated. ΔT_{ub}^2 is then given by

$$\Delta T_{ub}^2 = \frac{n_{O_2} \Delta H_r^o}{c_p \ m_{OC}} \tag{3-47}$$

where n_{O_2} denotes the number of moles of oxygen taken up or released, c_p is the mass based specific heat capacity of the bed material and m_{OC} is the mass of the solids, *i.e.* the oxygen carrier.

4 Equilibrium Partial Pressure Curves of Selected Oxygen Carriers

The objective of this chapter is to derive the equilibrium partial pressure curves for selected materials, namely $SrFeO_{3-\delta}$ and $SrMn_{0.1}Fe_{0.9}O_{3-\delta}$, from TGA experiments described in section 3.2.2. The TGA data, *i.e.* mass loss *versus* temperature, is converted to the oxygen non-stoichiometry, δ, *versus* temperature at constant oxygen partial pressures using equations set out in section 3.2.2. Then, using defect chemistry models described in this chapter, the equilibrium constant, K_{eq}, is fitted against $\delta(pO_2, T)$ at constant temperature and the different pO_2 used in the TGA experiments. From these isotherms of pO_2 *versus* δ, it is possible to construct equilibrium partial pressure curves as a function of the temperature, *i.e.* pO_2 *versus* temperature. The fitted equilibrium partial pressure of oxygen curves are then used in chapters 5 and 6 to derive the kinetic parameters of the oxygen carriers using the theory laid out in section 3.3.

4.1 Introduction

In any CLAS system the equilibrium partial pressure curve of the oxygen carrier determines the operating conditions of the CLAS unit and, therefore, significantly influences the overall efficiency of the system. As the equilibrium partial pressure curves used in chapter 2 were not based on experiments but first-principle calculations, significant errors were expected. In addition, the theoretical equilibrium values of $pO_{2,eq}(T)$ given in chapter 2, assume a complete phase change from one stoichiometric compound to another. The materials of interest here show variable stoichiometry in the absence of a complete reconstructive phase change, *e.g.* the oxygen non-stoichiometry, δ, in $SrFeO_{3-\delta}$ is a function of oxygen partial pressure and temperature,

and can change without a change to the underlying crystal structure. Thus, experiments were deemed necessary to evaluate the magnitude of such errors and, especially, to derive the equilibrium partial pressure curves of materials consisting of four elements or more, and to account for the non-stoichiometry.

The results obtained from the experiments described here also served as a basis for deriving the reaction kinetics of the investigated materials described in chapters 5 and 6. Here the TGA experiments are used to determine the effect $p\mathrm{O}_{2,eq}(T,\delta)$ for the materials of interest.

4.2 Defect Chemistry

In order to calculate the reaction kinetics later on, knowledge about the equilibrium partial pressure of oxygen, $p\mathrm{O}_{2,eq}$, for a given oxygen non-stoichiometry, δ, and temperature is required. Therefore, a model for the different materials describing $p\mathrm{O}_{2,eq}(T,\delta)$ must be derived. For perovskite-type materials, models based on defect chemistry have been found to fit experimental data well (van Roosmalen and Cordfunke, 1991; Mizusaki, 1992; Lankhorst, Bouwmeester and Verweij, 1997; Diethelm *et al.*, 2000; Hodges *et al.*, 2000; Haavik *et al.*, 2003; Cheng *et al.*, 2005; Yoo *et al.*, 2005; Stølen, Bakken and Mohn, 2006; Goldyreva *et al.*, 2012). The oxidation of a perovskite

$$ABO_{3-\delta} + \frac{\delta}{2} O_{2(g)} \rightleftarrows ABO_3 \tag{4-1}$$

where A and B denote the A-sites and B-sites, which are typically occupied by alkali, alkaline-earth, or rare-earth ions and transition metals, respectively, may be expressed in Kröger-Vink notation, assuming only the B-site cation changes its oxidation state, using the point defect model (4-2) and the cluster defect model (4-3). Both of these models have been widely applied to study defects in perovskites (van Roosmalen and Cordfunke, 1991, 1994; Wißmann and Becker, 1996; Lankhorst, Bouwmeester and Verweij, 1997; Diethelm *et al.*, 2000; Haavik *et al.*, 2003; Jones and Islam, 2008; Albrecht, Jackson and Braun, 2016; Yoo *et al.*, 2017). Here, an oxygen atom is inserted into a vacancy in the oxygen sublattice, $\mathrm{V}_\mathrm{O}^{\bullet\bullet}$, which leads to a change in the oxidation state of two B-site cations. The point defect model assumes that oxygen

vacancies and defects in the B-cation sublattice are distributed randomly and do not interact with one another. The cluster defect model, on the other hand, assumes that strong attractive interactions are present between neighbouring defects, resulting in a strictly clustered occurrence of defects, such as $\langle \mathrm{B_B^{'}} - \mathrm{V_O^{\bullet\bullet}} - \mathrm{B_B^{'}} \rangle$; *i.e.* the removal of an oxygen vacancy requires two electrons, which are provided by the oxidation of two neighbouring B-site cations ($2\mathrm{B_B^{'}} \rightleftarrows 2e^{'} + 2\mathrm{B_B^{\times}}$) (van Roosmalen and Cordfunke, 1991).

$$\frac{1}{2}O_{2(g)} + V_O^{\bullet\bullet} + 2B_B^{'} \rightleftarrows O_O^{\times} + 2B_B^{\times} \tag{4-2}$$

$$\frac{1}{2}O_{2(g)} + \langle B_B^{'} - V_O^{\bullet\bullet} - B_B^{'} \rangle \rightleftarrows O_O^{\times} + 2B_B^{\times} \tag{4-3}$$

From these models, the equilibrium constant, K_{eq}, can be derived. For the point defect model, reaction (4-2) in terms of the concentration of the species, becomes

$$pO_{2,eq}^{0.5}[V_O^{\bullet\bullet}]\left[B_B^{'}\right]^2 K_{p,eq} = [O_O^{\times}][B_B^{\times}]^2 \tag{4-4}$$

where $\mathrm{K_{p,eq}}$ denotes the equilibrium constant of the point defect model.

Furthermore, two requirements, namely, the structure conservation and the charge neutrality requirement, must be met to achieve thermodynamic consistency. The structure conservation requirement states that the ratio of cation and anion sites must be constant, *e.g.* when an oxygen atom is added to the material it either has to fill an oxygen vacancy or A-site and B-site cations must also be added in the correct stoichiometric ratios (Lankhorst, Bouwmeester and Verweij, 1997). The charge neutrality requirement demands that the compound must remain electronically neutral, *i.e.* the total effective charge must be the same before and after the formation of defects and the net charge on both sides of the reaction must be equal. Assuming the B-site cation is present in two oxidation states only, this introduces the following equations (when the B-site cation is expected to take more than two oxidation states, a disproportionation reaction, *e.g.* $2\mathrm{Mn_{Mn}^{\times}} \rightleftarrows \mathrm{Mn_{Mn}^{'}} + \mathrm{Mn_{Mn}^{\bullet}}$ must also be considered (Goldyreva *et al.*, 2012; Albrecht, Jackson and Braun, 2016))

$$\left[B_B^{'}\right] + [B_B^{\times}] = 1 \tag{4-5}$$

$$[\mathrm{V_O^{\bullet\bullet}}] + [\mathrm{O_O^{\times}}] = 3 \tag{4-6}$$

$$2\,[\mathrm{V_O^{\bullet\bullet}}] = [\mathrm{B_B^{'}}] \tag{4-7}$$

so that for every mole of an ideal perovskite, $\mathrm{ABO_3}$, the concentration of the B-site cations, being the sum of the concentrations of its considered species, here $\mathrm{B_B^{'}}$ and $\mathrm{B_B^{\times}}$, must equal to 1. Similarly, the concentration per formula unit of the sum of the oxygen species considered, here $\mathrm{V_O^{\bullet\bullet}}$ and $\mathrm{O_O^{\times}}$, must be 3; for example, for every mole of an ideal perovskite, $\mathrm{ABO_3}$, *i.e.* $[\mathrm{V_O^{\bullet\bullet}}]$=0, there are three moles of oxygen. Equation (4-4) can be expressed in terms of the concentration of oxygen vacancies, $[\mathrm{V_O^{\bullet\bullet}}]$, only using (4-5) to (4-7)

$$pO_{2,eq}^{0.5}\;4\,[V_O^{\bullet\bullet}]^3 = \frac{1}{K_{p,eq}}\,(3-[V_O^{\bullet\bullet}])(4\,[V_O^{\bullet\bullet}]^2 - 4\,[V_O^{\bullet\bullet}] + 1) \tag{4-8}$$

Substituting the relation $[\mathrm{V_O^{\bullet\bullet}}] = \delta$ into (4-8) then leads to the following equation

$$pO_{2,eq}^{0.5} = \frac{(3-\delta)(2\delta-1)^2}{4\delta^3 K_{p,eq}} \tag{4-9}$$

It should be emphasised that equation (4-9) is based on the point defect model and may therefore only be valid for small concentrations of defects (van Roosmalen and Cordfunke, 1991).

Applying the structure conservation and the charge neutrality requirements to the cluster model (reaction (4-3)), and noting that

$$\left[\langle B_B^{'} - V_O^{\bullet\bullet} - B_B^{'}\rangle\right] = \delta \tag{4-10}$$

gives the partial pressure of oxygen at equilibrium as

$$pO_{2,eq}^{0.5} = \frac{(3-\delta)(2\delta-1)^2}{\delta K_{c,eq}} \tag{4-11}$$

At high defect concentrations the aforementioned models are likely to be inaccurate owing to the neglect of already existing defects in the lattice. Ling (1994) presented an approach based on the fact that the number of ways a defect or defect cluster may be incorporated into the lattice shrinks with the number of already existing defects. The site exclusion factor, Λ_c, describes the number of ways that are excluded by placing a defect or defect cluster into the lattice (Lankhorst, Bouwmeester and Verweij,

1997). Extending the cluster model to include the site exclusion factor leads to the following expression of $pO_{2,eq}$ in terms of Λ_c and the equilibrium constant, $K_{se,eq}$.

$$pO_{2,eq}^{0.5} = \frac{(3 - \Lambda_c \delta)}{\delta K_{se,eq}} \tag{4-12}$$

The application and goodness of fit of these models will be discussed in the results section for each material individually.

From the point of view of thermodynamics, the proposed defect models rely on the introduction of a "virtual chemical potential" to describe the chemical potential of a vacancy or cluster without breaching the structure conservation and charge neutrality requirements elsewhere (Kröger, Stieltjes and Vink, 1959; Ling, 1994; Lankhorst, Bouwmeester and Verweij, 1997; Oates *et al.*, 2011). The thermodynamic analysis discussing the validity of such models has been extensively discussed elsewhere (Kröger, Stieltjes and Vink, 1959; Ling, 1994; Lankhorst, Bouwmeester and Verweij, 1997; Oates *et al.*, 2011).

4.3 Results

The typical masses recorded by the TGA during an experiment, here, $SrFeO_{3-\delta}$ in air, are shown in Figure 4-1. The change in mass has been normalised to 673 K, a temperature at which the decomposition reaction is negligible. The distinct step changes in temperature (red line) correlate well with a change in the mass of the oxygen carrier under investigation (black line). As can be seen in Figure 4-1, in the case of strontium ferrite, the temperature steps were increased to 100 K after 1023 K has been reached. Following the same temperature program for the different oxygen carrier materials at different partial pressure of oxygen, and having knowledge about the initial oxygen stoichiometry, then allows for the determination of the oxygen stoichiometry, 3-δ (equations (3-3) and (3-5)). Table 4-1 and Table 4-2 list the oxygen stoichiometry of $SrFeO_{3-\delta}$ and $SrMn_{0.1}Fe_{0.9}O_{3-\delta}$ with respect to the temperature and oxygen partial pressure, respectively. The temperature range used to determine kinetic parameters used is from 823 to 1323 K.

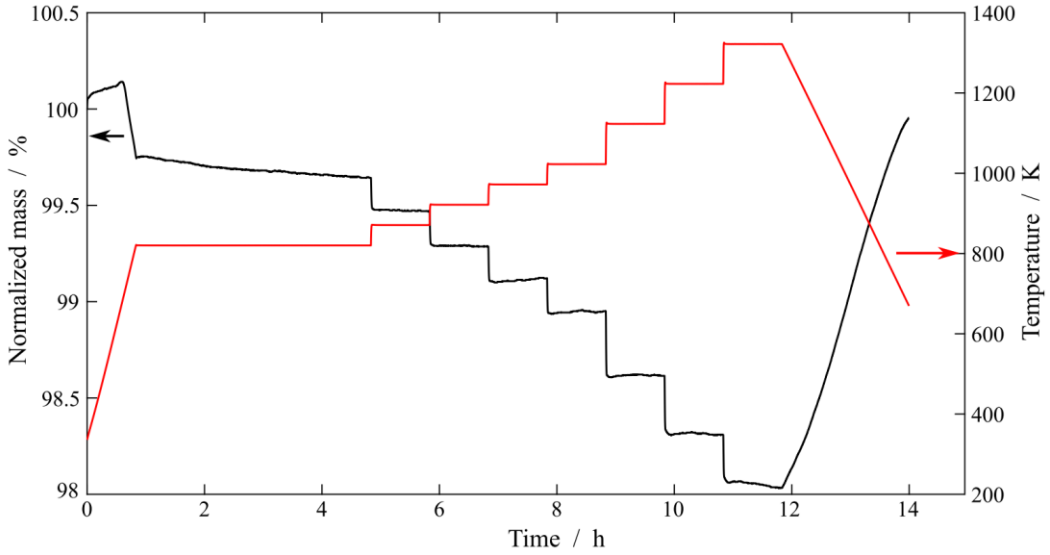

Figure 4-1: Change in mass of $SrFeO_{3-\delta}$ at pO_2 of 0.21 bar

Table 4-1: Oxygen stoichiometry, 3-δ, of $SrFeO_{3-\delta}$ as a function of temperature and partial pressure of oxygen.

Temperature	pO_2				
K	0.21 bar	0.15 bar	0.075 bar	0.015 bar	N_2
653	2.819	2.819	2.822	2.819	2.805 (623 K)
823	2.767	2.762	2.756	2.736	2.677
873	2.742	2.739	2.732	2.711	2.644
923	2.720	2.716	2.709	2.687	2.619
973	2.699	2.693	2.685	2.664	2.60
1023	2.680	2.670	2.662	2.643	2.584
1123	2.641	2.629	2.623	2.608	-
1223	2.605	2.595	2.590	2.581	-
1323	2.575	-	-	-	-

Table 4-2: Oxygen stoichiometry, 3-δ, of $SrMn_{0.1}Fe_{0.9}O_{3-\delta}$ as a function of temperature and partial pressure of oxygen.

	pO_2	N_2

Temperature K	0.21 bar	0.15 bar	0.075 bar	0.015 bar	
653	2.844	2.846	2.845	2.839	2.834
823	2.776	2.778	2.770	2.743	2.676
873	2.755	2.755	2.749	2.714	2.650
923	2.734	2.732	2.727	2.688	2.626
973	2.712	2.709	2.705	2.663	2.608
1023	2.692	2.686	2.684	2.641	2.593
1123	2.656	2.648	2.647	2.607	2.570
1223	2.624	2.615	2.617	2.581	2.537
1323	2.597	-	-	-	-

4.4 Discussion

4.4.1 $SrFeO_{3-\delta}$

The calculated oxygen stoichiometry of $SrFeO_{3-\delta}$ is plotted in Figure 4-2 at temperatures between 823 and 1323 K and compared against values found in literature for air, nitrogen and a partial pressure of oxygen, pO_2, of 0.15 bar. Here, the data are fit to a second-degree polynomial, which in the investigated temperature range achieved excellent results ($R^2 > 0.999$). The deviations from results found in this study may be explained by the method and conditions of the synthesis, the purity of the sample in terms of the cubic phase, the stability of the flow rate and the gas composition during the TGA experiments. Notable is the result obtained by Ikeda et al. (2016) when exposing their $SrFeO_{3-\delta}$ to a nitrogen atmosphere, they report three plateaus: an initial oxygen stoichiometry, $3-\delta$, of 2.89 between 323 and 473 K, 2.75 between 573 and 673 K and nearly complete reduction to the brownmillerite $Sr_2Fe_2O_5$ between 673 and 1073 K. For their study, they purchased the $SrFeO_{3-\delta}$ powder readily synthesized from TOSHIMA MFG, Co., Ltd, Japan. Given their high initial oxygen stoichiometry of 2.89, it is very likely that the powder has been exposed to a pO_2 greater than that of air during the calcination. In this study, the calcination atmosphere was air and an initial oxygen stoichiometry of 2.82 was calculated. A reduction to the brownmillerite at temperatures below 1173 K was only achieved under strongly reducing atmospheres, *e.g.* hydrogen or mixtures of CO_2 and CO (Marek *et al.*, 2018). Starkov *et al.* (2014), who calcined their sample under air, however, also found the brownmillerite, or vacancy ordered perovskite phase, to be present at temperatures below roughly 1073 K and pO_2 below approximately 0.018 bar. The absence of the brownmillerite phase in the $SrFeO_{3-\delta}$ used in this study might be explained simply by the sensitivity of the XRD measurements. Given such deviations of data collected *via* TGA, it is no surprise to find results from TGA experiments conducted at $pO_2 = 0.15$ bar (Yoo *et al.*, 2005) to overlap with results obtained under $pO_2 = 0.015$ bar during the course of this study. In the following, defect models are fitted to the results found from thermogravimetric analysis of this study.

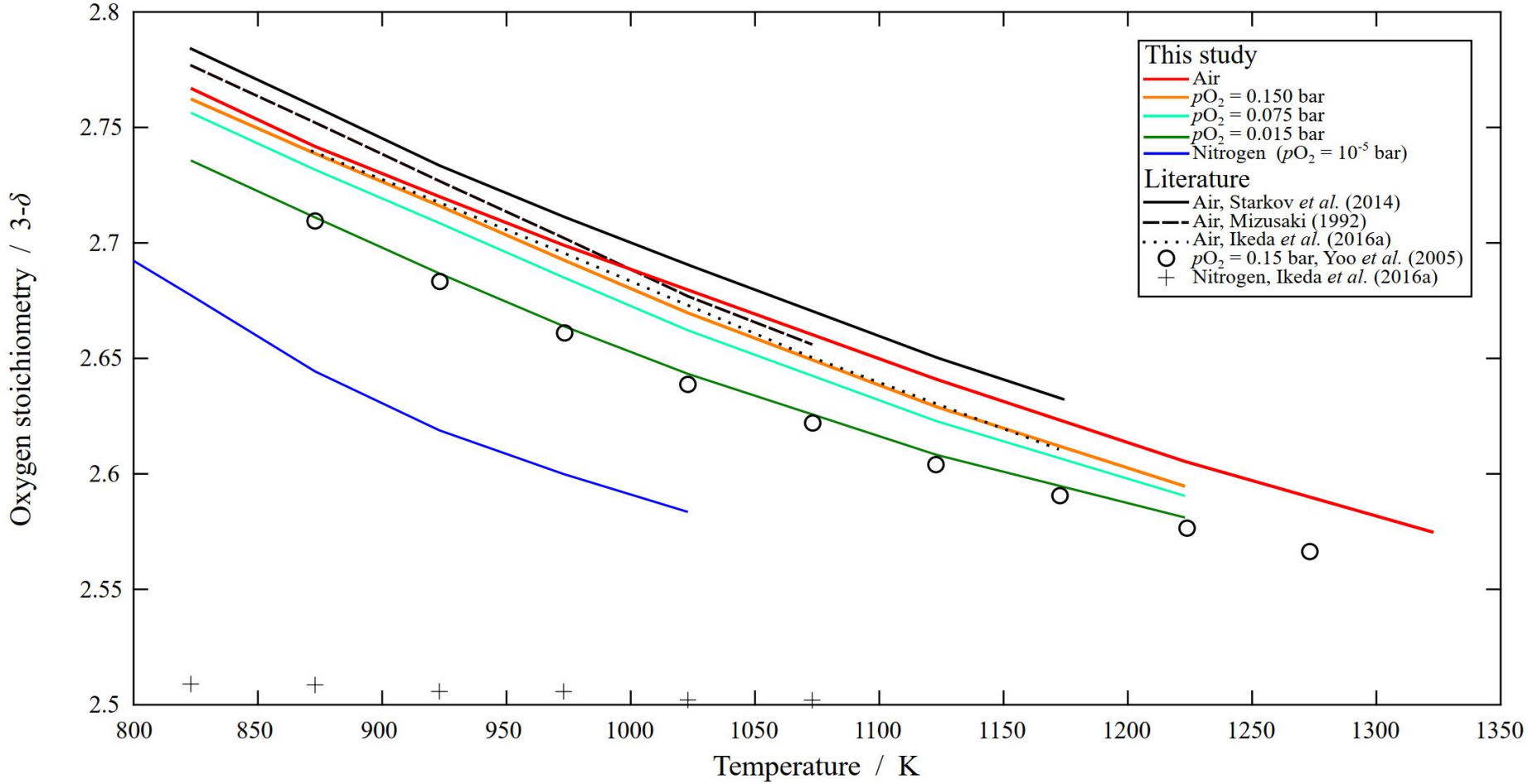

Figure 4-2: Equilibrium oxygen stoichiometry of $SrFeO_{3-\delta}$ under different partial pressures of oxygen as a function of temperature including results from literature.

To identify the formation of potential clusters, a closer look at the phases and their crystal structures is required. The phase diagram of the Sr-O-Fe system is depicted in Figure 4-3, in this case in an N_2 atmosphere. As noted previously, equilibrium under N_2 is difficult to achieve, with the result probably depending on flow rate (*i.e.* the rate at which the oxygen can be swept away). Thus, this diagram probably represents the final state at some low, but non-zero oxygen partial pressure. At high temperatures, this phase diagram suggests that only the cubic perovskite and the brownmillerite phases or mixtures thereof are present. When the cubic $SrFeO_{3-\delta}$ is cooled, the oxygen vacancies, which are unordered on the oxygen sublattice of the cubic phase, shift forming tetrahedral and orthorhombic oxygen cells around the iron cations. At temperature below approximately 523 K, the pure cubic perovskite phase exists only for oxygen non-stoichiometries, δ, of 0.03 and below. For $0.03 \leq \delta \leq 0.14$, the cubic phase exists only in a mixture with the tetragonal phase, as shown in Figure 4-3.

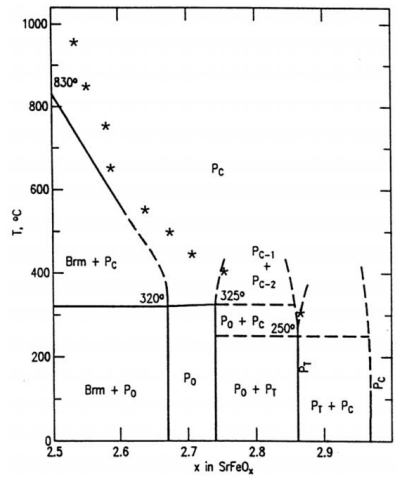

Figure 4-3: Phase diagram of the Sr-Fe-O system under 1 bar of nitrogen [reproduced from Takeda *et al.* (1986) and Schmidt (2001)][4]. P_c. P_T and P_O are the cubic, tetrahedral, orthorhombic perovskite phases, Brm denotes the brownmillerite phase. The asterisks denote the onset of the transition from the cubic perovskite to the brownmillerite found by Schmidt (2001).

[4] Published under the copyright license number 4726391446039

Wißmann & Becker (1996) found that the strontium does not change its oxidation state; they identified a relationship between the oxygen non-stoichiometry, δ, and the concentration of Fe^{3+} and Fe^{4+} where the concentration of Fe^{3+}, $[Fe'_{Fe}]$, is equal to 2δ and the remaining iron cations are Fe^{4+}. It was therefore concluded that only iron changes its oxidation state to maintain charge neutrality during the uptake or release of oxygen. Hence, in Kröger-Vink notation B'_B , and $B^{\times}_B$ denote Fe'_{Fe} (Fe^{3+}) and $Fe^{\times}_{Fe}$ (Fe^{4+}), respectively and at high temperatures $SrFeO_{3-\delta}$ may be written more precisely as $Sr^{2+}\left(Fe^{3+}_{2\delta}Fe^{4+}_{1-2\delta}\right)O^{2-}_{3-\delta}$.

For the cluster model described by reaction (4-3), the defect clusters formed during reduction of the cubic perovskite phase are $\langle Fe'_{Fe} - V^{\bullet\bullet}_O - Fe'_{Fe}\rangle$-clusters. Ling (1994) extended this cluster model by the site exclusion factor, Λ_c, which has an upper bound dictated by the crystal structure; the number of ways of placing a defect cluster into the crystal lattice that are removed by placing a single defect cluster. Thus, the site exclusion factor may be manually counted by investigating the crystal structure (Ling, 1994). Figure 4-4 shows the crystal structures of the cubic perovskite $SrFeO_3$, consisting of layers of $Fe^{4+}O_6$ octahedra, and the brownmillerite $Sr_2Fe_2O_5$ which is made up of alternating layers of $Fe^{3+}O_6$ octahedra and $Fe^{3+}O_4$ tetrahedra. If a $\langle Fe'_{Fe} - V^{\bullet\bullet}_O - Fe'_{Fe}\rangle$-defect cluster is placed at the location of the dashed circle, then a total of 11 ways to incorporate a defect cluster into the lattice would be removed for the cubic perovskite; locking a Fe^{4+} cation in a defect cluster removes the possibility that this iron ion could form a defect cluster with any of the surrounding six iron ions. Following the approach of Ling (1994), for the cubic perovskite $\Lambda_c = 2 \cdot 6 - 1 = 11$ as each iron ion is surrounded by six oxygen atoms, which then cannot be part of another $\langle Fe'_{Fe} - V^{\bullet\bullet}_O - Fe'_{Fe}\rangle$ defect cluster, *i.e.* 11 possibilities to place a defect cluster are excluded for every one formed. For the brownmillerite, however, the oxidation state of iron in each FeO_6 octahedra is +3 and, therefore, only consists of Fe'_{Fe} cations from the point of view of the cubic perovskite. Thus, for the brownmillerite and the cubic perovskite the upper bound of Λ_c is 0 and 11, respectively. Of course, it is possible to reduce the strontium ferrite below $Sr_2Fe_2O_5$, in which case the iron changes its oxidation state to +2 (Mizusaki *et al.*, 1985; Tsujimoto *et al.*, 2007; Yoo *et al.*, 2017). When exposed to 5 % H_2 in nitrogen at temperatures above 1073 K a reduction to SrO and Fe occurs (Marek *et al.*, 2018). Hence, fitting the data collected by the TGA experiments with the mass action law (4-12) to values $\delta \geq 0.5$ would still give

$\Lambda_c > 0$. At temperatures around 1173 K and $\delta \cong 0.5$ the best fit was obtained with $\Lambda_c = 6$ (Diethelm *et al.*, 2000).

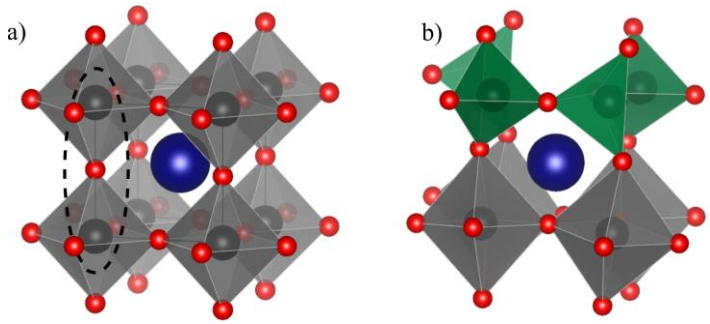

Figure 4-4: Crystal structures of a) the high temperature, cubic phase of $SrFeO_{3-\delta}$ and b) the brownmillerite phase $Sr_2Fe_2O_5$. The dashed circle represents a possible location for a $\langle Fe'_{Fe} - V_O^{\bullet\bullet} - Fe'_{Fe} \rangle$ defect cluster. The software VESTA (Momma and Izumi, 2011) was used to draw the crystal structures using data from Hodges *et al.* (2000) and Schmidt & Campbell (2001) for a) and b), respectively.

It could be argued that the oxygen vacancy in the $\langle Fe'_{Fe} - V_O^{\bullet\bullet} - Fe'_{Fe} \rangle$-cluster might affect the oxygen anions surrounding the Fe'_{Fe} cation. The oxygen anions should therefore be considered in the formation of potential defect clusters of two FeO_6 octahedra. During the reduction of the cubic perovskite phase the formation of such defect clusters may be described by

$$\langle \left(Fe'_{Fe}\, 5O_O^{\times}\right)' - V_O^{\bullet\bullet} - \left(Fe'_{Fe}\, 5O_O^{\times}\right)' \rangle \rightleftarrows 10\, O_O^{\times} + 2\, Fe'_{Fe} + V_O^{\bullet\bullet} \tag{4-13}$$

Here, the mass action law for the equilibrium constant of the oxidation of this model, $K_{FeO_5,eq}$, is subject to the following requirements for site conservation

$$[O_O^{\times}] + [V_O^{\bullet\bullet}] + 11\left[\langle \left(Fe'_{Fe}\, 5O_O^{\times}\right)' - V_O^{\bullet\bullet} - \left(Fe'_{Fe}\, 5O_O^{\times}\right)' \rangle\right] = 3 \tag{4-14}$$

$$[Fe_{Fe}^{\times}] + \left[Fe'_{Fe}\right] + 2\left[\langle \left(Fe'_{Fe}\, 5O_O^{\times}\right)' - V_O^{\bullet\bullet} - \left(Fe'_{Fe}\, 5O_O^{\times}\right)' \rangle\right] = 1 \tag{4-15}$$

$$[V_O^{\bullet\bullet}] + \left[\langle \left(Fe'_{Fe}\, 5O_O^{\times}\right)' - V_O^{\bullet\bullet} - \left(Fe'_{Fe}\, 5O_O^{\times}\right)' \rangle\right] = \delta \tag{4-16}$$

the charge neutrality requirement

$$\left[Fe_{Fe}^{\prime}\right] = 2[V_O^{\bullet\bullet}] \tag{4-17}$$

and is therefore given by (Mack, 2003)

$$pO_{2,eq}^{0.5} = \frac{(3-\delta-10A)(2\delta-1)^2}{4(\delta-A)^3 K_{FeO_5,eq}} \tag{4-18}$$

when substituting equations (4-14) to (4-17) into the point defect model (4-2). A denotes the concentration of the defect cluster, which can be derived from reaction (4-13) to give a 13th degree polynomial. Mack (2003) found that this polynomial may be satisfactorily linearised and, in fact, is mostly constant for $\delta \geq 0.2$.

The slope of $\ln(\delta)$ vs. $\ln(p\mathrm{O}_2)$ for the material can be used to determine which model is appropriate (van Roosmalen and Cordfunke, 1991). For each of the defect models, the equilibrium constant should be approximately proportional to the denominator of the oxidation reaction; for the point defect model $K_{p,eq} \propto \delta^{-3} p\mathrm{O}_{2,\mathrm{eq}}^{-0.5}$ and therefore $\delta \propto p\mathrm{O}_{2,\mathrm{eq}}^{-1/6}$, and for the cluster model $\delta \propto p\mathrm{O}_{2,\mathrm{eq}}^{-1/2}$. In Figure 4-5 such $\ln(\delta)$ vs. $\ln\left(\frac{p\mathrm{O}_2}{1\ bar}\right)$ lines are plotted for $SrFeO_{3-\delta}$ at temperatures between 823 and 1223 K; the figure shows a transformation of the experimental data plotted in Figure 4-2. For the range of temperatures, $p\mathrm{O}_2$ and δ investigated here, the point defect model or simple cluster model seem to fail to provide good fits, with the former describing the oxidation more accurately. However, with an increase in temperatures and partial pressures of oxygen the gradient decreases. This is confirmed by Yoo *et al.* (2017) who found the point defect model to accurately describe the uptake and release of oxygen of $SrFeO_{3-\delta}$ at 1313 K, but reported an increasingly worse fit as the temperature was reduced. At $10^{-5} \leq p\mathrm{O}_2 \leq 0.075$ bar the gradient is mostly around -25^{-1} or below. Wißmann & Becker (1996) found a gradient of -22.7^{-1} when plotting $\ln(\delta)$ vs. $\ln\left(\frac{p\mathrm{O}_2}{1\ bar}\right)$ for $SrFeO_{3-\delta}$ at 773 K.

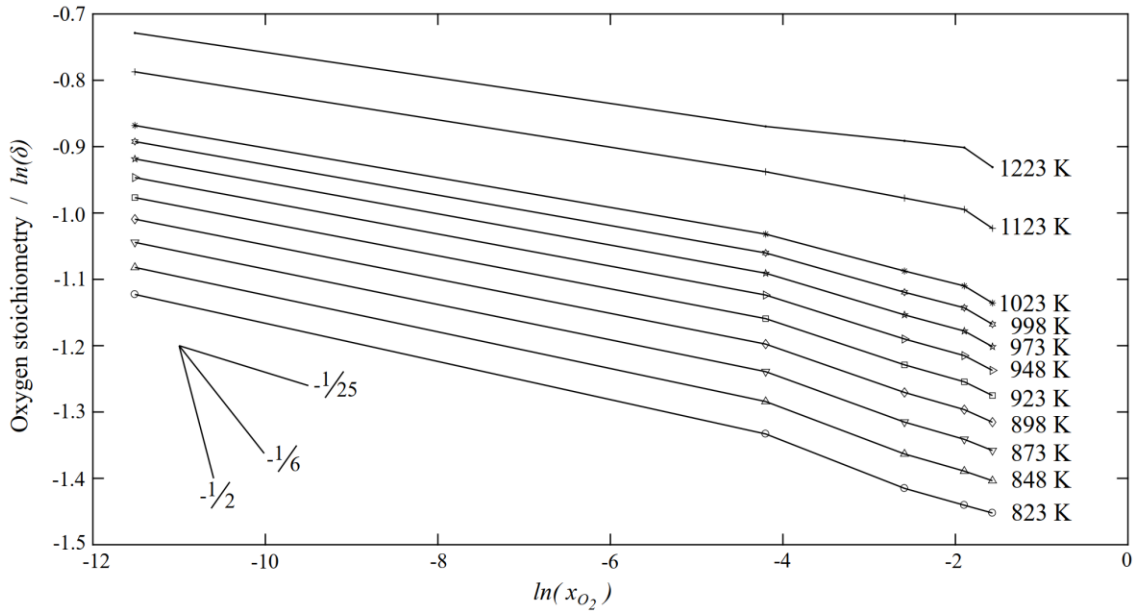

Figure 4-5: $ln(\delta)$ *vs.* $ln\left(\frac{pO_2}{1\ bar}\right)$ for $SrFeO_{3-\delta}$ at different temperatures.

Indeed, when fitting the described defect models to the experimental data, none of the models provide a satisfactory fit for the entire range of pO_2 and δ at different temperatures. The results of fitting these models are plotted in Figure 4-6. Disregarding the cluster model with the site exclusion factor, Λ_c, all models overestimate $\delta(pO_2)$ for $pO2$ below roughly 0.1 bar; a phenomenon that can be explained by the ordering of vacancies at lower temperatures (Dubinin *et al.*, 2005). Of these models, the point defect model fits the data best. As discussed previously, the fit improves with an increase in temperature for all models. Surprisingly, the $\langle\left(Fe_{Fe}^{'}\,5O_O^{\times}\right)^{'} - V_O^{\bullet\bullet} - \left(Fe_{Fe}^{'}\,5O_O^{\times}\right)^{'}\rangle$-cluster model performed the worst, despite offering the most degrees of freedom and Mack (2003) reporting the best results for this model. It should be noted, that following the suggestion of Mack (2003) to approximate the concentration of the cluster, A, by $A = A_0 + A_1\delta$ resulted in concentrations greater than 1, breaching the site conservation requirements (4-14)-(4-16). Both A_0, and A_1 mostly hit their upper boundary of 1. The cluster model with site exclusion (model (4-12)) seems to be able to capture data measured at higher pO_2 but fails to describe the data on the lower end, where due to its quadratic nature it diverges. Diethelm *et al.* (2000) note that for $SrFeO_{3-\delta}$ none of the defect models they investigated, *i.e.* the point defect, cluster and cluster with site exclusion model, were found to be valid over the entire range of pO_2, confirming the findings of this study.

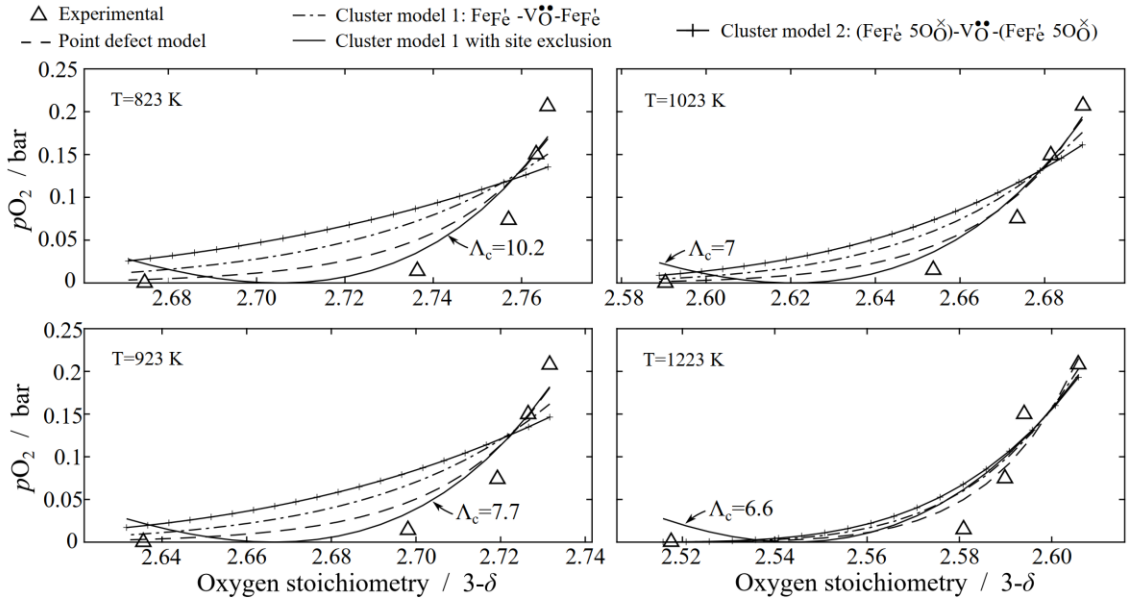

Figure 4-6: Least squares fit of defect models to the oxygen stoichiometry of $SrFeO_{3-\delta}$ at different temperatures and oxygen partial pressures, pO_2.

Hence, the data is split into two regions, pO_2 of below and above roughly 0.015 bar, and the models are then fitted to the two regions to determine an optimal combination of the models. The actual transition between the two regions is determined by the interception of the point defect model, which is fitted to a pO_2 of 10^{-5} bar (*i.e.* nitrogen) and 0.015 bar, and the cluster model with site exclusion, which is fitted to pO_2 of 0.075, 0.15 and 0.21 (*i.e.* air) bar, to allow for a smooth transition. At temperatures below 848 K, the site exclusion factor, Λ_c, exceeds 11, the aforementioned upper limit for cubic perovskites, when fitting the cluster model with site exclusion to $0.075 \leq pO_2 \leq 0.21$ bar. However, this upper limit assumed, that by placing a $\langle Fe_{Fe}^{'} - V_O^{\bullet\bullet} - Fe_{Fe}^{'} \rangle$-defect cluster the two involved $Fe_{Fe}^{'}$ ions cannot form another defect cluster with any of the neighbouring ten $Fe_{Fe}^{\times}$ ions. Λ_c greater than 11 therefore imply that introducing a defect cluster excludes the formation of clusters beyond just the directly adjacent iron ions, *i.e.* the number of simulated ABO_3-cells must be increased to truly isolate the defect.

The equilibrium partial pressure curves resulting from this two-region model are plotted over the oxygen stoichiometry in Figure 4-7a for the temperatures 823, 923 and 1023 K. It can be noted that, to achieve the best fit, the range of partial pressures described by the point defect model decreases with an increase in temperature. At low temperatures, this leads to less smooth transitions between the two models, as can be observed for 823 K. Using these isothermal equilibrium partial pressure curves (pO_2 vs oxygen stoichiometry), isosteric (constant δ) equilibrium partial pressure curves can be constructed, as shown in Figure 4-7b.

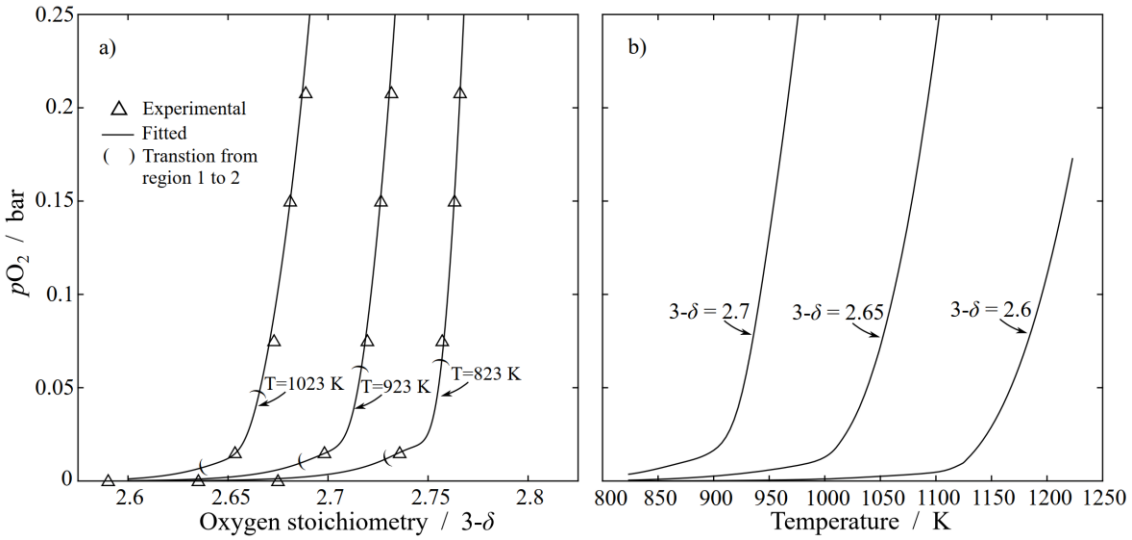

Figure 4-7: Equilibrium partial pressure of oxygen curves of $SrFeO_{3-\delta}$ under a) isothermal and b) isosteric conditions.

The equation used to combine the two defect models, the point defect model and the cluster model with site exclusion, is given by

$$pO_{2,eq} = \frac{(3-\delta)^2(2\delta-1)^4}{16\,\delta^6\,K_{p,eq}^2}\Phi + \frac{(3-\Lambda_c\delta)^2}{\delta^2\;K_{se,eq}^2}(1-\Phi) \qquad (4\text{-}19)$$

where the first term described the point defect model (equation (4-9)), the second term is cluster model with site exclusion (equation (4-11)) including Φ, the logistic function (equation (4-22)), which is used to smoothly transition between the two models.

$$\Phi = \frac{1}{1 + e^{-C_1(\delta - \delta_{mid})}} \tag{4-20}$$

In equation (4-20), the constant C_1 is used to define the steepness of the logistic curve. δ_{mid} is used to define the midpoint of the logistic curve, *i.e.* it is used to set the midpoint of the transition from one model to another. For $SrFeO_{3-\delta}$, C_1 is set to 600. The parameters for the temperature range of interest are given in Table 4-3. It can be seen, that, with an increase in temperature, *i.e.* the oxygen stoichiometry, 3-δ, reduces, $K_{p,eq}$ decreases significantly. Referring to Figure 4-7b and equation (2-1) this is expected behaviour; the further the material is reduced, the higher the temperature at which the material comes to equilibrium with a specific pO_2. The decrease in the site exclusion factor, Λ_c, with an increase in temperature occurs for aforementioned reasons. It is assumed that linear interpolation between the measurements taken with the TGA and extrapolation of up to 25 K is valid, as suggested in Figure 4-2. For convenience, a summary of the defect chemistry models used to fit the equilibrium partial pressure of oxygen curves for $SrFeO_{3-\delta}$ is presented in Table 4-4.

Table 4-3: Parameters of fitting the defect model to $SrFeO_{3-\delta}$ at a confidence interval of 95 %.

Temperature K	$K_{p,eq}$	$K_{se,eq}$	Λ_c	δ_{mid}
823	67.198±43.27	2.517±0.338	11.678±0.140	0.2468
848	50.372±37.62	2.474±0.475	11.076±0.190	0.2510
873	40.161±22.94	2.507±0.948	10.512±0.380	0.2735
898	30.818±17.50	2.722±1.516	9.930±0.615	0.2883
923	24.614±11.01	2.903±1.547	9.413±0.632	0.3039
1023	9.837±1.329	2.631±1.327	8.129±0.530	0.3534
1123	4.179±0.044	2.518±1.89	7.342±0.608	0.3950

Table 4-4: Summary of defect models used for $SrFeO_{3-\delta}$

Model name	Model equation	Equation number
Point defect model	$\mathrm{pO}_{2,\mathrm{eq}}^{0.5} = \frac{(3-\delta)(2\delta-1)^2}{4\delta^3 \mathrm{K}_{\mathrm{p,eq}}}$	(4-9)
Cluster defect model with site exclusion	$\mathrm{pO}_{2,\mathrm{eq}}^{0.5} = \frac{(3-\Lambda_c\delta)}{\delta \mathrm{K}_{\mathrm{se,eq}}}$	(4-12)
Combined defect model	$\mathrm{pO}_{2,\mathrm{eq}} = \frac{(3-\delta)^2(2\delta-1)^4}{16\,\delta^6\,\mathrm{K}_{\mathrm{p,eq}}^2}\Phi + \frac{(3-\Lambda_c\delta)^2}{\delta^2\ \mathrm{K}_{\mathrm{se,eq}}^2}(1-\Phi)$	(4-19) and (4-20)

The predicted equilibrium partial pressure of oxygen, $pO_{2,fit}$, for different temperatures and the experimentally derived oxygen stoichiometry of $SrFeO_{3-\delta}$, $pO_{2,exp}$, is shown in Table 4-5. The combined model significantly overestimates the equilibrium partial pressure of oxygen at very low pO_2 (nitrogen, 10 ppm of oxygen); the point defect model is used to fit these low pO_2 region, as mentioned above. For $0.075 \leq p\mathrm{O}_2 \leq 0.21$, the region for which the cluster defect model with site exclusion is used, there is no apparent trend in the accuracy of the prediction with respect to temperature.

Table 4-5: Experimental data and fitted pO_2 for $SrFeO_{3-\delta}$. δ_{exp} is the oxygen stoichiometry derived from the TGA experiments and listed in Table 4-1. $pO_{2,exp}$ and $pO_{2,fit}$ are the experimentally used and fitted partial pressure of oxygen.

Temperature K	$3-\delta_{exp}$	$pO_{2,exp}$ bar	$pO_{2,fit}$ bar
823	2.677	10^{-5}	0.001392
	2.736	0.015	0.015005
	2.756	0.075	0.059909
	2.752	0.150	0.140533
	2.767	0.210	0.225458
873	2.644	10^{-5}	0.000930
	2.711	0.015	0.015521
	2.732	0.075	0.069684
	2.739	0.150	0.149129
	2.742	0.210	0.194138
923	2.619	10^{-5}	0.000737
	2.687	0.015	0.015318
	2.709	0.075	0.092340
	2.716	0.150	0.157829
	2.720	0.210	0.201625
1023	2.584	10^{-5}	0.000642
	2.643	0.015	0.014387
	2.662	0.075	0.081473
	2.670	0.150	0.131419
	2.680	0.210	0.220654
	-	10^{-5}	-
1123	2.608	0.015	0.019892
	2.623	0.075	0.081379
	2.629	0.150	0.118965
	2.641	0.210	0.221066

4.4.2 $SrMn_{0.1}Fe_{0.9}O_{3-\delta}$

The results from the thermogravimetric analysis of $SrMn_{0.1}Fe_{0.9}O_{3-\delta}$ are plotted in Figure 4-8. The values found for $SrMn_{0.15}Fe_{0.85}O_{3-\delta}$ at 0.1 bar of oxygen by Vieten *et al.* (2017) are in good agreement for temperatures below 973 K, at higher temperatures however exceed the oxygen stoichiometry found at air in this study.

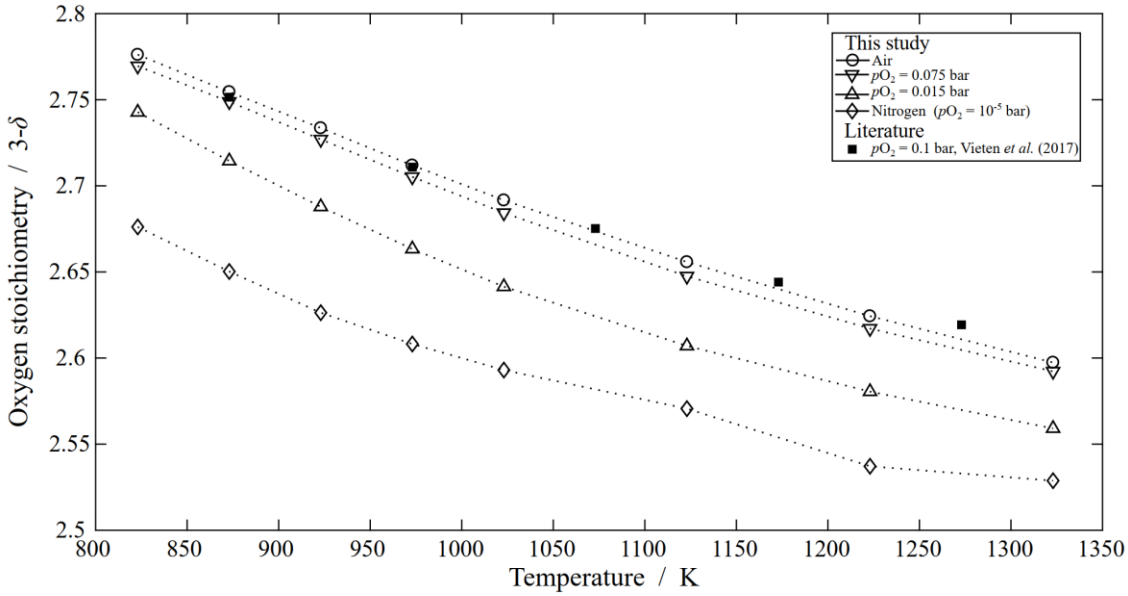

Figure 4-8: Oxygen stoichiometry of $SrMn_{0.1}Fe_{0.9}O_{3-\delta}$ as a function of temperature including results for $SrMn_{0.15}Fe_{0.85}O_{3-\delta}$ at 0.1 bar from literature.

For the Mn-doped $SrFeO_{3-\delta}$, the structure conservation and charge neutrality equations change depending on the assumed model. If, for instance, it is believed that only the iron ions change their oxidation state the structure conservation equations would become

$$[Fe_{Fe}^{\times}] + [Fe_{Fe}^{'}] + [Mn_{Fe}^{\times}] = 1 \tag{4-21}$$

$$[O_O^{\times}] + [V_O^{\bullet\bullet}] = 3 \tag{4-22}$$

$$[Mn_{Fe}^{\times}] = 0.1 \tag{4-23}$$

The charge neutrality requirement would need to fulfil

$$\left[Fe_{Fe}^{'}\right] = 2[V_O^{\bullet\bullet}] \tag{4-24}$$

The resulting mass action law is, in this case, given by

$$pO_{2,eq}^{0.5} = \frac{(3-\delta)(0.9-2\delta)^2}{4\delta^3 K_{p,eq}} \tag{4-25}$$

It should be noted that assuming only iron changes its oxidation state from Fe^{4+} to Fe^{3+} during the reduction, the maximum value of δ decreases to 0.45 as the manganese is assumed to be inert. If on the other hand, it is believed that both the iron and manganese participate in the oxidation and reduction simultaneously, then, in the limiting case of complete conversion of $[(\mathrm{Fe,Mn})_{\mathrm{Fe}}^{\times}]$ to $\left[(\mathrm{Fe,Mn})_{\mathrm{Fe}}^{'}\right]$, the mass action law would be equal to that of the B-site cation reduction point defect model, *i.e.* equation (4-9).

Similar to $SrFeO_{3-\delta}$, the aforementioned point defect and defect cluster models fail to describe the experimental data for the entire range of pO_2, as shown in Figure 4-9. Using these models, modelling the oxygen uptake and release of $SrMn_{0.1}Fe_{0.9}O_{3-\delta}$ would require a two-region approach to obtain an acceptable fit (as done for $SrFeO_{3-\delta}$). Another model (red solid line in Figure 4-9), however, that takes into account the formation of the associate $\langle \mathrm{B_B^{'}} - \mathrm{V_O^{\bullet\bullet}} \rangle^{\bullet}$ fits the range of investigated oxygen partial pressures reasonably well, especially at temperatures below 923 K. The formation of such defect associates has been observed by EPR spectroscopy for $BaTiO_3$ (Eichel, 2011). This means that some oxygen vacancies are trapped by reduced B-site cations, reducing the ionic conductivity of the compound. This was observed by Merkle & Maier (2003) for manganese-doped $SrTiO_3$ and iron-doped $SrTiO_3$, where at 873 to 1073 K and $10^{-5} \leq pO_2 \leq 1$ bar; it was also suggested to be important for manganese-doped $PbTiO_3$ by Eichel (2011). The formation of such an associate follows the reaction

$$2B_B^{\times} + 2e^{'} \rightleftarrows 2B_B^{'} \tag{4-26}$$

$$V_O^{\bullet\bullet} + 2_B^{'} \rightleftarrows \langle B_B^{'} - V_O^{\bullet\bullet} \rangle^{\bullet} + B_B^{'} \tag{4-27}$$

Introducing the equilibrium constant for the formation of this associate, K_A, the mass action law for the above reaction (4-27) is given by

$$K_A = \frac{\left[\langle B_B^{\prime} - V_O^{\bullet\bullet}\rangle^{\bullet}\right]}{\left[B_B^{\prime}\right][V_O^{\bullet\bullet}]} \tag{4-28}$$

The site conservation and electroneutrality requirements thus become

$$[B_B^{\times}] + \left[B_B^{\prime}\right] + \left[\langle B_B^{\prime} - V_O^{\bullet\bullet}\rangle^{\bullet}\right] = 1 \tag{4-29}$$

$$[O_O^{\times}] + [V_O^{\bullet\bullet}] + \left[\langle B_B^{\prime} - V_O^{\bullet\bullet}\rangle^{\bullet}\right] = 3 \tag{4-30}$$

$$[V_O^{\bullet\bullet}] + \left[\langle B_B^{\prime} - V_O^{\bullet\bullet}\rangle^{\bullet}\right] = \delta \tag{4-31}$$

$$\left[B_B^{\prime}\right] = 2[V_O^{\bullet\bullet}] + \left[\langle B_B^{\prime} - V_O^{\bullet\bullet}\rangle^{\bullet}\right] \tag{4-32}$$

Under these conditions, the equilibrium partial pressure of oxygen is calculated by

$$pO_{2,eq}^{0.5} = \frac{(3-\delta)(1-2\delta)^2}{\left(1-\left[\langle B_B^{\prime} - V_O^{\bullet\bullet}\rangle^{\bullet}\right]\right)\left(2\delta-\left[\langle B_B^{\prime} - V_O^{\bullet\bullet}\rangle^{\bullet}\right]\right)^2 K_{p,eq}} \tag{4-33}$$

where $$\left[\langle B_B^{\prime} - V_O^{\bullet\bullet}\rangle^{\bullet}\right] = -\frac{-1-3\delta K_A+\sqrt{1+6\delta K_A+\delta^2 K_A^2}}{2K_A} \tag{4-34}$$

It should be noted that this model has two fit parameters, K_A and $K_{p,eq}$, which leads to large confidence intervals in estimating these fit parameters when only few data points are given.

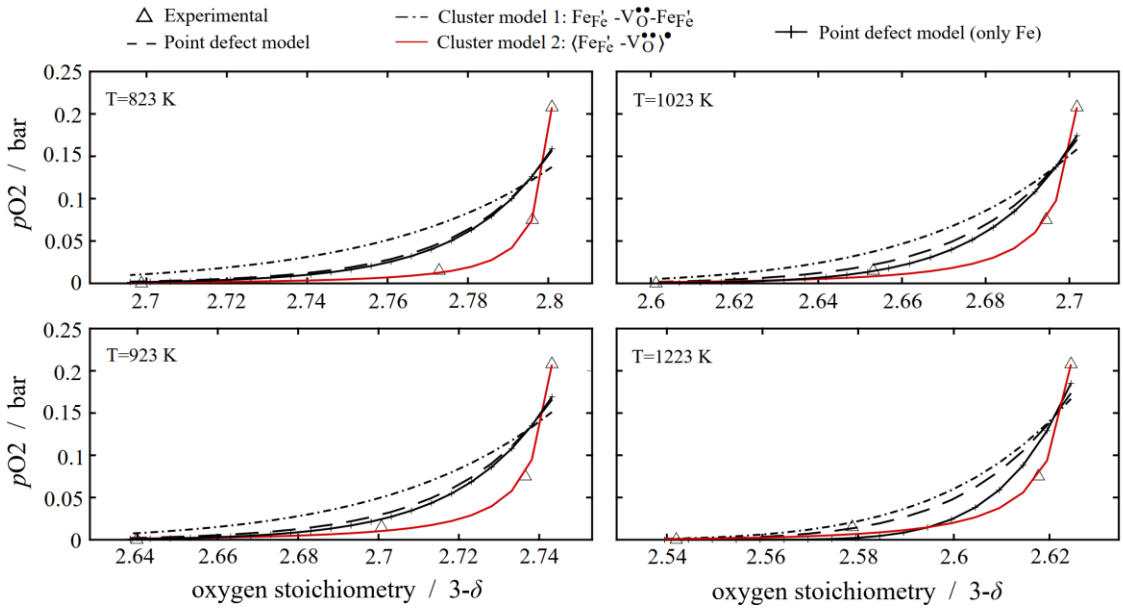

Figure 4-9: Least squares fit of defect models to the oxygen stoichiometry of $SrMn_{0.1}Fe_{0.9}O_{3-\delta}$ for oxygen partial pressures, pO_2, of 10^{-5}, 0.015 and 0.075 bar and different temperatures.

The concentrations of the species are plotted in Figure 4-10 for $0.25 \leq \delta \leq 0.5$. According to the defect model (4-33) most oxygen vacancies are trapped in the $\langle B'_B - V^{\bullet\bullet}_O\rangle^{\bullet}$ associates. In fact, considering that the charge of the oxygen vacancy can only be neutralised by a reduced B-cation, *i.e.* Fe^{3+} or Mn^{3+}, the electroneutrality requirement allows for all oxygen vacancies to be bound in associates, but only half of the B'_B cations (Merkle and Maier, 2003). As shown in Figure 4-10, at $\delta = 0.5$ the concentrations of $\langle B'_B - V^{\bullet\bullet}_O\rangle^{\bullet}$ and $V^{\bullet\bullet}_O$ are around 0.4 and 0.1, respectively. The B-site cations are assumed to be fully reduced at this stage.

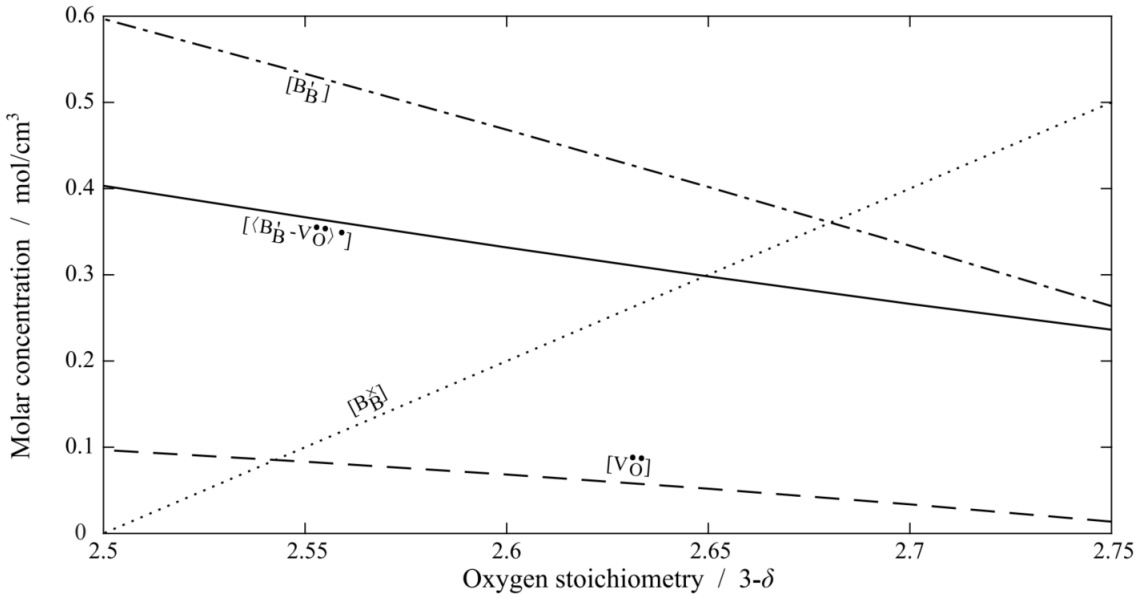

Figure 4-10: Concentrations of species of $SrMn_{0.1}Fe_{0.9}O_{3-\delta}$ for $[B]_{tot} = 1$ calculated from equations (4-29) to (4-32) at 923 K.

The isothermal and isosteric equilibrium partial pressure curves are constructed using only the point defect model extended to the formation $\langle B'_B - V^{\bullet\bullet}_O \rangle^{\bullet}$ associates over the entire range of investigated partial pressures of oxygen. As shown in Figure 4-11a, the oxygen non-stoichiometry is increasingly underestimated for pO_2 of 0.075 bar as the temperature is raised. The isosteric equilibrium partial pressure curves plotted in Figure 4-11b represent slices of the isothermal equilibrium partial pressure curves and, thus, inherit the errors shown in Figure 4-11a.

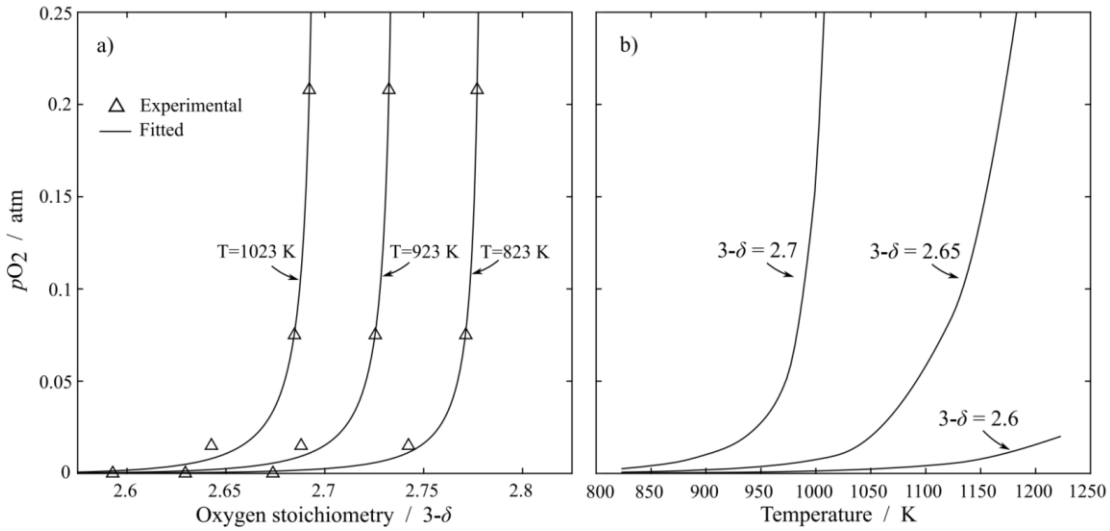

Figure 4-11: Equilibrium partial pressure curves of $SrMn_{0.1}Fe_{0.9}O_{3-\delta}$ under a) isothermal and b) isosteric conditions using the $\langle Fe'_{Fe} - V_O^{\bullet\bullet}\rangle^{\bullet}$ associate model.

The fitting parameters are listed in Table 4-6 for temperature 823, 873 and 923 K. It was decided that the increasing error with temperature is of reasonable magnitude for this temperature range (the experiments to extract kinetic parameters in chapter 5 are conducted at temperatures of up to 898 K).

Table 4-6: Parameters of fitting the defect model to $SrMn_{0.1}Fe_{0.9}O_{3-\delta}$

Temperature K	$K_{p,eq}$	K_A
823	44,844	0.5744
873	29,247	0.5786
923	20,875	0.5824

If, however, higher temperatures are of interest, then it is suggested to combine the defect model (4-33) with another defect model to decrease the introduced error. Here, excellent results were achieved by combining the cluster model with site exclusion with the $\langle B'_B - V_O^{\bullet\bullet}\rangle^{\bullet}$-defect model (4-33). As the combination of these models includes four pa-

rameters to fit the data, the confidence intervals of the individual parameters are very large. The fitted defect model is plotted versus the experimental data in Figure 4-12. Especially when comparing Figure 4-11b and Figure 4-12b it is apparent that higher temperatures are much better approximated by the combined model, however, with added uncertainty. The combined model is given by

$$pO_{2,eq} = f\left(\langle Fe_{Fe}^{\prime} - V_O^{\bullet\bullet}\rangle^{\bullet}\right)\Phi + \frac{(3-\Lambda_c\delta)^2}{\delta^2\ K_{se,eq}^2}(1-\Phi) \tag{4-35}$$

where $f\left(\langle Fe_{Fe}^{\prime} - V_O^{\bullet\bullet}\rangle^{\bullet}\right)$ is the $\langle \mathrm{Fe}_{\mathrm{Fe}}^{\prime} - \mathrm{V}_{\mathrm{O}}^{\bullet\bullet}\rangle^{\bullet}$-defect model (4-33). Here, C1 referred to in equation (4-20) is set to 2000 for a narrow transition region between the two models. The fitting parameters are given in Table 4-7 and Table 4-8 present a summary of the models used to construct the equilibrium partial pressure of oxygen curves for $SrMn_{0.1}Fe_{0.9}O_{3-\delta}$.

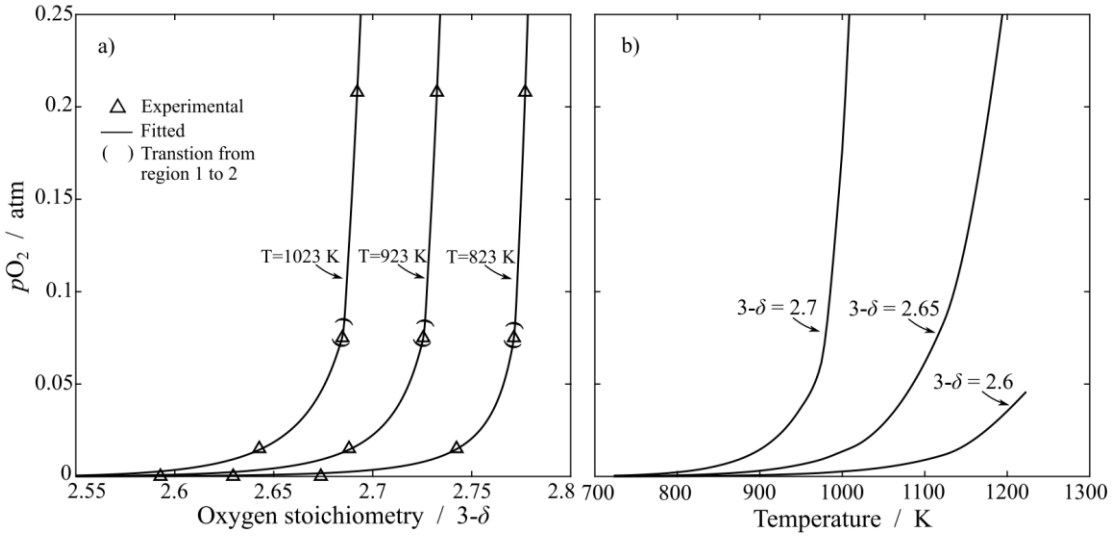

Figure 4-12: Equilibrium partial pressure of oxygen curves of $SrMn_{0.1}Fe_{0.9}O_{3-\delta}$ under a) isothermal and b) isosteric conditions. The transition from region 1 to 2 describes the region of pO_2 that is fitted by a combination of the $\langle \mathrm{Fe}_{\mathrm{Fe}}^{\prime} - \mathrm{V}_{\mathrm{O}}^{\bullet\bullet}\rangle^{\bullet}$ associate model and the cluster model with site exclusion REDO

Table 4-7: Parameters of fitting the two-region defect model to $SrMn_{0.1}Fe_{0.9}O_{3-\delta}$ at a confidence interval of 95 %. For the cluster model with site exclusion, *i.e.* $K_{se,eq}$ and Λ_c, no confidence interval is presented as the fit is done against only 2 points, pO_2 of 0.075 bar and 0.21 bar.

Temperature K	$K_{p,eq}$	K_A	$K_{se,eq}$	Λ_c	δ_{mid}
823	29,399±49,860	0.572±0.008	3.394	12.614	0.224
848	21,963±48,150	0.574±0.009	3.128	11.985	0.236
873	16,762±44,810	0.576±0.012	2.871	11.432	0.248
898	13,163±43,730	0.578±0.013	2.626	10.942	0.260
923	10,454±41,223	0.580±0.016	2.394	10.507	0.272
1023	4,345±29,973	0.586±0.023	1.613	9.166	0.314
1123	1,988±15,612	0.590±0.031	1.036	8.261	0.350

Table 4-8: Summary of defect models used for $SrMn_{0.1}Fe_{0.9}O_{3-\delta}$

Model name	Model equation	Equation number
Cluster defect model with site exclusion	$pO_{2,eq}^{0.5} = \frac{(3-\Lambda_c\delta)}{\delta K_{se,eq}}$	(4-12)
$\langle B_B^{'} - V_O^{\bullet\bullet}\rangle^{\bullet}$ −Cluster defect model $f\left(\langle Fe_{Fe}^{'} - V_O^{\bullet\bullet}\rangle^{\bullet}\right)$	$pO_{2,eq}^{0.5} = \frac{(3-\delta)(1-2\delta)^2}{\left(1-\left[\langle B_B^{'} - V_O^{\bullet\bullet}\rangle^{\bullet}\right]\right)\left(2\delta-\left[\langle B_B^{'} - V_O^{\bullet\bullet}\rangle^{\bullet}\right]\right)^2 K_{p,eq}}$	(4-33)
Combined defect model	$pO_{2,eq} = f\left(\langle Fe_{Fe}^{'} - V_O^{\bullet\bullet}\rangle^{\bullet}\right)\Phi + \frac{(3-\Lambda_c\delta)^2}{\delta^2\ K_{se,eq}^2}(1-\Phi)$	(4-22) and (4-35)

The partial pressure of oxygen calculated from the combined defect model, $pO_{2,fit}$, using the parameters listed in Table 4-7 is shown in Table 4-9. The models increasingly over-estimate the equilibrium partial pressure of oxygen for pO_2 = 10^{-5} bar with an increase in temperature. Further, in the high pO_2 region, the accuracy decreases leading to a significant underestimation for temperature above 923 K.

Table 4-9: Experimental data and fitted pO$_2$ for SrMn$_{0.1}$Fe$_{0.9}$O$_{3-\delta}$. δ_{exp} is the oxygen stoichiometry derived from the TGA experiments and listed in Table 4-2. $pO_{2,exp}$ and $pO_{2,fit}$ are the experimentally used and fitted partial pressure of oxygen.

Temperature K	$3-\delta_{exp}$	$pO_{2,exp}$ bar	$pO_{2,fit}$ bar
823	2.676	10^{-5}	0.00184
	2.743	0.015	0.01515
	2.770	0.075	0.06317
	2.776	0.210	0.17486
873	2.650	10^{-5}	0.00209
	2.714	0.015	0.01502
	2.749	0.075	0.08551
	2.755	0.210	0.21260
923	2.626	10^{-5}	0.00216
	2.688	0.015	0.01434
	2.727	0.075	0.08829
	2.734	0.210	0.23426
1023	2.593	10^{-5}	0.00275
	2.641	0.015	0.01375
	2.684	0.075	0.07319
	2.692	0.210	0.19237
1123	2.571	10^{-5}	0.00369
	2.607	0.015	0.01476
	2.647	0.075	0.06956
	2.656	0.210	0.19445

4.5 Conclusion

The change in mass observed *via* thermogravimetric analysis has been successfully mapped to defect models for $SrFeO_{3-\delta}$ and $SrMn_{0.1}Fe_{0.9}O_{3-\delta}$ to construct curves of the equilibrium partial pressure of oxygen, $pO_{2,eq}$. Under an atmosphere of nitrogen as supplied (~10 ppm O_2), both materials did not reduce to the pure brownmillerite phase. In the TGA experiments, it was possible to reduce the manganese-doped $SrFeO_{3-\delta}$ to higher oxygen non-stoichiometries, δ, than what was observed for $SrFeO_{3-\delta}$. Arguing that the energy required to reduce a non-stoichiometric oxygen carrier increases with a decrease in the iron content (Vieten *et al.*, 2017), contradicts the observations made in this study. However, Vieten *et al.* (2017) suggest that the lower $pO_{2,eq}$ observed for $SrMn_{0.1}Fe_{0.9}O_{3-\delta}$ can be explained by an increase in the entropic driving force due to the dopant; the Mn^{4+} was found to reduce only at high δ when most of the iron is already reduced to Fe^{3+}. Hence, when the manganese starts to reduce at high δ the change in entropy increases significantly, likely because the addition of a second species to the reduction process increases the number of possible configurations in the crystal lattice (Vieten *et al.*, 2017). This would suggest that adding further B-site cations would further increase the entropic driving force, allowing for a deeper reduction.

The best fits were obtained when combining two defect models to accurately describe a wide range of temperatures, one for the low pO_2 and one for high pO_2 regions. For $SrFeO_{3-\delta}$, the equilibrium partial pressure curve was most accurately described by the point defect model for $pO_2 \leq 0.015$ bar. For partial pressures of oxygen of above 0.015 bar, the cluster model with site exclusion was used to reproduce the high gradient at $pO_2 > 0.015$ bar. In case of the Mn-doped $SrFeO_{3-\delta}$, the gradient at high pO_2, *i.e.* above 0.075 bar, was found to be even higher than that observed for $SrFeO_{3-\delta}$. Here, again the cluster model with site exclusion in combination with a defect model allowing for charged defect, *i.e.* $\langle Fe'_{Fe} - V_O^{\bullet\bullet} \rangle^{\bullet}$ achieved the best fit. When limiting the temperature range to temperatures below 898 K, then the $\langle Fe'_{Fe} - V_O^{\bullet\bullet} \rangle^{\bullet}$-defect model describes the measured change in oxygen stoichiometry with sufficient accuracy. It should be noted that as only few data points were evaluated, the confidence intervals of the determination of the parameters are large.

5 Reaction Kinetics of $SrFeO_{3-\delta}$ and $SrMn_{0.1}Fe_{0.9}O_{3-\delta}$

The objective of this chapter is to determine the rate equations of the two strontium ferrites $SrFeO_{3-\delta}$ and $SrMn_{0.1}Fe_{0.9}O_{3-\delta}$. The rate equations for oxidation and reduction are of interest as they – together with the (known maximum) oxygen transfer capacity (*OTC*) – dictate the solid inventory, *i.e.* the amount of oxygen carrier, required.

5.1 Introduction

Of the many studies that investigate chemical looping air separation, only few quantified the kinetic parameters for oxidation and reduction in detail; a non-exhaustive list of materials that reversibly take up and release oxygen *via* a chemical reaction and for which kinetic parameters are reported include cobalt oxides (Li, Zhang and Cai, 2008; Zhang, Li and Cai, 2009; Hui Song, Shah, Doroodchi, Wall, *et al.*, 2014), copper oxides with various supporting materials (Cuadrat *et al.*, 2012; Clayton, Sohn and Whitty, 2014; Hu *et al.*, 2014; Hui Song, Shah, Doroodchi, Wall, *et al.*, 2014), *e.g.* SiO_2, TiO_2 or ZrO_2, the perovskites $SrFeO_{3-\delta}$ (Bychkov, Popov and Nemudry, 2016), $SrCo_{0.8}Fe_{0.2}O_{3-\delta}$ (Starkov *et al.* 2014).

The general form for the reaction of an oxygen carrier is given in equation (1.17) is typically represented by a rate constant, k, and is given by the Arrhenius equation

$$f(T) = k = A\ exp\left(-\frac{E_a}{RT}\right) \tag{5-1}$$

where A denotes the pre-exponential factor, E_a is the activation energy and R the universal gas constant.

For the reaction $6\ CoO + O_2 \rightleftarrows 2\ Co_3O_4$, Li, Zhang and Cai (2008) determined the rate equations to be

$$\frac{dX_{oxi}}{dt} = A\ exp\left(-\frac{E_{a,oxi}}{RT}\right)\left(C_{O_2} - C_{O_2,eq}\right)(1-X)^{2/3} \tag{5-2}$$

$$\frac{dX_{red}}{dt} = A\ exp\left(-\frac{E_{a,red}}{RT}\right)\left(\frac{pO_2 - pO_{2,eq}}{pO_{2,eq}}\right)^{0.8}(1-X)^{2/3} \tag{5-3}$$

where X is the conversion, C_{O_2} and $C_{O_2,eq}$ the actual and equilibrium concentrations of oxygen and $p\mathrm{O_2}$ and $p\mathrm{O_{2,eq}}$ the actual and equilibrium partial pressure of oxygen, respectively (Li, Zhang and Cai, 2008). The pre-exponential factor and the activation energy were determined to be 2.362×10^4 and 13.7 kJ mol^{-1} for the oxidation of CoO and 2.135×10^3 and 110 kJ mol^{-1} for the reduction of Co_3O_4. Co_3O_4 supported by 30 wt.-% of Al_2CoO_4 showed good stability over 20 cycles using air at 873 to 1123 K for the oxidation and CO_2 at 1198 to 1208 K for the reduction (Zhang, Li and Cai, 2009). It was possible to produce a continuous flow of oxygen with $p\mathrm{O_2}$ greater than 0.2 bar, when using two packed beds filled with 150 and 250 g of carrier material in parallel.

For CuO supported with SiO_2 (18/82 wt.-%), Song *et al.* (2014) used

$$\frac{dX}{dt} = A\ exp\left(-\frac{E_a}{RT}\right)\left(C_{O_2} - C_{O_2,eq}\right)^n f(X) \tag{5-4}$$

to fit the rate of reaction. Here, C_{O_2} and $C_{O_2,eq}$ denote the actual and equilibrium concentration of oxygen, n the order of the reaction and $f(X)$ a function determined by the reaction mechanism. The activation energies were reported to be 315 and 176 kJ/mol for the reduction process at 1073 to 1173 K and 1173 to 1248 K, respectively (Hu Song *et al.*, 2014); the two very different values for the activation energies of CuO are believed to be due to a diffusional effect being more intense in the lower temperature regime. The pre-exponential factors were found to be 1.595×10^{14} min^{-1} and 1.189×10^8 min^{-1}. The oxidation proceeded with pre-exponential factors of 2.67 m$^{3/2}$ mol$^{-1/2}$ min^{-1} and 0.024 m$^{3/2}$ mol$^{-1/2}$ min^{-1} and activation energies of 3 kJ/mol and -43 kJ/mol at 1073 to 1173 K and above 1173 K, respectively.

If instead, CuO was supported by 50 wt.-% TiO_2 or 45 wt.-% ZrO_2, for the oxidation, the pre-exponential factors and activation energies would be 6.2×10^{-13} g s^{-1}·bar$^{-1.3}$ and 172 kJ/mol, or 3.4×10^{-12} g s^{-1}·bar$^{-1.3}$ and 165 kJ/mol at temperatures below 1073 K (Clayton, Sohn and Whitty, 2014). The rate equation proposed was

$$\frac{dX}{dt} = A\, exp\left(-\frac{E_a}{RT}\right)\left(pO_2^{\beta} - pO_{2,eq}^{\beta}\right) f(X) \tag{5-5}$$

where β is a factor influencing the pressure driving force and $f(X)$ is given by $\exp(-X/\varsigma)$. Here, ς is the pore-blocking constant and determined to be -2.95 × 10^{-4} (T-273.15) + 0.34 and -3.55 × 10^{-4} (T-273.15) + 0.41 for the TiO_2-doped and ZrO_2-doped CuO, respectively; β is 1.3 in both cases. For temperatures above 1073 K, it is suggested $f(X)$ takes the form $1 - X$ and β remains at 1.3. At temperatures exceeding 1073 K, for 50 wt.-% TiO_2, the pre-exponential factor, A, was found to be 5.6 × 10^4 g s^{-1}·$bar^{-1.3}$ and E_a equal to 68 kJ/mol. In case of CuO doped with 45 wt. % ZrO_2, A and E_a were 5.65 × 104 g s^{-1}·$bar^{-1.3}$ and 71 kJ/mol, respectively.

For more complex (non-stoichiometric) materials the general form of the rate equation (1-17) is not sufficient, as the factors are no longer independent. In the case of perovskite-type materials, the equilibrium partial pressure of oxygen is not only dependent on the temperature, but also the oxygen non-stoichiometry, δ, *e.g.*

$$r_{O_2} = A\, e^{\frac{-E_a}{RT}}\left(pO_2 - pO_{2,eq}(T,\delta)\right) f(\delta) \tag{5-6}$$

$f(\delta)$ is a function representing the dependence of the rate on the oxygen non-stoichiometry, δ being a proxy for conversion. To analyse kinetic parameters, it is convenient to set the other parameters constant, although this is not always possible to achieve experimentally. Starkov *et al.* (2014) developed a method, where, by changing the inlet partial pressure of oxygen to a fixed bed incrementally, the conditions of the oxygen release can be described as approximately constant in δ. For example, the rate equation for the perovskite $SrCo_{0.8}Fe_{0.2}O_{3-\delta}$ at constant δ (~0.5-0.505) is suggested to be

$$X = exp(-kt) \tag{5-7}$$

$$k = A\, exp\left(-\frac{E_0 + \alpha_1\delta}{RT}\right) exp(-\alpha_0\delta) \tag{5-8}$$

where the parameters α_0 and α_1 are 171 ± 15 δ^{-1} and 2012 ± 137 kJ s^{-1} δ^{-1}, respectively, and E_0 denotes the part of the activation energy, E_a, that is independent of the oxygen non-stoichiometry, δ (Starkov *et al.* 2014). The conversion of the solid, X, is, in this case, a function of the initial oxygen non-stoichiometry, δ_0, and the final oxygen non-stoichiometry, δ_f, at the respective temperature and partial pressure of oxygen.

In this chapter, the reaction kinetics of strontium ferrites, doped with manganese and pure, are investigated. For both materials, the activation energy, E_a, and the pre-exponential factor, A, are determined for the oxygen release reaction.

5.2 Results

The packed bed micro reactor described in section 3.3.1 was used to extract information about the reaction kinetics of $SrFeO_{3-\delta}$ and $SrMn_{0.1}Fe_{0.9}O_{3-\delta}$.The two solid beds are made up of 0.611 g and 0.648 g of $SrFeO_{3-\delta}$ and $SrMn_{0.1}Fe_{0.9}O_{3-\delta}$, respectively, and surrounded by approximately 0.2 g of Al_2O_3 both upstream and downstream.

The total amount of oxygen released and taken up per gram of $SrFeO_{3-\delta}$ and $SrMn_{0.1}Fe_{0.9}O_{3-\delta}$ during each of the four redox cycles, cycling between air and nitrogen, of the 900 s lasting experiment is shown in Figure 5-1a and b, respectively. The amount of oxygen taken up and released increases with an increase in temperature for both materials. At 798 K, the pure strontium ferrite released more oxygen than the doped oxygen carrier. With an increase in temperature, however, $SrMn_{0.1}Fe_{0.9}O_{3-\delta}$ showed a significantly higher oxygen transfer capacity, *OTC*, than $SrFeO_{3-\delta}$ during the 90 s long reduction and oxidation intervals. For both materials and temperatures of above 873 K, the amount of oxygen taken up and released was found to be approximately equal to or higher than what was expected from the TGA experiments.

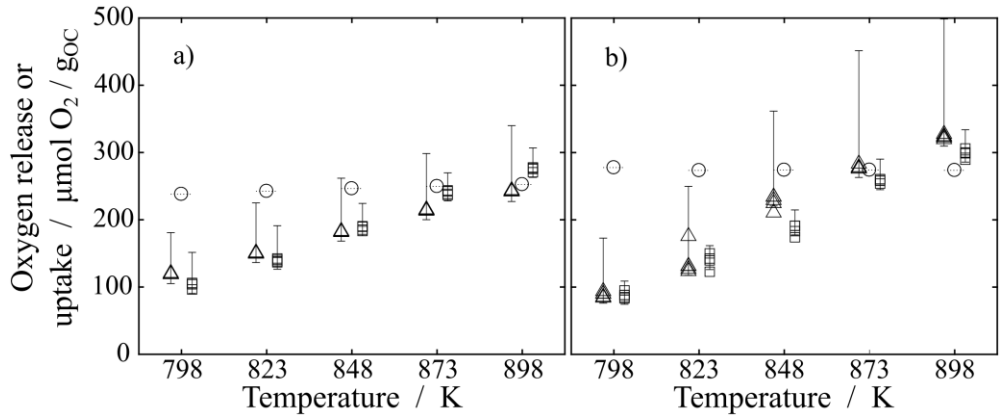

Figure 5-1: Molar amount of oxygen taken up and released during the oxidation (squares) and reduction (triangles) per gram of $SrFeO_{3-\delta}$ (left) and $SrMn_{0.1}Fe_{0.9}O_{3-\delta}$ (right), respectively. The circles indicate the expected molar uptake and release from TGA experiments after settling for ~1 hour as described in section 3.2.2. The error bars indicate errors of the fourth redox cycle, arising from potentially different calibration of the sensor at elevated temperature.

The difference in the blank and the high temperature experiment, Δx_{O_2}, is plotted in Figure 5-2 for $SrFeO_{3-\delta}$ over the four cycles of the experiment. Both the total amount of oxygen taken up and released and the rate at which the oxidation and reduction occur over time were very repeatable over the course of the four redox cycles, as shown in Figure 5-1 and Figure 5-2. At temperatures above 798 K, the maximum Δx_{O_2} of the reduction was only half of that of the oxidation, as shown in Figure 5-2 I. The reason for this is that, during the oxidation at those temperatures, the entire inflow of oxygen is taken up by the material for a certain period of time before the breakthrough at the oxygen sensor occurs, as indicated by $\Delta x_{O_2} \cong 0.21$. Therefore, the rate was limited by the amount of oxygen entering the bed and the oxidation at temperatures of above 798 K proceeds in an integral regime. This is supported by looking at the time delay observed between switching the inlet gas and observing a change in the output of the oxygen sensor. The average time delay and the corresponding standard deviation over four cycles is listed in Table 5-1 for the different temperatures. With an increase in temperature, the time delay decreases due to the increase in fluid velocity. In the case of the reduction reaction, the velocity increases not only due to the reduced density of the gaseous flow but also due to production of oxygen of up to a pO_2 of 0.1 bar at 898 K. For the oxidation reaction, this effect is reversed, especially given that at high temperatures the gaseous flow decreases by roughly 21 vol.-% as all of the oxygen is adsorbed.

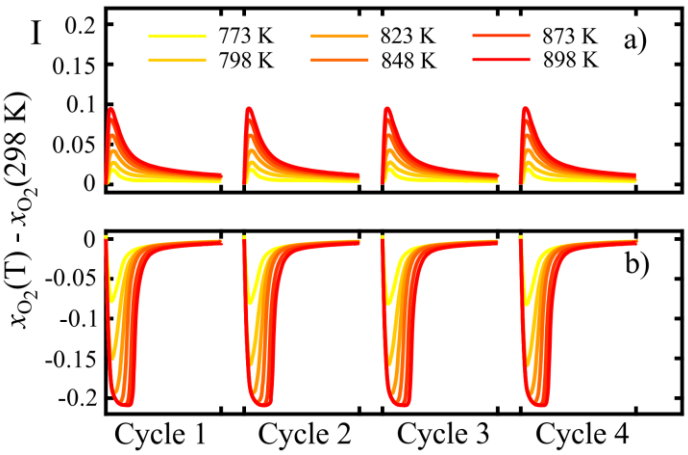

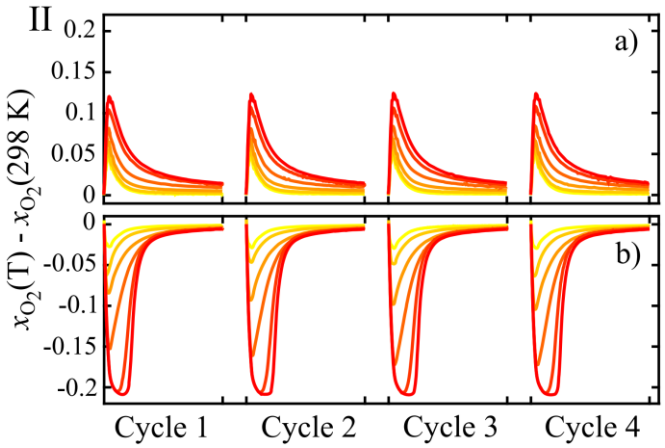

Figure 5-2: First 10 s of the difference in the mole fraction of oxygen, Δx_{O_2}, of the experiment conducted at 293 K and those conducted at higher temperatures for a) the reduction and b) the oxidation of $SrFeO_{3-\delta}$ (I) and $SrMn_{0.1}Fe_{0.9}O_{3-\delta}$ (II).

A more detailed view on the oxidation for both materials is presented in Figure 5-3. The figure shows the first 1.5 s after switching from nitrogen to air. The time delay until the breakthrough is observed increases significantly with an increase in temperature for both materials. However, there are differences to be observed: For $SrFeO_{3-\delta}$ (Figure 5-3a), at 798 K, for a brief period, all oxygen is taken up by the material, which occurs only at 848 K for $SrMn_{0.1}Fe_{0.9}O_{3-\delta}$. Further, $SrFeO_{3-\delta}$ exhibited a higher initial rate of oxidation than $SrMn_{0.1}Fe_{0.9}O_{3-\delta}$, but the response times, $\tau_{10\rightarrow90}$, was found to be lower, resulting in an overall lower amount of oxygen taken up during the oxidation interval.

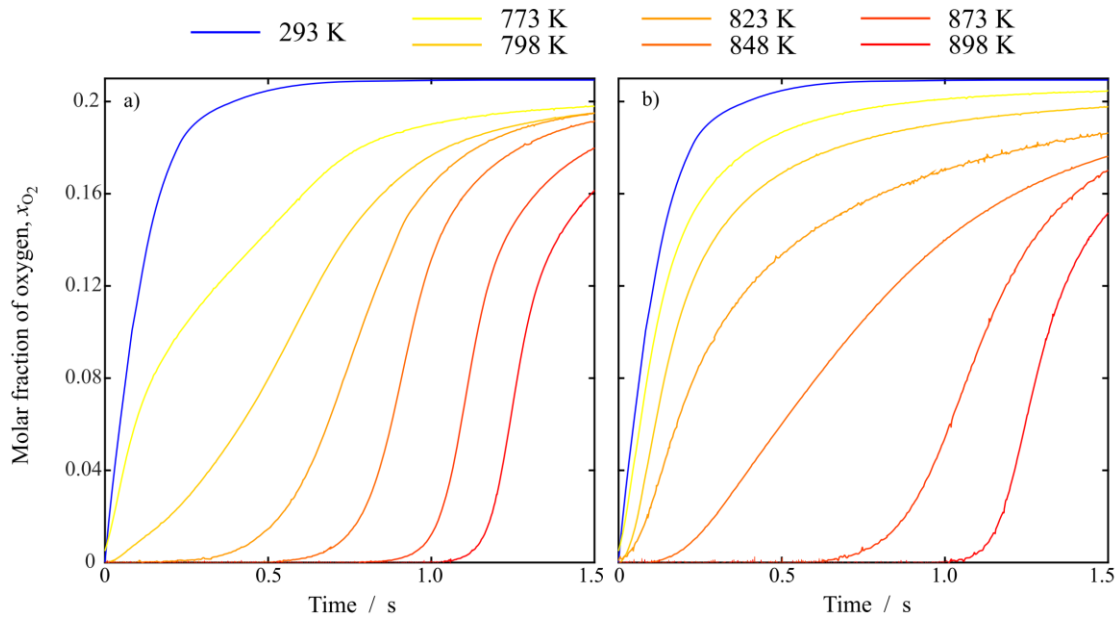

Figure 5-3: The first 1.5 s of the oxidation after switching from nitrogen to air for a) of $SrFeO_{3-\delta}$ and b) $SrMn_{0.1}Fe_{0.9}O_{3-\delta}$.

The observed rate of oxygen production per gram of oxygen carrier, $r_{O_2,prod}$, is plotted in Figure 5-4 at various temperatures. The triangles denote the maximum rate, $r_{O_2}^m$, at each temperature. The rate of reduction exhibited a clear dependence on temperature for both materials, as shown in Figure 5-4. When comparing the maximum rates, it was found that while the rates at 898 K differed by only about 25 %, at 798 K the rate of oxygen release of $SrMn_{0.1}Fe_{0.9}O_{3-\delta}$ was almost three times as high as that of $SrFeO_{3-\delta}$.

Table 5-1: Time delays observed in a bed of 0.611 g of $SrFeO_{3-\delta}$ contained in 0.21 and 0.23 g of Al_2O_3 upstream and downstream, respectively, at temperatures up to 898 K. Small values of the standard deviation of the sample, σ, indicate that values have been eliminated because they were found to be outliers as per Matlab's *isoutlier* function.

Temperature	Oxidation		Reduction	
	Time delay	σ	Time delay	σ
K	ms	ms	ms	ms
298	132	4.50	124	5.89
773	125	12.37	103	6.77
798	122	13.72	100	5.43
823	287	3.79	71	10.25
848	641	23.10	56	12.05
873	910	12.19	52	4.97
898	1116	10.58	54	6.58

$SrMn_{0.1}Fe_{0.9}O_{3-\delta}$ did not only exhibit a higher maximum rate but also released a substantial amount of oxygen for longer than $SrFeO_{3-\delta}$. For $SrFeO_{3-\delta}$ ($SrMn_{0.1}Fe_{0.9}O_{3-\delta}$), the response time of the system downstream of the gas switching valves, $\tau_{10\rightarrow90}$, was determined to be 273 (302), 714 (675), 1317 (971), 1670 (1773), 2074 (3120) and 2358 (3500) ms at 298 K and temperatures of 798 to 898 K in ascending order. Therefore, $SrMn_{0.1}Fe_{0.9}O_{3-\delta}$ released more oxygen before the molar fraction of oxygen dropped to 0.021 (10 % of the signal) at the oxygen sensor. In fact, despite the higher maximum rate of oxygen production, the manganese-doped strontium ferrite continued to release more oxygen than $SrFeO_{3-\delta}$ until the gas was switched to air again.

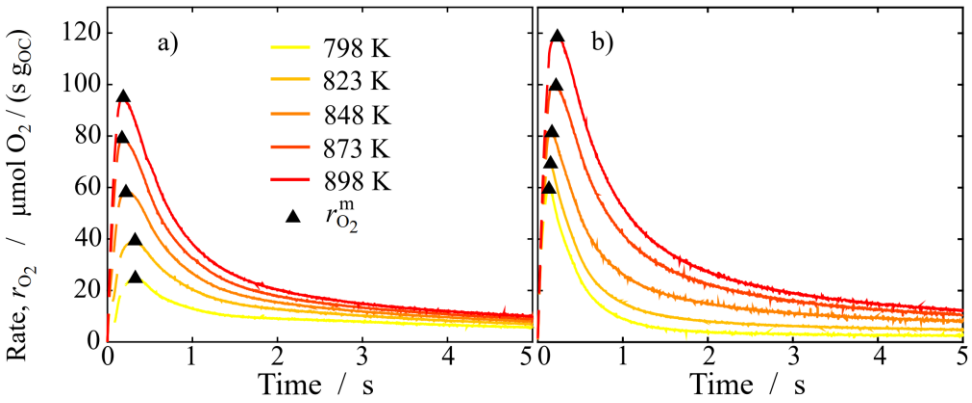

Figure 5-4: Observed rate of reduction of a) $SrFeO_{3-\delta}$ and b) $SrMn_{0.1}Fe_{0.9}O_{3-\delta}$ at various temperatures. The triangles denote the point at which the rate is at its maximum, $r^{m}_{O_2}$. The open symbols refer to the oxygen stoichiometry at that point.

In a second experiment, both the mass of the oxygen carrier in the bed was reduced from 0.611 g to 0.025 g and the mass flow rate increased from 750 sccm to 1000 sccm. The time delay, *i.e.* the time expired between triggering the valve system to switch the gases and recording a change in the signal of the oxygen sensor, is listed in Table 5-2. At high temperatures, the time delay decreased for both the oxidation and the reduction; in the case of the oxidation, this indicates that not all oxygen entering the reactor is adsorbed as observed at the previous experiment with > 600 mg of material. Therefore, using such small quantities of the oxygen carrier material, the oxidation proceeds under conditions that allow for the extraction of the kinetics.

Table 5-2: Time delays observed in a bed of 0.025 g of $SrFeO_{3-\delta}$ contained in 0.6 and 0.17 g of Al_2O_3 upstream and downstream, respectively, at temperatures up to 898 K. Small values of the standard deviation of the sample, s, indicate that values have been eliminated because they were found to be outliers as per Matlab's *isoutlier* function.

Temperature	Oxidation		Reduction	
	Time delay	σ	Time delay	σ
K	ms	ms	ms	ms
298	135	4.8	97	6.2
798	103	6.2	67	5.2
823	100	5.3	63	4.1
848	96	4.4	63	6.0
873	61	0.6	58	1.6
898	61	1.9	59	2.1

The first 500 ms of raw data of those experiments conducted at elevated temperatures are presented in Figure 5-5a) and b) for the reduction and oxidation, respectively. The blue line shows the mean of the four cycles for the reduction and oxidation at 298 K. However, as shown in Figure 5-5, the wiggles observed at temperature below 848 K make it difficult to extract meaningful data. During the reduction, the blank and the experiments conducted at temperatures above 848 K did not exhibit a significant difference to accurately determine the amount of oxygen released by the $SrFeO_{3-\delta}$. The data collected at 898 K during the oxidation shows enough of a difference to the blank at room temperature to extract information; from TGA experiments an uptake of 6 µmol of O_2 were expected and 5 µmol of O_2 were observed for all four cycles. The derivation of kinetic parameter, however, was not possible from these data as the signals at lower temperatures must be discarded because of aforementioned wiggles.

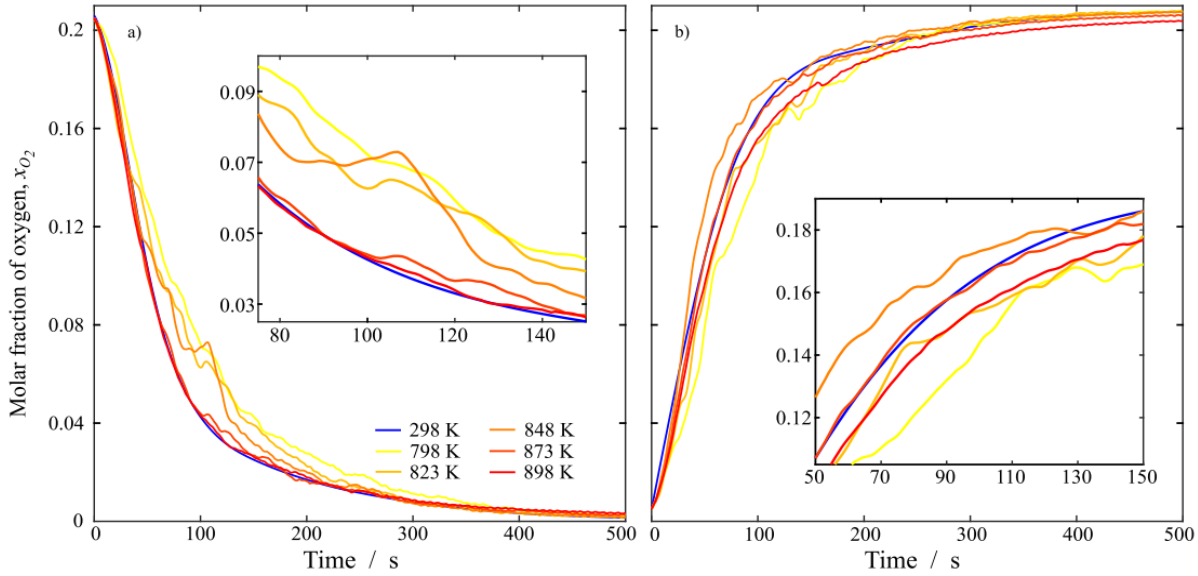

Figure 5-5: Raw data (signal at 298 K is averaged) for 25 mg of $SrFeO_{3-\delta}$ at a flow rate of 1000 sccm

5.3 Discussion

Arguing that the initial rate is approximately equal to the maximum rate, as observed in Figure 5-4, then the starting and end stoichiometries of the reduction and the oxidation for $SrFeO_{3-\delta}$ at the various temperatures investigated are listed in Table 5-3. The table also shows the amount of oxygen released and taken up as expected from TGA experiments. The quantification of the confidence interval of the oxygen uptake is explained in the appendix. Over the four redox cycles, the reduction was determined to repeatably give of less oxygen than is adsorbed during the oxidation. However, this is most likely an error that can be attributed to the calibration of the reference voltage for nitrogen at the different temperatures. A drift in the output voltage at different temperatures was observed for both the signal in air and in nitrogen. The one-point calibration arguably ensured only certainty about the voltage read when using air. For example, if the voltage recorded for nitrogen at high temperatures was used, then the results obtained are shown in Figure 5-1 and Table 5-3. If, however, it is believed that the accurate output voltage for a partial pressure of oxygen is that recorded at room temperature, *i.e.* the blank experiment, then the lower voltage would lead to an increase in the area between the blank and the curve recorded at high temperature, *i.e.* the calculated amount of oxygen produced over the interval would increase; this amount is taken as the maximum error shown in Figure 5-1. It can be seen

from Figure 5-1, that the potential difference in assumed zero voltage is more than sufficient to account for the small difference observed between yields in oxidation and reduction.

Table 5-3: Oxygen release and uptake of 0.611 g of SrFeO3-δ during 90 s in nitrogen and air for the reduction and oxidation, respectively. The 95 % confidence intervals shown for the oxidation at temperatures above 798 K correspond to ±1.96 $SE_t(T)$ (see appendix). The corresponding oxygen stoichiometry, 3-δ, for the oxidation is based on the end oxygen stoichiometry of the reduction. The starting oxygen stoichiometry is equal to the oxygen stoichiometry measured by TGA at the respective temperature and the final oxygen stoichiometry is calculated from the observed O_2 release and uptake in this experiment

Temperature	TGA	Reduction		Oxidation	
		O_2 release	3-δ (start → end)	O_2 uptake	3-δ (start → end)
K	µmol	µmol	µmol	µmol	µmol
798	145	73	2.78 → 2.73	82±1.7	2.73 → 2.78
823	148	92	2.77 → 2.71	107±1.1	2.71 → 2.77
848	151	114	2.75 → 2.68	129±2.9	2.68 → 2.76
873	154	133	2.74 → 2.66	155±1.5	2.65 → 2.74
898	156	151	2.73 → 2.64	178±1.4	2.63 → 2.73

A comparison of the rate constant derived from the integral and the differential analysis, *i.e.* equations (3-39) to (3-41), is plotted in Figure 5-6. It can be seen, that the rate constant for reduction of the manganese-doped strontium ferrite is larger than that for $SrFeO_{3-\delta}$. For the combination of high temperature and large reaction rate constant, *k*, it becomes apparent that the differential analysis (equation (3-41) is invalid for $SrMn_{0.1}Fe_{0.9}O_{3-\delta}$. At temperatures above 823 K, *viz.* $1.215 \cdot 10^{-3}$ K^{-1} in the figure, the differential and integral analysis diverge. This corresponds to the material producing a partial pressure of oxygen in the N_2, which is a large faction of the pO_2 of 0.21 bar the material was initially equilibrated with. In contrast, there is less difference between the integral and differential analysis for the more slowly reacting $SrFeO_{3-\delta}$, indicating that treating the reactor as being differential is not too bad of an approximation over the range of conditions examined; though at temperatures higher than 848 K the divergence between the integral and differential analysis becomes apparent. The average values of *k* are reported in Table 5-4.

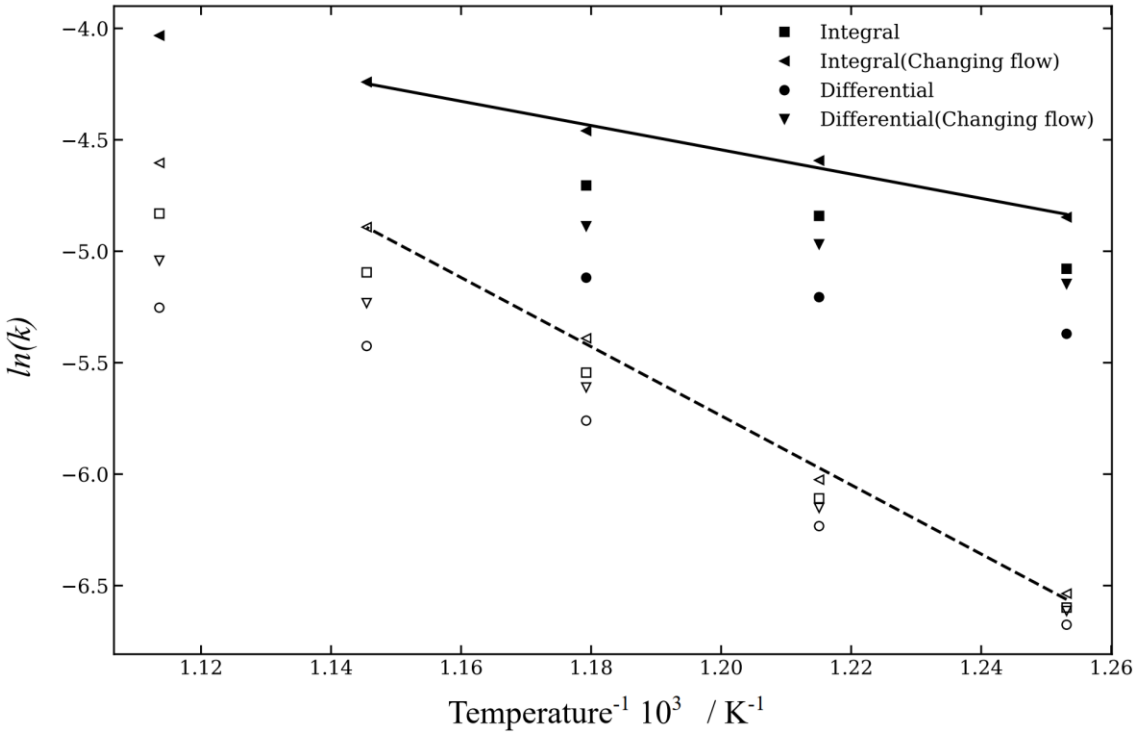

Figure 5-6: Arrhenius plots for $SrFeO_{3-\delta}$ (unfilled symbols) and $SrMn_{0.1}Fe_{0.9}O_{3-\delta}$ (filled symbols) using the different methods to evaluate the rate constant at the maximum observed rate, $r_{O_2}^m$. The solid line indicates the fit used to evaluate the activation energy (integral case, with changing flow).

Table 5-4: : Values of the kinetic constant, *k*, computed by the different methods and the values of $kRTL/v_{in}$. The average of 4 cycles is shown. The standard error is not shown, but is typically ~1% of the value.

Temperature K	kinetic rate constant, ***k*** mol/s/Pa/m^3				$\frac{kRTL}{v_{in}}$
	Differential	Integral	Differential accounting for changes in velocity	Integral Accounting for changes in velocity	
			$SrFeO_{3-\delta}$		
798	0.00126	0.00136	0.00134	0.00145	0.17
823	0.00196	0.00222	0.00213	0.00242	0.28
848	0.00315	0.00391	0.00366	0.00456	0.52
873	0.00440	0.00613	0.00534	0.00751	0.86
898	0.00523	0.00798	0.00646	0.01001	1.15
			$SrMn_{0.1}Fe_{0.9}O_{3-\delta}$		
798	0.00465	0.00623	0.00582	0.00785	0.77
823	0.00548	0.00790	0.00695	0.0101	1.00
848	0.00598	0.00905	0.00754	0.0116	1.14
873	0.00680	0.0113	0.00850	0.0144	1.42
898	0.00751	0.0137	0.00944	0.0177	1.75

The maximum apparent reaction rate constant in the external mass transfer limit, k^m, (equation (3-35)) is between 8.1 and 8.4 mol/s/Pa/m^3 , assuming a gas diffusivity, D_{O_2}, of 1.1 to 1.3·10^{-4} m^2/s at temperatures between 798 and 898 K. This is several orders of magnitudes larger than those presented in Table 5-4. Therefore, the kinetic constants are not strongly influenced by external mass transfer, and the lowering of the slope of the Arrhenius plots as the temperature increases is probably due to a break down in the assumption that there is no significant conversion of the oxygen carrier. The integral analysis that accounts for a change in the mass flow along the bed appears to have a consistent activation energy over the range studied. This is supported by the values of $kRTL/v_{in}$ which are about unity at the highest temperature as shown in Table 5-4.

From Figure 5-6, it can be noted that there is a much larger discrepancy between the values of the rate constant for the reduction of $SrMn_{0.1}Fe_{0.9}O_{3-\delta}$ for the different methods than for the pure strontium perovskite. At the lowest temperature, $kRTL/\,v_{in}$ for $SrMn_{0.1}Fe_{0.9}O_{3-\delta}$ (0.77) is higher than the highest temperature to which the kinetics of $SrFeO_{3-\delta}$ are evaluated (0.52). The differential analysis for the Mn-doped strontium ferrite is invalid and corresponds to the material producing oxygen at a partial pressure of oxygen which is initially a large fraction of the 0.21 bar the material was equilibrated with during the oxidation. In contrast, the difference between the integral and differential analysis is smaller for the more slowly reacting pure strontium ferrite.

The apparent activation energy for $SrFeO_{3-\delta}$ is computed excluding temperatures above 848 K and was found to be 129 kJ/mol. As shown in Table 5-5, similar activation energies are obtained for the other methods, providing the higher temperatures are excluded, as might be expected if the apparent reduction in activation energy is caused by deviations from the differential behaviour. These values are close to what can be found in literature; for pO_2 of 0.15 and 0.5 bar, Yoo *et al.* (2005) found activation energies of -128 and -98 kJ/mol, respectively. At an oxygen stoichiometry of approximately 2.64, which corresponds to the reduction in nitrogen at 898 K, as shown in Table 5-3, $E_{a,app}$ was determined to be around 135 kJ mol^{-1} by Bychkov *et al.* (2016). For $SrMn_{0.1}Fe_{0.9}O_{3-\delta}$, the apparent activation energy was much lower, 45.3 kJ mol, as shown in Table 5-6, which lists the kinetic parameters derived from the Arrhenius plot in Figure 5-6. It is likely that the doped material, with its higher rate constant, was subject to some internal mass transfer

limitation, thus giving a lower sensitivity to temperature than if it were controlled purely by chemical kinetics. It is also interesting to note that the activation energy for $SrFeO_{3-\delta}$ does appear to fall off slightly at the highest temperature. The lowering of the activation energy is not caused by the influence of external mass transfer, and the values of $kRTL/v_{in}$ being around unity along with the straight Arrhenius plot for the $SrMn_{0.1}Fe_{0.9}O_{3-\delta}$ at even higher values of k suggests that the material is not becoming equilibrium limited to the extent that the integral analysis can no longer account for gradients in the bed. During reduction the reaction is endothermic, and the temperature of the solid material could fall, resulting in slower reaction.

Table 5-5: Kinetic parameters computed by the different methods for $SrFeO_{3-\delta}$. The units of A' are mol/s/Pa/m^3. Temperatures above 848K have been excluded for all except the integral analysis which accounts for velocity changes

	Differential	Integral	Differential accounting for changes in velocity	Integral accounting for changes in velocity
$\ln(A')$	8.54	11.25	10.36	12.87
$E_{a,app}$ (kJ/mol)	103.0±3.5	117.6±3.2	112.7±4.1	128.9±4.7

Table 5-6: Kinetic parameters of the integral analysis taking into account the change in the flow rate; equation (3-38). The units of A' are mol/s/Pa/m^3

	$SrFeO_{3-\delta}$	$SrMn_{0.1}Fe_{0.9}O_{3-\delta}$
$\ln(A')$	12.87	1.99
$E_{a,app}$ (kJ/mol)	128.9±4.7	45.3±3.4

The deviations from the nominal temperature should be negligible, owing to the small mass used, the small amounts of oxygen transferred and the small radius of the reactor. The maximum change in temperature of the bed can be evaluated using equations (3-46) and (3-47), which are repeated at this point for convenience:

$$\Delta T_{ub}^{1} = \frac{r_{O_2}^{V} \Delta H_r^o \, r_r^2}{4 \, \lambda}$$

$$\Delta T_{ub}^{2} = \frac{n_{O_2} \Delta H_r^o}{c_p^m \, m_{OC}}$$

Here, the enthalpy of reaction, ΔH_r^o, is approximated using

$$\Delta H_r^o = T\Delta S_r^o - RTln\left(\frac{pO_2}{p_{tot}}\right) \quad (5\text{-}9)$$

where the entropy of reaction, ΔS_r^o, is assumed to be dominated by the release of two oxygen atoms into the gas phase, as described in section 2.2.2, *i.e.* $\Delta S_r^o(298\,K) \equiv S_{O_2}^o(298\,K) = 205.2$ J/mol/K and p_{tot} is the total pressure. ΔT_{ub}^1 and ΔT_{ub}^2 are given in Table 5-7 for $SrFeO_{3-\delta}$ and $SrMn_{0.1}Fe_{0.9}O_{3-\delta}$ for a partial pressure of oxygen of 0.21 bar and assuming a specific heat capacity of 700 J/kg/K and a radial thermal conductivity, λ, of 4 W/m/K, which are reasonable assumptions for most metal oxides and strontium hexaferrite; values for strontium ferrite at the temperature range of interest were not found in the literature.

From Table 5-7 it can be noted that the expected maximum change in the temperature due to the endothermic reduction reaction is negligible and that the maximum expected temperature change is highest at higher reaction rates and temperatures.

Table 5-7: Estimated upper bounds for the difference in solid temperature when the rate is evaluated for the experiments with $SrFeO_{3-\delta}$. The volume of the bed, V_{bed}, is roughly 0.588 mm^3.

Temperature	$r_{O_2}^V$	n_{O_2}	ΔH_r^o	ΔT_{ub}^1	ΔT_{ub}^2
K	mol/s/m^3	µmol	kJ/mol	K	K
		$SrFeO_{3-\delta}$			
798	25.5	3.5	173.9	1.57	1.40
823	40.9	5.6	179.4	2.59	2.31
848	63.0	5.2	184.8	4.12	2.21
873	86.8	6.0	190.3	5.84	2.63
898	103.8	7.2	195.7	7.19	3.25
		$SrMn_{0.1}Fe_{0.9}O_{3-\delta}$			
798	65.8	3.5	173.9	4.05	1.40
823	77.0	4.1	179.4	4.89	1.69
848	89.9	5.3	184.8	5.88	2.26
873	112.3	8.2	190.3	7.57	3.60
898	128.4	10.4	195.7	8.90	4.69

The outlet concentration predicted for the equilibrium limited reduction of $SrFeO_{3-\delta}$ at 898 K is shown in Figure 5-7. The outlet concentration is calculated using equation (3-33). The time taken for the 21 % front to break through is still much longer than the

gas residence time so that the production of a constant flow of oxygen would be possible during this period. However, this breakthrough happens sooner than for oxidation and the breakthrough curve has broadened compared to the input to the bed. This would limit bed utilisation in a practical system. The experimental curve breaks through immediately and for the first 500 ms the rate of O_2 production is less than for equilibrium. After this point the "equilibrium" bed is largely exhausted, but the real bed is still able to produce oxygen, having experienced much less conversion. Thus, as might be expected from the value of $kRTL/v_{in}$, the experiment is far from equilibrium limited.

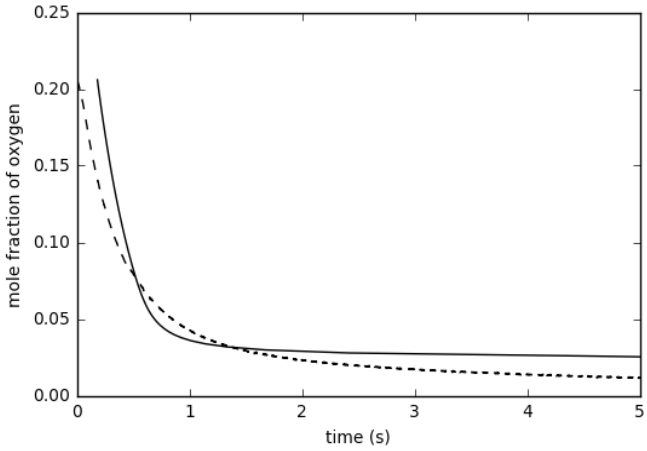

Figure 5-7: First 5 s of the measured (dashed line) mole fraction of oxygen during the reduction of $SrFeO_{3-\delta}$ at 898 K, compared with the expected concentration if reduction is limited by equilibrium.

Regarding the assumption of $\delta_i = \delta_m$, where δ_m is the oxygen non-stoichiometry at the maximum rate, it might be invalid to simply cut the first ~100 ms as, at high temperatures, the reaction kinetics might, in fact, be sufficiently fast to account for most of the observed difference in the signal of the blank and the high temperature experiment. Of course, this is a trade-off between accepting an error introduced by mixing effects and temperature effects not captured by the blank (298 K) on the one hand, and an error introduced by the release of oxygen from the material on the other hand.

Although kinetic parameters for the oxidation were not extracted as the oxidation proceeded too quickly for the quantities of material used here, the cause of the rapid initial rates of oxidation can be discussed. One possible explanation for the difference in the rate between oxidation and reduction would be that transport of the oxygen through the lattice is fast (*i.e.* not rate limiting), since both oxidation and reduction would be expected to

show comparable rates. It seems that the rapid oxygen uptake of the material is caused by the strontium ferrite perovskites possessing very quick surface reaction kinetics. In contrast, the reduction seems to be more limited by surface reaction. It may be that the conduction of oxygen atoms through the crystal lattice, *i.e.* chemical diffusion, limits the speed at which the oxidation proceeds, as, after a while, when the surface vacant sites are saturated, it takes time for the oxygen atoms to migrate further into the crystal lattice, vacating oxygen sites at the surface (for the oxidation process to proceed) (Merkle and Maier, 2008). Chemical diffusion as a limiting step may also explain the low activation energy observed for $SrMn_{0.1}Fe_{0.9}O_{3-\delta}$ which may operate at a low effectiveness factor. The effectiveness factor relates the observed rate of reaction to the rate of reaction in the absence of chemical diffusion inside the particle *via* (Fogler, 2016)

$$\eta_{eff} = \frac{r_{obs}}{r_{max}} = \frac{3}{\varphi_T}\left(\frac{1}{tanh(\varphi_T)} - \frac{1}{\varphi_T}\right) \tag{5-10}$$

where r_{obs} and r_{max} are the observed and the true maximum rate of reaction, respectively. Equation (5-10) is valid for a spherical particle undergoing a first-order reaction under isothermal and isobaric conditions. φ_T is the Thiele modulus which describes the relationship between the reaction rate and the diffusion of a particle with no mass transfer limitations. Therefore, when the reaction is limited by the intraparticle chemical diffusion, the observed rate of reaction may be a fraction of the true maximum rate of reaction and the true activation energy is equal to twice the apparent activation energy (Fogler, 2016).

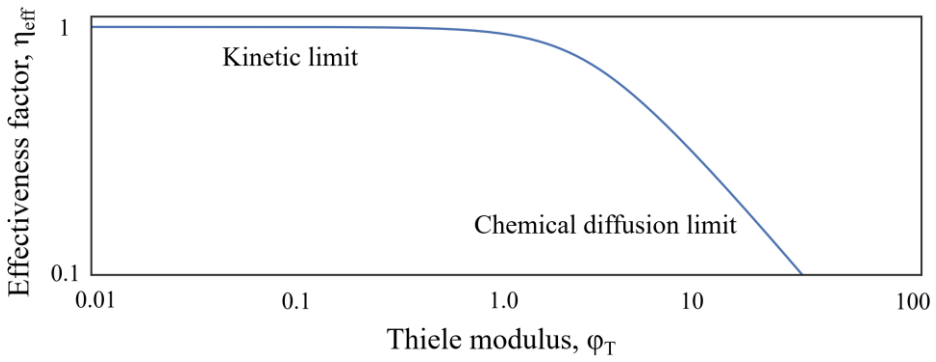

Figure 5-8: Effectiveness factor of a spherical particle for a first-order reaction as a function of the Thiele modulus.

5.4 Conclusion

The comparison of $SrFeO_{3-\delta}$ and $SrMn_{0.1}Fe_{0.9}O_{3-\delta}$ showed that doping with 10 mol% of manganese significantly increases the oxygen transfer capacity and decreases the apparent activation energy, $E_{a,app}$; both features that are desirable in oxygen carriers, as less oxygen carrier needs to be cycles to produce the same amount of oxygen and the heat demand of the reduction decreases. $E_{a,app}$ was found to be 129 kJ/mol and 45 kJ/mol for the pure and the Mn-doped strontium ferrite, respectively. However, the pre-exponential factor was also found to be much smaller for the Mn-doped material, $ln(A')$ was determined to be 12.87 and 1.99 for $SrFeO_{3-\delta}$ and $SrMn_{0.1}Fe_{0.9}O_{3-\delta}$, respectively. Whilst the integral analysis appeared to be able to account for the formation of gradients across the micro-reactor, it is likely that the low activation energy for the manganese-doped material is a result of the rate becoming limited by reaction-diffusion within the pores of the material. At the temperatures range investigated, 798 K $\leq T \leq$ 898 K, $SrMn_{0.1}Fe_{0.9}O_{3-\delta}$ exhibited an overall higher rate of reduction, with an increase in the difference of the rate constants of the two materials with a decrease in the temperature.

The tests here were deliberately run far from equilibrium during reduction to allow extraction of kinetic parameters, rather than as a demonstration of oxygen production. This required the residence time of the gas to be set very low to reduce the value of $kRT\tau_g$ to a sufficiently small value. The kinetic parameters indicated that reducing the gas space velocity by only a factor of ~10 would be sufficient to reach the equilibrium limit, *i.e.*, it would be possible to run a practical system of packed beds producing 21% oxygen without any temperature or pressure swing using packed beds. Owing to the wide variety of non-stoichiometry of the oxide material, the oxide material "remembers" the oxidizing potential of the gas it has seen during oxidation and with sufficiently fast kinetics will produce this same concentration during reduction.

In this chapter, is was also shown that if the oxidation front in the packed bed system is sharp, it is not possible to produce a sharp breakthrough front during reduction in a long, packed bed for this kind of non-stoichiometric material, *i.e.*, a constant oxygen output can only be produced before the breakthrough occurs. All these factors suggest the materials would be more suited to applications, in which they are swung rapidly between oxidation states to separate oxygen from air.

Furthermore, it was found that the oxidation proceeds at very fast rates. For practical applications, this suggests that the residence time of the solids under an oxidising atmosphere can be significantly lower than the residence time under a reducing atmosphere, as the oxidised phase is regenerated much quicker.

If the materials were used in a fluidised system, or a higher concentration of oxygen was required for oxyfuel combustion, the mixed nature of such a reactor would require the reducer to operate at a much higher temperature than the regenerator, or at a lower pressure. The TGA data indicates that $SrFeO_3$-based perovskites operate in this way over a wide temperature range, and over the temperatures examined, kinetics would be fast enough to allow the material to operate effectively.

6 Reaction kinetics of cobalt-doped $SrFeO_{3-\delta}$

In this chapter, the rate of oxygen release from $SrCo_{0.4}Fe_{0.6}O_{3-\delta}$ is investigated at various temperatures. Further, the effect of doping Co into $SrFeO_{3-\delta}$ on the oxygen transfer capacity, *OTC*, and the rate constant, *k*, is investigated, and compared with the results of Chapter 5, *i.e.* with both $SrFeO_{3-\delta}$ and $SrMn_{0.1}Fe_{0.9}O_{3-\delta}$. This is of interest here because to tune the material would widen the envelope of materials for a CLAS process. For example, the list of materials presented in chapter 2 for temperature swing could potentially be drastically extended as it did not regard dopants.

This chapter uses the same methodology as chapter 5, however, the results from the thermogravimetric analysis did not allow for the determination of the inflection point at which the brownmillerite phase is reached. Therefore, no information about the oxygen stoichiometry of the material is available as opposed to the pure strontium ferrite, $SrFeO_{3-\delta}$, and the Mn-doped strontium ferrite, $SrMn_{0.1}Fe_{0.9}O_{3-\delta}$ discussed in chapter 5.

6.1 Introduction

The addition of dopants to strontium ferrite has been shown to change kinetics and the equilibrium partial pressure of oxygen, pO_2. Vieten *et al.* (2017) investigated how the thermodynamics changed when the perovskites $SrFeO_{3-\delta}$ and $SrMnO_{3-\delta}$ were mixed and found that for x of 0.15 in $SrMn_xFe_{1-x}O_{3-\delta}$ the oxygen transfer capacity, *OTC* (oxygen release per unit mass) increases slightly, at values of x greater than 0.33, however, the *OTC* decreases significantly. When using cobalt as a dopant, a maximum in the change in mass and, therefore, in the oxygen transfer capacity was recorded for $x = 0.4$ in $SrCo_xFe_{1-x}O_{3-\delta}$ (Kusaba *et al.*, 2002). Further, Kusaba *et al.* (2002) found that only those cobalt-doped strontium ferrites with a cubic perovskite structure, *i.e.* $0.2 \leq x \leq 0.8$, showed reversible oxygen uptake and release; at $x \approx 1$ and $x \approx 0$, $SrMn_xFe_{1-x}O_{3-\delta}$ is re-

ported to adopt a 2H-$BaNiO_3$ and brownmillerite-like structure, respectively. $SrCo_xFe_{1-x}O_{3-\delta}$ doped with small quantities of copper, gadolinium, manganese, or yttrium gave a perovskite-type structure that was able to reversibly oxidise and reduce; however, with smaller *OTC* than the undoped $SrCo_xFe_{1-x}O_{3-\delta}$ (Kusaba *et al.*, 2002). Zhang *et al.* (1990) who investigated the effect of A-site and B-site doping on the perovskite $La_ySr_{1-y}Co_xFe_{1-x}O_{3-\delta}$, showed that doping the B-site with cobalt improved the oxygen release at lower temperatures. They found the maximum amount of oxygen release for x = 0.4, suggesting that the bonding strength of the sorbed oxygen is the weakest for the combination of 0.6 Fe and 0.4 Co.

The catalytic activity of $La_ySr_{1-y}Co_xFe_{1-x}O_{3-\delta}$ for the decomposition of H_2O_2 and the combustion of methane was also shown to change with both A-site and B-site doping (Zhang *et al.*, 1990). For $SrFeO_{3-\delta}$, it was shown that the addition of 0.1 and 0.33 mol % of copper enhanced the reactivity with both hydrogenous fuel (3 % H_2 in Ar) and air (Ksepko, 2018).

In contrast to the $SrFeO_{3-\delta}$ and $SrFe_{.9}Mn_{.1}O_{3-\delta}$ materials examined in chapter 3, here initial thermogravimetric experiments did not give clear information on the initial oxygen non-stoichiometry, δ_0, for the cobalt-doped strontium ferrite. Therefore, equilibrium partial pressure curves in terms of δ and the temperature could not be derived. However, for the derivation of kinetic parameters from the experiment described in chapter 5, knowledge about δ_0 is not required. In fact, only the shape of the equilibrium curve is important if the assumption is valid that the oxygen carrier has reached equilibrium with air after being exposed to an air flow of 750 sccm over the duration of 30 minutes.

In a typical experiment in the micro-reactor used in chapter 5, the material is first brought to equilibrium with a known partial pressure oxygen (in this case air), and will adopt a particular non-stoichiometry, δ, which should be on the equilibrium curve. When the step change in concentration occurs, the driving force in the kinetic expression (equation (3-10)) requires knowledge of the initial $pO_{2,eq}(\delta, T)$ = 0.21 bar, not the actual value of δ. Thus, for the initial rate only, the rate constant can be determined. For anything other than the initial rate, this would of course be invalid. It should also be noted that if different starting values of $pO_{2,eq}(\delta, T)$ were used, the kinetics at different points on the equilibrium curve could be evaluated.

6.2 Results

Experiments were performed in the micro-reactor described in section 3.3.1, and used in chapter 5. Details of the cobalt-doped material ($SrCo_{0.4}Fe_{0.6}O_{3-\delta}$) are given in sections 3.1 and 3.2.1. As in chapter 5, a mass of 560 mg was used in the reactor, and the material was subjected to alternating cycles of oxidation in air and reduction in nitrogen, lasting 90 s each. The duration of each measurement series at temperatures of 798, 823, 848, 873 and 898 K was set to 900 s in total. Therefore, four full redox cycles are recorded.

Figure 6-1 shows typical results obtained from the TGA when the $SrCo_{0.4}Fe_{0.6}O_{3-\delta}$ is heated in air and nitrogen. This data allows the difference in δ to be obtained and the expected oxygen uptake and release (as shown in Figure 6-2). However, measurement of the absolute value of δ, and thus construction of the equilibrium curve, requires the starting stoichiometry to be known. In the previous chapter, for the undoped and manganese doped material, it was possible to reduce the material in a mixture of 5 % H_2 in N_2 to a defined point where the stoichiometry was known (the brownmillerite phase). For the cobalt-doped material, there are no clear points in the reduction where a well-defined phase transition takes place, as indicated in Figure 6-1.

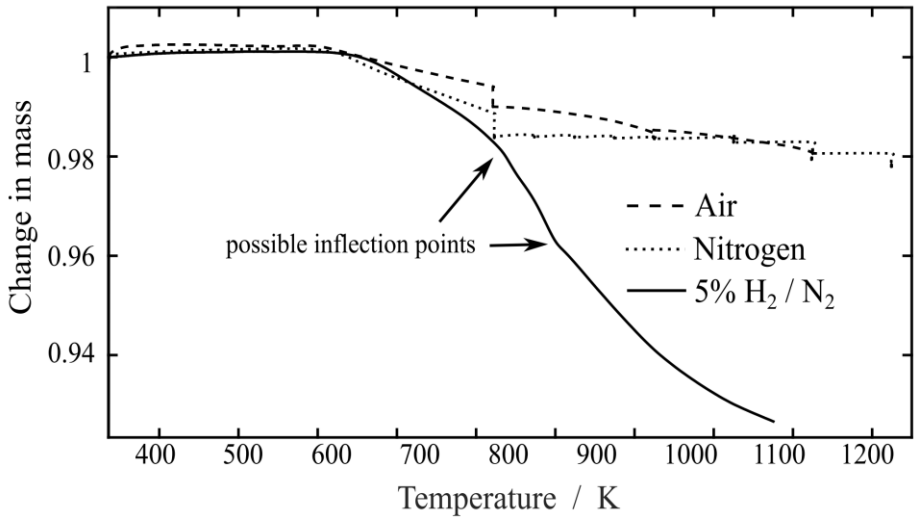

Figure 6-1: Change in mass over temperature as measured *via* thermogravimetric analysis for $SrCo_{0.4}Fe_{0.6}O_{3-\delta}$

From Figure 6-2 it can be seen that, after being exposed to 90 s of nitrogen, for all temperatures investigated, $SrCo_{0.4}Fe_{0.6}O_{3-\delta}$ does not reduce to the state expected from TGA experiments, indicating that full conversion to the phase in equilibrium with pO_2 of 10

ppm is not reached. However, a correlation between temperature and the oxygen transfer capacity was observed. Furthermore, the material has repeatedly released and taken up approximately the same amount of oxygen over the four redox cycles as shown in Figure 6-3. From the figure it can be noted that not all oxygen is taken up by the material when switching the gas from nitrogen to air; the oxygen sensor records partial pressure of oxygen above 0.03 bar at any point in time. The values for the moles of oxygen taken up and released during the oxidation and the reduction are listed in Table 6-1. The comparatively small error bars are attributable to the short tail of the reaction versus the blank experiment conducted at 293 K. In Table 6-1, the fourth reduction cycles at 848 K was disregarded for the following reason: The amount of oxygen released up to the point where the maximum reaction rate is reached was determined to be 36 µmol for the fourth reduction cycle at 848 K, whereas, in the previous three cycles, only 32.1±0.4 µmol were released on average. Therefore, the fourth cycle is disregarded as an outlier in further calculations.

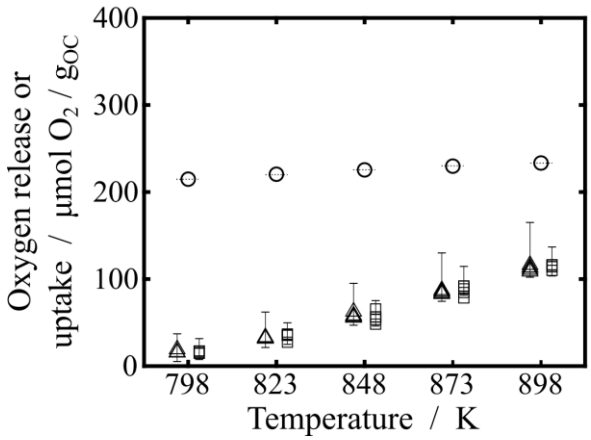

Figure 6-2: Molar amount of oxygen taken up and released during the oxidation (squares) and reduction (triangles) per gram of $SrCo_{0.4}Fe_{0.6}O_{3-\delta}$. The circles indicate the expected molar uptake and release from TGA experiments. The error bars indicate errors of the third redox cycle

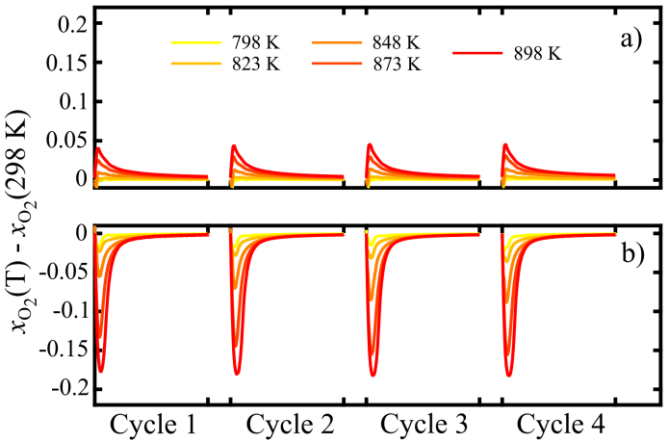

Figure 6-3: First 5 s of the difference in the mole fraction of oxygen, Δx_{O_2}, of the experiment conducted at 293 K and those conducted at higher temperatures for a) the reduction and b) the oxidation of $SrCo_{0.4}Fe_{0.6}O_{3-\delta}$.

Table 6-1: Molar amount of O_2 taken up and released per gram of $SrCo_{0.4}Fe_{0.6}O_{3-\delta}$ at different temperatures. The 95 % confidence intervals shown for the oxidation include ±1.96 times the standard error described in appendix 12.3. The fourth reduction cycle for 848 K is disregarded due to bad data.

Temperature K	TGA µmol	Reduction µmol	Oxidation µmol
798	214	9.0±0.4	9.2±1.5
823	220	17.8±0.2	18.8±2.5
848	225	32.1±0.4	32.3±3.9
873	230	49.5±0.7	49.5±3.4
898	234	65.6±1.1	64.3±2.6

The maximum rate, $r_{O_2}^m$, at which $SrCo_{0.4}Fe_{0.6}O_{3-\delta}$ releases oxygen under nitrogen is indicated in Figure 6-4. At 798 K, hardly any oxygen release reaction was observed and the maximum reaction rate occurred with a significant delay as compared to the time at which $r_{O_2}^m$ is recorded at other temperatures. At temperatures above 823 K, the observed rate was found to significantly increase with temperature.

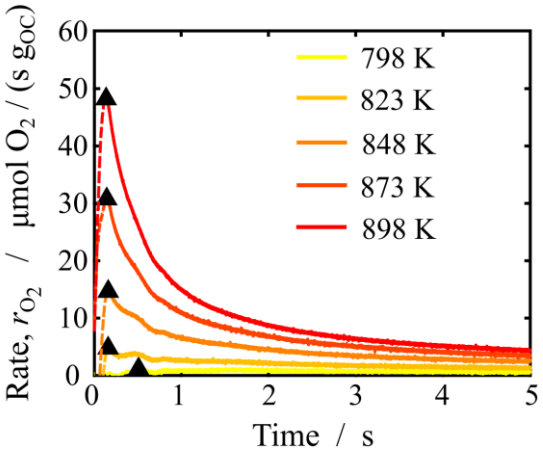

Figure 6-4: Observed rate of reduction of $SrCo_{0.4}Fe_{0.6}O_{3-\delta}$ at various temperatures. The triangles denote the point at which the rate is at its maximum, $r_{O_2}^m$.

6.3 Discussion

Despite of a difference in the *OTC* of only ~10 % at 898 K compared to $SrFeO_{3-\delta}$, the observed rate of reduction of $SrCo_{0.4}Fe_{0.6}O_{3-\delta}$ was found to be only about half that of the pure strontium ferrite (see Figure 5-4a and Figure 6-4). Especially at temperatures below 800 K, the Mn-doped and pure materials discussed in chapter 5 already showed the release of significant amounts of oxygen, whereas doping with cobalt seems to shift the $pO_{2,eq}$ curve towards higher temperatures.

The kinetic constant, *k*, is listed in Table 6-2 for different temperatures and the methods discussed in section 0, namely differential analysis (equation (3-41) and integral analysis (equation (3-40)) at constant gas velocities and when considering a change in the mass flow rate, equations (3-42) and (3-38), respectively. For $SrCo_{0.4}Fe_{0.6}O_{3-\delta}$, the standard errors are relatively large, ranging from below roughly 5.5 % for 798 K to ~17.7 % at 898 K; if the fourth reduction cycle at 848 K was accounted for, the standard error at this temperature would be around 40 % for 848 K.

Table 6-2: Values of the kinetic constant, *k*, of $SrCo_{0.4}Fe_{0.6}O_{3-\delta}$ computed by the different methods and the values of $kRTL/v_{in}$. The average of 4 cycles is shown including the 95 % confidence intervals. For 848 K, the fourth cycle was disregarded due to bad data.

Temperature K	kinetic rate constant, ***k*** mmol/s/Pa/m³				$\frac{kRTL}{v_{in}}$
	Differential	Integral	Differential accounting for changes in velocity	Integral Accounting for changes in velocity	
798	0.062±0.0035	0.062±0.0035	0.062±0.0035	0.062±0.0035	0.0065
823	0.188±0.0286	0.190±0.0292	0.196±0.0326	0.199±0.0332	0.0208
848	0.811±0.0659	0.849±0.0844	0.918±0.0758	0.962± 0.0823	0.1738
873	1.909±0.0841	2.132±0.1043	2.252±0.1045	2.518±0.1293	0.2642
898	3.300±0.4019	4.116±0.6536	4.062±0.5643	5.097±0.9054	0.5349

The comparison of the integral analysis and the differential analysis is shown in Figure 6-5. In the figure, the solid black line denotes the linear regression for the integral analysis accounting for a change in the gas velocity along the bed. For the investigated temperature range, 798 K ≤ *T* ≤ 898 K, the reaction constant, *k*, was much lower for the Co-doped strontium ferrite as compared to the pure or Mn-doped strontium ferrites (Table 5-4 *versus* Table 6-2). The pre-exponential factor, $\ln(A')$, and the apparent activation energy, E_{app}, were determined to be 31.3 mol/s/Pa/m³ and 271.3±4.0 kJ/mol for the integral analysis accounting for changes in the gas velocity, respectively, as shown in Table 6-3; much higher values than those found for $SrFeO_{3-\delta}$ or $SrMn_{0.1}Fe_{0.9}O_{3-\delta}$. Although the kinetic constant, *k*, of $SrCo_{0.4}Fe_{0.6}O_{3-\delta}$ is much smaller in the investigated temperature range, the much higher activation energy indicates that already at temperatures above 923 K, *k* is higher for the Co-doped strontium ferrite. It should be noted that the Co-doped strontium ferrite was the impurest with respect to the cubic perovskite phase of the three strontium ferrites; $SrFeO_{3-\delta}$, $SrMn_{0.1}Fe_{0.9}O_{3-\delta}$ and $SrCo_{0.4}Fe_{0.6}O_{3-\delta}$ of 96.9 %, 93.0 % and 83.3 % of the cubic phase, respectively. Further investigations into the effect of the relative amount of the cubic perovskite phase on the reaction kinetics would have been of interest to shed further light on tuning the strontium perovskite by doping.

The value of $kRTL/v_{in}$ is well below 1 at all temperatures investigated, indicating that the differential analysis is a valid assumption. However, as can be seen from the Arrhenius plot for the Co-doped strontium ferrite, *i.e.* Figure 6-5, values for the different meth-

ods start to diverge at temperatures above 873 K. Therefore, only the integral analysis accounting for change in the flow rate includes the last data point at 898 K. It should be further noted, that the time at which the maximum reaction rate is recorded for 798 K is significantly later than for other temperatures, as mentioned earlier. However, it was found that negligence of this data point did not affect the calculated number significantly and was hence included in the calculations.

Table 6-3: Kinetic parameters computed by the different methods for $SrCo_{0.4}Fe_{0.6}O_{3-\delta}$. The units of A' are mol/s/Pa/m^3. The solid line represents the least squares fit to the integral analysis accounting for changes in the gas velocity.

	Differential	Integral	Differential accounting for changes in velocity	Integral accounting for changes in velocity
$\ln(A')$	31.3	32.5	33.3	31.2
$E_{a,app}\ (kJ/mol)$	272.2±3.8	280.4±3.7	285.4±4.2	271.3±4.0

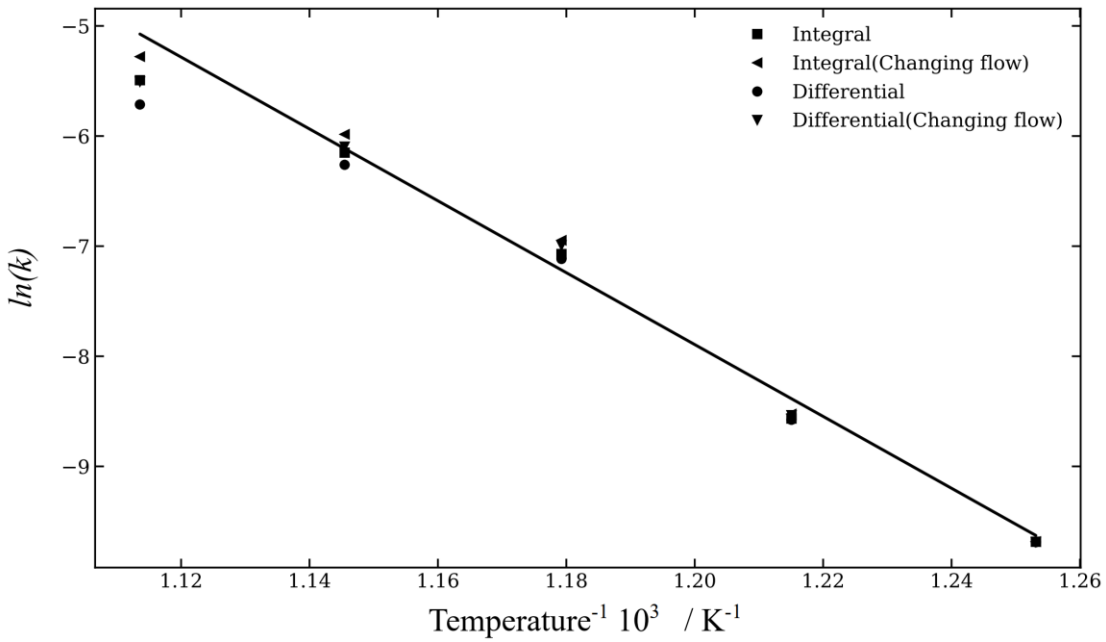

Figure 6-5: Arrhenius plot for $SrCo_{0.4}Fe_{0.6}O_{3-\delta}$ using the initial (or maximum) rate, $r^{m}_{O_2}$. The filled in markers denote data points for the different analysis methods and the solid black represents the linear regression for the integral analysis accounting for changes in the gas velocity, *viz.* equation (3-38).

To ensure that deviations in the temperature of the solid bed are negligible, the maximum change in temperature in the bed due to the reduction reaction is calculated as described in section 3.3.3. The maximum expected deviation from the nominal temperature is small, as shown in Table 6-4. At such low values, the temperature should have only very little effect on the observed reaction rate and was neglected in the calculations for the kinetic parameters, A' and $E_{a,app}$.

Table 6-4: Estimated upper bounds for the difference in solid temperature when the rate is evaluated for the experiments with $SrCo_{0.4}Fe_{0.6}O_{3-\delta}$. The volume of the bed, V_{bed}, is roughly 0.538 mm^3

Temperature	$\mathbf{r}_{O_2}^{V}$	n_{O_2}	ΔH_r^o	ΔT_{ub}^1	ΔT_{ub}^2
K	$mol/s/m^3$	µmol	kJ/mol	K	K
798	1.32	0.15	173.9	0.081	0.062
823	3.81	0.20	179.4	0.242	0.083
848	14.59	0.27	184.8	0.954	0.115
873	33.17	2.00	190.3	2.235	0.878
898	55.96	2.55	195.7	3.878	1.152

6.4 Conclusion

In this chapter, the reaction kinetics of cobalt-doped $SrFeO_{3-\delta}$ have been evaluated at temperatures between 798 and 898 K. A comparison to the kinetic parameters extracted for $SrFeO_{3-\delta}$, as described in chapter 5, showed that doping with cobalt significantly decreases the observed rate of oxygen release. The apparent activation energy, however, was found to be much larger for $SrCo_{0.4}Fe_{0.6}O_{3-\delta}$ and, therefore, at temperatures above 923 K, the material is expected to possess higher rates of reaction than $SrFeO_{3-\delta}$. The apparent activation energy, $E_{a,app}$, and the pre-exponential factor, A', were determined to be 271.3±4.0 kJ/mol and $35.5 \cdot 10^{12}$ mol/s/Pa/m^3, respectively. The Rietvield refinement on the XRD results showed that in the fresh sample of $SrCo_{0.4}Fe_{0.6}O_{3-\delta}$, the phases found were 83.3 % of the cubic perovskite phase and 16.7 % of the Ruddlesden-Popper phase, *i.e.* $Sr_3Fe_2O_7$. Further analysis of the effect of the phase purity of the cubic perovskite phase and the effect of doping with different amounts of Co on the kinetics would have helped

to better understand the mechanisms and sensitivity of the oxygen release from Co-doped Sr-Fe-O systems. The porosity for the Co-doped material was also not determined so that a comparison to $SrFeO_{3-\delta}$ and $SrMn_{0.1}Fe_{0.9}O_{3-\delta}$ with respect to the porosity of the particles is not possible.

7 Redox Stability over many Cycles

In this chapter, the stability of the pure and Mn-doped strontium ferrite over 1000 redox cycles is investigated. The stability of the oxygen carrier over many reduction-oxidation cycles is used to determine the suitability of the oxygen carrier material both economically and with respect to the fluidisability depending on attrition and agglomeration (Adanez *et al.*, 2012).

7.1 Introduction

For the commercial application of oxygen transfer materials, knowledge about the behaviour of the material over an extended period of time is crucial. One example of the importance in assessing the stability over many cycles in chemical looping is the first attempt to produce oxygen from chemical looping air separation itself: In 1852, the French chemist Jean-Baptiste Boussingault attempted to produce oxygen using barium oxide, but found that it deactivated after only few redox cycles (Jensen, 2009). As mentioned earlier, however, the commercial breakthrough was achieved roughly 30 years later when the brothers Léon and Arthur Brin noticed that BaO reacted irreversibly with the carbon dioxide in the air, resulting in the deactivation of the material over time. This highlights the importance of the stability of the oxygen carrier over many redox cycles.

Today, extensive efforts are undertaken to investigate the cyclability of potential oxygen carrier materials. Oxygen carriers have been tested for over 2000 hours in reactors ranging from 0.5 kW to 3 MW (Lyngfelt and Leckner, 2014). For materials suitable for chemical looping air separation, most tests were conducted in a TGA did not exceed 50 redox cycles; Song *et al.* (2014) investigated the stability of a copper and magnesium-based oxygen carrier over 41 cycles in a TGA. It was found that the decrease in oxygen transfer capacity for the optimum candidate of the Cu-Mg-O family, *i.e.* 70 wt% CuO and 30 wt% MgO, was around 1 %. The stability of strontium ferrite perovskites was assessed over 20 cycles *via* thermogravimetric analysis. For mixtures of $SrMnO_{3-\delta}$ and $SrNiO_{3-\delta}$, *i.e.* $SrMn_xNi_{1-x}O_{3-\delta}$ for $0 \leq x \leq 1$, no change in the crystal structure and *OTC* was observed

(Ksepko, 2014). Further, the undoped $SrFeO_{3-\delta}$ did not show a deterioration of its *OTC* over the course of 20 redox cycles (Lau *et al.*, 2017). $SrFeO_{3-\delta}$ doped with 0.33 moles of copper, *i.e.* $SrCu_{0.33}Fe_{0.67}O_{3-\delta}$, was also found to be stable over 20 redox cycles, releasing and taking up the same amount of oxygen (Ksepko, 2018). However, doping with a smaller quantity of copper ($SrCu_{0.1}Fe_{0.9}O_{3-\delta}$), the initially cubic perovskite changed to a two-phase solid solution containing orthorhombic and tetragonal phases. Despite this change in phase, no effect on the reactivity was observed, making these perovskite-type materials great oxygen transfer materials in terms of their stability.

7.2 Methods

Here, the solids were subjected to 1000 redox cycles at 898 K (873 K for $SrFeO_{3-\delta}$). During the 1000 redox cycles, the gas was switched every 60 s between air and nitrogen. Here, the flow rate was set to 500 sccm during the 1000 redox cycles. Without cooling down the reactor, the experiment discussed in chapter 5 has been repeated at 898 K (873 K for $SrFeO_{3-\delta}$) and room temperature to enable a comparison of the influence of the repeated oxidation and reduction.

7.3 Results

Figure 7-1 shows the first and last 20 cycles of the experiment for $SrFeO_{3-\delta}$. At the beginning as well as at the end of the experiment, the individual redox cycles appear to not change much over the duration of the cycling experiment. The oxidation proceeded notably faster than the reduction reaction (as demonstrated in chapter 5 in more detail).

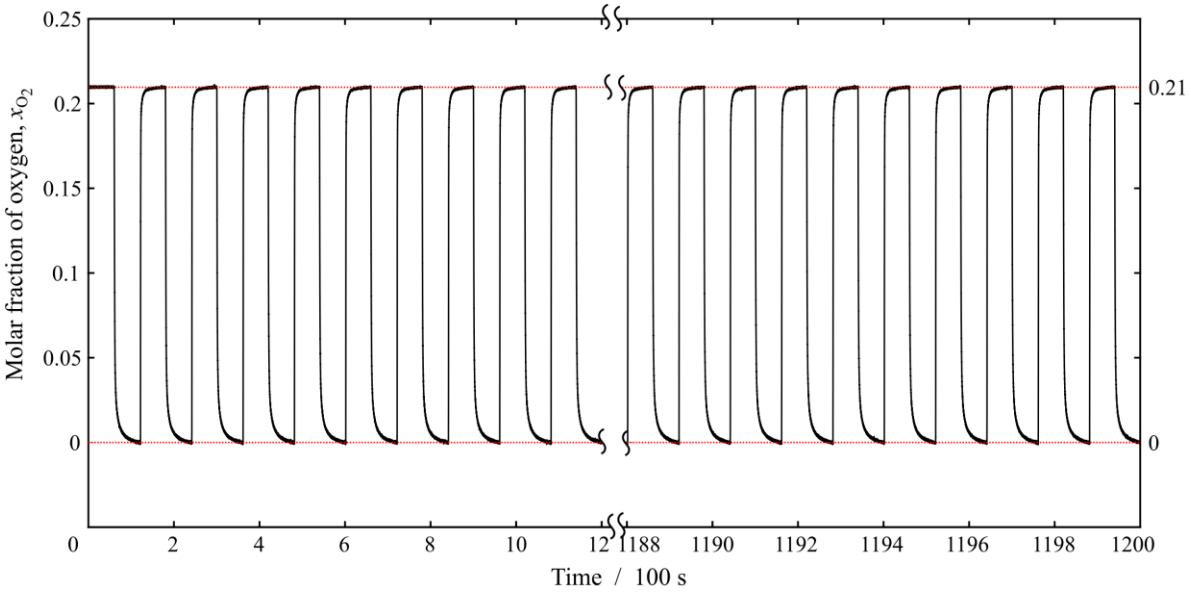

Figure 7-1: The first and last 20 cycles of the 1000 redox cycles for $SrFeO_{3-\delta}$

On a closer look, however, subtle changes for $SrFeO_{3-\delta}$ are observed, as shown in Figure 7-2, which depicts the first five seconds of the reduction and oxidation at the start and end of the 1000 cycles, respectively. Here, an increase in the oxygen transfer capacity and the maximum rate of reduction was observed. The first five seconds of the reduction and oxidation are shown in Figure 7-3, which compares the redox cycles 1-4 (black solid line) to 1000-1004 (red solid line). It can be observed that the initial rate of reduction significantly increased over the 1000 cycles. The difference between the oxidation for cycles 1-4 and the four cycles reported after the 1000 redox cycles long experiment, is found to be not as distinct as is the case for the reduction. Nevertheless, a marginal increase in the duration until the breakthrough was observed can be noted from Figure 7-2. In total, at 873 K, during the reduction interval of length 90 s, a total of 311 µmol O_2 per gram of $SrFeO_{3-\delta}$ is observed on average over the four reduction intervals. Before the 1000 cycles, only 255 µmol O_2 per gram of $SrFeO_{3-\delta}$ were released, as reported in chapter 5. The four cycles, those at the beginning and at the end of the cycling experiment, showed good repeatability; the initial rate as well as the release and uptake of oxygen did not change over the course of the four redox cycles.

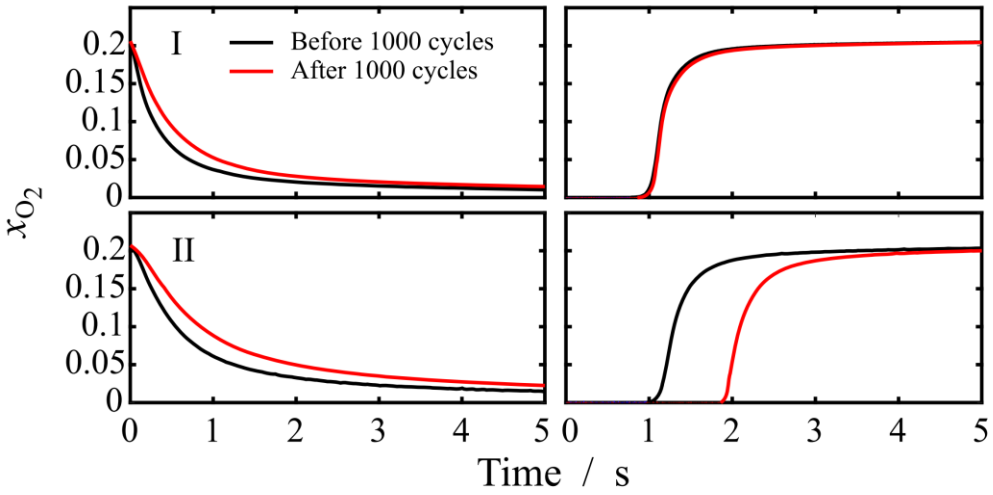

Figure 7-2: First 5 s of the fourth redox cycle, reduction (left column) and oxidation (right column), for $SrFeO_{3-\delta}$ (I) and $SrMn_{0.1}Fe_{0.9}O_{3-\delta}$ (II) before and after 1000 redox cycles.

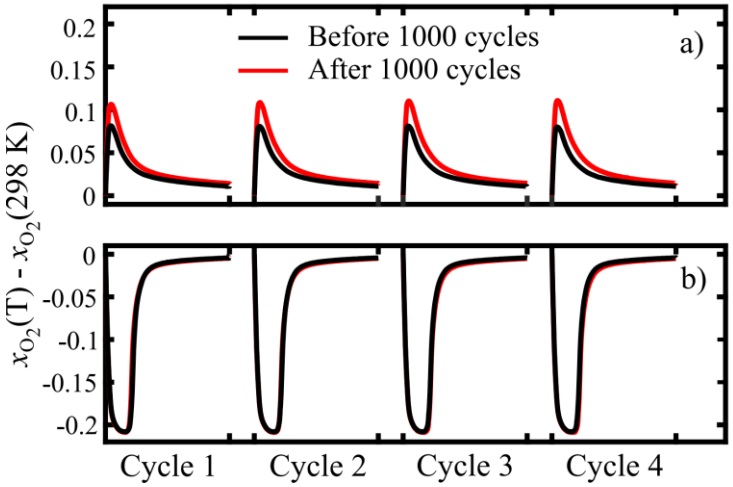

Figure 7-3: First 5 s of the a) reduction and b) oxidation of $SrFeO_{3-\delta}$ before the 1000 cycles (black line) and after 1000 cycles (red line) at 873 K

In contrast to the pure strontium ferrite, the Mn-doped oxygen carrier showed significant changes in its redox behaviour over the 1000 cycles, as shown in Figure 7-2. A release of 402.5 µmol of oxygen per gram of oxygen carrier is recorded after the 1000 cycles. For comparison, before the 1000 cycles, the $SrMn_{0.1}Fe_{0.9}O_{3-\delta}$ gave off around 320 µmol O_2 on average over the four reduction cycles, as reported in chapter 5. The initial rate also increased significantly, producing a partial pressure of oxygen of about 0.15 bar after the gas was switched from ait to nitrogen, as shown in Figure 7-4. During the oxidation, the breakthrough time significantly increased from roughly 1.1 s to almost 2 s.

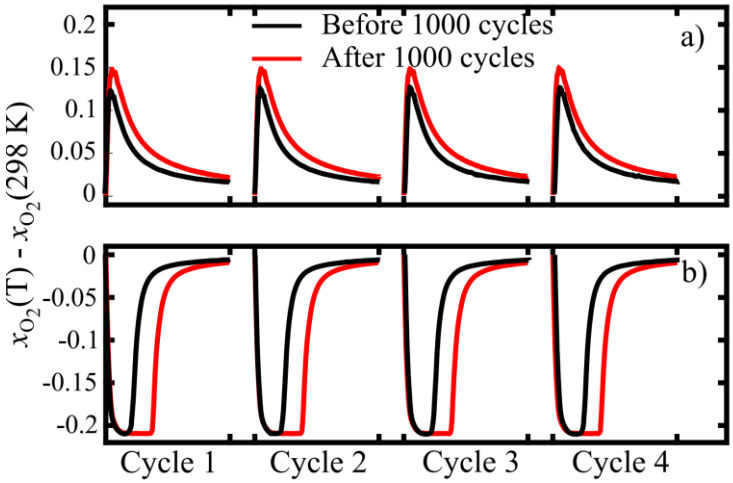

Figure 7-4: First 5 s of the a) reduction and b) oxidation of $SrMn_{0.1}Fe_{0.9}O_{3-\delta}$ before the 1000 cycles (black line) and after 1000 cycles (red line) at 898 K

$SrFeO_{3-\delta}$ and $SrMn_{0.1}Fe_{0.9}O_{3-\delta}$ cycled 1000 times in a TGA was analysed *via* X-ray powder diffraction (XRD), to assess any changes in the composition of the materials. The results are shown in Table 7-1; the results from the Rietveld refinement for the fresh sample are repeated at this point for convenience. The phases considered when evaluating the XRD results are enumerated in section 3.2.1.

Table 7-1: Results from Rietveld refinement of the collected XRD spectra. The precision in the last digit is given in the parentheses, and corresponds to the estimated standard deviations determined by the regression.

Oxygen carrier	$Sr_2Fe_2O_7$	$SrFeO_3$	Mn_3O_4
Fresh sample			
$SrFeO_{3-\delta}$	3.0 (5)	96.9 (5)	-
$SrMn_{0.1}Fe_{0.9}O_{3-\delta}$	2.8 (2)	93.0 (4)	4.1 (3)
After 1000 redox cycles			
$SrFeO_{3-\delta}$	-	100.0	-
$SrMn_{0.1}Fe_{0.9}O_{3-\delta}$	-	100.0	-

7.4 Discussion

There are several potential explanations for the observed change in the redox behaviour of the materials. As observed for $SrCu_{0.1}Fe_{0.9}O_{3-\delta}$ by Ksepko (2018), a change in the phase would lead to a change in the *OTC*, but not in the reactivity. On the other hand, a change in the morphology would affect the reaction kinetics, but not the *OTC* (Jeon and Kim, 2000; Kittilsen and McKenna, 2001).

For the pure strontium ferrite, an increase in the oxygen transfer capacity for both oxygen release and oxygen uptake is observed, indicating phase changes occur over the course of the 1000 redox cycles which has been confirmed by XRD. This is in agreement with Lau *et al.* (2017) who reported that multiphase solid solutions for strontium ferrite have a lower *OTC* then the cubic phase alone (Lau *et al.*, 2017). It should be noted, that in the study of Lau *et al.* (2017), only the cubic phase and the Ruddlesden-Popper ($Sr_3Fe_2O_{7-\delta}$) phase were investigated. Arguably, the change in the phases towards the cubic phase is interesting as the materials were exposed to air at 1273 K for 3 hours during the calcination step of the synthesis and other phases of $SrFeO_{3-\delta}$ are not to be expected at these temperatures and oxygen non-stoichiometries (Takeda *et al.*, 1986; Schmidt and Campbell, 2001). Comparing the oxygen release of the sample before and after the 1000 cycles, the increase in the maximum reaction rate might be attributable to a change in the morphology. SEM or gas adsorption which would have helped in the investigation for changes in the morphology have not been conducted in this work.

In terms of the oxygen transfer capacity, similar observations were made using the Mn-doped $SrFeO_{3-\delta}$; the amount of oxygen released and taken up increased significantly over the 1000 redox cycles. The maximum rate of reduction was found to also increase, giving off oxygen at partial pressure of around 0.15 bar, whereas before the cycling experiment, the material produced oxygen only at a pO_2 of approximately 0.125 bar, as shown in Figure 5-2 IIa. During the oxidation, the behaviour changed significantly, as shown in Figure 7-2. However, despite the increase in the breakthrough times observed for the Mn-doped strontium ferrite, a very similar shape of the molar fraction of oxygen, x_{O_2}, curve is observed once the breakthrough was recorded at the oxygen sensor, as shown in Figure 7-4b.

Besides a change in the phase and the morphology, a change in the pressure inside the bed is another possible explanation. Comparing the pressures upstream of the bed before and after the 1000 cycles, no significant changes could be observed.

7.5 Conclusion

In this chapter, the behaviour of $SrFeO_{3-\delta}$ and $SrMn_{0.1}Fe_{0.9}O_{3-\delta}$ is investigated, comparing the behaviour of the materials before and after 1000 redox cycles. In both cases, it was found that the oxygen transfer capacity significantly increased. For $SrFeO_{3-\delta}$, the amount of oxygen released per gram of oxygen carrier increased by about 55 µmol to 311 µmol O_2 per gram of $SrFeO_{3-\delta}$. In the case of $SrMn_{0.1}Fe_{0.9}O_{3-\delta}$, the increase in *OTC* was even more pronounced as an additional 80 µmol of O_2 were released after the material was subjected to 1000 redox cycles. After the long-term cycling, the Mn-doped material released around 402 µmol O_2 per gram at 898 K. The observed increases in the *OTC* can be at least partially explained by changes in structural phases; before the cycling experiment, both materials showed phases other than the cubic perovskite phase, after the cycling, however, only the cubic phase was found to be present. The more pronounced increase in the *OTC* of the Mn-doped $SrFeO_{3-\delta}$, which had a higher percentage of impure phases before the cycling, compared to $SrFeO_{3-\delta}$ corresponds to findings in the literature where the cubic phase showed a higher *OTC* than solid solutions of different phases of strontium ferrite.

Further, for both materials, the maximum reaction rate of reduction increased significantly. An increase in the reaction rate has also been observed during the uptake of oxygen of $SrMn_{0.1}Fe_{0.9}O_{3-\delta}$, but not for $SrFeO_{3-\delta}$. The cause for the observations has been discussed, including potentials changes in the morphology.

8 Conclusions

The objective of this Dissertation was to suggest novel materials suitable for the separation of oxygen from air *via* a chemical loop. Here, chemical looping air separation is employed to provide oxygen to an oxy-fuel power plant process to eventually capture the CO_2 from the combustion. The review of literature on this topic undertaken in Chapter 1 highlighted the importance of regarding the process as a whole and not evaluate the oxygen carrier materials in isolation or modelling the power plant for a select few promising materials. Therefore, in this Dissertation, the entire process from the identification of, in theory, suitable oxygen transfer materials *via* the synthesis and evaluation (regarding thermochemical properties) of these materials through to the investigation of the kinetic parameters and stability over many redox cycles was investigated.

The findings in this Dissertation, ranked from most important to least important in the point of view of the author, are:

1. Using a fully heat-integrated model of a steam power plant, linked to a model of a chemical looping air separation system, it was found that electricity could be generated at an energy penalty of as little as 1.5 percentage points; a drastic reduction in the estimated energy penalty of roughly 8 percentage points imposed by currently mature technologies such as cryogenic air separation. This energy penalty, however, neglects the possible CO_2 compression and flue gas processing. Furthermore, this minimum energy penalty is only achieved for materials possessing a narrow range of thermochemical properties (the enthalpy and entropy of reaction per mole of oxygen produced and the specific heat capacity), where this range is limited by the lower heating value per mole of oxygen combusted of the fuel, whether a stabilising support material is required and if full conversion can be assumed.

   In this work, a 2D map was constructed to serve as a guide for the rough estimation of the efficiency of the power plant for a given ΔH_r^o and ΔS_r^o per mole of oxygen produced. The map fully characterises the CLAS-oxy-fuel process by

mapping combinations of ΔH_r^o and ΔS_r^o (or, as presented in Chapter 3, the temperature at which the material is in equilibrium with 0.34 mol-% O_2 , T_{eq}, and the heat of reaction at T_{eq}, $\Delta H_r^o(T_{eq})$ to the net efficiency of the process.

2. Materials of the Sr-Fe-O family are well suited as oxygen carriers for chemical looping air separation. These materials were found to react very fast, in fact the oxidation proceeded at rates that were too rapid to measure in the tubular microreactor constructed for this Dissertation. For the reduction reaction, *i.e.* the oxygen releasing reaction, the kinetic parameters are listed in Table 8-1. The comparison of $SrFeO_{3-\delta}$ and $SrMn_{0.1}Fe_{0.9}O_{3-\delta}$ showed that doping with 10 mol-% of manganese significantly increases the oxygen transfer capacity and decreases the apparent activation energy, $E_{a,app}$; both features that are desirable in oxygen carriers for chemical looping air separation. Doping with 40 mol-% cobalt, however, lead to significantly decreased observed rates of oxygen production in the investigated temperature range, 798 K to 898 K.

Table 8-1: Kinetic parameters of SrFeO3-δ, SrMn0.1Fe0.9O3-δ and SrCo0.4Fe0.6O3-δ for the oxygen release reaction.

Oxygen carrier	$E_{a,app}$ kJ mol^{-1}	A' mol s^{-1} Pa^{-1} m^{-3}
$SrFeO_{3-\delta}$	128.9±4.7	$3.9 \cdot 10^5$
$SrMn_{0.1}Fe_{0.9}O_{3-\delta}$	45.3±3.4	6.29
$SrCo_{0.4}Fe_{0.6}O_{3-\delta}$	271.3±4.0	$35.5 \cdot 10^{12}$

3. Perovskites of the strontium ferrite family exhibit good structural stability when cycled over 1000 redox cycles. Therefore, doping with inert support materials, which would adversely affect the heat integration, is not required.
4. By means of defect chemistry, models to calculate the equilibrium partial pressure of oxygen curves of $SrFeO_{3-\delta}$ and $SrMn_{0.1}Fe_{0.9}O_{3-\delta}$ were suggested for different temperatures. For the entire range of temperature investigated, 798 K to 898 K, no single defect model provided a satisfactory fit. Therefore, two-region models were used, which consisted of one defect model describing the low pO_2 range and another defect model describing the equilibrium partial pressure of oxygen at high pO_2.

5. This Dissertation shows that modelling an entire process, taking material properties as the input which then allows for a parameter sweep, offers an efficient way to explore suitable material when linked to a material database, such as the Materials Project. In this work, a list of 34 oxygen carrier systems was suggested, of which five systems seem particularly promising, namely $BaFeO_3/Ba_2Fe_2O_5$, $LiBiO_3/LiBiO_2$, $MnPO_4/Mn_2P_2O_7$, $SrFeO_3/Sr_2Fe_2O_5$, and $Sr_2Cu_2O_5/SrCuO_2$.

In summary, the perovskite $SrFeO_{3-\delta}$ was selected for experimental investigation based on a steady-state model of an oxy-fuel power station that is supplied with oxygen from a chemical looping air separation system. The effect of doping $SrFeO_{3-\delta}$ with manganese and cobalt was investigated in terms of the oxygen transfer capacity and the reaction rate. It was found that using manganese as a dopant increased both the oxygen transfer capacity and the reaction rate, but doping with cobalt lead to the adverse effect. The rate constant was extracted for the reduction reaction, which was not possible for the oxidation as the uptake of oxygen was too rapid. The experimental parameters, *i.e.* the reactor system, flow conditions and solid bed, could certainly be improved to increase the accuracy of the measurements and, perhaps, enable the extraction of the oxygen uptake kinetics.

9 Future work

In chapter 2, oxygen carrier materials were identified that, in theory, allow for the heat integration into a steam power plant at a low energy penalty, however, the approach taken in the heat integration assumed the availability of an infinite number of heat exchangers. A more accurate model properly simulating the heat exchanger network will likely arrive at a higher energy penalty imposed by chemical looping air separation when constraints on the capital and operating expenditures are considered. Further, the CLAS model employed in chapter 2 produced the oxygen by subjecting the oxygen carrier material to different temperatures for the oxidation and reduction, so-called temperature swing. It would be of practical and academic interest to shed light on potential benefits of swinging the pressure in a heat-regenerative fixed bed reactor, *i.e.* the oxygen carrier remains fixed and the inlet conditions are alternated, *e.g.*, between (pressurised) air and a low pO_2 (and low-pressure) gas. For the continuous production of oxygen this would require several fixed bed reactors to run in parallel. Also, in this thesis, only the integration of chemical looping air separation into a steam cycle was investigated, however, there are other processes requiring high pO_2 gases, such as steelmaking, which may well integrate with CLAS.

The construction of the equilibrium partial pressure of oxygen curves for $SrFeO_{3-\delta}$ and $SrMn_{0.1}Fe_{0.9}O_{3-\delta}$ described in chapter 4 made use of defect chemistry models found in the literature. However, the formation of oxygen vacancies giving rise to the various defect chemistry models are not fully understood for the entire region of pO_2 fitted in this thesis. Well characterised equilibrium pO_2 curves are crucial for the accurate derivation of the reaction kinetics and, subsequently, the simulation of the behaviour of the materials in different systems. To get more accurate equilibrium pO_2 curves, one could, for example, repeat the experiments carried out in this thesis using a finer step size in the temperature in the TGA or follow Starkov *et al.* (2014) who proposed a method to directly measure the equilibrium pO_2 curve at isosteric (iso-stoichiometric) conditions, *i.e.* the material is reduced at constant δ. However, also these approaches may not provide insights into the

physical processes, such as the formation of defect clusters, that occur during the reduction or oxidation of these perovskite-type materials. Possible pathways to explore the evolution of the defects in these materials are by examining the electrical conductivity (Mizusaki, 1992) or electron paramagnetic resonance (Eichel, 2011).

Lastly, as indicated in chapter 5, the derivation of kinetic parameters, especially at high temperatures, was not uncomplicated. The accurate extraction of reaction kinetics from a step response, as performed in the experiments in this thesis, is problematic, as information to precisely decouple dispersion and reaction rate is missing. The ability to model these materials is crucially important to their evaluation, but this necessitates knowledge of the reaction kinetics. Therefore, further research on the reaction kinetics of perovskite-type materials are necessary.

In this thesis, it has been shown that these perovskite-type materials offer great potential for modifying their kinetic and thermodynamic behaviour through the substation of the A-site and B-site cations. Future work should thus investigate these substitutions in more detail. Further, this work outlined the experimental procedures and a modelling framework for evaluating oxygen carrier materials for CLAS, which can be extended to investigate more complex materials than those used here.

10 Nomenclature

Acronyms and Abbreviations

Acronym or abbreviation	Descritpions
ASU	Air separation unit
CAS	Cryogenic air separation
CCS	Carbon capture and storage
CDCL	Coal direct chemical looping
CLAS	Chemical looping air separation
CLC	Chemical looping combustion
CLOU	Chemical looping with oxygen uncoupling
DCFB	Dual circulating fluidised bed
DFT	Density functional theory
Gtce	Gigatons coal equivalent
HRSG	Heat recovery steam generator
IEA	International Energy Agency
Me	Arbitrary metal
MeO	Arbitrary metal oxide
OTC	Oxygen transport capacity
PSA	Pressure swing adsorption
TGA	Thermogravimetric analyser/analysis
TRL	Technology readiness level

Dimensionless numbers

Dimensionless Number	Descritpions
$K_{FeO_5,eq}$	Equilibrium constant for the $\langle Fe'_{Fe} - V_O^{\bullet\bullet} - Fe'_{Fe}\rangle$-defect-cluster model
$K_{c,eq}$	Equilibrium constant of the cluster-defect model
$K_{p,eq}$	Equilibrium constant of the point-defect model
K_p	Equilibrium constant in terms of the partial pressures
$K_{se,eq}$	Equilibrium constant of the cluster-defect model with site exclusion
Pe_f	Fluid Péclet number
Pe_r	Reactor Péclet number
Re	Reynold number
Sh_0	Sherwood number in stagnant flow
Sh	Sherwood number
Sc	Schmidt number
X	Conversion of the oxygen carrier
x_{O_2}	Mole fraction of oxygen

Greek symbols

Symbol	Descritpions	Units
Λ_c	Site exclusion factor of for the cluster-defect model with site exclusion	-
δ	Oxygen non-stoichiometry of an oxygen carrier	-
δ_f	Oxygen non-stoichiometry of an oxygen carrier at the final, reduced state	-
τ_p	Tortuosity factor of a spherical particle	-
δ_0	Initial oxygen non-stoichiometry of the oxygen carrier	-
Θ	Lower heating value per mole of oxygen	kJ/mol O_2
α	Thermodynamic activity	-
ν	Stoichiometric coefficient	-
ϵ	Voidage of the packed bed	-
θ	Dimensionless time	-

μ	Chemical potential	J/mol
ρ_{OC}	Molar density of the oxygen carrier	mol/m^3
τ_c	Time constant for the conversion of the oxygen carrier (equation 3.17)	s

Symbols

Symbol	Descritpions	Units
A_p	Surface area of a particle	m^2
C_p	Molar heat capacity	J/K/mol
c_p	Specific heat capacity	J/K/kg
D_{O_2}	Gas molecular diffusivity of oxygen in the surrounding gas	m^2/s
D_{ax}	Axial dispersion coefficient	m^2/s
D_e	Effective gas diffusivity	m^2/s
E_N	Nernst potential	V
$E_{a,app}$	Apparent activation energy	kJ/mol
$E_{a,oxi}$	Activation energy of the oxidation reaction	kJ/mol
$E_{a,red}$	Activation energy of the reduction reaction	kJ/mol
E_a	Activation energy	kJ/mol
T_{eq}	Temperature at which the material is in equilibrium with a certain pO_2	K
V_{bed}	Volume of the packed bed	m^3
V_m	Molecular volume	m^3/mol
V_p	Volume of a particle	m^3
d_p	Particle diameter	m
$j_{N_2}^m$	Molar flux of nitrogen	mol/s/m^2
k_{app}	Apparent (or measured) reaction rate constant	mol/s/Pa/m^3
k_{eg}	External mass transfer coefficient	m/s
k^m	Reaction rate constant at the external mass transfer limit	mol/s/Pa/m^3
$\dot{n}$	Molar flow rate	mol/s
p_{tot}	Total pressure of the system	bar
$r_{O_2}^V$	Rate of oxygen production per volume of the bed	mol/s//m^3

$r_{O_2}^m$	Maximum measured rate of reaction	mol O_2/s/g_{OC}
r_p	Particle radius	m
v_{in}	Superficial velocity at the inlet (mole averaged)	m/s
$\Delta\dot{H}_{hot}$	Heating utility	kJ/mol
$\Delta\dot{H}_{cold}$	Cooling utility	kJ/mol
Δh_{vap}	Specific enthalpy of vaporization between two temperatures	kJ/mol
$pO_{2,ox}$	Partial pressure of oxygen in the CLAS oxidizer	bar
$pO_{2,red}$	Partial pressure of oxygen in the CLAS reducer	bar
$pO_{2,req}$	Partial pressure of oxygen required by the oxy-fuel combustor	bar
Q	Heat	J
A	Pre-exponential factor	mol/s/Pa/m^3
C	Concentration	mol/m^3
F	Faraday's constant	F
H	Enthalpy	kJ
L	Length of the packed bed	m
R	Universal gas constant	J/mol/K
S	Entropy	J/K
T	Temperature	K
k	Rate constant	mol/s/Pa/m^3
m	Mass	g
$pO_{2,eq}$	Equilibrium partial pressure of oxygen	bar
pO_2	Partial pressure of oxygen	bar
ΔG_r^o	Gibbs free energy of reaction	kJ/mol
ΔH_r^o	Enthalpy of reaction	kJ/mol
ΔS_r^o	Entropy of reaction	J/K/mol

11 References

Adanez, J. *et al.* (2004) 'Selection of Oxygen Carriers for Chemical-Looping Combustion', *Energy & Fuels*, 18, pp. 371–377.

Adanez, J. *et al.* (2012) 'Progress in Chemical-Looping Combustion and Reforming technologies', *Progress in Energy and Combustion Science*. Elsevier Ltd, 38(2), pp. 215–282. doi: 10.1016/j.pecs.2011.09.001.

Adánez, J. *et al.* (2004) 'Selection of Oxygen Carriers for Chemical-Looping Combustion', (3), pp. 371–377.

Albrecht, K. J., Jackson, G. S. and Braun, R. J. (2016) 'Thermodynamically consistent modeling of redox-stable perovskite oxides for thermochemical energy conversion and storage', *Applied Energy*. Elsevier Ltd, 165, pp. 285–296. doi: 10.1016/j.apenergy.2015.11.098.

Alfa Aesar (2015) *Safety Data Sheet Cobalt (II) Selenide*. Available at: https://www.alfa.com/de/content/msds/british/40224.pdf (Accessed: 22 November 2016).

American Elements (2016) *Ámerican Elements Database*. Available at: https://www.americanelements.com/ (Accessed: 21 November 2016).

Arjmand, M. *et al.* (2013) '$CaZrO_3$ and $SrZrO_3$-based CuO oxygen carriers for chemical-looping with oxygen uncoupling (CLOU)', *Energy Procedia*, 51, pp. 75–84. doi: 10.1016/j.egypro.2014.07.009.

Barin, I. and Knacke, O. (1974) *Thermochemical Properties of Inorganic Substances*. Springer.

Buhre, B. J. P. *et al.* (2005) 'Oxy-fuel combustion technology for coal-fired power generation', *Progress in Energy and Combustion Science*, 31(4), pp. 283–307. doi: 10.1016/j.pecs.2005.07.001.

Bui, M. *et al.* (2018) 'Carbon capture and storage (CCS): the way forward', *Energy &*

Environmental Science, 11(5), pp. 1062–1176. doi: 10.1039/C7EE02342A.

Bychkov, S. F., Popov, M. P. and Nemudry, A. P. (2016) 'Study of the oxygen exchange kinetics in the nonstoichiometric oxide $SrFeO_{3-\delta}$ under isostoichiometric conditions using the oxygen partial pressure relaxation technique', *Kinetics and Catalysis*, 57(5), pp. 697–703. doi: 10.1134/S0023158416050050.

Chase, M. W. J. (1998) *NIST-JANAF Thermochemical Tables*. New York: American Institute of Physics.

Chen, B. H. *et al.* (1996) 'Synthesis and structure of a new perovskite, $SrCuO_{2.5}$', *Journal of Solid State Chemistry*, 121(2), pp. 498–501. doi: 10.1006/jssc.1996.0070.

Cheng, J. *et al.* (2005) 'Thermochemistry of $La_{1-x}Sr_xFeO_{3-\delta}$ Solid Solutions ($0.0 \leq x \leq 1.0$, $0.0 \leq \delta \leq 0.5$)', *Chemistry of Materials*, 17(8), pp. 2197–2207. doi: 10.1021/cm048613o.

Chuang, S. Y. *et al.* (2008) 'Development and performance of Cu-based oxygen carriers for chemical-looping combustion', *Combustion and Flame*, 154(1–2), pp. 109–121. doi: 10.1016/j.combustflame.2007.10.005.

Clayton, C. K., Sohn, H. Y. and Whitty, K. J. (2014) 'Oxidation Kinetics of Cu_2O in Oxygen Carriers for Chemical Looping with Oxygen Uncoupling', *Industrial & Engineering Chemistry Research*, 53(8), pp. 2976–2986. doi: 10.1021/ie402495a.

Cooper, J. R. *et al.* (2012) *Revised Release on the IAPWS Industrial Formulation 1997 for the Thermodynamic Properties of Water and Steam*.

Cuadrat, A. *et al.* (2012) 'Theoretical approach on the CLC performance with solid fuels: Optimizing the solids inventory', *Fuel*, 97, pp. 536–551. doi: 10.1016/j.fuel.2012.01.071.

Davis, M. E. and Davis, R. J. (2003) *Fundamentals of Chemical Reaction Engineering*. 1st edn. Edited by E. D. Glandt, M. T. Klein, and T. F. Edgar. McGraw-Hill.

Davison, J. (2007) 'Performance and costs of power plants with capture and storage of CO_2', *Energy*, 32, pp. 1163–1176. doi: 10.1016/j.energy.2006.07.039.

Dennis, J. S., Müller, C. R. and Scott, S. A. (2010) 'In situ gasification and CO_2 separation using chemical looping with a Cu-based oxygen carrier: Performance with bituminous coals', *Fuel*. Elsevier Ltd, 89(9), pp. 2353–2364. doi: 10.1016/j.fuel.2010.01.037.

Diethelm, S. *et al.* (2000) 'Oxygen transport and nonstoichiometry in $SrFeO_{3-d}$',

Electrochemistry, 68(6), pp. 440–450.

Donat, F. *et al.* (2016) 'Use of a Chemical-Looping Reaction to Determine the Residence Time Distribution of Solids in a Circulating Fluidized Bed', *Energy Technology*, 4(10), pp. 1230–1236. doi: 10.1002/ente.201600140.

Dubinin, S. F. *et al.* (2005) 'Ordering of Oxygen Vacancies in a $CaMnO_{3-\delta}$ Perovskite Single Crystal', *Physics of the Solid State*, 47(7), pp. 1267–1272. doi: 10.1134/1.1992603.

Dunstan, M. T. *et al.* (2016) 'Large scale computational screening and experimental discovery of novel materials for high temperature CO_2 capture', *Energy Environ. Sci.* Royal Society of Chemistry, 9(4), pp. 1346–1360. doi: 10.1039/C5EE03253A.

Eichel, R. A. (2011) 'Structural and dynamic properties of oxygen vacancies in perovskite oxides - Analysis of defect chemistry by modern multi-frequency and pulsed EPR techniques', *Physical Chemistry Chemical Physics*, 13(2), pp. 368–384. doi: 10.1039/b918782k.

Elrashidi, M. *et al.* (1987) 'Chemical Equilibria of Selenium in Soils: A Theoretical Development', *Soil Science*, 144(2), pp. 141–152.

Fogler, H. S. (2011) *Essentials of Chemical Reaction Engineering*. Prentice Hall. Available at: https://books.google.com/books?id=eyGKAwAAQBAJ&pgis=1 (Accessed: 26 July 2015).

Fogler, H. S. (2016) *Elements of chemical reaction engineering*. 5th edn. Boston: Prentice Hall. Available at: http://umich.edu/~elements/5e/index.html.

Francis, T. M., Perkins, C. and Weimer, A. W. (2010) 'Manganese oxide dissociation kinetics for the Mn_2O_3 thermochemical water-splitting cycle. Part 2: CFD model', *Chemical Engineering Science*. Elsevier, 65(15), pp. 4397–4410. doi: 10.1016/j.ces.2010.03.048.

Froment, G. F., Bischoff, K. B. and De Wilde, J. (2011) *Chemical Reactor Analysis and Design*. doi: 10.1017/CBO9781107415324.004.

Galinsky, N. *et al.* (2015) '$Ca_{1-x}A_xMnO_3$ (A = Sr and Ba) perovskite based oxygen carriers for chemical looping with oxygen uncoupling (CLOU)', *Applied Energy*. Elsevier Ltd, 157, pp. 358–367. doi: 10.1016/j.apenergy.2015.04.020.

Gayán, P. *et al.* (2012) 'Development of Cu-based oxygen carriers for Chemical-Looping with Oxygen Uncoupling (CLOU) process', 96, pp. 226–238. doi: 10.1016/j.fuel.2012.01.021.

Goldyreva, E. I. *et al.* (2012) 'Oxygen non-stoichiometry and defect equlibria in $CaMnO_{3-\delta}$', 281, pp. 1187–1191. doi: 10.1007/s10008-011-1499-0.

Görke, R. H. *et al.* (2018) 'Exploration of the material property space for chemical looping air separation applied to carbon capture and storage', *Applied Energy*, 212, pp. 478–488. doi: 10.1016/j.apenergy.2017.11.083.

Görke, R. H. *et al.* (2020) 'Reduction and oxidation behavior of strontium perovskites for chemical looping air separation', *International Journal of Greenhouse Gas Control*. Elsevier, 94(October 2019), p. 102891. doi: 10.1016/j.ijggc.2019.102891.

Grote, K.-H. and Feldhusen, J. (2007) *Dubbel — Taschenbuch für den Maschinenbau*. 22nd edn. Berlin, Heidelberg: Springer Berlin Heidelberg. doi: 10.1007/978-3-662-06774-1.

Gunn, D. J. (1987) 'Axial and radial dispersion', *Chem. Eng. Sci.*, 42(2), pp. 363–373. doi: 10.1016/0009-2509(87)85066-2.

Haavik, C. *et al.* (2003) 'Heat capacvity of $SrFeO_{3-d}$; d=0.5, 0.25, 0.15 – configurational entropy of structural entities in grossly non-stoichiometric oxides', *Dalton Transactions*, 0(3), pp. 361–368. doi: 10.1039/B209236K.

Harris, J. A. and Collings, N. (2015) 'The transient start-up response of a universal exhaust gas oxygen sensor to investigate the Nernst equation in platinum/zirconia cells', *Sensors and Actuators, B: Chemical*. Elsevier B.V., 221, pp. 81–87. doi: 10.1016/j.snb.2015.05.131.

Hayhurst, A. N. (2000) 'The mass transfer coefficient for oxygen reacting with a carbon particle in a fluidized or packed bed', *Combustion and Flame*, 121(4), pp. 679–688. doi: 10.1016/S0010-2180(99)00178-9.

Hodges, J. P. *et al.* (2000) 'Evolution of oxygen-vacancy ordered crystal structures in the perovskite series Sr(n)Fe(n)O(3n-1) (n = 2, 4, 8, and ∞), and the relationship to electronic and magnetic properties', *Journal of Solid State Chemistry*, 151(2), pp. 190–209. doi: 10.1006/jssc.1999.8640.

Hopper, A. (2019) *University of Cambrigde, Digital Technology Group, Cambrigde weather*. Available at: https://www.cl.cam.ac.uk/research/dtg/weather/ (Accessed: 28 October 2019).

Hu, W. *et al.* (2014) 'Characterisation of a Copper based Oxygen Carrier: Stability, Attrition Resistance and Reaction Kinetics', in *3rd International Conference on Chemical Looping*. Göteburg, Sweden, pp. 1–20.

Hu, W. *et al.* (2016) 'The interaction between CuO and Al_2O_3 and the reactivity of copper aluminates below 1000 °C and their implication on the use of the Cu-Al-O system for oxygen storage and production', *RSC Advances*. Royal Society of Chemistry, 6(114), pp. 113016–113024. doi: 10.1039/c6ra22712k.

IEA (2012) *The Global Value of Coal*. 2012/2013. Paris.

IEA (2017) *World Energy Outlook 2017*. OECD/IEA. doi: 10.1787/weo-2010-en.

IFA (2016) *GESTIS - substance database of the Institute for Occupational Safety and Health of the German Social Accident Insurance*. Available at: http://www.dguv.de/ifa/gestis/gestis-stoffdatenbank/index-2.jsp (Accessed: 21 November 2016).

Ikeda, H., Nikata, S., *et al.* (2016) 'Oxygen sorption/desorption behavior and crystal structural change for $SrFeO_{3-\delta}$', *Chemical Engineering Science*. Elsevier, 147, pp. 166–172. doi: 10.1016/j.ces.2016.03.034.

Ikeda, H., Tsuchida, A., *et al.* (2016) '$SrCo_xFe_{1-x}O_{3-\delta}$ Oxygen Sorbent Usable for High-Temperature Pressure-Swing Adsorption Process Operating at Approximately 300 °C', *Industrial and Engineering Chemistry Research*, 55(22), pp. 6501–6505. doi: 10.1021/acs.iecr.6b01284.

Imtiaz, Q., Hosseini, D. and Rüdiger, C. (2013) 'Review of Oxygen Carriers for Chemical Looping with Oxygen Uncoupling (CLOU): Thermodynamics , Material Development , and Synthesis', *Energy Technology*, 1, pp. 633–647. doi: 10.1002/ente.201300099.

Ishida, M. and Jin, H. (1994) 'A new advanced power-generation system using chemical-looping combustion', *Energy*, 19(4), pp. 415–422. doi: 10.1016/0360-5442(94)90120-1.

Jain, A. *et al.* (2011) 'Formation enthalpies by mixing GGA and GGA + U calculations', *Physical Review B - Condensed Matter and Materials Physics*, 84(4), pp. 1–10. doi:

10.1103/PhysRevB.84.045115.

Jain, A. *et al.* (2013) 'Commentary: The materials project: A materials genome approach to accelerating materials innovation', *APL Materials*, 1(1). doi: 10.1063/1.4812323.

Jansen, D. *et al.* (2015) 'Pre-combustion CO_2 capture', *International Journal of Greenhouse Gas Control*. Elsevier Ltd, 40, pp. 167–187. doi: 10.1016/j.ijggc.2015.05.028.

Jensen, W. B. (2009) 'Ask the Historian The Origin of the Brin Process for the Manufacture of Oxygen', *Journal of Chemical Education*, 86(11), pp. 1266–1267.

Jeon, H. K. and Kim, J. K. (2000) 'Effect of Reaction Rate on Morphological Change of Reactive Blends', *Macromolecules*, 33(22), pp. 8200–8210. doi: 10.1021/ma000842i.

Jin, H. and Ishida, M. (2002) 'Reactivity Study on Natural-Gas-Fueled Chemical-Looping Combustion by a Fixed-Bed Reactor', *Industrial & Engineering Chemistry Research*, 41, pp. 4004–4007. doi: 10.1021/ie020184l.

Jin, H. and Ishida, M. (2004) 'A new type of coal gas fueled chemical-looping combustion', *Fuel*, 83(17–18), pp. 2411–2417. doi: 10.1016/j.fuel.2004.06.033.

Jones, A. and Islam, M. S. (2008) 'Atomic-scale insight into $LaFeO_3$ perovskite: Defect nanoclusters and ion migration', *Journal of Physical Chemistry C*, 112(12), pp. 4455–4462. doi: 10.1021/jp710463x.

Kanniche, M. *et al.* (2010) 'Pre-combustion, post-combustion and oxy-combustion in thermal power plant for CO_2 capture', *Applied Thermal Engineering*. Elsevier Ltd, 30(1), pp. 53–62. doi: 10.1016/j.applthermaleng.2009.05.005.

Karthikeyan, M., Zhonghua, W. and Mujumdar, A. S. (2009) 'Low-rank coal drying technologies - Current status and new developments', *Drying Technology*, 27(3), pp. 403–415. doi: 10.1080/07373930802683005.

Kather, A. and Scheffknecht, G. (2009) 'The oxycoal process with cryogenic oxygen supply', *Naturwissenschaften*, 96(9), pp. 993–1010. doi: 10.1007/s00114-009-0557-2.

Keller, E. and Röhr, C. (2008) 'Structural changes within and between the two isotypic series $ABiO_2$ (A = Na, K, Rb, Cs) and $ASbO_2$ (A = K, Rb, Cs)', *Zeitschrift für Kristallographie*, 223(7), pp. 431–440. doi: 10.1524/zkri.2008.0045.

Killick, R., Fearnhead, P. and Eckley, I. A. (2012) 'Optimal detection of changepoints with a linear computational cost', *Journal of the American Statistical Association*, 107(500), pp. 1590–1598. doi: 10.1080/01621459.2012.737745.

Kimura, N. *et al.* (1995) 'The characteristics of pulverized coal combustion in O_2/CO_2 mixtures for CO_2 recovery', *Energy Conversion and Management*. doi: 10.1016/0196-8904(95)00126-X.

Kittilsen, P. and McKenna, T. F. (2001) 'Study of the kinetics, mass transfer, and particle morphology in the production of high-impact polypropylene', *Journal of Applied Polymer Science*, 82(5), pp. 1047–1060. doi: 10.1002/app.1939.

Kohn, K. *et al.* (1975) 'Crystal Structure and Magnetic Properties of $MnSeO_3$, $CoSeO_3$, $NiSeO_3$ and $CuSeO_3$', *Journal of the Physical Society of Japan*, 38, p. 587. doi: 10.1143/JPSJ.38.587.

Koleva, V. (1999) 'DTA, DSC and X-ray studies on copper and manganese selenate hydrates', *Thermochimica Acta*, 342(1–2), pp. 89–95. doi: 10.1016/S0040-6031(99)00238-5.

Krishnamurthy, K., Acharya, D. and Fitch, F. (2008) *Pilot-Scale Demonstration of a Novel, Low-Cost Oxygen Supply Process and its Integration with Oxy-Fuel Coal-Fired Boilers*.

Kröger, F. A., Stieltjes, F. H. and Vink, H. J. (1959) 'Thermodynamics and Formulation of Reactions involving Imperfections in Solids', *Phillips Res. Repts.*, 14, pp. 557–601.

Ksepko, E. (2014) 'Perovskite-type $Sr(Mn_{1-x}Ni_x)O_3$ materials and their chemical-looping oxygen transfer properties', *International Journal of Hydrogen Energy*. Elsevier Ltd, 39(15), pp. 8126–8137. doi: 10.1016/j.ijhydene.2014.03.093.

Ksepko, E. (2015) 'Examining $SrCuO_2$ as an oxygen carrier for chemical looping combustion', *Journal of Thermal Analysis and Calorimetry*. Springer Netherlands, 122(2), pp. 621–633. doi: 10.1007/s10973-015-4813-8.

Ksepko, E. (2018) 'Perovskite $Sr(Fe_{1-x}Cu_x)O_{3-\delta}$ materials for chemical looping combustion applications', *International Journal of Hydrogen Energy*, 43(20), pp. 9622–9634. doi: 10.1016/j.ijhydene.2018.04.046.

Kumada, N. (1996) 'Preparation and Crystal Structure of a New Lithium Bismuth Oxide:

$LiBiO_3$', *Journal of Solid State Chemistry*, 126(1), pp. 121–126. doi: 10.1006/jssc.1996.0319.

Kumada, N., Kinomura, N. and Sleight, A. W. (2000) 'Neutron powder diffraction refinement of ilmenite-type bismuth oxides: $ABiO_3$ (A = Na, Ag)', *Materials Research Bulletin*, 35(14–15), pp. 2397–2402. doi: 10.1016/S0025-5408(00)00453-0.

Kusaba, H. *et al.* (2002) 'Oxygen-sorptive and -desorptive properties of perovskite-related oxides under temperature-swing conditions for oxygen enrichment', *Solid State Ionics*, 152–153, pp. 689–694. doi: 10.1016/S0167-2738(02)00410-1.

Lane, H. (1909) 'The Lane Hydrogen Producer', *Flight*, 1(35), p. 524.

Lane, H. (1913) 'Process for the Production of Hydrogen'. USA.

Lankhorst, M. H. R., Bouwmeester, H. J. M. and Verweij, H. (1997) 'Thermodynamics and Transport of Ionic and Electronic Defects in Crystalline Oxides', *Journal of the American Ceramic Society*, 80(9), pp. 2175–2198. doi: 10.1111/j.1151-2916.1997.tb03107.x.

Larrañaga, M. D., Lewis, R. J. S. and Lewis, R. A. (2007) *Hawley's Condensed Chemical Dictionary*. 15th edn. Edited by R. J. Lewis Sr. Wiley. doi: 10.1021/ja0769144.

Lau, C. Y. *et al.* (2017) 'Large scale in silico screening of materials for carbon capture through chemical looping', *Energy Environ. Sci.* Royal Society of Chemistry, 10, pp. 818–831. doi: 10.1039/C6EE02763F.

Lavielle, M. (2005) 'Using penalized contrasts for the change-point problem', *Signal Processing*, 85(8), pp. 1501–1510. doi: 10.1016/j.sigpro.2005.01.012.

Levenspiel, O. (1999) *Chemical reaction engineering*. 3rd edn, *Chemical Engineering Science*. 3rd edn. John Wiley & Sons. doi: 10.1016/0009-2509(64)85017-X.

Lewis, W. K. and Gilliland, E. R. (1954) 'Production of Pure Carbon Dioxide'. United States.

Li, Z., Zhang, T. and Cai, N. (2008) 'Experimental Study of O_2 - CO_2 Production for the Oxyfuel Combustion Using a Co-Based Oxygen Carrier', *Ind. Eng. Chem. Res.*, 47, pp. 7147–7153.

Lin, Y.-S., MacLean, D. L. and Zeng, Y. (2000) 'High Temperature Adsorption Process'.

USA: United States Patent Office.

Ling, S. (1994) 'Statistical thermodynamic formulation of high concentration point defect chemistry in perovskite crystalline systems: Application to strontium doped lanthanum chromite', *Journal of Physics and Chemistry of Solids*, 55(12), pp. 1445–1460. doi: 10.1016/0022-3697(94)90570-3.

Lyday, P. A. and Kaiho, T. (2015) 'Iodine and Iodine Compounds', *Ullmann's Encyclopedia of Industrial Chemistry*, pp. 1–13. doi: 10.1002/14356007.a14.

Lyngfelt, A. and Leckner, B. (2014) 'A 1000MW_{th} boiler for chemical-looping combustion of solid fuels - Discussion of design and costs', *Applied Energy*. Elsevier Ltd, 157, pp. 475–487. doi: 10.1016/j.apenergy.2015.04.057.

Lyngfelt, A. and Linderholm, C. (2017) 'Chemical-Looping Combustion of Solid Fuels - Status and Recent Progress', *Energy Procedia*. The Author(s), 114(November 2016), pp. 371–386. doi: 10.1016/j.egypro.2017.03.1179.

Mack, D. E. (2003) *In-situ Untersuchungen zu Fehlordnung und Ladungstransport in Eisenoxiden mit Perowskitstruktur*. TU Braunschweig.

Mallet, J. T. A. (1868) 'Improved Processes for Producing Oxygen and Chlorine'.

Marek, E. *et al.* (2018) 'The use of strontium ferrite in chemical looping systems', *Applied Energy*. Elsevier, 223(November 2017), pp. 369–382. doi: 10.1016/j.apenergy.2018.04.090.

Mason, D. M. and Gandhi, K. N. (1983) 'Formulas for calculating the calorific value of coal and coal chars: Development, tests, and uses', *Fuel Processing Technology*, 7(1), pp. 11–22. doi: 10.1016/0378-3820(83)90022-X.

Mattisson, T. *et al.* (2007) 'Chemical-looping combustion using syngas as fuel', *International Journal of Greenhouse Gas Control*, 1, pp. 158–169. doi: 10.1016/S1750-5836(07)00023-0.

Mattisson, T., Lyngfelt, A. and Leion, H. (2009) 'Chemical-looping with oxygen uncoupling for combustion of solid fuels', *International Journal of Greenhouse Gas Control*, 3(1), pp. 11–19. doi: 10.1016/j.ijggc.2008.06.002.

McBride, B. J., Zehe, M. J. and Gordon, S. (2002) *NASA Glenn Coefficients for Calculating Thermodynamic Properties of Individual Species*. 2002–211556. Ohio.

Available at: http://hdl.handle.net/2060/20020085330.

McCauley, K., Moorman, S. and McDonald, D. (2011) *Oxy-Coal Combustion for Low Carbon Electric Power Generation, Fifth International Conference on Clean Coal Technologies*. BR-1850. Zaragoza, Spain.

Melot, B. C. *et al.* (2010) 'Magnetic ordering and magnetodielectric phenomena in $CoSeO_4$.', *Journal of physics. Condensed matter : an Institute of Physics journal*, 22(50), p. 506003. doi: 10.1088/0953-8984/22/50/506003.

Merkle, R. and Maier, J. (2003) 'Defect association in acceptor-doped $SrTiO_3$: Case study for Fe′Ti VO.. and Mn″TiVO..', *Physical Chemistry Chemical Physics*, 5(11), pp. 2297–2303. doi: 10.1039/b300205p.

Merkle, R. and Maier, J. (2008) 'How Is Oxygen Incorporated into Oxides? A Comprehensive Kinetic Study of a Simple Solid-State Reaction with $SrTiO_3$ as a Model Material', *Angewandte Chemie International Edition*, 47(21), pp. 3874–3894. doi: 10.1002/anie.200700987.

Messerschmitt, A. (1910) 'Process of Producing Hydrogen'. USA.

Mizusaki, J. *et al.* (1985) 'Nonstoichiometry and defect structure of the perovskite-type oxides $La_{1-x}Sr_xFeO_{3-d}$', *Journal of Solid State Chemistry*, 58(2), pp. 257–266. doi: 10.1016/0022-4596(85)90243-9.

Mizusaki, J. (1992) 'Nonstoichiometry, diffusion, and electrical properties of perovskite-type oxide electrode materials', *Solid State Ionics*, 52(1–3), pp. 79–91. doi: 10.1016/0167-2738(92)90093-5.

Moghtaderi, B. (2010) 'Application of Chemical Looping Concept for Air Separation at High Temperatures', *Energy & Fuels*, 24(1), pp. 190–198. doi: 10.1021/ef900553j.

Momma, K. and Izumi, F. (2011) 'VESTA 3 for three-dimensional visualization of crystal, volumetric and morphology data', *Journal of Applied Crystallography*, 44(6), pp. 1272–1276. doi: 10.1107/S0021889811038970.

Mortimer, R. G. (2008) *Physical Chemistry*. Third Edit. Burlington, MA, USA: Elsevier.

Du Motay, C. M. T. and Maréchal, C. R. (1867) 'Improved Mode of Producing Oxygen Gas'.

Mullhaupt, J. T. and Stern, S. A. (1969) 'Process and Composition for Separation of Oxygen from Air using Strontium Oxide-Peroxide as the Carrier'. USA: United States Patent Office.

Nguyen, T. N. *et al.* (1993) 'Electrosynthesis of Kbio3 - a Potassium-Ion Conductor with the Ksbo3 Tunnel Structure', *Chemistry of Materials*, 5(9), pp. 1273–1276. Available at: http://gateway.webofknowledge.com/gateway/Gateway.cgi?GWVersion=2&SrcAuth=mekentosj&SrcApp=Papers&DestLinkType=FullRecord&DestApp=WOS&KeyUT=A1993LY92900015%5Cnpapers2://publication/uuid/9951D5D9-067C-4D73-9B3C-C7AAB353DB9E.

Oates, W. A. *et al.* (2011) 'Evaluation of the Component Chemical Potentials in Analytical Models for Ordered Alloy Phases', *Journal of Thermodynamics*, 2011, pp. 1–4. doi: 10.1155/2011/874979.

Olivier, J. *et al.* (2015) *Trend in Global CO_2 Emissions: 2015 Report*. The Hague. Available at: https://www.pbl.nl/sites/default/files/cms/publicaties/pbl-2015-trends-in-global-co2-emisions_2015-report_01803.pdf.

Ong, S. P. *et al.* (2008) 'Li−Fe−P−O_2 Phase Diagram from First Principles Calculations', *Chemistry of Materials*, 20(5), pp. 1798–1807. doi: 10.1021/cm702327g.

Ong, S. P. *et al.* (2010) 'Thermal stabilities of delithiated olivine MPO_4 (M = Fe, Mn) cathodes investigated using first principles calculations', *Electrochemistry Communications*. Elsevier B.V., 12(3), pp. 427–430. doi: 10.1016/j.elecom.2010.01.010.

Parras, M. *et al.* (1993) 'A high temperature study of the $BaFeO_{3-y}$ system', *Solid State Ionics*, 63–65, pp. 714–718. doi: 10.1016/0167-2738(93)90185-6.

Perrin, N. *et al.* (2014) 'Oxycombustion for coal power plants: Advantages, solutions and projects', *Applied Thermal Engineering*. Elsevier Ltd, 74, pp. 75–82. doi: 10.1016/j.applthermaleng.2014.03.074.

Pfaff, I. and Kather, A. (2009) 'Comparative thermodynamic analysis and integration issues of CCS steam power plants based on oxy-combustion with cryogenic or membrane based air separation', *Energy Procedia*. Elsevier, 1(1), pp. 495–502. doi: 10.1016/j.egypro.2009.01.066.

Reed, C. H. and Berg, O. C. (1953) 'Hydrogen Process'. USA.

Reidies, A. H. (2000) 'Manganese Compounds', *Ullmann's Encyclopedia of Industrial Chemistry*, 22, pp. 223–244. doi: 10.1002/14356007.a16.

Richter, H. J. and Knoche, K. F. (1983) 'Reversibility of Combustion Processes', in R.A., G. (ed.) *ACS Symposium Series, vol. 235*. Washington D.C.: American Chemical Society, pp. 71–85. doi: 10.1021/bk-1983-0235.ch003.

Romano, M. C., Chiesa, P. and Lozza, G. (2010) 'Pre-combustion CO_2 capture from natural gas power plants, with ATR and MDEA processes', *International Journal of Greenhouse Gas Control*. Elsevier Ltd, 4(5), pp. 785–797. doi: 10.1016/j.ijggc.2010.04.015.

van Roosmalen, J. A. M. and Cordfunke, E. H. P. (1991) 'A new defect model to describe the oxygen deficiency in perovskite-type oxides', *Journal of Solid State Chemistry*, 93(1), pp. 212–219. doi: 10.1016/0022-4596(91)90290-X.

van Roosmalen, J. A. M. and Cordfunke, E. H. P. (1994) 'The defect chemistry of $LaMnO_{3-\delta}$', *Journal of Solid State Chemistry*, pp. 113–117. doi: 10.1006/jssc.1994.1144.

Sabrowsky, H. and Hoppe, R. (1958) 'Darstellung und Kristallstruktur von KAgO und CsAgO', *Zeitschrift für anorganische und allgemeine Chemie*, 358(5–6), pp. 241–256. doi: 10.1002/zaac.19683580507.

Saffari, M. and Weihong, Y. (2014) 'Performance of pulverized coal combustion under high temperature air diluted by steam', *ISRN Mechanical Engineering*, 2014. doi: 10.1155/2014/217574.

Sarkar, D. (2015) *Thermal Power Plant: Design and Operation*. 1st edn. Amsterdam, Netherlands: Joe Hayton. Available at: https://books.google.co.uk/books?id=k5_vAwAAQBAJ&pg=PA234&lpg=PA234&dq=vapour+88+%25+steam+turbine+outlet&source=bl&ots=j_cRntbo3K&sig=D6wdiSd_YQmEg8n9xM_c98_5bI0&hl=de&sa=X&ved=0ahUKEwiX2puB0v_WAhUHY1AKHYiWBHkQ6AEIZzAM#v=onepage&q=vapour 88 %25 steam tur.

Sathiyamoorthi, R. *et al.* (2005) 'Preparation of nanoparticle size $LiBiO_2$ by combustion method and its electrochemical studies for lithium secondary cells', *Pramana - Journal of Physics*, 65(5), pp. 973–980. doi: 10.1007/BF02704099.

Schmidt, M. and Campbell, S. J. (2001) 'Crystal and Magnetic Structures of $Sr_2Fe_2O_5$ at

Elevated Temperature', *Journal of Solid State Chemistry*, 156(2), pp. 292–304. doi: 10.1006/jssc.2000.8998.

Schmidt, M. W. (2001) *Phase Transformation and Structural Transformation of Strontium Ferrite $SrFeO_x$*. Australian National University. Available at: https://openresearch-repository.anu.edu.au/bitstream/1885/48187/6/02whole.pdf.

Schnellmann, M. A. *et al.* (2016) 'Sensitivity of chemical-looping combustion to particle reaction kinetics', *Chemical Engineering Science*. Elsevier, 152, pp. 21–25. doi: 10.1016/j.ces.2016.05.028.

Schnellmann, M. A. *et al.* (2018) 'The effect of different particle residence time distributions on the chemical looping combustion process', *Applied Energy*, 216(December 2017), pp. 358–366. doi: 10.1016/j.apenergy.2018.02.046.

Shah, K. *et al.* (2013) 'Integration options for novel chemical looping air separation (ICLAS) process for oxygen production in oxy-fuel coal fired power plants', *Fuel*, 107, pp. 356–370. doi: 10.1016/j.fuel.2013.01.007.

Shah, K., Moghtaderi, B. and Wall, T. (2012) 'Selection of suitable oxygen carriers for chemical looping air separation: A thermodynamic approach', *Energy and Fuels*, 26, pp. 2038–2045. doi: 10.1021/ef300132c.

Shulman, A. *et al.* (2009) 'Manganese/iron, manganese/nickel, and manganese/silicon oxides used in chemical-looping with oxygen uncoupling (CLOU) for combustion of methane', *Energy and Fuels*, 23(10), pp. 5269–5275. doi: 10.1021/ef9005466.

Sigma Aldrich (2016) *Cesium Iodide: Safety Information*. Available at: http://www.sigmaaldrich.com/catalog/product/aldrich/203033?lang=en&region=GB (Accessed: 17 November 2016).

Siriwardane, R. *et al.* (2015) 'Fluidized bed testing of commercially prepared MgO-promoted hematite and $CuO–Fe_2O_3$ mixed metal oxide oxygen carriers for methane and coal chemical looping combustion', *Applied Energy*. Elsevier Ltd, 157, pp. 348–357. doi: 10.1016/j.apenergy.2015.04.042.

Song, Hu *et al.* (2014) 'Analysis on Chemical Reaction Kinetics of CuO / SiO_2 Oxygen Carriers for Chemical Looping Air Separation', *Energy & Fuels*, 28(1), pp. 173–182. doi: dx.doi.org/10.1021/ef401487x.

Song, H. (2014) *Chemical Looping Air Separation for Oxy-fuel Power Plants*. University of Newcastle, Australia.

Song, Hui, Shah, K., Doroodchi, E. and Moghtaderi, B. (2014) 'Development of a Cu–Mg-Based Oxygen Carrier with SiO_2 as a Support for Chemical Looping Air Separation', *Energy & Fuels*, 28, pp. 163–172. doi: 10.1021/ef401485p.

Song, Hui, Shah, K., Doroodchi, E., Wall, T., *et al.* (2014) 'Reactivity of Al_2O_3 - or SiO_2-Supported Cu-, Mn-, and Co-Based Oxygen Carriers for Chemical Looping Air Separation', *Energy & Fuels*, 28(2), pp. 1284–1294. doi: 10.1021/ef402268t.

Sonntag, D. (1990) 'Important New Values of the Physical Constants of 1986, Vapour Pressure Formulations based on the IST-90 and Psychrometer Formulae', *Zeitung für Meteorologie*, 70(5), pp. 340–344.

Sperlich, V. (2002) *Übungsaufgaben zur Thermodynamik mit Mathcad*. Leipzig: Carl Hanser Verlag. doi: 10.3139/9783446222380.

Starkov, Ilya A. *et al.* (2014) 'Oxygen Release from Grossly Nonstoichiometric $SrCo_{0.8}Fe_{0.2}O_{3-\delta}$ Perovskite in Isostoichiometric Mode', *Chemistry of Materials*, 26(6), pp. 2113–2120. doi: 10.1021/cm4040775.

Starkov, I. A. *et al.* (2014) 'Oxygen release technique as a method for the determination of "'d–pO_2–T'" diagrams for MIEC oxides', *Phys. Chem. Chem. Phys.*, 16, pp. 5527–5535. doi: 10.1039/c3cp52143e.

Stølen, S., Bakken, E. and Mohn, C. E. (2006) 'Oxygen-deficient perovskites: linking structure, energetics and ion transport', *Phys. Chem. Chem. Phys.*, 8(4), pp. 429–447. doi: 10.1039/B512271F.

Suda, T. *et al.* (2002) 'A study of combustion behavior of pulverized coal in high-temperature air', *Proceedings of the Combustion Institute*, 29(1), pp. 503–509. doi: 10.1016/s1540-7489(02)80065-7.

Tagliaferri, C. *et al.* (2018) 'Life cycle assessment of optimised chemical looping air separation systems for electricity production', *Chemical Engineering Research and Design*. Institution of Chemical Engineers, 131, pp. 686–698. doi: 10.1016/j.cherd.2017.11.010.

Takeda, Y. *et al.* (1986) 'Phase relation in the oxygen nonstoichiometric system, $SrFeO_x$

($2.5 \leq x \leq 3.0$)', *Journal of Solid State Chemistry*, 63(2), pp. 237–249. doi: 10.1016/0022-4596(86)90174-X.

Tan, Y. *et al.* (2006) 'Combustion characteristics of coal in a mixture of oxygen and recycled flue gas', *Fuel*. doi: 10.1016/j.fuel.2005.08.010.

Taylor, D. D. *et al.* (2016) 'Oxygen storage properties of $La_{1-x}Sr_xFeO_{3-\delta}$ for chemical-looping reactions – an in-situ neutron and synchrotron X-ray study', *Chemistry of Materials*, 28, pp. 3951–3960. doi: 10.1021/acs.chemmater.6b01274.

Till, L. (1971) 'Thermochemical data of barium peroxide from thermogravimetric measurements', *Journal of Thermal Analysis*, 3(2), pp. 177–180. doi: 10.1007/BF01904681.

Tong, A. *et al.* (2014) 'Iron-based syngas chemical looping process and coal-direct chemical looping process development at Ohio State University', *Applied Energy*. Elsevier Ltd, 113, pp. 1836–1845. doi: 10.1016/j.apenergy.2013.05.024.

Touzain, P. (1976) 'Systemes Metaux Alcalins-Oxygene', *Journal of Thermal Analysis*, 9, pp. 441–450.

Trainer, J. P., Perrin, N. and Darde, A. (2008) 'Update on Advanced Developments for ASU and CO_2 Purification Units for Oxy-Combustion (Air Liquide, France)', in *3rd Meeting of the Oxy-Combustion Network*. Yokohama, Japan, March 5th.

Tsai, K.-R., Harris, P. M. and Lassettre, E. N. (1956) 'The Crystal Structure of Tricesium Monoxide', *Journal of Physical Chemistry*, 60(3), pp. 345–347. doi: 10.1021/j150537a023.

Tsujimoto, Y. *et al.* (2007) 'Infinite-layer iron oxide with a square-planar coordination', *Nature*, 450(7172), pp. 1062–1065. doi: 10.1038/nature06382.

Vieten, J. *et al.* (2017) 'Redox thermodynamics and phase composition in the system $SrFeO_{3-\delta}$ — $SrMnO_{3-\delta}$', *Solid State Ionics*, 308(April), pp. 149–155. doi: 10.1016/j.ssi.2017.06.014.

Vlaev, L. T., Genieva, S. D. and Georgieva, V. G. (2006) 'Study of the crystallization fields of Cobalt(II) Selenites in the system $CoSeO_3$-SeO_2-H_2O', *Journal of Thermal Analysis and Calorimetry*, 81(2), pp. 469–475. doi: 10.1007/s10973-005-7397-x.

Vlaev, L. T. and Tavlieva, M. P. (2007) 'Structural and Thermal Studies on the Solid

Products in the System $MnSeO_3$-SeO_2-H_2O', *Journal of Thermal Analysis and Calorimetry*, 90, pp. 385–392.

Vuori, E. *et al.* (1994) 'A long-term study of selenate sorption in Finnish cultivated soils', *Agriculture, Ecosystems and Environment*, 48, pp. 91–98.

Wall, T. (2005) 'Fundamentals of Oxy-Fuel Combustion', in *Oxy-Fuel Combustion Research Network*. Cottbus, Germany.

Wall, T. *et al.* (2009) 'An overview on oxyfuel coal combustion-State of the art research and technology development', *Chemical Engineering Research and Design*, 87(8), pp. 1003–1016. doi: 10.1016/j.cherd.2009.02.005.

Wang, H., Li, Z. and Cai, N. (2019) 'A multiscale model of oxidation kinetics for Cu-based oxygen carrier in chemical looping with Oxygen Uncoupling', *Materials*, 12(7). doi: 10.3390/ma12071170.

Wang, K. *et al.* (2014) 'Feasibility of a Co Oxygen Carrier for Chemical Looping Air Separation: Thermodynamics and Kinetics', *Chemical Engineering & Technology*, 37(9), pp. 1500–1506. doi: 10.1002/ceat.201400178.

Wang, K., Yu, Q. and Qin, Q. (2013) 'The thermodynamic method for selecting oxygen carriers used for chemical looping air separation', *Journal of Thermal Analysis and Calorimetry*, 112(2), pp. 747–753. doi: 10.1007/s10973-012-2596-8.

Wang, L., Maxisch, T. and Ceder, G. (2006) 'Oxidation energies of transition metal oxides within the GGA+U framework', *Physical Review B - Condensed Matter and Materials Physics*, 73(19), pp. 1–6. doi: 10.1103/PhysRevB.73.195107.

Wißmann, S. and Becker, K. D. (1996) 'Localization of electrons in nonstoichiometric $SrFeO_{3-d}$', *Solid State Ionics*, 85(1–4), pp. 279–283.doi:10.1016/0167-2738(96)00071-9.

Yang, Z., Lin, Y. S. and Zeng, Y. (2002) 'High-Temperature Sorption Process for Air Separation and Oxygen Removal', *Industrial & Engineering Chemistry Research*, 41, pp. 2775–2784. doi: 10.1021/ie010736k.

Yeon, J., Kim, S. H. and Halasyamani, P. S. (2009) 'New Thallium Iodates - Synthesis, Characterization, and Calculations of $Tl(IO_3)_3$ and $Tl_4(IO_3)_6$, $[Tl{+}3Tl3{+}(IO_3)_6]$', *Journal of Solid State Chemistry*. Elsevier, 182(12), pp. 3269–3274. doi: 10.1016/j.jssc.2009.09.021.

Yin, Q., Kniep, J. and Lin, Y. S. (2008) 'High temperature air separation by perovskite-type oxide sorbents-Heat effect minimization', *Chemical Engineering Science*, 63(24), pp. 5870–5875. doi: 10.1016/j.ces.2008.09.004.

Yoo, J. *et al.* (2005) 'Oxygen Transport Kinetics in $SrFeO_{3-\delta}$, $La_{0.5}Sr_{0.5}FeO_{3-\delta}$, and $La_{0.2}Sr_{0.8}Cr_{0.2}Fe_{0.8}O_{3-\delta}$ Measured by Electrical Conductivity Relaxation', *Journal of The Electrochemical Society*, 152(3), p. A497. doi: 10.1149/1.1854617.

Yoo, J. *et al.* (2017) 'Determination of oxygen nonstoichiometry in $SrFeO_{3-\delta}$ by solid-state Coulometric titration', *Journal of the American Ceramic Society*, 100(6), pp. 2690–2699. doi: 10.1111/jace.14755.

Zaabout, A. *et al.* (2014) 'A Novel Gas Switching Combustion Reactor for Power Production with Integrated CO 2 Capture : Sensitivity to the Fuel Type', pp. 1–14.

Zafar, Q. *et al.* (2007) 'Reduction and oxidation kinetics of Mn_3O_4/Mg-ZrO_2 oxygen carrier particles for chemical-looping combustion', *Chemical Engineering Science*, 62(23), pp. 6556–6567. doi: 10.1016/j.ces.2007.07.011.

Zakutayev, A. *et al.* (2013) 'Theoretical Prediction and Experimental Realization of New Stable Inorganic Materials Using the Inverse Design Approach', *Journal of the American Chemical Society*, 135, pp. 10048–10054. doi: 10.1021/ja311599g.

Zhang, H. *et al.* (1990) 'Oxygen sorption and catalytic properties of $La_{1-x}Sr_xCo_{1-y}Fe_yO_3$ perovskite-type oxides', *Journal of Catalysis*, 121(2), pp. 432–440. doi: 10.1016/0021-9517(90)90251-E.

Zhang, J. *et al.* (2017) 'The search of proper oxygen carriers for chemical looping partial oxidation of carbon', *Applied Energy*. Elsevier Ltd, 190, pp. 1119–1125. doi: 10.1016/j.apenergy.2017.01.024.

Zhang, T., Li, Z. and Cai, N. (2009) 'Continuous O_2-CO_2 production using a Co-based oxygen carrier in two parallel fixed-bed reactors', *Korean Journal of Chemical Engineering*, 26(3), pp. 845–849. doi: 10.1007/s11814-009-0141-7.

Zhang, X. *et al.* (2012) 'Sorting stable versus unstable hypothetical compounds: The case of multi-functional ABX Half-Heusler filled tetrahedral structures', *Advanced Functional Materials*, 22(7), pp. 1425–1435. doi: 10.1002/adfm.201102546.

Zhu, S. *et al.* (2018) 'Numerical investigation towards HiTAC conditions in laboratory-

scale ethanol spray combustion', *Fuel*. Elsevier, 211(September 2017), pp. 375–389. doi: 10.1016/j.fuel.2017.09.002.

Zoughaib, A. (2017) 'Energy Integration of Continuous Processes: From Pinch Analysis to Hybrid Exergy/Pinch Analysis', in *From Pinch Methodology to Pinch-Energy Integration of Flexible Systems*. London, UK: Elsevier, pp. 1–53. doi: 10.1016/B978-1-78548-194-9.50001-6.

12 Appendix

12.1 Example flow sheet of the CLAS-oxy-fuel power plant

In this section, a flow sheet of the CLAS-oxy-fuel power plant producing 500 MW_{el} is presented for an oxygen carrier releasing oxygen according to

$$4MeO \rightleftarrows 2Me_2O + O_2$$

with ΔH_r^o of 250 kJ/mol at a temperature where the material is in equilibrium with oxygen at 0.34 bar, T_{eq}, of 973 K. As described in section 2.2.6.1 and shown in Figure 2-4a, which is replotted as Figure 12-1a for convenience, in this case there is a mismatch between the heat of combustion supplied by the oxy-fuel combustor and the heat required to drive the reduction reaction in the reducer to produce the oxygen necessary for the combustion. From the reaction stated at the beginning of this chapter, the gaseous in- and outflows as well as the molar circulation rate of the solids of the CLAS unit are listed in Table 12-1 per mole of oxygen. It should be noted that, in this example, the inflows to the oxidiser are fully pre-heated by, *e.g.*, using parts of the heat in the outflow of the oxidiser. However, the inflow the reducer is takes place at room temperature. The effect of pre-heating is discussed in section 2.3.7; pre-heating the inflow to the reducer would decrease the heat required at the operating temperature of the reducing reactor. The steam that is introduced to the reducing reactor is subsequently condensed, as described in section 2.2.2; after the condensation, roughly 0.063 moles of steam remain. At the outlet of the CLAS condenser (inlet of the oxy-fuel combustor), the gaseous flow is at 298 K.

Table 12-1: Outflow of the reducer operating at 973 K and the oxidiser operating at 893 K

	Reducer		Oxidiser	
	Inflow	Outflow	Inflow	Outflow
Temperature K	298	973	893	893
Species		mol/s		
CO	0	5.1177E-08	0	0
CO_2	1.7942	1.7942	0	0
H_2	0	4.0057E-08	0	0
H_2O	0.1471	0.1471	0	0
O_2	0	1	1.14381	0.14381
N_2	0	0	4.3030	4.3030
MeO	4.0002	1.4145E-05	1.4145E-05	4.0002
Me_2O	8.07E-06	2.0001	2.0001	8.07E-06

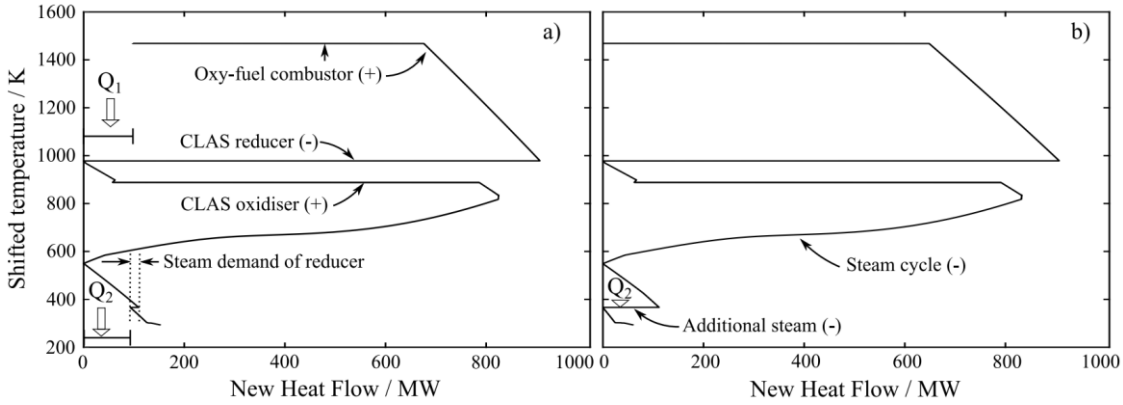

Figure 12-1: Grand composite curve of the a) non-optimized and b) optimized power plant producing 500 $MW_{el,net}$ running at a heat deficit (Q_1, the part of the heat demand of the CLAS reducer that cannot be satisfied by the oxy-fuel combustor) and using an oxygen carrier system with $T_{eq}(pO_{2,red}$=0.34 bar) = 973 K and ΔH_r^o = 250 kJ/mol; here, the maximum temperature of the unmodified steam cycle is 835 K. Q_1 in b) is assumed to be overcome by supplying additional oxygen. Q_2 is heat available at temperatures below the steam generator (HRSG) inlet temperature of 549 K. (-) and (+) denote heat sinks and heat sources, respectively

The dried outflow of the reducer, now at a temperature of 298 K, is then fed into the oxy-fuel combustor. Using Illinois No. 5 coal, the composition of which is shown in section 2.2.5, the inflows and outflows of the oxy-fuel combustor are listed in Table 12-2. The percentage of the heat requirement of the reducing reactor ($H_{red}(T_{red})$) that is covered from heat supplied by the oxy-fuel combustor ($H_{comb}(T_{red})$) is calculated by taking the ratio of $H_{red}(T_{red})$ and $H_{comb}(T_{red})$; in this case

$$\frac{H_{red}(T_{red})}{H_{comb}(T_{red})} = \frac{929\ MW}{838.6\ MW} = 90.27\ \%$$

Table 12-2: Inflows and outflows of the oxy-fuel combustor per mole of oxygen produced by the CLAS unit.

	Fuel	Gaseous inflow	Outflow
Temperature K	298	298	>1500
Species		mol/s	
CO	0	5.11772E-08	6.36836E-05
CO_2	0	1.7942	2.6251
H_2	0.3085	4.00569E-08	4.23473E-06
H_2O	0.0609	0.0630	0.4324
O_2	0.0529	1.0	0.0560
N_2	0.0087	1.21367E-23	0.0087
SO_2	0	0	0.0117
C_{solid}	0.8394	0	0.0084
S_{solid}	0.0117	0	4.36358E-13

Here, it is assumed that the extra oxygen is covered by a cryogenic air separation unit (CASU), as described in section 2.2.6.1, *i.e.* 0.16 kWh per kg of oxygen at a purity of 95 %. The Grand Composite curve of the optimised power plant, *i.e.* raising steam from low temperature heat which is introduced into the low-pressure turbine, which reduced the overall heat demand of the heat recovery steam generator (HRSG), and covering the entire heat demand of the reducer by combustion, made possible by supplying additional oxygen from a CASU, is shown in Figure 12-1b. The inflows and outflows of the CLAS unit and the oxy-fuel combustor listed in Table 12-1 and Table 12-2 were scaled by a factor of 2878 to match the heat demand of the steam cycle, which is fixed to produce 500 $MW_{el,net}$. As indicated in Figure 12-1b, the heat available at temperature below the HRSG inlet temperature, *i.e.* 548.7 K, is used to provide the steam introduced into the reducer (503.7 mol/s) and inject 64.2 kg/s (3567 mol/s) of steam into the second stage of the low-pressure turbine (shown in Figure 1-4). This increase in the steam flow to the low-pressure turbine is the only modification to the flow sheet of the power plant, so that all other values given in Figure 1-4 remain valid. At the fixed output of 500 $MW_{el,net}$ of the steam cycle, this lowers the heat demand of the HRSG to 1,075 MW which is entirely met by the combined heat supplied by the oxidiser, its gaseous outflow, the gaseous outflow of the reducer and the exhaust of the oxy-fuel combustor, as shown in Figure 12-1b.

12.2 Analytical solution to equation (3-38)

$$\int_{x_{O_2,in}}^{x_{O_2,out}} \frac{1}{\left(x_{O_2} - x_{O_2,eq}(\delta_0)\right)\left(1 - x_{O_2}\right)^2} dx_{O_2} = F_3\left(F_4 + F_5 + F_4F_5(-F_6 + +F_7 + F_8 - F_9)\right)$$

where

$$F_1 = \left(1 - x_{O_2,eq}(\delta_0) + x_{O_2,in}\left(x_{O_2,eq}(\delta_0) - 1\right)\right)$$

$$F_2 = \left(1 - x_{O_2,eq}(\delta_0) + x_{O_2,out}\left(x_{O_2,eq}(\delta_0) - 1\right)\right)$$

$$F_3 = \frac{1}{\left(x_{O_2,eq}(\delta_0) - 1\right)^2 F_1\, F_2}$$

$$F_4 = \left(x_{O_2,eq}(\delta_0) - 1\right)^2 \left(2x_{O_2,in} - 1 - x_{O_2,eq}(\delta_0)\right)$$

$$F_5 = \left(x_{O_2,eq}(\delta_0) - 1\right)^2 \left(2x_{O_2,out} - 1 - x_{O_2,eq}(\delta_0)\right)$$

$$F_6 = log\left(\frac{1}{\left(x_{O_2,eq}(\delta_0) - 1\right)^2}\left(-x_{O_2,eq}(\delta_0)^3 + 3x_{O_2,eq}(\delta_0)^2 - 3x_{O_2,eq}(\delta_0) + F_4 + 1\right)\right)$$

$$F_7 = log\left(\frac{1}{\left(x_{O_2,eq}(\delta_0) - 1\right)^2}\left(-x_{O_2,eq}(\delta_0)^3 + 3x_{O_2,eq}(\delta_0)^2 - 3x_{O_2,eq}(\delta_0) + F_5 + 1\right)\right)$$

$$F_8 = log\left(\frac{1}{\left(x_{O_2,eq}(\delta_0) - 1\right)^2}\left(-x_{O_2,eq}(\delta_0)^3 + 3x_{O_2,eq}(\delta_0)^2 - 3x_{O_2,eq}(\delta_0) + F_4 - 1\right)\right)$$

$$F_9 = log\left(\frac{1}{\left(x_{O_2,eq}(\delta_0) - 1\right)^2}\left(-x_{O_2,eq}(\delta_0)^3 + 3x_{O_2,eq}(\delta_0)^2 - 3x_{O_2,eq}(\delta_0) + F_5 - 1\right)\right)$$

12.3Quantification of measurement errors in Chapter 5

The curves showing the molar fraction of oxygen at the oxygen sensor, x_{O_2}, are simply subtracted from the blank (temperature of 298 K) and vice versa for oxidation and reduction, respectively. The standard error of the curve, SE_c, of this new curve is

$$SE_c(T) = \sqrt{\frac{s_c^2(T = 298K)}{N_c(T = 298K)} + \frac{s_c^2(T)}{N_c(T)}} \qquad (12\text{-}1)$$

where $\mathbf{s_c^2}(\mathbf{T})$ and $\mathbf{N_c}(\mathbf{T})$ are the sample variance and the number of data points collected by the oxygen sensor at temperature *T*. Due to the high frequency at which data is collected (1 kHz) and the duration of the intervals of 90 s, the standard error is small ($< 5 \cdot 10^{-6}$).

For the oxidation, however, a second and by far more significant error is introduced when the difference in the time constant of the oxidation and reduction intervals as listed in Table 5-1 is used to determine the difference in time of the observed and expected breakthrough. The standard error of calculating the real time constant for the gas switch from nitrogen to air, $\mathbf{SE_t}$, is given by

$$SE_t(T) = \sqrt{\frac{s_{t,oxi}^2(T)}{N_{t,oxi}(T)} + \frac{s_{t,red}^2(T)}{N_{t,red}(T)}} \qquad (12\text{-}2)$$

where $\mathbf{s_t^2}(\mathbf{T})$ and $\mathbf{N_t}(\mathbf{T})$ are the sample variance and number of data points describing the gas switches, respectively. The subscript oxi and red refer to gas switches from nitrogen to air and air to nitrogen, respectively. For example, $\mathbf{SE_t}$ of the time interval during which the entire incoming oxygen is taken up by the $SrFeO_{3-\delta}$ is 5.3 ms. Therefore, there is 95 % chance that the true mean time during which all oxygen is taken up lies within the interval (1105.6 ms, 1126.4 ms). In terms of moles of oxygen taken up the difference between the lower and upper boundary of this interval is 1.4 µmol of O_2.

A third error is introduced by conducting the one-point calibration of the oxygen sensor in air. Here, the reference voltage for nitrogen changes marginally with temperature. The effect this has on the maximum observed rate of reaction, $r_{O_2}^m$, is legible. However, there is great impact on the overall amount of oxygen released or taken up by the material due to the "tail" of the signal. If for example the higher reference voltage for nitrogen at ele-

vated temperatures is taken, then, the produced amount of oxygen during the reduction would be significantly less than if the reference voltage for nitrogen taken at 298 K were to serve as the reference case.

The amount of oxygen taken up and released in this experiment using 0.611 g of strontium ferrite is listed in Table 5-3. At most temperatures, the release of oxygen is significantly less than the oxygen taken up when switching the inlet gas from nitrogen to air. Furthermore, the potential of oxygen release and uptake determined by thermogravimetric analysis (see section 4.4.1) is realised only at high temperatures; in the case of oxygen uptake and 898 K even exceed by ~14 %.

12.4 List of candidate materials

Table 12-3: Potential oxygen carrier systems with an equilibrium temperature $T_{eq}(pO_{2,red} = 0.34\ bar)$ between 523 and 1323 K based on enthalpies of reactions supplied by the Materials Project.(Jain *et al.*, 2013) The efficiencies of oxygen carriers for which insufficient heat is supplied by the oxy-fuel combustion of 1 mol of oxygen are discarded.

Oxidised OC	Reduced OC	$T_{eq}(pO_{2,red} = 0.34$ bar) K	$\Delta H_r^o(T_{eq})$ kJ/mol	ΔH_r^o (298K) kJ/mol	Net efficiency	Case
BaO_2	BaO	778	152	161	31.5%	2B
$CdSeO_4$	$CdSeO_3$	777	152	161	31.4%	2B
$LiBiO_3$	$LiBiO_2$	782	153	162	31.7%	2B
$Mn(SeO_3)_2$	$MnSe_2O_5$	788	154	163	32.2%	2B
$SrCr_2O_7$	$SrCr_2O_4$	788	155	163	32.2%	2B
$Sr_2Cu_2O_5$	$SrCuO_2$	794	156	165	32.6%	2B
$Na_2Cr_2O_7$	$NaCrO_2$	808	158	167	33.6%	2B
$La_3Pt_3O_{11}$	$La_2Pt_2O_7$	817	159	169	n/a	1
$MnPO_4$	$Mn_2P_2O_7$	817	159	169	34.0%	2B
RbO_3	Rb_2O_3	816	159	169	33.9%	2B
$SrFeO_3$	$Sr_2Fe_2O_5$	813	159	168	34.7%	2B
$Ho_2(SeO_4)_3$	$Ho_2(SeO_3)_3$	832	162	172	35.0%	2B
Eu_3ReO_8	Eu_3ReO_7	857	166	177	39.3%	2B
Hg_2SeO5	Hg_2SeO_3	859	166	177	39.4%	2B
$NaAgO_2$	NaAgO	862	167	178	39.6%	2B
V_2O_5	V_3O_7	858	167	177	39.4%	2B
MnO_2	Mn_3O_4	866	168	179	39.8%	2B
Ti_2O_7	Ti_3O_5	864	168	178	39.7%	2B
Ag_2SeO_4	Ag_2SeO_3	889	171	183	40.4%	2B
$SbOF_3$	SbF_3	886	172	182	40.4%	2B
$BaFeO_3$	$Ba_2Fe_2O_5$	919	176	189	40.6%	2B
$CoSeO_4$	$CoSeO_3$	925	178	190	40.6%	2A
CsO_2	Cs_3O	939	180	193	40.6%	2A
PbO_2	PbO	932	180	191	40.6%	2A
$CsIO_4$	CsI	943	181	193	40.6%	2A
$KBiO_3$	$KBiO_2$	942	181	193	40.6%	2A
$KAgO_2$	KAgO	962	184	197	40.6%	2A
$MnSeO_4$	$MnSeO_3$	967	185	198	40.6%	2A
Mo_2P2O_{11}	$MoPO_5$	966	185	198	n/a	1
KIO_4	KI	970	186	199	40.6%	2A
$V_2Hg_2O_7$	$VHgO_3$	966	186	198	40.6%	2A

$NaMnO_4$	$Na_2Mn_2O_3$	979	188	200	40.6%	2A
Sm2Mn2O7	$SmMnO_3$	979	188	200	41.1%	2A
$Bi_3Pt_3O_{11}$	$Bi_2Pt_2O_7$	1012	192	207	n/a	1
$NaBiO_3$	$NaBiO_2$	1006	192	206	42.4%	2A
$Hg(IO_3)_2$	HgI_2	1013	193	207	40.6%	2A
I2O5	I	1021	194	208	40.6%	2A
CsO_2	$Cs_{11}O_3$	1038	197	212	40.6%	2A
$TlPO_4$	$TlPO_3$	1030	197	210	41.1%	2A
$Tl(IO_3)_3$	TlI_3	1035	198	211	40.6%	2A
$Mo_2P_3O_{13}$	$Mo_2(PO_4)_3$	1044	199	213	n/a	1
Cu_2O_3	Cu_2O	1055	200	215	41.9%	2A
$MgSeO_4$	$MgSeO_3$	1049	200	214	n/a	1
$PbSeO_4$	$PbSeO_3$	1109	210	225	n/a	1
$Lu_2Mn_2O_7$	$LuMnO_3$	1119	211	227	n/a	1
RbO_3	Rb_2O	1130	214	229	n/a	1
$Er_2Mn_2O_7$	$ErMnO_3$	1150	216	233	n/a	1
$Tm_2Mn_2O_7$	$TmMnO_3$	1141	216	231	n/a	1
$Dy_2Mn_2O_7$	$DyMnO_3$	1153	217	234	n/a	1
$Ho_2Mn_2O_7$	$HoMnO_3$	1156	217	234	n/a	1
V_2O_5	VO_2	1152	218	234	n/a	1
Ti_2O_7	Ti_2O_3	1171	221	237	n/a	1
$Y_2Mn_2O_7$	$YMnO_3$	1168	221	237	n/a	1
Sb_2O_5	SbO_2	1175	222	238	n/a	1
$Bi(IO_3)_3$	BiI_3	1203	225	243	n/a	1
$PdSeO_4$	PdSe	1196	225	242	n/a	1
$Cd(IO_3)_2$	CdI_2	1211	226	245	n/a	1
$Pb(IO_3)_2$	PbI_2	1205	227	244	n/a	1
PtO_2	Pt_3O_4	1215	228	245	n/a	1
$AsPO_5$	$AsPO_4$	1228	229	248	n/a	1
CsO_2	Cs_7O	1234	230	249	n/a	1
HgO	Hg	1237	231	250	n/a	1
P_2WO_8	P_2WO_7	1238	232	250	n/a	1
$In(IO_3)_3$	InI_3	1245	233	251	n/a	1
$Ni(IO_3)_2$	NiI_2	1244	233	251	n/a	1
$Zn(IO_3)_2$	ZnI_2	1240	233	250	n/a	1
$K(TeO_3)_2$	$K_2Te_4O_9$	1261	235	254	n/a	1
TaO_{10}	Ta	1269	238	256	n/a	1
$Ga(IO_3)_3$	GaI_3	1294	241	260	n/a	1

$SrSeO_4$	$SrSeO_3$	1290	241	260	n/a	1
Tl_2TeO_6	Tl_2TeO_3	1292	242	260	n/a	1
$BaSeO_4$	$BaSeO_3$	1312	243	264	n/a	1
NaO_2	Na	1305	243	262	n/a	1
$CsAuO_2$	CsAuO	1314	244	264	n/a	1
$HgSeO_4$	HgSe	1311	244	263	n/a	1
$P_2W_2O_{11}$	PWO_5	1309	244	263	n/a	1
$Tb_2Mn_2O_7$	$TbMnO_3$	1310	245	263	n/a	1
VPO_5	VPO_4	1318	246	265	n/a	1